Étude du repliement tridimensionnel de la chromatine en domaines topologiques

Quentin Szabo

THÈSE POUR OBTENIR LE GRADE DE DOCTEUR DE L'UNIVERSITÉ DE MONTPELLIER

En Biologie Moléculaire et Cellulaire

École doctorale CBS2, Sciences Chimiques et Biologiques pour la Santé

Institut de Génétique Humaine, UMR 9002

Étude du repliement tridimensionnel de la chromatine en domaines topologiques

Présentée par Quentin SZABO
Le 27 Novembre 2019

Sous la direction de Frédéric BANTIGNIES et Giacomo CAVALLI

Devant le jury composé de

Marcelo NOLLMANN, Directeur de recherche, CBS, Montpellier	Président du jury
Olivier GADAL, Directeur de recherche, LBME, Toulouse	Rapporteur
Luca GIORGETTI, Directeur de recherche, FMI, Basel	Rapporteur
Yad GHAVI-HELM, Chargée de recherche, IGFL, Lyon	Examinatrice
Frédéric BANTIGNIES, Directeur de recherche, IGH, Montpellier	Directeur de thèse
Giacomo CAVALLI, Directeur de recherche, IGH, Montpellier	Directeur de thèse

UNIVERSITÉ DE MONTPELLIER

Three-dimensional chromatin folding into topologically associating domains

Table of contents

Résumé de la thèse en français

Mon projet de thèse a consisté à étudier les mécanismes du repliement tridimensionnel du génome dans les cellules eucaryotes. L'organisation des chromosomes est étroitement liée à la régulation de nombreuses fonctions biologiques, telles que le contrôle de l'expression génique, la réplication de l'ADN ou encore la stabilité génomique. La méthode de « chromosome conformation capture » Hi-C, qui permet la cartographie des interactions entre régions d'ADN, a révélé que chez de nombreuses espèces, le génome est organisé en domaines enrichis en interactions chromatiniennes, les « Topologically Associating Domains » (TADs). Les TADs sont apparus être des acteurs majeurs de la régulation du génome par leur capacité à définir spatialement des domaines fonctionnels. Cependant, les méthodes de chromosome conformation capture générèrent des profils d'interactions généralement moyennés à partir d'ensemble de cellules. Déterminer la nature du repliement des TADs en cellules individuelles est donc crucial pour comprendre la relation structure-fonction de ces domaines génomiques. Au cours de ma thèse, j'ai utilisé des techniques de marquage fluorescent d'ADN combinés à de la microscopie en super-résolution afin d'étudier l'organisation des chromosomes en cellules uniques. Chez la drosophile, les TADs coïncident avec le partitionnement de la chromatine en domaines épigénétiques distincts. Nous avons pu caractériser chez cette espèce que les chromosomes sont organisés en une série d'unités discrètes qui correspondent aux TADs, reflétant l'exclusion mutuelle de régions transcriptionnellement actives et inactives. Ces résultats indiquent que les TADs de drosophile forment des domaines physiques qui caractérisent un niveau d'organisation structurale des chromosomes en cellules uniques. Chez les mammifères, la majorité des TADs est formée grâce à l'action du complexe cohésine et à la présence de la protéine CCCTC-binding factor (CTCF) à leurs frontières. L'application de l'imagerie à super-résolution dans des cellules souches embryonnaires et des cellules progénitrices neuronales de souris nous a permis de caractériser l'hétérogénéité du repliement des TAD d'une cellule à l'autre. Nous avons notamment pu observer leur organisation en sous-domaines globulaires qui semblent représenter une propriété générale du repliement de la chromatine à l'échelle de la centaine de nanomètres. De plus, nos résultats indiquent que les interactions chromatiniennes sont fortement favorisées à l'intérieur des TADs dans la majorité des cellules. La déplétion de CTCF abolie l'organisation spatiale de la fibre de chromatine associée aux TAD, soulignant le rôle de cette protéine dans la génération de barrières physiques entre TAD adjacents. Ces données démontrent que le repliement dynamique des TAD est compatible avec l'établissement d'environnements chromosomiques dans lesquels les contacts sont privilégiés, et réconcilient ainsi la nature probabiliste du repliement de la chromatine avec le rôle proposé des TAD dans la définition spatiale d'unités génomiques fonctionnelles.

Thesis summary

My thesis project consisted in studying the mechanisms of the three-dimensional genome folding in eukaryotic cells. The organization of chromosomes is closely related to the regulation of many biological processes, such as gene expression control, DNA replication or genomic stability. The Hi-C "chromosome conformation capture" method, which allows the mapping of interactions between DNA regions, has revealed that the genome of many species is organized into domains enriched in chromatin interactions, the "Topologically Associating Domains" (TADs). TADs have emerged as major players of genome regulation by their ability to spatially define functional domains. However, chromosome conformation capture methods generate averaged interaction profiles that generally come from an ensemble of cells. Determining the nature and the folding of TADs in individual cells is therefore crucial to better understand the structure-function relationship of these domains. During my thesis, I used a combination of fluorescent DNA labeling and super-resolution microscopy to characterize the organization of chromosomes in single cells. In *Drosophila*, TADs coincide with the partitioning of the chromatin into distinct epigenetic domains. In this species, we could characterize the folding of the chromosomes into a series of discrete units that correspond to TADs, reflecting the mutual exclusion of transcriptionally active and inactive regions. These results indicate that *Drosophila* TADs form physical domains that characterize a higher-order layer of chromosome folding in individual cells. In mammals, the majority of TADs emerge through the action of the cohesin complex and the CCCTC-binding factor (CTCF) bound at their borders. The application of super-resolution imaging in mouse embryonic stem cells and neuronal progenitor cells revealed the high degree of cell-to-cell heterogeneity of TAD folding, ranging from condensed and globular objects to dispersed and stretched conformations. We were able to observe their organization into discrete subdomains which seem to represent a general property of the folding of the chromatin fiber at the nanoscale. Furthermore, our data indicate that the physical intermingling of the chromatin is highly favored within TADs in a large majority of cells. Depletion of CTCF abolishes the TAD-dependent spatial organization of the chromatin fiber, highlighting the role of this protein in generating physical barriers between adjacent TADs. Altogether, our results demonstrate that the dynamic folding of TAD is compatible with the establishment of chromosomal environments in which contacts are privileged, and thus reconcile the probabilistic nature of chromatin folding with the proposed role of TADs in the spatial definition of functional genomic units.

Acknowledgments

Before presenting my thesis work, I would first like to warmly thank my thesis supervisors, Frédéric Bantignies and Giacomo Cavalli, for their guidance and the sharing of their scientific experience. I had the opportunity to enjoy both a certain autonomy in carrying out my work and exceptional support thanks to their advice and their supervision. I found in this laboratory a particularly stimulating intellectual environment and a working atmosphere conducive to the development and the realization of my thesis projects. I also greatly benefited from the kindness and attention of the people in the lab and in my work environment. I would therefore like to thank Thierry, Anne-Marie, Julio, Marcelo, Julien, Bernd, Lauriane, Caroline, Axelle, Yuki, Stefan, Ivana, Boyan, Satish, Giorgio and Filippo. A special gratitude goes to Vincent for his presence and support throughout my thesis.

Author's note

This manuscript is organized in three chapters. The first chapter will present the background of my thesis project as a general introduction on higher-order chromosome organization. The second chapter will be dedicated to the results I achieved during my thesis. I have been mainly working on the folding of the chromatin fiber into topologically associating domains (TADs) in both *Drosophila* and mouse using super-resolution imaging. The first sub-part of the chapter 2 will correspond to a published article in Science Advances in which I could describe and characterize the structural organization of *Drosophila* chromosomes as a succession of discrete units that correspond to TADs. The second sub-part will present an ongoing project that aims to better understand the principles of the physical folding of TADs during mammalian cell differentiation. The chapter 3 will be a general discussion concerning the implication of my thesis work and the resulting perspectives. Last, in the supplementary material section of this manuscript, I included results obtained in another ongoing project in which I was involved, centered on the role of the *barrier-to-autointegration factor* gene in the regulation of higher-order chromatin organization in *Drosophila*. I also included a protocol accepted for publication in Methods in Molecular Biology of DNA fluorescent in situ hybridization, an experimental approach to study chromosome folding at the center of my research projects.

I already had the opportunity to publish or prepare for submission a part of my work. Therefore, for the convenience of the reader, these manuscripts will be directly included in the core of the thesis in their edited or prepared version.

Abbreviations table

3C/4C/5C/Hi-C: Chromosome conformation capture/circular chromosome conformation capture - chromosome conformation capture-on-chip/chromosome conformation capture carbon copy/high-throughput chromosome conformation capture

3D: Three-dimensional

BAF: Barrier-to-autointegration factor

bp/kb/Mb: Base pair/kilobase/megabase

CLSM: Confocal laser scanning microscopy

CT: Chromosome territory

(q)ChIP(-seq): (quantitative)Chromatin immunoprecipitation(-sequencing)

CTCF: CCCTC-binding factor

Dam: DNA adenine methyltransferase

DHS: DNase I hypersensitive site

DNA: Deoxyribonucleic acid

dsRNA: double-stranded RNA

ESC: Embryonic stem cell

(Hi-)FISH: (High-throughput) Fluorescence in situ hybridization

H2AK119ub: Mono-ubiquitinated lysine 119 of histone H2A

H3K4me1/2/3: Mono/di/trimethylated lysine 4 of histone H3

H3K9me1/2/3: Mono/di/trimethylated lysine 9 of histone H3

H3K27ac/me2/3: Acetylated/di/trimethylated lysine 27 of histone H3

H3K36me3: Trimethylated lysine 36 of histone H3

HMT: Histone methyltransferase

HP1: Heterochromatic protein 1

KD: Knock-down

LAD: Lamina-associated domain

LBR: Lamin B receptor

NA: Numerical aperture

(ncx)NPC: (neocortex)Neural progenitor cell

OTF: Optical transfer function

PcG: Polycomb group

PC: Polycomb

PCR: Polymerase chain reaction

Pol: Polymerase

PRC1/2: Polycomb repressive complex 1/2

PRE: Polycomb response element

PSF: Point-spread function

PSS: Pairing sensitive silencing

PTM: Post-translational modifications

RNA(-seq): Ribonucleic acids(-sequencing)

RNAi: RNA interference

RT-qPCR: Reverse-transcription and real-time polymerase chain reaction

nm/µm: Nanometer/micrometer

(3D-)SIM: (3D-)Structured illumination microscopy

SMLM: Single-molecule localization microscopy

SNR: Signal-to-noise

STED: Stimulated emission depletion

TAD: Topologically associating domains

TF: Transcription factor

TrxG: Trithorax group

TSS: Transcription start site

WF: Widefield

Chapter 1: Introduction

In this first chapter, I will review current knowledges of three-dimensional (3D) chromosome folding at different scales, from the formation of the chromatin fiber to the organization of chromosome territories, highlighting the intricate link between genome architecture and activity. Special attention will be paid to the genome folding into topologically associating domains (TADs), which will be mainly presented by a review I wrote and recently published in the journal Science Advances. Imaging and chromosome conformation capture methods will be emphasized for their major contributions to the field. In the annex of this chapter, I will present general concepts of fluorescence microscopy, focusing on super-resolution 3D-structured illumination microscopy (3D-SIM). Last, I also included in the annex another review that I co-wrote. This short review aims to summarize general aspects of higher-order genome organization and function, which will have been presented in more details during the introduction.

1.1 Historical perspectives and early observations of nuclear organization

The genetic information is encoded within the deoxyribonucleic acid (DNA) molecule. In 1953, the structure of the DNA is resolved (Watson and Crick, 1953), providing a structural basis for the molecule that was identified to support heredity (Avery et al., 1944). These fundamental discoveries supplemented pioneer studies and revolutionary concepts of modern biology. In 1839, the *cell theory* introduced by Matthias Schleiden and Theodor Schwann proposed that cells, originally described by Robert Hooke in 1665, are the organizational units of living organisms. In 1831, Robert Brown coined an organelle present within the cells, the nucleus, which was suggested to be involved in heredity by Ernst Haeckel in 1866. Using dye staining within the nucleus, Walther Flemming discovered at the end of the 1870's the chromatin, named from the Greek *khroma* which means "colored". He also described the process of meiosis, and in the early 1900s, Walter Sutton and Theodor Bovari formulated *the chromosome theory inheritance* that proposed that chromosomes carry genes and are the support of the heredity. These decades have seen the first descriptions of chromosome organization in interphase. In 1885 Carl Rabl described a polarized organization of the chromosomes, and this concept of specific territorial organization of the chromosomes was supported by Theodor Boveri who introduced the term of chromosome territories (CTs) in 1909. In 1928, Emil Heitz described two different cytological organizations of the chromatin in interphase using chromosome staining. He defined as heterochromatin regions that remain condensed through the cell cycle as opposite to euchromatin that is decondensed in interphase (Passarge, 1979). He proposed that this differential organization reflects different functional characteristics, such as euchromatin is associated with the gene activity, while heterochromatin is composed of genetically inert regions. His contemporary Hermann Muller observed the phenomenon of position effect variegation, in which artificial relocation of a gene close to heterochromatin represses its activity (Brown, 1966; Dillon, 2004). These early works thus established a relationship between the structure and the function of the genome and paved the way for what is still nowadays an extensive field of research.

The application of electron microscopy around the 1970s highlighted the different condensation and nuclear positioning of the heterochromatin, condensed and generally located at the nuclear periphery, and the euchromatin, less condensed and found preferentially toward the interior of the nucleus. Electron microscopy also enabled the characterization of the primary structure of the chromatin fiber, organized as "beads-on-string", corresponding to nucleosomes separated by linker DNA (Woodcock and Ghosh, 2010). The chromatin was also though to arrange in 30 nanometers (nm) fiber, but this organization has been controversial and recent evidences suggest that this conformation doesn't exist in nuclei under physiological conditions (Ou et al., 2017). Development of fluorescence microscopy and the labeling of specific genomic regions with fluorescence in situ hybridization (FISH) confirmed the interphase organization of the genome into CTs, with gene-poor regions located more often close to the periphery of the nucleus compared to the gene-rich ones (Cremer and Cremer 2010; Croft et al., 1999), and led to

the appearance of new models of higher-order chromosome folding at the turn of the 21st century. It was proposed that chromatin regions can undergo long-range contacts through chromatin loops (Branco and Pombo, 2006; Osborne et al., 2004; de Laat, 2007), or that the fiber fold into higher-order, discrete chromatin domains (Belmont et al., 1989; Albiez et al., 2006, Cremer and Cremer, 2010). In the last decades, the constant improvement of imaging methods combined with technological breakthroughs in genomics and molecular biology techniques has allowed significant improvements in our understanding of nuclear organization, the mechanisms involved, and its relevance for genome regulation. Current knowledges of higher-order chromosome folding will be reviewed in this introduction.

1.2 The chromatin fiber: a dynamic template for genome organization

1.2.1 Ultrastructure of the chromatin fiber

In eukaryotic cells, the association between the DNA and other biomolecules such as proteins or ribonucleic acids (RNAs) gives rise to the chromatin fiber. The phosphate backbone of the DNA, negatively charged, interacts with the basic histone proteins that are organized in octamers composed of one pair of each histones: H2A, H2B, H3 and H4. This DNA-histone association forms the nucleosome, the first layer and repeating basic unit of chromatin organization, in which 147 base pairs (bp) of DNA are wrapped around the histone octamer in 1.65 left-handed super helical turns allowing ~7 fold compaction of genomic DNA [(Luger et al., 1997; Richmond and Davey, 2003) Figure 1A]. Adjacent nucleosomes are connected by short linker DNA segments of ~20-75 bp which can be bound by the H1 histone protein (Woodcock and Ghosh 2010; Cutter and Hayes, 2015). This organization corresponds to the primary structure of the chromosomes: the ~11 nm chromatin fiber (Ou et al., 2017). Spacing between nucleosomes, defined for example by chromatin remodeling complexes, and short-range nucleosome-nucleosome interactions result in various chromatin structures (Luger et al., 2012). Recent *in situ* electron microscopy tomography revealed that nucleosomes arrange into disordered chains of various particle densities that have a diameter from 5 to 24 nm (Ou et al., 2017). Nucleosome density is heterogeneous along the genome and non-adjacent nucleosomal contacts occur more frequently in heterochromatin which forms dense clutches compared to the more open euchromatin (Risca et al., 2017; Ricci et al., 2015).

In addition to its role in packaging the genome into the nucleus, the chromatin structure regulates gene accessibility for various functional processes such as transcription, replication or DNA repair. The regulation of chromatin structure and its dynamics has emerged as a crucial mechanism of genome activity. On top of the histone core-DNA interactions, evolutionary conserved N-terminal tails of histones exit out of nucleosomes and are subjected to various post-translational modifications (PTMs)

from ‘writer’ enzymes. These marks can affect nucleosome-nucleosome interactions and serve as platforms to recruit ‘reader’ proteins and complexes that can in turn also change chromatin structure (Kouzarides, 2007; Venkatesh and Workman, 2015). The nature of these PTMs, together with nucleosome density and local compaction, reflects functional chromatin states. Open and accessible DNA is often associated with active regulatory regions, such as gene promoters or enhancers that can be bound by transcription factors (TFs) or RNA polymerase (RNA pol). On the other hand, densely arranged nucleosomes, condensed chromatin and presence of linker histones including H1 variants reflect non-permissive and repressed states [(Klemm et al., 2019) Figure 1B]. The mechanisms and the biochemistry of chromatin modifications represent a broad field of research in biology, with a growing number of discovered PTMs and a wide range of molecules involved in their regulation (Bannister and Kouzarides, 2011). Among these various histone marks, some have been well characterized and tightly linked to functional and structural regulation of the chromatin fiber. For example, the di and tri-methylation of the lysine 9 of the histone H3 (H3K9me2/3), hallmarks of constitutive heterochromatin, are recognized by the chromodomain of the heterochromatic protein 1 (HP1) which forms dimers and bridges neighboring nucleosomes (Lachner et al., 2001; Bannister et al., 2001; Machida et al., 2018), associated with further chromatin condensation (Saksouk et al., 2015). Another mark, H3K27me3, is deposited by the Polycomb repressive complex 2 (PRC2) and can be bound by the PRC1 that is able to compact chromatin (Francis et al., 2004) and decrease nucleosome spacing (King et al., 2018), preventing transcriptional initiation by RNA pol II (Dellino et al., 2004). Acetylation neutralizes lysine’s positive charges and potentially reduces DNA-histone interactions, which is associated with active transcription, while its deacetylation counterpart correlates with transcriptional repression (Bannister and Kouzarides, 2011). In agreement with their distinct characteristics, different nucleosomal stacking organizations and local chromatin compactions were observed between active and H3K9me3 or H3K27me3 repressed chromatin states (Risca et al., Nature 2017).

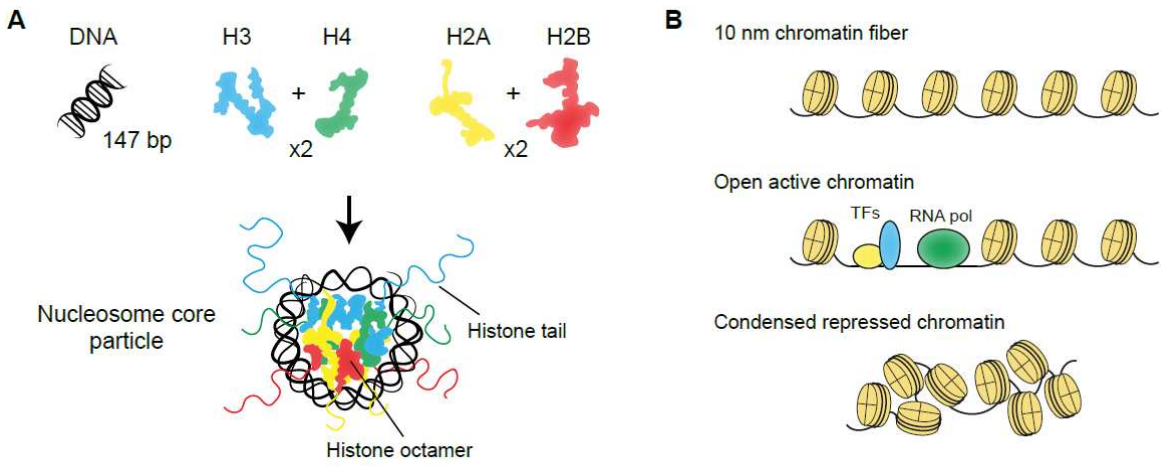

Figure 1. Structure of the chromatin fiber. (**A**) Schematic representation of a nucleosome, the basic unit of the chromatin fiber. 147 bp of a DNA molecule is wrapped in ~1.7 left-handed superhelix around an octamer of core histones formed by H3/H4 and H2A/H2B tetramers (2 copies of each histone). Artwork was inspired from (Draizen et al., 2016). (**B**) Chromatin fiber undergoes different local structural organizations and nucleosome densities. Active chromatin is associated to an open conformation and accessibility to TFs and transcriptional machinery as opposed to repressed and condensed chromatin conformations.

1.2.2 Metazoan genome partitioning into chromatin domains

In line with its local 3D conformation, the chromatin fiber can be classified into different types associated to distinct functional "epigenetic states", hereafter defined by the nature of the underlying histones PTMs and the binding of specific chromatin factors (Mikkelsen et al., 2007; Kharchenko et al., 2011; Filion et al., 2010; Ho et al., 2014).

Active chromatin, in which genes are permissive to transcription, is characterized by its high accessibility to TFs and transcriptional machinery. DNase I hypersensitive sites (DHS) are found at transcription start sites (TSSs), but also at untranslated transcribed regions, exonic and intronic sequences, as well at distal enhancer cis-regulatory elements (Thurman et al., 2012; Boyle et al., 2008; Lee et al., 2004). If active chromatin is characterized by extensive acetylation, notably by the acetylation of the lysine 27 of histone H3 (H3K27ac), it appears heterogeneous and can be subdivided into different classes as the various genomic elements that compose it are associated to distinct epigenetic signatures. Gene promoters are decorated by H3K4me2/me3, transcription elongation at gene body is associated with H3K36me3, and enhancers are enriched in H3K4me1 (Mikkelsen et al., 2007; Kharchenko et al., 2011; Filion et al., 2010; Ho et al., 2014; Heintzman et al., 2009). The deposition of these activity-related histones marks relies notably on the action of the large family of trithorax group (TrxG) proteins through diverse mechanisms (Schuettengruber et al., 2017).

Polycomb associated chromatin, sometimes referred to as facultative heterochromatin, is associated with transcriptional repression and forms at developmentally regulated genes. Polycomb group (PcG) genes are organized into two main complexes, PRC1 and PRC2 (Schuettengruber et al., 2017). A canonical model for PcG-mediated repression involves their recruitment by DNA-binding factors at specific genomic locations, characterized as Polycomb response elements (PREs) in *Drosophila* (Nègre et al., 2006; Tolhuis et al., 2006; Kassis and Brown 2013), followed by the tri-methylation of H3K27 by the methyltransferase (HMT) enhancer of zeste of the PRC2 complex (Müller et al., 2002, Wang et al,. 2004). The mark is then recognized through the chromodomain of the subunit Polycomb (PC) of the PRC1, which then mediates the ubiquitylation of the lysine 119 of the histone H2A (H2AK119ub in mammals, H2AK118ub in Drosophila) by the RING1 and Polycomb group ring-finger domain protein subunits (Schuettengruber et al., 2017). The transcriptional repression of the chromatin bound by the PcG proteins is probably mediated at least in part by the compaction of the chromatin which becomes inaccessible to the transcription machinery and remodeling complexes (Shao et al., 1999). Polycomb repressed regions are scattered along the genome and recognizable by their enrichment in H3K27me3 (Schuettengruber et al., 2017; Kharchenko et al., Nature 2011; Filion et al., 2010; Ho et al., 2014). If these repressed domains are a clear and well characterized feature of metazoan genomes, some regions called bivalent domains are decorated both with PcG associated H3K27me3 and TrxG associated H3K4me3 marks (Bernstein et al., 2006; Voigt et al,. 2013). These regions, originally characterized in mouse embryonic stem cells (ESCs), were proposed to silence developmental genes in a poised state before further activation during specific cell lineage, but precise mechanisms for bivalency chromatin establishment and resolution during development are still missing. Last, different studies showed that PRC1 subunits are able to act independently of PRC2 and that their role in gene regulation are not uniquely restricted to transcriptional repression (Gao et al., 2014; Loubiere et al., 2016; Cohen et al., 2018; Cohen et al., 2019).

Constitutive heterochromatin, as opposed to the facultative one, is present along the genome as large blocks mainly at pericentromeric regions and at telomeres. This chromatin type is gene-poor and enriched in repeat sequences satellites and transposable elements (Maison and Almounzi, 2004; Saksouk et al., 2015). It harbors H3K9me2/3 marks, the reader HP1 (Lachner et al., 2001; Bannister et al., 2001), is generally hypo-acetylated and has a low density of DHS (Kharchenko et al., 2011). Di and tri methylation of H3K9 at pericentromeric heterochromatin is catalyzed by the SUV39 family of HMTs. Heterochromatic spreading and maintenance are mediated by a self-assembly mechanism. K9 methylation is first deposited and can then be recognized by HMTs themselves or by HP1 which also interacts with HMTs, leading to the methylation of the adjacent nucleosomes (Stewart et al., 2005; Wang et al., 2016). The ability of HP1 to bind a wide range of other proteins including histone deacetylases (Grewal and Jia, 2007) and to dimerize and modify nucleosome organization (Canzio et al., 2013; Machida et al., 2018) provides then a mechanism for heterochromatin confinement and condensation.

Last, in mammals and *Drosophila*, another type of silent chromatin appears to be devoid of the known histone PTMs associated with heterochromatin. This gene-poor chromatin type represents about half of the *Drosophila* genome and is enriched in the linker histone H1 and interacts with Lamin (Filion et al., 2010; Kharchenko et al., 2011; Ernst and Kellis, 2010; Ernst et al., 2011). This 'void' chromatin contains genes that have cell-type specific expression programs (Filion et al., 2010), but little is known about the constitution of this chromatin state or in the mechanism of silencing associated with. This chromatin may correspond to a "default" state, inactive because of the lack of specific activating TFs. On the other hand, the presence in these regions of the H3K27me2 mark, necessary for the maintenance of their repressed transcriptional state, has been reported in *Drosophila* (Lee et al., 2015).

1.3 Imaging nuclear organization

Imaging has been a pioneering and powerful method to characterize genome folding, which historically goes back to the description of the organization of chromosomes into distinct territories by Carl Rabl in 1885 and Theodor Boveri in 1909. Fluorescence microscopy allowed the discovery of many principles of chromosome organization, including the formation of chromatin loops and discrete chromatin domains. Imaging has always provided some advantages compared to genomics and cell-population based assays, such as the study of single-cell behaviors or the ability to probe chromatin folding within tissues, keeping the information of the spatial organization of cells within their endogenous context. However, the identification of a given biomolecule in fluorescence imaging relies on the color -the emission wavelength- of the probe directed to it, therefore, the simultaneous imagining of many targets requires non overlapping emission spectra. Practically, it is difficult to use more than 4 different colors in fluorescence microscopy, limiting the number of different targets that can be examined at a time. The resolution of conventional microscopy is also limited to a few hundreds of nanometers, a scale at which are encompassed genes and chromatin domains. Recent developments have started to overcome these issues, such as new labeling and imaging strategies that permit the visualization and the identification of thousands of biomolecules in a given cell, and super-resolution microscopy that allows the characterization of chromosomal structures at an unprecedented resolution. A more detailed presentation of the concept of resolution in fluorescence microscopy and the methods used to bypass this limit will be presented in annex (section 1.9: Breaking the limit of resolution using super-resolution microscopy).

1.3.1 DNA fluorescent in situ hybridization

DNA FISH is a widely used method to probe chromosome organization. This technique consists in labeling genomic regions of interest *in situ* using fluorescent DNA probes that are then imaged using microscopy. Historically, probes were generated from cloned sequences from bacterial artificial chromosome libraries or from polymerase chain reaction (PCR) on extracted genomic DNA. Traditional labeling of probes is made by nick-translation reaction that incorporates fluorescently labeled nucleotides to a DNA template that will be further hybridized by base-complementarity to the genomic region of interest. Nicks are introduced by a DNAse I and are then filled with the modified nucleotides by the elongation activity of the DNA pol I. New generation of probes such as Oligopaints are made from complex libraries of single-stranded DNA oligos and can be efficiently used to label chromosomal regions from few kilobases to full chromosomes (Beliveau et al., 2012; Beliveau et al., 2015; Beliveau et al., 2018; Fields et al., 2019). FISH procedure typically involves 4 main steps: gentle fixation using paraformaldehyde, permeabilization, denaturation of the cellular DNA (2-3 minutes at 78-80°C), and hybridization of the fluorescent probes to the genomic DNA. These steps have been shown to preserve well the nuclear structure at least up to a spatial resolution of ~120 nm (Solovei et al., 2002; Markaki et al., 2012). Simultaneous imaging of different loci typically requires probes labeled with different fluorophores. A detailed FISH protocol will be presented at the end of this manuscript (Supplementary material; 4.2 Method article: Higher-order chromatin organization using 3D DNA Fluorescent in Situ Hybridization). FISH allows then the visualization of genomic loci in 3D-preserved nuclei and is particularly efficient to assess the variability of chromatin folding within a population of cells. This approach has then shed light on the probabilistic nature of many layers of nuclear organization. FISH being compatible with immunostaining, genomic loci positioning can be integrated with different features of the nucleus such as nuclear periphery or protein foci. However, because of the intrinsic resolution limit in conventional microscopy, the structure of loci of tens or hundreds of kb, a privileged scale of functional chromatin folding, cannot be resolved using conventional microscopy. Therefore, FISH has been classically used to probe the relative positioning of genomic loci by measuring distances rather than to directly visualize the structure or the shape of the labeled region (Figure 2A). The development of various super-resolution imaging methods now makes possible the visualization of chromosomal sub-structures with a spatial resolution beyond the diffraction limit, opening new opportunities in the characterization of nanoscale chromatin folding [Figure 2A (Markaki et al., 2012; Lakadamyali and Cosma, 2015)]. Furthermore, multiplexed approaches allow the sequential labeling and imaging of tens to hundreds of loci and bring FISH into the “omics” era (Figure 2B). These methods will be further described in the next sections.

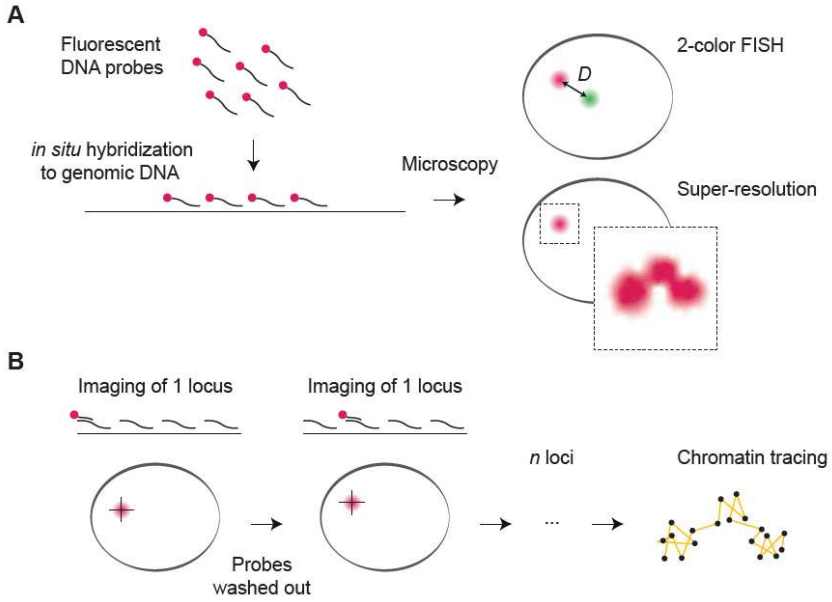

Figure 2. DNA FISH. This method consists in labeling specific genomic regions using fluorescent DNA probes. (**A**) FISH probes can be labeled in different colors, allowing the measurement of distances between loci of interest. Super-resolution imaging allows the characterization of the structure of genomic loci labeled by FISH at a nanoscale resolution. (**B**) Multiplexed barcoded probes allow sequential imaging of the chromatin fiber (Wang et al., 2016; Bintu Zhuang 2018; Nir et al., 2018; Cardozo Gizzi et al., 2019; Mateo et al., 2019). In these methods, all the probes are first hybridized to the genomic regions of interests. Fluorescent secondary probes are then hybridized to individual subregions that contain specific complementary barcodes. Cycles of imaging of individual subregion followed by washing of the probes are then used to trace chromatin path and/or to generate matrices of distances or interactions between loci.

1.3.2 Probing chromosome organization with conventional microscopy

DNA FISH has been used to demonstrate a non-random distribution of CTs in human cells, where gene-rich chromosomes are found more often toward the nucleus interior compared to gene-poor chromosomes (Croft et al., 1999; Cremer and Cremer, 2003; Boyle et al., 2001; Bolzer et al., 2005). CTs distribution also changes during cell differentiation, indicating a cell-type specific genome organization (Mayer et al., 2005). Importantly, this spatial organization is probabilistic and not fixed, i.e. the exact location and the neighbors of each chromosome vary in a cell population. Within CTs, a polarized organization is also observed with gene-dense, active and early-replicating regions preferentially located toward the nuclear interior (Murmann et al., 2005; Küpper et al., 2007; Goetze et al., 2007; Grasser et al., 2008). Moreover, transcribed gene-rich regions and less-expressed gene-poor regions were shown to have distinct structural properties, the latest being more condensed, more spherical and preferentially found at the nuclear periphery (Goetze et al., 2007). The radial positioning of loci seems however not inherited through mitosis (Thomson et al., 2004). A closer look into the CTs

revealed that they are made of basic chromatin domains that were estimated to encompass ~1 Mb (Albiez et al., 2006). This observation appears now particularly relevant considering the more recent discovery of TADs (see section 1.5: The topologically associating domains), which have a similar genomic size (Nora et al., 2012; Dixon et al., 2012). These pioneer studies combined with electron microscopy data led to the "chromosome territory-interchromatin compartment" model, in which CTs are made of an interconnected network of higher-order chromatin domains, forming a "sponge-like' structure, separated by a contiguous space, the interchromatin compartment [Figure 3 (Cremer and Cremer, 2010)].

Microscopy also revealed the presence of long-range associations between genomic regions scattered along chromosomes. In such fashion, gene-dense and transcribed regions spaced by hundreds of kb were shown to undergo spatial clustering (Shopland et al., 2006; Boutanaev et al., 2005). The observation of active regions that cluster together into RNA pol II foci led to the concept of "transcription factories" (Iborra et al., 1996; Osborne et al., 2004). This model, in which genes move to pre-existing static factories to be transcribed, has however been controversial (Sutherland and Bickmore, 2009). Long-range clustering of transcribed genes may indeed rather result from probabilistic and transient yet specific contacts between active chromatin loci (Cisse et al., 2013; Cattoni et al., 2017; Finn et al., 2019). Nevertheless, functional hubs of interactions associated with gene transcription have been well described using both microscopy and molecular biology techniques, some of them relying on the presence of specific TFs [Figure 2 (van Steensel and Furlong, 2019)]. Also, spatial proximity of genes around nuclear speckles that are enriched in splicing factors was observed (Brown et al., 2006; Brown et al., 2008; Fraser and Bickmore, 2007). The nuclear organization of the Polycomb proteins as foci (Bucheneau et al., 1998; Saurin et al., 1998) and the association of extreme long-range association between polycomb domains is another example of such functional association, in this case linked to transcriptional repression [(Bantignies et al., 2011) see also section 1.6: Polycomb-mediated chromatin architecture]. Live imaging has also been applied to study the dynamic behavior of chromosome organization. Tracking of fluorescently labeled chromosomal loci showed that chromatin is not static within the nucleus and undergoes constrained motion with a confinement radius of few hundreds of nanometers (Marshall et al., 1997). Consistently, fluorescence recovery after photobleaching experiments showed that chromatin doesn't diffuse over distances larger than several hundreds of nanometers (Abney et al., 1997). Interestingly, the chromatin motion varies depending on the locus positioning within the nucleus, with a lower motility associated to the nucleolus or the nuclear periphery, suggesting that specific nuclear structures constrain chromosome folding at the nucleus scale (Chubb et al., 2002). Yet, it was also shown that upon transcriptional activation, a locus can move from the nuclear periphery to the interior over distances of 1 to 5 µm, which illustrates that chromatin organization is not fixed and able to undergo substantial rewiring even in interphase (Chuang et al., 2006).

Last, the development of automatized imaging and analysis pipelines allows the use of microscopy in the realization of screens to identify factors involved in nuclear organization. These high-throughput

approaches are typically performed in 384-well plates in which cells are exposed to RNA interference (RNAi) for knock-down (KD) of genes of interests, and the quantitative analysis of FISH (or immunostaining) serves as a readout. Genome-wide screening has been applied to identify genes involved in the pairing of homologous chromosomes in *Drosophila* (Joyce et al., 2012), or genes regulating the 3D organization of Polycomb foci (Gonzalez et al., 2014). In human cells, an RNAi screen of hundreds of genes enabled the identification of factors implicated in the radial positioning of gene loci (Shachar et al., 2015).

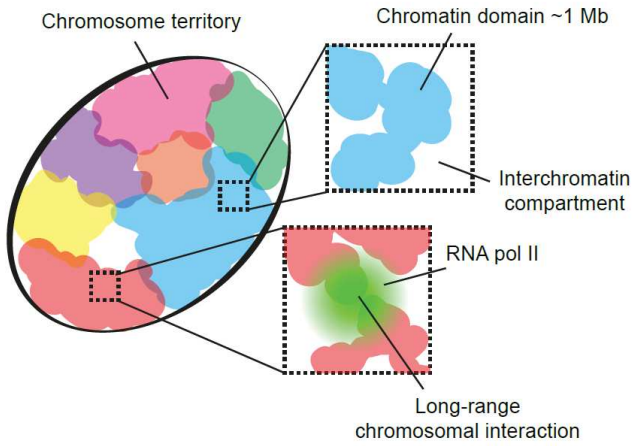

Figure 3. Higher-order chromosome organization. Individual chromosomes occupy distinct nuclear territories. Chromatin fold into ~1 Mb higher-order domains and is interspersed by a contiguous space, the interchromatin compartment. Long-range contacts can occur between transcriptionally active sites, visualized as RNA pol II foci within the nucleus.

1.3.3 Super-resolution microscopy and chromatin folding

If conventional microscopy has allowed the characterization of key features of chromosome organization, how the chromatin fiber fold at small length scales has remained difficult to address because of the limitation of the spatial resolution. The introduction of super-resolution microscopy has now made possible the investigation of chromatin structure at the nanoscale [Figure 2A (Lakadamyali and Cosma, 2015)]. One of the very first studies applying super-resolution microscopy to nuclear architecture revealed novel features of chromatin and nuclear lamina organization using 3D-structured illumination microscopy [3D-SIM (Gustafsson et al., 2008; see also Annexe 1.9.2: Structured illumination microscopy)]. This study showed the folding of the chromatin into fibrous substructures of different degrees of compaction, with an exclusion of the condensed chromatin and the lamin at nuclear pore complexes (Schermelleh et al., 2008). 3D-SIM could also resolve the organization of the chromosomes into higher-order chromatin domains and less condensed perichromatin regions (Markaki

et al., 2010). Perichromatin regions were then shown to be transcriptionally active and enriched in H3K4me3, as opposed to transcriptionally silent and condensed chromatin domains (Smeets et al., 2014). Single-molecule localization microscopy [(SLML) see also Annexe 1.9.3: Single molecule localization microscopy and stimulated emission depletion] combined with fluorescently labeled histones were used to describe the non-random distribution of nucleosomes at the nanometer scale (Bohn et al., 2010; Matsuda et al., 2010). Nucleosomes arrange into clutches that vary in size and density, the smaller ones being associated with RNA pol II, the larger and denser with H1 (Ricci et al., 2015). Similarly, different organizations were shown to be associated with different epigenetic features, with repressive marks organized into condensed and larger aggregates than the active ones (Xu et al., 2018). SMLM combined with direct DNA staining revealed various degree of chromatin organization including dispersed chromatin structures, nanodomains of tens of nanometers and higher-order cluster of these nanodomains (Zessin et al., 2012; Benke and Manley, 2012; Szczurek et al., 2017; Fang et al., 2018). Imaging in living cells showed that chromatin nanodomains move coherently, suggesting they form relatively stable building blocks of higher-order chromosome organization (Nozaki et al., 2017). However, it is hard to determine the folding of specific genomic regions using DNA intercalant or histone labeling, and the correspondence to the genome of the chromatin nanodomains, estimated to contain from few to few hundreds of kb, remains to be investigated. The combination of super-resolution microcopy and FISH started to shed new lights on this relationship (Beliveau et al., 2015). The application of SMLM to image probes targeted to different epigenetically defined domains in *Drosophila* revealed different degrees of chromatin condensation, the transcriptionally active chromatin being the more decondensed, the Polycomb-repressed the more condensed, the inactive/transcriptionally silent chromatin (void chromatin) being in between (Boettiger et al., 2016). FISH and super-resolution microscopy were also used to precisely measure the contact frequencies between a large number of chromosomal loci in *Drosophila*, describing the probabilistic nature of long-range chromosomal interactions (Cattoni et al., 2017). To conclude, if the application of super-resolution microscopy in the study of nuclear organization is quite recent, it seems already promising for the characterization of the structure of the chromatin fiber in individual cells.

1.3.4 Sequential imaging of the chromatin fiber

Very recently, different methods have taken a crucial step concerning the number of loci that can be analyzed at a time using FISH. In these approaches, instead of simultaneously imagining different probes labeled with different colors, loci of interests are labeled and imaged in a sequential manner, allowing to probe and record the position of tens to hundreds of loci in individual cells. These methods can then be used to trace the path of the chromatin fiber or to reconstruct matrices of distances or contact frequencies between individual loci (Wang et al., 2016; Bintu et al., 2018; Nir et al., 2018; Cardozo

Gizzi et al., 2019; Mateo et al., 2019). Technically, the FISH is realized with a series of small oligonucleotides-derived probes such as Oligopaints that contain a sequence of complementarity to the genomic DNA concatenated with a specific "barcode" or "readout" sequence that will be further recognize by another fluorescent oligo. The entire region of interest is divided into different sub-regions that contain a unique barcode. All probes are first hybridized to the genomic DNA. Thereafter, one barcode imaging oligo is added, imaged, and washed out in a sequential manner. Repeat of this cycle *n* times allows the sequential imaging of all the individual *n* sub-regions (Figure 2B). These methods have proved particularly effective in characterizing different complex levels of chromatin organization at the single-cell level. At the chromosomal scale, the imaging of more than thirty consecutive TADs showed that they are spatially arranged in a polarized manner and form two spatial compartments that correspond to the segregation of active and inactive chromatin observed from Hi-C, the so-called A and B compartments [(Wang et al., 2016) see also section 1.4.3: Capturing genome-wide chromosome conformation with Hi-C]. Similarly, the labeling of consecutive chromosomal segments showed that 3D clusters of genomic regions can be predictive for the compartments defined by Hi-C despite the heterogeneity of chromosome folding in individual cells (Nir et al., 2018). At a shortest scale, the sequential imaging of 30 kb genomic segments in human cells revealed the folding of the chromatin into large TAD-like and globular structures that segregate preferentially at the TAD borders identified by cell-population based Hi-C (Bintu et al., 2018). Sequential imaging of the chromatin fiber has also been combined with direct or indirect RNA labelling. In such way, the structure of chromatin domains could be specifically assessed given their transcriptional activity in *Drosophila* embryos (Cardozzo et al., 2019; Mateo et al., 2019). These studies revealed that TAD folding varies according to the epigenome and the transcriptional activity, consistent with a dynamic behavior of TADs during cell differentiation or gene activation. More information on TADs will be provided in a dedicated chapter (section 1.5: The topologically associating domains).

1.4 The advancement in understanding genome organization with the "C" techniques

1.4.1 3C: Chromosome conformation capture

Our comprehension of chromosome organization has drastically increased the last decades with the introduction of a molecular biology method called chromosome conformation capture (3C). This method consists in measuring contact frequencies between pairs of loci based on a proximity-ligation assay (Dekker et al., 2002). Basically, nuclei are crosslinked using formaldehyde before digestion of DNA by a restriction enzyme. DNA fragments that are in close spatial proximity are then ligated to each

other using a ligase and further detected using PCR (Figure 4). Thus, genomic loci that are frequently in contact will likely be more often detected in a population of cells than those that rarely interact. 3C enabled the characterization of specific chromatin interactions between functional genomic elements with a high genomic resolution. Its application to the β-globin locus revealed the presence of active chromatin hubs, in which specific looping contacts occur between DHS sites of the locus control region and active genes of the β-globin locus, with switches in interactions correlated with differential activities during development (Tolhuis et al., 2002; Palstra et al., 2003). This method also showed different architectures associated with the paternal and maternal imprinted genes Igf2 and H19 (Murrell et al., 2004), interchromosomal interactions between loci that are alternatively expressed (Spilianakis et al., 2005), or contacts between gene promoters and enhancers (Vernimmen et al., 2007). 3C has also been used to demonstrate the presence of discrete chromatin loops between gene promoters and PREs in Polycomb domains (Lanzuolo et al., 2007), or the role of insulator elements in modulating chromatin folding (Comet et al., 2011). All these early applications of 3C provided strong evidences for a link between specific chromatin contacts and genome regulation, for both gene activity and repression.

1.4.2 Extending 3C throughput with 4C and 5C

The 3C technology has then been expended by multiple derivatives to increase the efficiency, the resolution and the throughput, referred here to as "C" methods [Figure 4 (Sati and Cavalli, 2017)]. Given that a DNA fragment potentially interacts with all the others and that the large majority of the contacts occurs at the kb-scale, 3C was not suitable for low-frequency and long-range interactions at the Mb scale. Several extensions of the 3C, referred to as 4C, allowed the detection of contacts between a locus of interest and multiple other loci using microarrays or sequencing [Figure 4 (Simonis et al., 2006; Zhao et al., 2006)]. The high potential of this technology in detecting "one versus all" interactions has been applied to detect specific 3D chromatin contact networks, or "interactomes". 4C-based studies strengthened the structural-functional relationship of chromosomal organization, revealing long-range cis and trans interactions linked to gene activity (Simonis et al., 2006), interaction networks of the H19 imprinting control region (Zhao et al., 2006), the dynamics of contacts of the *HoxB1* locus depending on its induction (Würtele and Chartrand, 2006), or specific enhancer-gene interactions (Lomvardas et al., 2006; Ghavi-Helm et al., 2014). Functional networks involving co-transcribed genes (Schoenfelder et al., 2010), pluripotency-associated genes (Apostolou et al., 2013), or Polycomb domains (Bantignies et al., 2011; Tolhuis et al., 2011) were also identified with 4C. Furthermore, this method revealed the dynamic organization of the Polycomb associated *Hox* clusters, organized as single domains when repressed that eventually switch to bimodal organizations during development, allowing the separation of the active and the repressed parts of the locus (Noordermeer et al., 2011; Andrey et al., 2013). If 3C and 4C afford the identification of chromatin contacts with a high-genomic resolution, they probe

interactions from specific viewpoints, making difficult the characterization of global and integrated architectures. A variant of 3C, called 5C for "chromosome conformation capture carbon copy", permits the mapping of multiple "many-to-many" interactions (Dostie et al., 2006). 3C ligated products are annealed and ligated to a collection of oligonucleotides corresponding to the restriction sites of interests before PCR amplification (Figure 4). This method allows then the generation of matrices of interactions, where the contact frequency between any pairs of loci can be assessed relatively to the others. 5C confirmed the presence of loops between globin genes and their cis-regulatory elements and suggested globular organization of chromatin domains (Dostie et al., 2006; Baù and Marti-Renom, 2011). The 3D folding of the *Hox* gene clusters could also be assessed with 5C (Ferraiuolo et al., 2010; Rousseau et al., 2014).

1.4.3 Capturing genome-wide chromosome conformation with Hi-C

The most popular extension of 3C technology is certainly its genome-wide, "all versus all" version, called Hi-C (Lieberman et al., 2009). In Hi-C, the digested DNA molecules are filled and marked with biotin before ligation. DNA is then purified and sheared, and a biotin pull-down allows the enrichment of ligated products. They are then sequenced using paired-end sequencing (Figure 4). The first Hi-C study confirmed the existence of CTs and showed the genome-wide segregation of the chromosomes into two major compartments of interactions, coined "A" compartment for gene rich, active, and open chromatin, and "B" compartment for repressed chromatin (Lieberman et al., 2009). Thereafter, Hi-C and 5C with increased genomic resolution revealed the organization of the chromosomes into discrete domains enriched in chromatin contacts compared to the surrounding regions, now commonly referred to as topologically associating domains [TADs (Sexton et al., 2012; Nora et al., 2012; Dixon et al., 2012; Hou et al., 2012)]. TADs are one of the most striking structural features revealed by C technologies (Szabo et al., 2019). A detailed description of TADs will be presented in section 1.5: The topologically associating domains. Since, Hi-C has been extensively used in a wide range of organisms and revealed many architectural principles of genome folding linked to functional genome activity, including TADs, chromatin loops, compartments and sub-compartments (Eagen, 2018), which will be further discussed. The single-cell application of Hi-C revealed heterogeneous and variable contacts in individual cells, reflecting dynamic chromosome organization (Nagano et al., 2013; Stevens et al., 2017; Flyamer et al., 2017; Nagano et al., 2017; Tan et al., 2018). Given the very large number of potential interactions, uncovering fine architectural details using Hi-C requires deep sequencing. A way to increase the resolution of contacts of specific regions of interests has been introduced with Capture-C, in which biotin-labeled probes are used to enrich specific restriction fragments [Figure 4 (Hughes et al., 2014)]. For example, the capture of all interactions involving promoters allowed the identification of their cis-regulatory elements (Mifsud et al., 2015;

Schoenfelder et al., 2015). Promoter-centered interactomes were also shown to reflect cell identity in the hematopoietic lineage (Javierre et al., 2016). Hi-C can also be combined with immuno-precipitation (ChIA-PET), in ordered to center the analysis to contacts specifically associated with loci bound by protein of interest (Horike et al., 2005; Fullwood et al., 2009). Recently, derivatives of Hi-C enabling the identification of multipartite interactions uncovered higher-order hubs of interactions within the nucleus (Quinodoz et al., 2018), such as interactions between Polycomb sites (Olivares-Chauvet et al., 2016), multiple and simultaneous enhancer-promoter contacts (Allahyar et al., 2018; Oudelaar et al., 2018) or extensive multipartite interactions within TADs (Zheng et al., 2019).

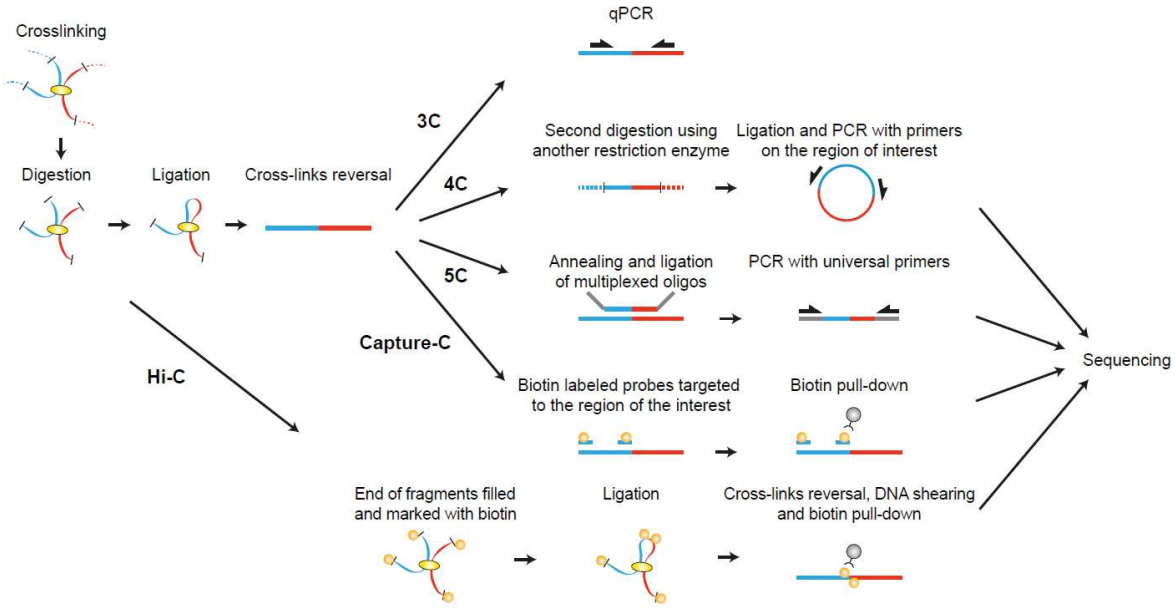

Figure 4. C techniques. These methods involve crosslinking of chromatin interactions, DNA digestion using restriction enzyme, and ligation of the fragments that are in close spatial proximity. In 3C ("one versus one"), the interacting regions are detected using specific primers of the region of interest. In 4C ("one versus all"), a second round of digestion and ligation allows the circularization of DNA which is then amplified by reverse PCR using primers specific to the "bait" region of interest. PCR products are detected by microarray (historically) or sequencing. 5C and Capture-C ("many versus many") consist in detecting all pair-wise interactions that occur between genomic regions of interest. In 5C, ligation products are hybridized with oligos specific to the ligation junctions that are further amplified by PCR. PCR products are then sequenced. In Capture-C, probes labeled by biotin are hybridized to the restriction fragments containing the regions of interests, which allows their enrichment before sequencing. In Hi-C ("all versus all"), the ends of the DNA fragments are filled and labeled with biotin. After ligation of fragments, de-crosslinking, DNA shearing, and biotin pull-down, the fragments are sequenced using pair-end sequencing.

Importantly, the principles of genome folding characterized using C data were also observed using independent approaches such as microscopy (see section 1.3: Imaging nuclear organization) but also other molecular biology-based methods. The genome architecture mapping, or GAM technology, consists in generating contact maps based on the frequency at which DNA regions are found together in a set of ultrathin cryosections of nuclei (Beagrie et al., 2016). In addition to recapitulate features described by Hi-C, this method is also able to detect multi-way interactions. More recently, a novel method called DamC, based on the bacterial DNA adenine methyltransferase (Dam)-mediated methylation of DNA, confirmed the presence of TADs and loops in vivo (Redolfi et al., 2019). Importantly, this method is free of crosslinking and ligation events, indicating that these features are not Hi-C artefacts, and quantitively agreed with 4C.

1.4.4 Toward an integration of chromosome conformation capture, imaging and modeling approaches

C techniques have largely contributed to our understanding of genome organization. However, these methods generally generate pairwise and cell-population averaged interaction profiles, which makes difficult the interpretation and the reconstruction of single chromosomal structures. Thus, many studies combined C methods with FISH, which provides distance distributions from individual cells between loci of interest (Giorgetti and Heard, 2016; Fudenberg and Imakaev, 2017). Historically, pairs of loci labeled in two different colors were used to measure and compare 3D distances (or "contact frequency" defined by a distance cutoff) with contacts identified using C methods, limiting the FISH to a validating role. However, with the development of imaging methods such as super-resolution microscopy and the development of new generations of probes, FISH and other imaging approaches have become very powerful in characterizing chromosome conformation in individual cells. FISH and C techniques are then very complementary and overall quite consistent to each other.

Modeling has also been extensively used in combination to C data to extract or predict chromosome structures (Tiana and Giorgetti, 2018; Wang et al., 2015). In the first Hi-C study, the authors compared the cis contact probability to the genomic distance between genomic loci (here referred to as cis-decay), which showed a power law with a slope close to -1, to different polymer behaviors (Lieberman et al., 2009). At the scale of few Mb, the experimental cis-decay fitted with a fractal globule polymer organization, linking experimental data to physical principles of chromosome folding. Similar comparisons using higher-resolution contact maps showed that fractal globule organization cannot explain all the experimental features of chromosome organization, such as the lower cis-decay slope at the TAD scale. This highlighted the heterogeneous behavior of chromosomes at different genomic scales (Sanborn et al., 2015). Averaged 3D reconstructions of chromosomal structures were produced from Hi-C, allowing appreciation of global chromatin organization (Duan et al., 2010; Baù and Marti-Renom,

2011; Umbarger et al., 2011). However, these models cannot assess whether the obtained reconstructions are consistent with the reality and the dynamics of individual chromosome conformations in single cells. Another modeling strategy has been used to generate ensemble of individual configurations that reproduce Hi-C or 5C data when they average (Giorgetti et al., 2014). Basically, the chromatin fiber is represented as a chain of beads that have a probability of interaction proportional to the contacts detected by Hi-C. The strength of the interactions between the beads is then optimized until the contact probabilities obtained from thousands of conformations converge with the experimental dataset. Individual conformations from the ensemble that best fit with Hi-C can then be extracted. This method has been used to characterize structural fluctuations of TADs in relationship with their activity (Giorgetti et al., 2014). Another approach called "string and binder switch" aimed to explore the relationship of chromosome folding upon the binding of molecules on specific loci (Barbieri et al., 2012) and was used to describe the differential organization of *Hox* loci upon cell differentiation (Barbieri et al., 2017; Bianco et al., 2019). Modeling from single-cell Hi-C data also recapitulated features of spatial genome organization, such as its folding into chromosome territories or compartments (Nagano et al., 2017; Stevens et al., 2017; Tan et al., 2018; Nir et al., 2018). Moreover, modeling and simulations were used to propose mechanisms of higher-order chromatin organization, such as the "loop-extrusion" mechanism which would explain the formation of mammalian TADs (Sanborn et al., 2015; Fudenberg et al., 2016). This model proposes that chromatin is progressively extruded by an extruding factor, presumably cohesin, until this factor dissociates or encounter specific proteins bound to the chromatin, such as the CCCTC-binding factor (CTCF) which is present at the border of TADs. This model implies the formation of loops between the extremities of the TADs, seen as interaction peaks at their edge in mammalian Hi-C maps. This model has been supported by various experimental studies; a further description will be presented in the next section.

1.5 The Topologically Associating Domains

This chapter will present current understanding of chromatin folding into TADs across different species, depicting their common and specific features and describing the mechanisms involved in their formation. As I had the opportunity to recently publish a review article in Science Advances about TADs, the core of this chapter will be the edited version of the manuscript. For reading convenience, the references belonging to the review are directly included at the end of the article as in its edited version. Another paragraph that emphasizes the functional role of TADs will follow this review.

Regarding my participation for this review, I first wrote an outline of the chapters on which we agreed with my supervisors. I then wrote a first draft of the entire manuscript, including references and figures.

This version was then reviewed and improved by my supervisors, and after agreeing with the last modifications, we submitted the manuscript.

1.5.2 Review article: Principles of genome folding into topologically associating domains

GENETICS

Principles of genome folding into topologically associating domains

Quentin Szabo, Frédéric Bantignies*, Giacomo Cavalli*

Understanding the mechanisms that underlie chromosome folding within cell nuclei is essential to determine the relationship between genome structure and function. The recent application of "chromosome conformation capture" techniques has revealed that the genome of many species is organized into domains of preferential internal chromatin interactions called "topologically associating domains" (TADs). This chromosome compartmentalization has emerged as a key feature of higher-order genome organization and function through evolution. Although TADs have now been described in a wide range of organisms, they appear to have specific characteristics in terms of size, structure, and proteins involved in their formation. Here, we depict the main features of these domains across species and discuss the relation between chromatin structure, genome activity, and epigenome, highlighting mechanistic principles of TAD formation. We also consider the potential influence of TADs in genome evolution.

INTRODUCTION

The three-dimensional (3D) folding of the eukaryotic genome in the nucleus is a highly organized process tightly linked to functional DNA-dependent processes, such as DNA replication and transcription. The nuclear positioning of genes within nuclei can correlate with transcription, with active genes being located more often in the nuclear interior compared to repressed or heterochromatic regions, which are found closer to the periphery (*1*). Chromosomes occupy distinct subnuclear territories (*2*), with transcriptionally active loci positioned at their surface (*3*). In the last decade, key features of genome organization have been revealed by chromosome conformation capture methods (*4*, *5*), in particular by their high-throughput version called Hi-C (*6*), which allows the genome-wide identification of chromatin contacts [for review, see (*7*)]. Hi-C uncovered general principles of chromosome folding, such as the decay of the frequency of chromosomal contacts following a power law that has a scaling exponent close to −1 in many species (*6*, *8*–*12*), but genome folding is far from being homogeneous (*13*). At large scales, chromosomes segregate into regions of preferential long-range interactions that form two mutually excluded types of chromatin, referred to as "A" and "B" compartments (*6*, *14*, *15*). A compartments correspond to gene-rich and active chromatin, while B compartments are mostly enriched in repressive chromatin (*6*, *14*). At a scale of tens to hundreds of kilobases, chromosomes fold into domains with preferential intradomain interactions compared to interdomain interactions with the neighboring cis chromatin domains, i.e., spanning domain borders (*11*, *16*–*18*). These contact domains are now commonly referred to as topologically associating domains (TADs) (Fig. 1) (*18*). The presence of these domains has been described in many species, indicating that they may represent a conserved feature of genome organization. TADs are architectural chromatin units that define regulatory landscapes, suggesting their fundamental implication in shaping functional chromosomal organization. TAD boundaries correspond to those of replication domains (*19*), and genes tend to be coregulated during cell differentiation when they are located within the same TAD (*18*, *20*–*22*). A reporter gene inserted within the genome is subjected to the influence of enhancers over large regulatory domains that correlate strongly with TADs (*23*), and contacts between enhancers and gene promoters are mainly restricted within TADs (*24*). This is consistent with TADs representing a functionally privileged scale of chromosome folding (*22*), and the constraint of functional contacts within TADs appears to be essential to ensure proper gene regulation. Disruption of TAD structures by altering their boundaries can lead to ectopic contacts between cis-regulating elements and gene promoters, and thus gene misexpression, which can contribute to developmental defects and cancer (*25*–*30*). Therefore, deciphering the structural and the functional nature of TADs has become crucial to elucidate the rules of higher-order genome organization and regulation, and given their importance in pathology, understanding TADs has acquired medical relevance. However, even if genome folding into self-interacting domains has been a widely adopted strategy in evolution, TADs or contact domains can differ in size, chromatin features, and mechanisms underlying their formation. This suggests that TADs might be subdivided in different subtypes, each of them characterized by specific structural and functional properties. Moreover, the identification of TADs strongly depends on the resolution of Hi-C data and the method of TAD annotation. Increasing sequencing depth and resolution reveals finer patterns of chromatin contacts as well as internal insulation regions (Fig. 1). Thus, the identification of TAD borders has proven to be difficult. Furthermore, to what extent these chromatin domains represent the same layer of genome organization in different species remains unclear. In this review, we will first present the main features of chromosome folding at the submegabase scale, highlighting similarities and differences between TADs observed in various organisms. We will then consider their relationship with physical and functional organization of the chromatin fiber and their potential role in genome evolution.

TADs ACROSS SPECIES

TADs in mammals

TAD features appear to be strongly conserved in mammals (*16*, *31*). 5C and Hi-C studies first showed the partitioning of the chromosomes

Institute of Human Genetics, CNRS and University of Montpellier, Montpellier, France. *Corresponding author. Email: frederic.bantignies@igh.cnrs.fr (F.B.); giacomo.cavalli@igh.cnrs.fr (G.C.)

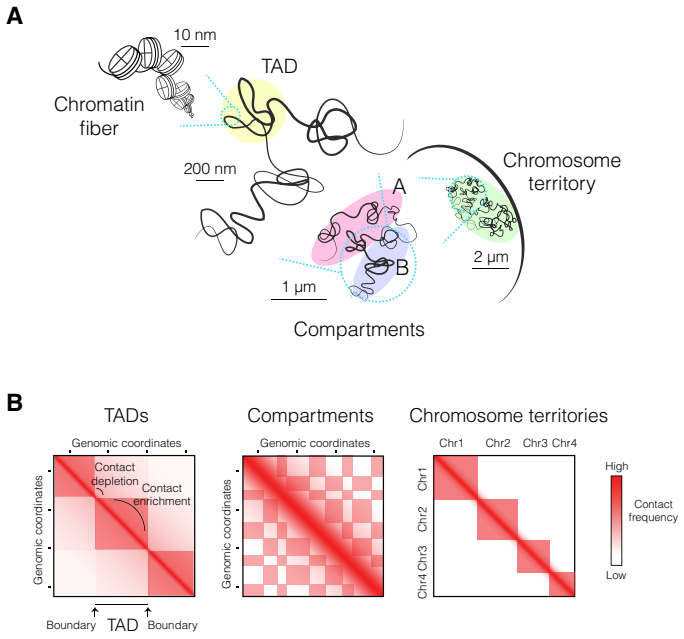

Fig. 1. Hierarchical folding of the eukaryotic genome. (**A**) Schematic view of chromosome folding inside the nucleus. The finest layer of chromatin folding is at the DNA-histone association level, forming nucleosomes organized into the ~11-nm chromatin fiber (*133*). Chromatin is packed at different nucleosome densities depending on gene regulation and folds at the submegabase scale into higher-order domains of preferential internal interactions, referred to as TADs. At the chromosomal scale, chromatin is segregated into active "A" and repressed "B" compartments of interactions, reflecting preferential contacts between chromatin regions of the same epigenetic features. Individual chromosomes occupy their own space within the nucleus, forming chromosome territories. (**B**) Schematic representation of Hi-C maps at different genomic scales, reflecting the different layers of higher-order chromosome folding. Genomic coordinates are indicated on both axes, and the contact frequency between regions is represented by a color code. At the submegabase scale, TADs appear as squares along the diagonal enriched in interactions, separated by contact depletion zones delimited by TAD boundaries. At the chromosomal scale, chromatin long-range interactions form a characteristic plaid pattern of two mutually excluded A and B compartments. Last, intrachromosomal interactions are overrepresented compared to interchromosomal contacts, consistent with the formation of individual chromosome territories.

into domains of hundreds of kilobases (median size of 880 kb) (*16*, *18*), occupying 91% of the mouse genome. Higher-resolution Hi-C map detected finer domains, also dubbed sub-TADs, with a median size of 185 kb and associated with enrichment of specific chromatin marks (*14*, *32*). A notable feature of most mammalian TAD boundaries is the presence of the CCCTC-binding factor (CTCF) together with the structural maintenance of chromosomes (SMC) cohesin complex (*14*, *16*, *31*, *33*). These borders are engaged in strong interactions, seen as "corner peaks" on Hi-C maps (Fig. 2), suggesting the formation of loops between CTCF binding sites. Notably, these loop-anchored TADs almost always form between CTCF sites positioned in a convergent orientation, and the removal or change in orientation of a single CTCF site can be sufficient to abolish or shift the position of a TAD boundary (*13*, *28*, *34*, *35*), demonstrating the crucial role of CTCF in defining mammalian TAD borders. The propensity of CTCF to form homodimers and to bind RNA molecules may be important for this function (*36*). A linear tracking mechanism, which is referred to as the "loop extrusion model," has been proposed for the formation of these TADs (*13*, *37*, *38*). According to this model, chromatin would be extruded by an engaged cohesin SMC complex until the complex is dissociated or until it encounters two convergent and bound CTCF sites at TAD borders [for review, see (*39*)]. In line with this, cohesin subunit chromatin immunoprecipitation–sequencing (ChIP-seq) peaks tend to be more interior to the loop relative to CTCF peaks (*13*, *37*). This model has been supported by recent molecular genetic studies. The depletion of CTCF, cohesin, or the cohesin-loading factor Nipbl leads to the disruption of loop domains (*40*–*43*). Conversely, the removal of the cohesin release factor Wapl reinforces the strength of the loops at TAD borders (*44*). The CTCF/cohesin association forming the loop-anchored TADs thus appears to come from an equilibrium between loading and removal of the cohesin complex, with corner peak loops reflecting an increased residence time of the complex at TAD boundaries (*45*). In agreement, loops disappear when the cohesin complex is not loaded on chromatin or when it does not stop at CTCF borders, while they are stabilized when cohesin stays on chromatin (*40*–*45*). Cohesin restoration rapidly reverses these effects, consistent with a model where loop extrusion is a dynamic process (*41*). Another SMC protein complex, condensin II, together with TFIIIC, has been found enriched at TAD borders (*46*). Consistent with a potential role of condensin, loop extrusion has been observed in vitro by live imaging, where naked DNA can be extruded (1500 base pairs per second) by this complex (*47*). This demonstrates the existence of such a mechanism and calls for an analysis of the interplay between condensin and cohesin in TAD formation. However, super-resolution microscopy data suggest that cohesin (and, most likely, CTCF) is required to position TAD boundaries coherently in different cells rather than for TAD formation. Chromatin tracing with sequential fluorescence in situ hybridization (FISH) labeling showed TAD-like structural units in individual cells, in both wild-type and cohesin-depleted conditions, but the position of the boundaries lies at CTCF sites in wild-type cells, whereas it is randomized in cohesin-depleted cells (*48*). These data suggest that other loop extruding mechanisms might exist in the absence of cohesin or that TADs can form by spontaneous chromatin contact features. In addition to defining boundaries, CTCF is also present at enhancer-promoter pairs within TADs, forming smaller loop domains (*14*) involving Mediator and cohesin (*33*), and another protein, YY1, may also contribute to enhancer-promoter interactions, together with cohesin, in a more cell type–specific manner (*49*). Furthermore, modeling of chromatin fibers suggests that transcription-associated supercoiling could also be involved in the process of loop extrusion (*50*). Consistently, type II DNA topoisomerase is often found positioned with CTCF and cohesin at domain borders, which may help to solve topological problems (*51*). If loop-associated domains represent a key feature of TADs in mammals, with approximately 75 to 95% of boundaries being associated with CTCF depending on the cell type (*16*, *24*), then some boundaries are CTCF independent, consistent with approximately 20% of TAD boundaries being resistant to CTCF loss (*40*). These boundaries are associated with transcription (*16*, *24*) or correspond to a demarcation between active and repressed chromatin regions, i.e., between A and B chromatin type (*14*, *32*). For example, Hi-C profiling of embryonic mouse stem cells and differentiated neuronal progenitor cells revealed the appearance of boundaries at promoters of newly transcribed genes during differentiation in the absence of CTCF binding (*24*). Mammalian TADs seem therefore not to be always the result of CTCF/cohesin loops and could sometimes rather be defined by chromatin state and transcription (*32*). However,

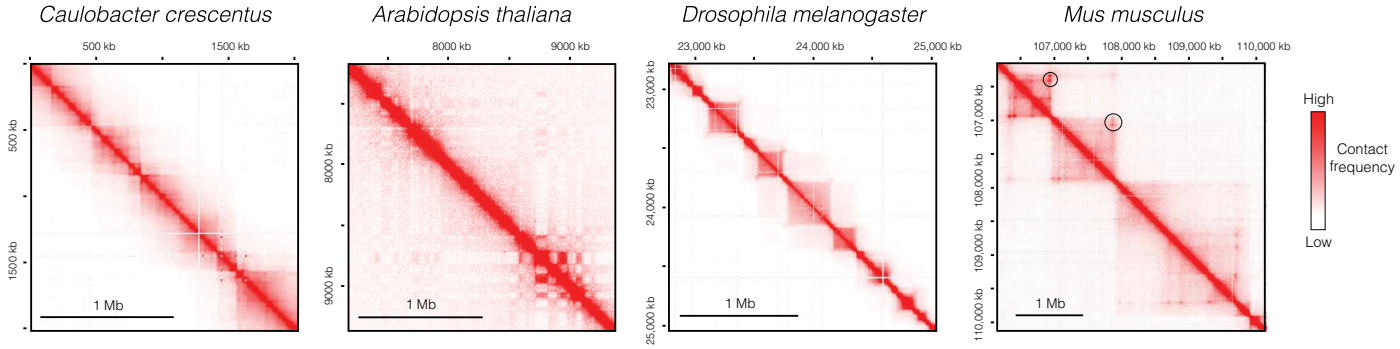

Fig. 2. Examples of Hi-C profiles from different species. Hi-C maps [visualized with Juicebox (*134*)] of different species (*24*, *67*, *75*, *90*, *135*) showing more or less pronounced 3D partitioning of the genome. TADs are not obvious in *Arabidopsis* genome, but boundary-like regions and insulated genome units are discernible. In *Drosophila*, TADs are well demarcated and correlate well with the epigenetic landscape. A specific feature of mammalian TADs is the presence of "corner peaks," i.e., peaks of interactions at the edges of TADs (indicated by black circles), revealing the presence of chromatin loops.

CRISPR-dCas9–mediated transcriptional activation does not create a new boundary (*24*). Hi-C analysis in mouse sperm, which is transcriptionally silent, but has bound RNA polymerase II (RNAPII) and active or silent histone modifications, shows similar interaction domains as embryonic stem cells (*52*). These data suggest that transcription per se is not sufficient and that transcription factors are likely involved in insulating CTCF-independent TAD borders. Last, TADs appear gradually during early mouse embryogenesis (*53*, *54*) and they are still observed after the inhibition of the transcription with α-amanitin (*53*, *54*), whereas blocking of DNA replication with aphidicolin inhibits TAD establishment (*54*), suggesting a potential role of replication in the primary establishment of TADs.

TADs in *Drosophila*

In *Drosophila*, the presence of TADs has first been identified using Hi-C in whole embryos (*11*), revealing the presence of discrete interaction domains along chromosomes (Fig. 2). *Drosophila* TADs appear well correlated with epigenetic states and were classified in four main classes according to their specific chromatin signatures: transcriptionally active TADs, associated with active histone modifications such as trimethylation of histone H3 lysine 4 and 36 (H3K4me3 and H3K36me3) (active TADs); Polycomb-repressed TADs enriched in H3K27me3 and Polycomb group (PcG) proteins (PcG TADs); TADs devoid of known specific marks (null or void TADs); and classical heterochromatin enriched in H3K9me2, HP1, and Su(var)3-9 (heterochromatin TADs) (*11*). Originally, Hi-Cs in *Drosophila* revealed approximately 1300 TADs with an average size of nearly 100 kb (*11*, *17*), but recent studies using higher map resolution showed a finer partitioning into >2000 (*21*, *55*) or >4000 TADs (*56*), where TADs and inter-TAD regions can be subdivided into smaller domains with a median size of few tens of kilobases (*56*). The calling and the annotation of TADs depend on the computational method and the algorithm used (*57*), which can explain such variability in the number of identified TADs despite similar Hi-C resolution. Independently on the number of identified TADs, the transcriptionally silent TADs (PcG, null/void, and HP1, i.e., B-type chromatin) occupy the largest portion of the genome and are larger in genomic size than the active ones (*11*, *17*, *21*, *56*). The large majority of TAD boundaries are present in gene-dense, chromatin-accessible, transcribed regions enriched in active chromatin marks (*17*, *58*–*60*), most of them occurring at active gene promoters (*21*). Various insulator proteins have been found enriched at boundaries, including BEAF-32, Chromator, CP190, or M1BP (*11*, *17*, *21*, *59*, *60*), and combination of these proteins such as BEAF-32/Chromator or BEAF-32/CP190 is a good predictor of boundaries (*56*). Cohesin and condensin II subunits, as well as TFIIIC, were also found enriched at TAD borders (*61*). However, in contrast to mammals, there is little enrichment of CTCF nor interaction loops at TAD borders. This is a startling observation, because *Drosophila* CTCF has a conserved Zn finger domain that binds to the same sequence as the mammalian counterpart. The reason why fly CTCF is not a major TAD boundary definition protein and, instead, is rather involved in Hox gene regulation (*62*) remains to be studied. Despite their enrichment, the role of insulator proteins in *Drosophila* TAD formation is still unclear, for example, small interfering RNA (siRNA)–mediated depletion of BEAF-32 does not abolish boundaries (*21*). Whether a total degradation of the protein or whether the depletion of a combination of these factors is required to see clear effects remains to be investigated. Of importance, the description of boundary features largely depends on the calling of the TADs and therefore on the resolution of Hi-C. Using high-resolution Hi-C, it was recently proposed that TAD organization in *Drosophila* reflects the switch between active and inactive chromatin and that many of the previously identified boundaries actually correspond to small active domains (*32*, *56*). TAD patterning mirrors the transcriptional state, with large inactive regions forming prominent repressed TADs separated by transcribed genes that are often clustered in the genome (*32*, *60*). The size and the degree of transcriptional activity of these active regions correlate with the local strength of compartmentalization, with broader and more active TADs forming the most pronounced A compartment domains (*63*). To decipher mechanisms driving TAD formation, chromatin interaction profiling has been performed during *Drosophila* embryogenesis (*59*, *64*). At early stages, before zygotic genome activation (ZGA)—a wave of zygotic transcriptional activation occurring during embryonic development—the genome is mostly unstructured but contains few boundary-like regions enriched in housekeeping genes and associated with RNAPII occupancy. During ZGA, TAD boundaries progressively appear at housekeeping genes concomitantly with de novo recruitment of RNAPII, reaching a plateau after these activation waves. Consistent with the link between transcription and boundaries, α-amanitin or triptolide-induced inhibition of transcription leads to a decrease of TAD insulation, although boundaries do not completely disappear (*32*, *59*), indicating that the reduction of RNAPII and transcription is not sufficient to abolish TAD formation.

A role for the Zelda transcription factor was uncovered in establishing insulation at TAD boundaries (*59*). Zelda may cooperate with other factors, such as BEAF-32 and GAGA factor (GAF), found at TAD borders. Moreover, Zelda at RNAPII-bound sites is also implicated in the formation of active long-range chromatin loops, often spanning multiple TADs. This first wave of active chromatin loops depending on Zelda might correspond to the onset of genome folding in *Drosophila*. These loops are located close to strong TAD boundaries, a situation reminiscent to CTCF in mammalian nuclei (*64*). Whether this organization necessitates cohesin or cohesin-like activity remains to be addressed. Later during embryogenesis, TADs and TAD insulation become more and more pronounced, and the formation of chromatin loops in repressive PcG domains, which involves GAF, represents another specific feature of *Drosophila* TADs (*55*, *64*). However, these loops do not occur between TAD boundaries but are present at the interior of PcG TADs and correspond to contacts between PcG protein binding sites. Given these specificities, these loops do not seem to be a general feature of TAD formation in *Drosophila* but rather a mechanism involved in PcG gene silencing (*64*). Of note, no Zelda or GAF homologs have been found in vertebrates, indicating that some of these looping mechanisms maybe peculiar to *Drosophila*.

TADs in *Caenorhabditis elegans*

In *Caenorhabditis elegans*, self-interacting domains of ~1 Mb size are present on the X chromosome but are not a clear feature of autosomal chromosome organization (*65*). While some boundary-like regions are found in autosomes, they are stronger and more abundant on the X chromosome. The hermaphrodite X chromosome is specifically bound by the dosage compensation complex (DCC), a condensin complex. High-affinity DCC binding sites overlap with X TAD boundaries, and DCC depletion strongly reduces insulation at these boundaries, consistent with a pivotal role of the DCC. Moreover, CRISPR-Cas9–mediated deletion of a binding site of the DCC complex was sufficient to remove its cognate boundary. Intriguingly, these DCC-bound boundaries are also engaged in long-range interactions and it would be important to understand whether these features can be separated or whether they are interdependent.

TADs in plants

Genome compartmentalization into TADs, in the sense of a complete partitioning into adjacent self-interacting domains, was not obvious in the model plant *Arabidopsis thaliana* (Fig. 2). However, the *Arabidopsis* genome harbors compacted domains of interactions enriched with repressed chromatin marks such as H3K27me3 or H3K9me2 (*9*, *66*, *67*). More than 1000 "boundary-like regions," defined as starting or ending points of interacting domains, were identified (*67*). These regions are composed of transcriptionally active and open chromatin that separate inactive genomic regions (*32*, *67*). If TADs are not a clear feature of *Arabidopsis* genome, then they have been distinctly observed in rice and cotton (*68*–*70*), where chromatin at TAD boundaries is highly expressed and enriched in active chromatin marks. Another study described the presence of TAD-like domains in various plant species, including maize, tomato, sorghum, foxtail millet, and rice (*71*). Similar to *Drosophila* TADs (*11*), they can be classified into four chromatin types according to their epigenetic signatures: active domains, repressive domains enriched in DNA methylation, Polycomb domains enriched in H3K27me3, and domains devoid of specific marks. Thus, the link between transcription, epigenetic status, and chromatin topology appears as a main feature of chromosome organization in these species. In plants, no protein with insulator function such as CTCF has been identified. However, DNA GC-rich motifs similar to sequences bound by plant-specific transcription factors belonging to the TCP family have been identified at rice TAD boundaries (*69*). Studies focusing on the function of these proteins found at boundaries would be required to characterize their potential role in shaping plant TADs.

Self-interacting domains in yeast

Self-interacting domains, called globules, have been identified in *Schizosaccharomyces pombe* (*10*). These globules (50 to 100 kb in size) are separated by boundaries enriched in cohesin binding. The partial loss of function of rad21, a cohesin subunit, is associated with a disruption of globules, seen as a loss of insulation at cohesin peaks. The presence of globules and the role of cohesin in their formation are conserved in G1 cells, indicating a different role for cohesin than in sister chromatid cohesion. In *Saccharomyces cerevisiae*, TAD-like structures were not initially observed using a derivative of the 4C method (*72*). More recently, a method similar to Hi-C called Micro-C, in which micrococcal nuclease is used instead of restriction enzymes to produce small chromatin fragments to be ligated when close in 3D, allowed the generation of contact maps at single-nucleosome resolution, which revealed the presence of small self-interacting domains (*73*). These domains generally contain one to five genes and are approximately 5 kb in size. The boundaries between these small domains are enriched for highly expressed gene promoters—although not all promoters form boundaries—transcription-associated marks, the remodeling the structure of chromatin (RSC) adenosine triphosphate (ATP)–dependent chromatin remodeling complex, and the cohesin loading factor ssc2. A recent model proposes that transcription-induced supercoiling, together with the action of topoisomerases at TAD borders, can explain the formation of self-interacting chromatin domains in *S. pombe* (*74*).

TAD-like domains in bacteria

Hi-C performed in *Caulobacter crescentus* revealed the presence of discrete chromosomal interaction domains (CIDs) resembling eukaryote TADs (Fig. 2), ranging from 30 to 420 kb in size (*75*), with boundaries enriched in highly expressed genes. Inhibition of transcription elongation disrupted CID boundaries, and moving highly expressed genes in a different genomic location led to *neo* boundaries. This study suggests that regions enriched in plectonemes form CIDs, while boundaries are established by highly expressed genes and the formation of plectoneme-free regions. CIDs of similar genomic sizes have also been identified in *Bacillus subtilis* (*76*, *77*), and macrodomain-like regions have been reported for the *Escherichia coli* chromosome (*78*). Even in *Mycoplasma pneumoniae*, a model organism with a small genome size and a simplified gene regulatory network, CIDs have been observed. In this case, CIDs range from 15 to 33 kb in size, smaller than those reported for *C. crescentus* and *B. subtilis*. Genes within the same domain tend to be coregulated, suggesting that, even in such a small genome, chromosome organization may influence transcriptional regulation (*79*). A common theme in *C. crescentus* and *M. pneumoniae* is that the sharpness of CIDs depends on supercoiling. Moreover, prokaryotic model organisms have provided crucial information on the role of SMC complexes in genome organization. Studies in *B. subtilis* and *C. crescentus* revealed that SMC rings are able to encircle DNA and tether chromosome arms, forming processive loops

(*77*, *80*, *81*) that depend on the adenosine triphosphatase (ATPase) activity of the complex (*82*). These data thus provide strong evidence that an active loop extrusion mechanism is involved in shaping bacterial chromosome organization. However, SMC-mediated extrusion does not seem to be necessary for CID formation, because SMC depletion in *C. crescentus* leads to a decrease of inter-arm chromosomal contacts but CID boundaries remain unchanged (*75*).

General and specific features of TADs

Although TADs or interaction domains emerge as a fundamental component of genome organization, their features are not universally conserved (Fig. 2). Contact domains can be more or less pronounced, and their boundaries can be more or less sharp. In addition, the molecular mechanisms underlying their formation can be diverse, consistent with the existence of different types of TADs. It is therefore unclear whether TADs are the universal unit of higher-order genome organization or whether they emerged repeatedly during evolution as a consequence of the interplay between different molecular engines acting on chromatin. Nevertheless, one notable feature conserved across species is the relationship between gene activity and genome folding. Boundary regions are often found to be highly enriched in active chromatin in *Drosophila* (*11*, *17*, *21*, *58*–*60*), mammals (*16*, *24*), zebrafish (in which TADs are similar to those of mammals) (*83*), plants (*67*, *69*), *S. cerevisiae* (*73*), and *Plasmodium falciparum*, which also shows domain-like structures of 5 to 10 kb (*32*, *84*). In the bacteria *C. crescentus*, boundaries are also found at transcribed gene promoters (*75*). In the fungus *Neurospora crassa*, the genome is compartmentalized into heterochromatic and euchromatic regions, where gene-rich regions form domains <100 kb in genomic size that are comparable to metazoan TADs or yeast globules and separated by heterochromatic islands enriched in H3K9me3 (*8*). By comparing different species, including *Drosophila*, *Arabidopsis*, *N. crassa*, *C. elegans*, and the protozoan *P. falciparum*, Rowley and colleagues (*32*) suggested that the transcriptional activity partitions the genome into Hi-C domains, with active genes interacting more frequently with other active genes and forming active domains when they cluster on the genome. Contact domain boundaries would then correspond to the switches between transcribed and inactive genomic regions (*32*). The distribution and the transcriptional output of transcribed gene clusters along the genome of various species might therefore define the strength of local insulation of their TADs, as recently observed in *Drosophila* (*63*). However, transcription per se does not appear to be sufficient to create boundaries (*24*), and not all transcribed sites make boundaries, indicating that other factors, perhaps DNA binding of transcription factors, insulator/architectural proteins, or a combination of both, are required. Mammalian Hi-C maps display an additional TAD feature, which is the presence of CTCF/cohesin chromatin loops between CTCF convergent sites (*14*). Enrichment of inverted CTCF sites at TAD boundaries was also observed in zebrafish (*83*), suggesting that this characteristic is conserved through vertebrate lineage. However, CTCF has not been found in other organisms such as plants, yeast, or *C. elegans* (*85*), and consistently, loop-anchored domains are not found in these species. Conversely, other insulator proteins may play a similar role in defining TAD boundaries at transcribed domains in other species, such as BEAF-32 and CP190 in *Drosophila* (*56*), or TCP proteins in plants (*69*). The localization of cohesin depends on transcription in mammals (*86*), and cohesin-mediated boundaries may form at transcribed sites even in the absence of CTCF-like proteins. For instance, cohesin and its loader Nipped-B are associated with transcriptionally active regions in *Drosophila* (*87*, *88*). Depletion of cohesin and associated factors in other species than mammals would be interesting to decipher its role in TAD formation, and it would help elucidate whether self-interacting domains emerge from a conserved mechanism regulating DNA-dependent processes during evolution. Alternatively, in some species, TADs could arise from the differential folding of chromatin regions with different epigenomic states and thus rather reflect differential chromatin contacts in regions of different gene expression output.

PHYSICAL NATURE OF TADs

TADs and compartments

The relation between epigenome and genome organization raises the question of how the physical properties of chromatin shape chromosome structure. In *Drosophila*, active chromatin domains display a weaker contact density in Hi-C (*11*, *60*) or a stronger contact depletion between adjacent active TADs (*56*) compared to inactive TADs, indicating differential folding. Super-resolution stochastic optical reconstruction microscopy (STORM) revealed that active domains are more decondensed than the inactive ones (*89*). The classification based on global run-on sequencing (GRO-seq) of the *Drosophila* genome into active or inactive chromatin states reflects very well the TAD pattern obtained with Hi-C (*32*). Therefore, the correspondence between interactions obtained with Hi-C and chromatin state (*11*, *32*, *60*), together with the different folding of active compared to inactive chromatin, suggested that, in *Drosophila*, the compartmentalization of the chromosome into TADs may reflect the physical exclusion of active and inactive chromatin. Ulianov and colleagues (*60*) proposed that *Drosophila* inactive TADs are condensed chromosomal domains separated by active chromatin regions. Recent super-resolution analysis of chromatin organization accredited this view by showing the partitioning of the chromatin fiber into TAD-based physical domains, where repressed TADs form condensed globular nanocompartments interspersed by more open active regions (*90*). Similarly, STORM imaging of immunolabeled repressive H3K27me3 or active H3K4me3 marks showed clear separation of these two chromatin types, where active domains were found at the borders of repressed ones (*91*). This feature of chromosome organization is even observed in endoreplicated *Drosophila* polytene chromosomes in which TADs correspond to dense bands, while decompacted interbands correspond to inter-TAD regions (*60*, *92*, *93*). In *Drosophila*, chromatin state and genome structure seem therefore tightly linked at both the TAD and compartment levels. These two layers of organization, i.e., TADs enriched in internal interactions and compartments representing long-range interactions between domains of the same epigenetic features, correspond to the folding of genome units that preferentially interact within themselves and with homotypic domains (Fig. 3A) (*11*, *32*, *90*). The fact that compartments are not observed in polytene chromosomes presumably reflects the absence of long-range contacts because of the extensive pairing in trans of endoreplicated chromosomes. The correspondence between epigenome and interaction profiles is also observed in plants, where both short- and long-range contacts are correlated with epigenetic profiles (*9*, *66*–*68*, *71*). In species where chromosomal contacts correlate well with the epigenome, the mutual exclusion of different chromatin types may then be sufficient to create a TAD-based pattern for chromosome organization. Gene transcription

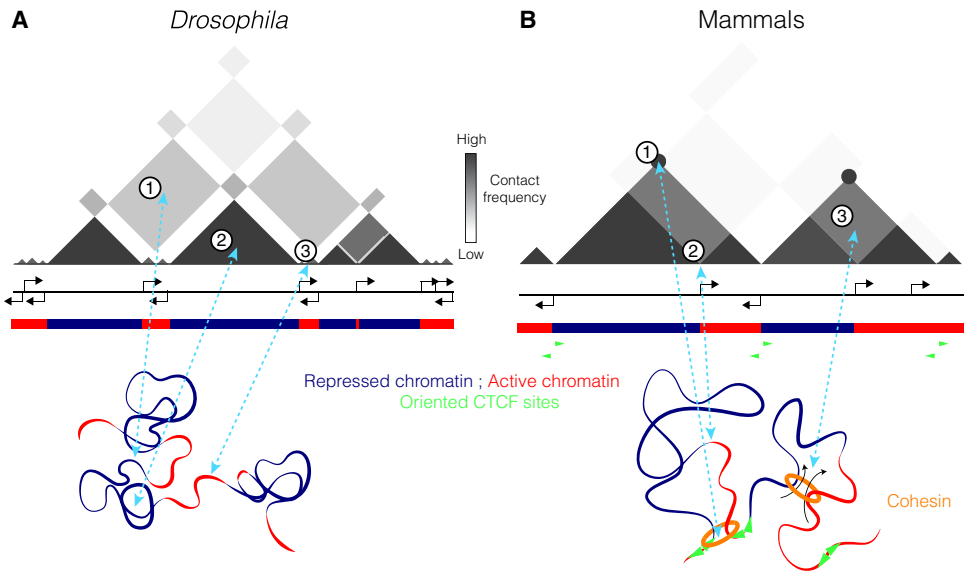

Fig. 3. Schematic representation of chromatin folding in *Drosophila* and mammals. (**A**) In *Drosophila*, both TADs and compartments correspond to epigenetic domains that preferentially fold within themselves and in far-cis with homotypic TADs (1). Large repressed chromatin region forms prominent and condensed TADs (2), separated by transcribed genes that can form clusters of small active TAD or inter-TAD–like regions of decondensed chromatin (3). (**B**) In mammals, the "loop extrusion model" proposed for TAD formation involves a loop extrusion factor, here cohesin, loaded on the chromatin by Nipbl and unloaded by Wapl. Cohesin extrudes chromatin until it dissociates, bumps into another cohesin, or reaches the border of the TAD bound by CTCF proteins in inverted orientation or by other boundary components. These loops are seen as a strong peak of interaction between TAD borders (1). Insulation can also be observed at active transcription start sites (2), and as recently suggested, the loop extrusion process could compete with the local segregation of active and inactive chromatin by mixing them (3) (*45*).

and delimitation of epigenetic landscapes, for example, mediated by insulator proteins (*94*), would then provide the framework of genome organization.

In mammals, the mutual exclusion of active and inactive chromatin is not sufficient to generate TAD boundaries. These regions are frequently transcribed and often correspond to transitions between different chromatin states (*14*, *16*, *18*), but TADs can include multiple chromatin types. Instead, a correspondence between chromatin activity and long-range interactions appears more prominently at the compartment scale (*14*, *15*, *95*). The effect of cohesin depletion on Hi-C contact maps as well as on super-resolution imaging maps suggests the presence of two parallel mechanisms of chromatin organization (*41*, *42*, *48*). Without cohesin, mammalian TAD-like domains might form spontaneously by chromatin interactions, which probably are preferential for same-type chromatin. However, these interactions rarely form domains with coherent boundaries in every cell. These boundaries are therefore implemented by the action of CTCF/cohesin-mediated loops (*48*). At the longer range, epigenetic features dominate, with TADs of similar chromatin type interacting preferentially to define chromosome compartments (*14*, *41*, *42*). The fact that zygotic maternal chromatin contains TADs and loops, but not compartments, also suggests that TADs and compartments are formed by distinct mechanisms (*96*). Using polymer simulations, Nuebler and colleagues (*45*) proposed that chromatin folding in mammals comes from a competition between dynamic loop extrusion and the compartmentalization defined by the epigenetic status, in which the processing of loop extrusion factors counteracts the segregation of compartments (Fig. 3B). In Hi-C data, the preferential interactions at short cis genomic distance of chromatin of the same type would then be blurred by the mechanism of extrusion. Therefore, CTCF/cohesin loops in mammals may correspond to an additional layer of genome organization on top of chromatin compartmentalization defined by its epigenetic state. This view is coherent with the fact that mammalian TADs have been shown to contain subdomains corresponding to active or repressed chromatin (*14*, *32*). This is also consistent with cohesin removal experiments, which abrogate CTCF/cohesin-mediated loops while revealing a finer chromatin compartmentalization that accurately reflects the underlying epigenetic landscape (*41*, *42*). This compartmentalization resembles that of *Drosophila* Hi-C maps, and this may actually reflect the absence in this species of such a process (Fig. 3).

Concerning the mechanism that segregates active from inactive chromatin, Ulianov and colleagues (*60*) proposed an attractive "self-assembly" model, whereby the stickiness of nonacetylated (inactive) nucleosomes, as opposed to the absence of bridging ability for acetylated (active) nucleosomes, could explain chromatin partitioning into TADs and TAD boundaries (also called inter-TADs). Moreover, the concentration of repressive histone methylation marks such as H3K9me2/3 and H3K27me3, which can spread over large genomic regions (*97*), and which serve as a platform to recruit large multimeric complexes, could help in the agglomeration and separation of active and inactive chromatin inside the nucleus. Recently, exclusion and compartmentalization of chromatin domains have been directly investigated on the basis of the physicochemical properties of their components. On the one hand, the classical heterochromatin segregation is driven by phase separation, mediated, at least in part, by HP1a and HP1α multivalent hydrophobic interactions in *Drosophila* and mammals, respectively (*98*, *99*). On the other hand, active domains may also generate phase-separated compartments. Clusters of enhancers, regulating cooperatively gene expression and defined as super-enhancers, can undergo phase separation by transcriptional coactivators, ensuring local concentration of regulating factors in a segregated

3D environment (*100*). These observations are in agreement with the visualization of chromatin-associated clusters of RNAPII and Mediator enriched at super-enhancers, behaving as phase-separated condensates (*101*). Phase separation has also been shown through kinase-mediated hyperphosphorylation of the RNAPII C-terminal repeat domain (CTD) (*102*). Last, polymer simulations of chromosome folding are consistent with phase-separated A and B compartments in mammals (*45*). In general, the components involved in phase-separated condensates contain intrinsically disordered protein domains and can exhibit multivalent interactions with each other to create specific environments, in which biochemical reactions and interactions might be highly favored (*103*, *104*). These studies shed new light on how physicochemical properties of chromatin-associated factors can form segregated compartments, and further investigations will be directed at understanding how this can be linked to TAD formation and/or stabilization.

TAD structure and dynamics

It appears clearer and clearer that TADs correspond to a functional subdivision of the genome into regions in which regulatory contacts are spatially confined. The fact that disruptions of TADs lead to de novo enhancer-promoter interactions and gene misexpression emphasizes this crucial role (*25*–*30*). This functional property could reflect the formation of physically insulated genomic units or a higher contact probability between gene promoters and cis-regulatory elements confined within a TAD. Hi-C data generally represent averaged interaction profiles coming from millions of cells, making the characterization of the physical nature of TADs difficult. Therefore, whether TADs reflect statistical frequencies of chromatin interactions within cell population or whether they represent genuine physical units in each cell nucleus has been a crucial question recently investigated by numerous studies.

Single-cell Hi-C (scHi-C) has been lately introduced. Although the first study suggested a generally conserved TAD organization at the single-cell level (*105*), subsequent scHi-C studies reveal substantial heterogeneity in contacts at the TAD scale from cell to cell (*96*, *106*, *107*), with domains appearing as mere tendencies that become more visible when averaged over a population of cells. Individual nuclear structures may, however, be difficult to address with scHi-C, given coverage and resolution limitations, and because this technique can identify a maximum of one interaction per genomic fragment at a time without information concerning the relative spatial positioning of each fragment. However, microscopy and polymer modeling are in agreement with scHi-C, suggesting that mammalian TADs can display various conformations, ranging from condensed and globular objects to more stretched configurations (*106*, *108*). This might depend, in part, on the cell-specific transcriptional output, consistent with the finding that different levels of transcriptional activity of Tsix alleles were related to fluctuations in TAD conformations (*108*). Boundary precision and degree of insulation of TADs can also vary among different cell types (*24*, *53*, *54*, *109*) or during cell cycle progression (*110*).

The recent application of super-resolution microscopy, such as STORM or 3D-structured illumination microscopy (3D-SIM), has allowed finer-scale chromatin architecture to be analyzed at the single-cell level, opening the possibility of studying the structural properties of chromosome domains [for review, see (*111*)]. Using FISH and 3D-SIM, it was shown that, despite heterogeneous folding of individual TADs and diversity in their relative arrangement in 3D space, discrete nanocompartments corresponding to repressed chromatin (repressed TADs) interspersed by decondensed active domains can be observed in individual cells, suggesting that the *Drosophila* TAD pattern reflects a fairly stable segregation of active and inactive chromatin domains (*90*). Therefore, a dynamic intra-TAD folding is compatible with a steady separation of autonomous chromosomal units, at least in *Drosophila*. In mammals, TADs can contain various epigenetic marks and may be more flexible in shape, as suggested by the dynamic binding of CTCF and cohesin at loop anchors (*112*). However, recent super-resolution microscopy has also revealed the existence of nanosized chromatin domains in mammals (*113*–*115*), which correlate with epigenetic features, similarly to *Drosophila*. In both mammals and fly, H3K27me3 repressed regions form discrete and compacted domains (*91*, *116*), with active chromatin domains located at their periphery (*91*, *117*). Focusing on the imaging of several histone modifications associated with differential epigenetic states in mammals, Xu and colleagues (*118*) were able to resolve the higher-order chromatin organization into three major structural characteristics, including segregated nanoclusters for lysine acetylation, dispersed nanodomains for active histone methylation, and compact large aggregates for repressive histone methylation. This is consistent with previous observations of large and dense "clutches" of nucleosomes corresponding to heterochromatic regions compared to smaller and less dense RNAPII-associated chromatin (*115*), and with chromatin decondensation at transcribed sites (*119*). The combination of super-resolution microscopy and live imaging showed that chromatin nanodomains move coherently and that their structure depends on cohesin and nucleosome-nucleosome interactions (*114*). These domains have a peak diameter of approximately 160 nm, which was estimated to cover 130 to 200 kb. This estimated genomic size is in good agreement with the nanocompartments (approximately 190 nm for a 200-kb repressed TAD) observed in *Drosophila* (*90*), and with that of sub-TADs identified in mammals (median size, 185 kb) (*14*), but is smaller than in mammalian TADs (average size, 880 kb) (*16*). However, when STORM super-resolution microscopy was combined with sequential DNA labeling of multi-megabase genomic regions, larger globular nanocompartments of several hundred nanometers, equivalent to full TADs, were observed (*48*). In the future, it will be important to assess the relation between TADs and sub-TADs in different types of mammalian chromatin to understand whether sub-TADs exist in each cell and to determine their prevalence in each type of chromatin.

Differentiation processes may also represent a source of variability of TAD structures. At the megabase scale, TAD patterns in mammals appear largely conserved in different cell lines and even across species (*16*, *31*), whereas on a submegabase scale, subdomains within a TAD could become merged or disconnected, depending on developmentally regulated events (*16*, *24*, *33*, *109*, *120*). In this case, the dynamics is largely due to the appearance of new regulatory enhancer-promoter contacts involving specific transcription factors, concomitant to gene expression during lineage specification or cell reprogramming (*24*, *109*, *120*). It was recently shown that TADs can be variable in different cells (*48*), but it will be important to study whether the variability depends on specific activities of enhancers and target promoters. Related to this point, recent live-cell imaging methods have started to shed light into the dynamics of functional elements (*121*–*123*). The observation of coordinated transcriptional bursts and the fact that enhancer and promoter interactions seem to adopt a "stirring model," in which the search will be confined and potentiated rather

than a conventional stable loop, suggest a dynamic view of enhancer-promoter interactions (*122*, *123*). Moreover, the act of transcription per se might stabilize proximal chromatin conformation, reducing enhancer-promoter distances (*121*). Last, it has been proposed that transcription-induced supercoiling could participate in the establishment of contact between functional elements within TADs (*124*). Therefore, TADs may establish a local chromosomal environment in which regulatory signals might act to tune the probability of dynamic interaction among distally located enhancers and promoters.

TADs AND GENOME EVOLUTION

TADs are generally present in metazoans (*125*) and, despite different mechanisms in TAD formation and the open questions concerning their structure and dynamics, function as regulatory units of the genome, and genes contained within them tend to be coregulated during development (*18*, *20*–*22*). Furthermore, they define the limits of the chromosomal domains in which gene promoters are contacted by cis-regulatory elements (*23*, *24*). Therefore, TADs appear particularly interesting for the study of genome evolution (*125*). In particular, they might act as buffering elements, allowing mutations to exert local effects without affecting surrounding extra-TAD loci. As an example of this, CTCF binding sequences were shown to be more prone to changes within TADs than in boundaries, allowing the creation of potential new regulatory contacts within chromosomal domains to emerge in a modular fashion, preventing them from affecting extra-TAD loci (*31*). Furthermore, TADs appear relatively flexible in size and can tolerate the gain or loss of DNA sequence (*126*), which can also favor the emergence of novel regulatory effects. The TAD organization could allow the evolution of new cis-regulatory elements by limiting the influence of these regulatory changes to a few genes, namely, those located within the same TAD (*125*). On the other hand, a subset of TADs is associated with high level of noncoding conservation, which may be important to preserve the expression regulation of key developmental genes. Therefore, these 3D structures may also contribute to the maintenance of selective pressure of internal elements that are necessary for the precise control of specific loci (*126*).

If TADs are advantageous for genome function, then one might expect their boundaries to be highly conserved. Dixon and colleagues (*16*) showed that syntenic regions between mouse and human are very similar in chromatin structure and that 75.9% of boundaries in mouse are present in human, while 53.8% of human boundaries are present in mouse. Another study investigated the evolution of chromosomal topology across four mammalian species (mouse, dog, rabbit, and macaque) and again observed the conservation of chromatin structure within syntenic regions (*31*). Conserved TADs are associated with conserved CTCF binding sites and motif orientation at their borders, while changes in internal domain structures are correlated with changes in binding and orientation of CTCF, indicating a co-evolution of CTCF binding and chromatin structure. In addition, comparison of gibbon and human genomes showed that gibbon breaks of synteny mainly occur at TAD boundaries and that epigenetic landscapes are maintained after rearrangement (*127*). Consistently, pairs of genes situated within the same TAD in zebrafish are found more often close to each other in other vertebrate genomes than those situated in two neighboring TADs (*83*). Moreover, the comparison of gene expression data from many mouse and human tissues indicates that genes within TADs have more conserved expression patterns, and disruption of TADs by evolutionary rearrangements is associated with changes in gene expression profiles (*128*). Therefore, it appears that TADs are maintained as intact modules during evolution, which may help the conservation of functional regulatory landscapes. An example of this conservation can be illustrated with the analysis of the *Six* homeobox gene cluster in distant species: the echinoderm sea urchin, zebrafish, and mammals. Despite subsequent rounds of whole genomic duplications, this cluster remained organized into two adjacent TADs that have different expression patterns, with borders associated with orientation-inverted CTCF sites (*129*). In addition to the selective pressure for the maintenance of intact TADs, another force that might contribute to the same result is linked to frequent organization of TAD borders into a locally open chromatin structure, consistent with more frequent DNA double-strand breaks and repair relative to internal TAD sequences, such that TAD boundaries may represent hotspots for genomic rearrangements (*127*). This feature, together with the fact that the disruption of TAD borders can have detrimental effects by leading to ectopic contacts and gene deregulation, might contribute to the maintenance of TADs during evolution.

On the other side of the coin, changes in TAD architecture could sometimes represent an evolutionary advantage. Some gibbon breaks of synteny did not colocalize with TAD boundaries, indicating that, even if these events are rare, they may play a role in generating new regulatory landscapes (*127*). Genomic duplications in patient cells can result in the formation of new chromatin domains (neo-TADs). Sometimes, neo-TADs can explain the pathology, but in other cases, they have no phenotype (*26*). In this last case, the neo-TAD appears well insulated from the rest of the genome, and this may provide a potential window of opportunity for divergent genome evolution. Hox gene regulation represents a remarkable example to illustrate how new regulatory landscape may have arisen from changes in 3D chromatin structures. Important for mouse limb development, the HoxD cluster resides precisely over a TAD boundary flanked by two TADs with distinct regulatory capacities. This specific configuration allows *HoxD* genes to read regulatory information on both sides, with a switch occurring from the posterior to the anterior genomic regions to ensure proper gene expression pattern (*130*). The boundary between the two TADs is therefore dynamic during development and corresponds to a transition between active and inactive promoters of the *HoxD* genes. This bimodal and flexible regulation of *HoxD* clusters by cis-regulatory elements located in two adjacent TADs is conserved in zebrafish (*131*), but is absent in the invertebrate Amphioxus, where a unique *Hox* gene cluster is present within a single TAD (*125*). The split into two TADs is robust against perturbation, because only a large deletion, including the whole cluster, eventually leads to the fusion of the two TADs (*132*). The appearance of a new genomic region may therefore have led to novel cis-regulatory inputs in the vertebrate lineage.

CONCLUSIONS AND PERSPECTIVES

The hierarchical folding of chromosomes is a conserved feature of genome 3D organization during evolution. Notably, the segregation of active and repressed chromatin represents a key principle of chromosome organization at multiple scales, from the formation of mutually excluded compartments at the chromosomal scale to the local segregation of submegabase domains, forming TAD-like structures (*32*). In mammals, the presence of inverted CTCF binding sites is associated with the formation of chromatin loops, acting in addition

to the preexisting compartmentalization defined by the chromatin state. This may correspond to an additional layer of organization that is partially overriding homotypic chromatin cis interactions to build large-scale TADs. It will be interesting to study whether this role of CTCF in defining TAD borders might have been specifically gained in the vertebrate lineage or, alternatively, whether it was lost in *Drosophila* but is still present in other phylogenetic branches characterized by the presence of CTCF proteins. Certainly, it is not a necessary requisite as in other species, such as *C. elegans*, CTCF is absent, whereas self-interacting domains exist (*125*). Moreover, other eukaryotes like plants or yeast display TAD-like structures in the absence of CTCF proteins. This indicates that TADs are a more fundamental chromatin architecture that can exist without CTCF in other species, and in these cases, they are more correlated with transcriptional clustering. The distribution and density of transcribed genes and the presence and localization of insulator/architectural proteins may provide a framework to explain the contact patterns observed in these species. Therefore, different mechanisms leading to the compartmentalization of genome into autonomous units could produce similar output, i.e., the definition of regulatory landscapes within chromosomes. The conservation of TAD-like structures during evolution would then be functional, rather than structural.

If our understanding of the 3D genome organization has recently increased drastically, then outstanding questions remain to be addressed. Transcription has been tightly linked to chromosome folding, especially at TAD borders, but neither does its inhibition abolish boundaries (*32*, *53*, *54*, *59*), nor is its induction sufficient to create insulation (*24*). Hence, what drives CTCF-independent boundary formation? To what extent do TADs regulate genome activity, as opposed to emerging as a consequence of genome function? Also, if many studies focused on the role of mammalian TADs in transcription through the spatial regulation of contacts between gene promoters and cis-regulatory elements, then it is not clear whether this applies to other organisms. Is the partitioning of genomes into domains generally required to ensure proper gene regulation or are other genome functions the reason to be of TADs, at least in a subset of nonmammalian species? The development of single-cell omics, live imaging, super-resolution microscopy, and modeling of the chromatin fiber, combined with state-of-the-art genome engineering technologies, offers a powerful toolset for addressing these questions in the coming years.

REFERENCES AND NOTES

1. W. A. Bickmore, The spatial organization of the human genome. *Annu. Rev. Genomics Hum. Genet.* **14**, 67–84 (2013).
2. T. Cremer, M. Cremer, Chromosome territories. *Cold Spring Harb. Perspect. Biol.* **2**, a003889 (2010).
3. S. Shah, Y. Takei, W. Zhou, E. Lubeck, J. Yun, C.-H. L. Eng, N. Koulena, C. Cronin, C. Karp, E. J. Liaw, M. Amin, L. Cai, Dynamics and spatial genomics of the nascent transcriptome by intron seqFISH. *Cell* **174**, 363–376.e16 (2018).
4. B. Bonev, G. Cavalli, Organization and function of the 3D genome. *Nat. Rev. Genet.* **17**, 661–678 (2016).
5. J. Dekker, K. Rippe, M. Dekker, N. Kleckner, Capturing chromosome conformation. *Science* **295**, 1306–1311 (2002).
6. E. Lieberman-Aiden, N. L. van Berkum, L. Williams, M. Imakaev, T. Ragoczy, A. Telling, I. Amit, B. R. Lajoie, P. J. Sabo, M. O. Dorschner, R. Sandstrom, B. Bernstein, M. A. Bender, M. Groudine, A. Gnirke, J. Stamatoyannopoulos, L. A. Mirny, E. S. Lander, J. Dekker, Comprehensive mapping of long-range interactions reveals folding principles of the human genome. *Science* **326**, 289–293 (2009).
7. S. Sati, G. Cavalli, Chromosome conformation capture technologies and their impact in understanding genome function. *Chromosoma* **126**, 33–44 (2017).
8. J. M. Galazka, A. D. Klocko, M. Uesaka, S. Honda, E. U. Selker, M. Freitag, *Neurospora*chromosomes are organized by blocks of importin alpha-dependent heterochromatin that are largely independent of H3K9me3. *Genome Res.* **26**,1069–1080 (2016).
9. S. Grob, M. W. Schmid, U. Grossniklaus, Hi-C analysis in *Arabidopsis* identifies the *KNOT*, a structure with similarities to the flamenco locus of *Drosophila*. *Mol. Cell* **55**, 678–693 (2014).
10. T. Mizuguchi, G. Fudenberg, S. Mehta, J.-M. Belton, N. Taneja, H. D. Folco, P. FitzGerald, J. Dekker, L. Mirny, J. Barrowman, S. I. S. Grewal, Cohesin-dependent globules and heterochromatin shape 3D genome architecture in S. *pombe*. *Nature* **516**, 432–435 (2014).
11. T. Sexton, E. Yaffe, E. Kenigsberg, F. Bantignies, B. Leblanc, M. Hoichman, H. Parrinello, A. Tanay, G. Cavalli, Three-dimensional folding and functional organization principles of the *Drosophila* genome. *Cell* **148**, 458–472 (2012).
12. Y. Zhang, R. P. McCord, Y.-J. Ho, B. R. Lajoie, D. G. Hildebrand, A. C. Simon, M. S. Becker, F. W. Alt, J. Dekker, Spatial organization of the mouse genome and its role in recurrent chromosomal translocations. *Cell* **148**, 908–921 (2012).
13. A. L. Sanborn, S. S. P. Rao, S.-C. Huang, N. C. Durand, M. H. Huntley, A. I. Jewett, I. D. Bochkov, D. Chinnappan, A. Cutkosky, J. Li, K. P. Geeting, A. Gnirke, A. Melnikov, D. McKenna, E. K. Stamenova, E. S. Lander, E. L. Aiden, Chromatin extrusion explains key features of loop and domain formation in wild-type and engineered genomes. *Proc. Natl. Acad. Sci. U.S.A.* **112**, E6456–E6465 (2015).
14. S. S. P. Rao, M. H. Huntley, N. C. Durand, E. K. Stamenova, I. D. Bochkov, J. T. Robinson, A. L. Sanborn, I. Machol, A. D. Omer, E. S. Lander, E. L. Aiden, A 3D map of the human genome at kilobase resolution reveals principles of chromatin looping. *Cell* **159**, 1665–1680 (2014).
15. S. Wang, J.-H. Su, B. J. Beliveau, B. Bintu, J. R. Moffitt, C.-t. Wu, X. Zhuang, Spatial organization of chromatin domains and compartments in single chromosomes. *Science* **353**, 598–602 (2016).
16. J. R. Dixon, S. Selvaraj, F. Yue, A. Kim, Y. Li, Y. Shen, M. Hu, J. S. Liu, B. Ren, Topological domains in mammalian genomes identified by analysis of chromatin interactions. *Nature* **485**, 376–380 (2012).
17. C. Hou, L. Li, Z. S. Qin, V. G. Corces, Gene density, transcription, and insulators contribute to the partition of the *Drosophila* genome into physical domains. *Mol. Cell* **48**, 471–484 (2012).
18. E. P. Nora, B. R. Lajoie, E. G. Schulz, L. Giorgetti, I. Okamoto, N. Servant, T. Piolot, N. L. van Berkum, J. Meisig, J. Sedat, J. Gribnau, E. Barillot, N. Blüthgen, J. Dekker, E. Heard, Spatial partitioning of the regulatory landscape of the X-inactivation centre. *Nature* **485**, 381–385 (2012).
19. B. D. Pope, T. Ryba, V. Dileep, F. Yue, W. Wu, O. Denas, D. L. Vera, Y. Wang, R. S. Hansen, T. K. Canfield, R. E. Thurman, Y. Cheng, G. Gülsoy, J. H. Dennis, M. P. Snyder, J. A. Stamatoyannopoulos, J. Taylor, R. C. Hardison, T. Kahveci, B. Ren, D. M. Gilbert, Topologically associating domains are stable units of replication-timing regulation. *Nature* **515**, 402–405 (2014).
20. J. R. Dixon, D. U. Gorkin, B. Ren, Chromatin domains: The unit of chromosome organization. *Mol. Cell* **62**, 668–680 (2016).
21. F. Ramirez, V. Bhardwaj, L. Arrigoni, K. C. Lam, B. A. Grüning, J. Villaveces, B. Habermann, A. Akhtar, T. Manke, High-resolution TADs reveal DNA sequences underlying genome organization in flies. *Nat. Commun.* **9**, 189 (2018).
22. Y. Zhan, L. Mariani, I. Barozzi, E. G. Schulz, N. Blüthgen, M. Stadler, G. Tiana, L. Giorgetti, Reciprocal insulation analysis of Hi-C data shows that TADs represent a functionally but not structurally privileged scale in the hierarchical folding of chromosomes. *Genome Res.* **27**, 479–490 (2017).
23. O. Symmons, V. V. Uslu, T. Tsujimura, S. Ruf, S. Nassari, W. Schwarzer, L. Ettwiller, F. Spitz, Functional and topological characteristics of mammalian regulatory domains. *Genome Res.* **24**, 390–400 (2014).
24. B. Bonev, N. M. Cohen, Q. Szabo, L. Fritsch, G. L. Papadopoulos, Y. Lubling, X. Xu, X. Lv, J.-P. Hugnot, A. Tanay, G. Cavalli, Multiscale 3D genome rewiring during mouse neural development. *Cell* **171**, 557–572.24 (2017).
25. W. A. Flavahan, Y. Drier, B. B. Liau, S. M. Gillespie, A. S. Venteicher, A. O. Stemmer-Rachamimov, M. L. Suvà, B. E. Bernstein, Insulator dysfunction and oncogene activation in *IDH* mutant gliomas. *Nature* **529**, 110–114 (2016).
26. M. Franke, D. M. Ibrahim, G. Andrey, W. Schwarzer, V. Heinrich, R. Schöpflin, K. Kraft, R. Kempfer, I. Jerković, W. L. Chan, M. Spielmann, B. Timmermann, L. Wittler, I. Kurth, P. Cambiaso, O. Zuffardi, G. Houge, L. Lambie, F. Brancati, A. Pombo, M. Vingron, F. Spitz, S. Mundlos, Formation of new chromatin domains determines pathogenicity of genomic duplications. *Nature* **538**, 265–269 (2016).
27. D. Hnisz, A. S. Weintraub, D. S. Day, A.-L. Valton, R. O. Bak, C. H. Li, J. Goldmann, B. R. Lajoie, Z. P. Fan, A. A. Sigova, J. Reddy, D. Borges-Rivera, T. I. Lee, R. Jaenisch, M. H. Porteus, J. Dekker, R. A. Young, Activation of proto-oncogenes by disruption of chromosome neighborhoods. *Science* **351**, 1454–1458 (2016).
28. D. G. Lupiáñez, K. Kraft, V. Heinrich, P. Krawitz, F. Brancati, E. Klopocki, D. Horn, H. Kayserili, J. M. Opitz, R. Laxova, F. Santos-Simarro, B. Gilbert-Dussardier, L. Wittler, M. Borschiwer, S. A. Haas, M. Osterwalder, M. Franke, B. Timmermann, S. Mundlos, Disruptions of

topological chromatin domains cause pathogenic rewiring of gene-enhancer interactions. *Cell* **161**, 1012–1025 (2015).
29. D. G. Lupiáñez, M. Spielmann, S. Mundlos, Breaking TADs: How alterations of chromatin domains result in disease. *Trends Genet.* **32**, 225–237 (2016).
30. J. Weischenfeldt, T. Dubash, A. P. Drainas, B. R. Mardin, Y. Chen, A. M. Stütz, S. M. Waszak, G. Bosco, A. R. Halvorsen, B. Raeder, T. Efthymiopoulos, S. Erkek, C. Siegl, H. Brenner, O. T. Brustugun, S. M. Dieter, P. A. Northcott, I. Petersen, S. M. Pfister, M. Schneider, S. K. Solberg, E. Thunissen, W. Weichert, T. Zichner, R. Thomas, M. Peifer, A. Helland, C. R. Ball, M. Jechlinger, R. Sotillo, H. Glimm, J. O. Korbel, Pan-cancer analysis of somatic copy-number alterations implicates *IRS4* and *IGF2* in enhancer hijacking. *Nat. Genet.* **49**, 65–74 (2017).
31. M. Vietri Rudan, C. Barrington, S. Henderson, C. Ernst, D. T. Odom, A. Tanay, S. Hadjur, Comparative Hi-C reveals that CTCF underlies evolution of chromosomal domain architecture. *Cell Rep.* **10**, 1297–1309 (2015).
32. M. J. Rowley, M. H. Nichols, X. Lyu, M. Ando-Kuri, I. S. M. Rivera, K. Hermetz, P. Wang, Y. Ruan, V. G. Corces, Evolutionarily conserved principles predict 3D chromatin organization. *Mol. Cell* **67**, 837–852.e7 (2017).
33. J. E. Phillips-Cremins, M. E. G. Sauria, A. Sanyal, T. I. Gerasimova, B. R. Lajoie, J. S. K. Bell, C.-T. Ong, T. A. Hookway, C. Guo, Y. Sun, M. J. Bland, W. Wagstaff, S. Dalton, T. C. McDevitt, R. Sen, J. Dekker, J. Taylor, V. G. Corces, Architectural protein subclasses shape 3D organization of genomes during lineage commitment. *Cell* **153**, 1281–1295 (2013).
34. E. de Wit, E. S. M. Vos, S. J. B. Holwerda, C. Valdes-Quezada, M. J. A. M. Verstegen, H. Teunissen, E. Splinter, P. J. Wijchers, P. H. L. Krijger, W. de Laat, CTCF binding polarity determines chromatin looping. *Mol. Cell* **60**, 676–684 (2015).
35. Y. Guo, Q. Xu, D. Canzio, J. Shou, J. Li, D. U. Gorkin, I. Jung, H. Wu, Y. Zhai, Y. Tang, Y. Lu, Y. Wu, Z. Jia, W. Li, M. Q. Zhang, B. Ren, A. R. Krainer, T. Maniatis, Q. Wu, CRISPR inversion of CTCF sites alters genome topology and enhancer/promoter function. *Cell* **162**, 900–910 (2015).
36. R. Saldaña-Meyer, E. González-Buendía, G. Guerrero, V. Narendra, R. Bonasio, F. Recillas-Targa, D. Reinberg, CTCF regulates the human p53 gene through direct interaction with its natural antisense transcript, Wrap53. *Genes Dev.* **28**, 723–734 (2014).
37. G. Fudenberg, M. Imakaev, C. Lu, A. Goloborodko, N. Abdennur, L. A. Mirny, Formation of chromosomal domains by loop extrusion. *Cell Rep.* **15**, 2038–2049 (2016).
38. L. Vian, A. Pękowska, S. S. P. Rao, K.-R. Kieffer-Kwon, S. Jung, L. Baranello, S.-C. Huang, L. E. Khattabi, M. Dose, N. Pruett, A. L. Sanborn, A. Canela, Y. Maman, A. Oksanen, W. Resch, X. Li, B. Lee, A. L. Kovalchuk, Z. Tang, S. Nelson, M. D. Pierro, R. R. Cheng, I. Machol, B. G. St. Hilaire, N. C. Durand, M. S. Shamim, E. K. Stamenova, J. N. Onuchic, Y. Ruan, A. Nussenzweig, D. Levens, E. L. Aiden, R. Casellas, The energetics and physiological impact of cohesin extrusion. *Cell* **173**, 1165–1178.e20 (2018).
39. G. Fudenberg, N. Abdennur, M. Imakaev, A. Goloborodko, L. A. Mirny, Emerging evidence of chromosome folding by loop extrusion. *Cold Spring Harb. Symp. Quant. Biol.* **82**, 45–55 (2017).
40. E. P. Nora, A. Goloborodko, A.-L. Valton, J. H. Gibcus, A. Uebersohn, N. Abdennur, J. Dekker, L. A. Mirny, B. G. Bruneau, Targeted degradation of CTCF decouples local insulation of chromosome domains from genomic compartmentalization. *Cell* **169**, 930–944.e22 (2017).
41. S. S. P. Rao, S.-C. Huang, B. G. St. Hilaire, J. M. Engreitz, E. M. Perez, K.-R. Kieffer-Kwon, A. L. Sanborn, S. E. Johnstone, G. D. Bascom, I. D. Bochkov, X. Huang, M. S. Shamim, J. Shin, D. Turner, Z. Ye, A. D. Omer, J. T. Robinson, T. Schlick, B. E. Bernstein, R. Casellas, E. S. Lander, E. L. Aiden, Cohesin loss eliminates all loop domains. *Cell* **171**, 305–320.e24 (2017).
42. W. Schwarzer, N. Abdennur, A. Goloborodko, A. Pekowska, G. Fudenberg, Y. Loe-Mie, N. A. Fonseca, W. Huber, C. H. Haering, L. Mirny, F. Spitz, Two independent modes of chromatin organization revealed by cohesin removal. *Nature* **551**, 51–56 (2017).
43. G. Wutz, C. Várnai, K. Nagasaka, D. A. Cisneros, R. R. Stocsits, W. Tang, S. Schoenfelder, G. Jessberger, M. Muhar, M. J. Hossain, N. Walther, B. Koch, M. Kueblbeck, J. Ellenberg, J. Zuber, P. Fraser, J.-M. Peters, Topologically associating domains and chromatin loops depend on cohesin and are regulated by CTCF, WAPL, and PDS5 proteins. *EMBO J.* **36**, 3573–3599 (2017).
44. J. H. I. Haarhuis, R. H. van der Weide, V. A. Blomen, J. O. Yáñez-Cuna, M. Amendola, M. S. van Ruiten, P. H. L. Krijger, H. Teunissen, R. H. Medema, B. van Steensel, T. R. Brummelkamp, E. de Wit, B. D. Rowland, The cohesin release factor WAPL restricts chromatin loop extension. *Cell* **169**, 693–707.e14 (2017).
45. J. Nuebler, G. Fudenberg, M. Imakaev, N. Abdennur, L. A. Mirny, Chromatin organization by an interplay of loop extrusion and compartmental segregation. *Proc. Natl. Acad. Sci. U.S.A.* **115**, E6697–E6706 (2018).
46. K. C. Yuen, B. D. Slaughter, J. L. Gerton, Condensin II is anchored by TFIIIC and H3K4me3 in the mammalian genome and supports the expression of active dense gene clusters. *Sci. Adv.* **3**, e1700191 (2017).
47. M. Ganji, I. A. Shaltiel, S. Bisht, E. Kim, A. Kalichava, C. H. Haering, C. Dekker, Real-time imaging of DNA loop extrusion by condensin. *Science* **360**, 102–105 (2018).
48. B. Bintu, L. J. Mateo, J.-H. Su, N. A. Sinnott-Armstrong, M. Parker, S. Kinrot, K. Yamaya, A. N. Boettiger, X. Zhuang, Super-resolution chromatin tracing reveals domains and cooperative interactions in single cells. *Science* **362**, eaau1783 (2018).
49. A. S. Weintraub, C. H. Li, A. V. Zamudio, A. A. Sigova, N. M. Hannett, D. S. Day, B. J. Abraham, M. A. Cohen, B. Nabet, D. L. Buckley, Y. E. Guo, D. Hnisz, R. Jaenisch, J. E. Bradner, N. S. Gray, R. A. Young, YY1 is a structural regulator of enhancer-promoter loops. *Cell* **171**, 1573–1588.e28 (2017).
50. D. Racko, F. Benedetti, J. Dorier, A. Stasiak, Transcription-induced supercoiling as the driving force of chromatin loop extrusion during formation of TADs in interphase chromosomes. *Nucleic Acids Res.* **46**, 1648–1660 (2018).
51. L. Uusküla-Reimand, H. Hou, P. Samavarchi-Tehrani, M. V. Rudan, M. Liang, A. Medina-Rivera, H. Mohammed, D. Schmidt, P. Schwalie, E. J. Young, J. Reimand, S. Hadjur, A.-C. Gingras, M. D. Wilson, Topoisomerase II beta interacts with cohesin and CTCF at topological domain borders. *Genome Biol.* **17**, 182 (2016).
52. Y. H. Jung, M. E. G. Sauria, X. Lyu, M. S. Cheema, J. Ausio, J. Taylor, V. G. Corces, Chromatin states in mouse sperm correlate with embryonic and adult regulatory landscapes. *Cell Rep.* **18**, 1366–1382 (2017).
53. Z. Du, H. Zheng, B. Huang, R. Ma, J. Wu, X. Zhang, J. He, Y. Xiang, Q. Wang, Y. Li, J. Ma, X. Zhang, K. Zhang, Y. Wang, M. Q. Zhang, J. Gao, J. R. Dixon, X. Wang, J. Zeng, W. Xie, Allelic reprogramming of 3D chromatin architecture during early mammalian development. *Nature* **547**, 232–235 (2017).
54. Y. Ke, Y. Xu, X. Chen, S. Feng, Z. Liu, Y. Sun, X. Yao, F. Li, W. Zhu, L. Gao, H. Chen, Z. Du, W. Xie, X. Xu, X. Huang, 3D chromatin structures of mature gametes and structural reprogramming during mammalian embryogenesis. *Cell* **170**, 367–381.e20 (2017).
55. K. P. Eagen, E. L. Aiden, R. D. Kornberg, Polycomb-mediated chromatin loops revealed by a subkilobase-resolution chromatin interaction map. *Proc. Natl. Acad. Sci. U.S.A.* **114**, 8764–8769 (2017).
56. Q. Wang, Q. Sun, D. M. Czajkowsky, Z. Shao, Sub-kb Hi-C in *D. melanogaster* reveals conserved characteristics of TADs between insect and mammalian cells. *Nat. Commun.* **9**, 188 (2018).
57. M. Forcato, C. Nicoletti, K. Pal, C. M. Livi, F. Ferrari, S. Bicciato, Comparison of computational methods for Hi-C data analysis. *Nat. Methods* **14**, 679–685 (2017).
58. C. Cubeñas-Potts, M. J. Rowley, X. Lyu, G. Li, E. P. Lei, V. G. Corces, Different enhancer classes in *Drosophila* bind distinct architectural proteins and mediate unique chromatin interactions and 3D architecture. *Nucleic Acids Res.* **45**, 1714–1730 (2017).
59. C. B. Hug, A. G. Grimaldi, K. Kruse, J. M. Vaquerizas, Chromatin architecture emerges during zygotic genome activation independent of transcription. *Cell* **169**, 216–228.e19 (2017).
60. S. V. Ulianov, E. E. Khrameeva, A. A. Gavrilov, I. M. Flyamer, P. Kos, E. A. Mikhaleva, A. A. Penin, M. D. Logacheva, M. V. Imakaev, A. Chertovich, M. S. Gelfand, Y. Y. Shevelyov, S. V. Razin, Active chromatin and transcription play a key role in chromosome partitioning into topologically associating domains. *Genome Res.* **26**, 70–84 (2016).
61. K. Van Bortle, M. H. Nichols, L. Li, C.-T. Ong, N. Takenaka, Z. S. Qin, V. G. Corces, Insulator function and topological domain border strength scale with architectural protein occupancy. *Genome Biol.* **15**, R82 (2014).
62. M. C. Gambetta, E. E. M. Furlong, The insulator protein CTCF is required for correct *Hox* gene expression, but not for embryonic development in *Drosophila*. *Genetics* **210**, 129–136 (2018).
63. A. V. Luzhin, I. M. Flyamer, E. E. Khrameeva, S. V. Ulianov, S. V. Razin, A. A. Gavrilov, Quantitative differences in TAD border strength underly the TAD hierarchy in *Drosophila* chromosomes. *J. Cell. Biochem.* **120**, 4494–4503 (2019).
64. Y. Ogiyama, B. Schuettengruber, G. L. Papadopoulos, J.-M. Chang, G. Cavalli, Polycomb-dependent chromatin looping contributes to gene silencing during *Drosophila* development. *Mol. Cell* **71**, 73–88.e5 (2018).
65. E. Crane, Q. Bian, R. P. McCord, B. R. Lajoie, B. S. Wheeler, E. J. Ralston, S. Uzawa, J. Dekker, B. J. Meyer, Condensin-driven remodelling of X chromosome topology during dosage compensation. *Nature* **523**, 240–244 (2015).
66. S. Feng, S. J. Cokus, V. Schubert, J. Zhai, M. Pellegrini, S. E. Jacobsen, Genome-wide Hi-C analyses in wild-type and mutants reveal high-resolution chromatin interactions in Arabidopsis. *Mol. Cell* **55**, 694–707 (2014).
67. C. Wang, C. Liu, D. Roqueiro, D. Grimm, R. Schwab, C. Becker, C. Lanz, D. Weigel, Genome-wide analysis of local chromatin packing in *Arabidopsis thaliana*. *Genome Res.* **25**, 246–256 (2015).
68. Q. Dong, N. Li, X. Li, Z. Yuan, D. Xie, X. Wang, J. Li, Y. Yu, J. Wang, B. Ding, Z. Zhang, C. Li, Y. Bian, A. Zhang, Y. Wu, B. Liu, L. Gong, Genome-wide Hi-C analysis reveals extensive hierarchical chromatin interactions in rice. *Plant J.* **94**, 1141–1156 (2018).
69. C. Liu, Y.-J. Cheng, J.-W. Wang, D. Weigel, Prominent topologically associated domains differentiate global chromatin packing in rice from *Arabidopsis*. *Nat. Plants* **3**, 742–748 (2017).
70. M. Wang, P. Wang, M. Lin, Z. Ye, G. Li, L. Tu, C. Shen, J. Li, Q. Yang, X. Zhang, Evolutionary dynamics of 3D genome architecture following polyploidization in cotton. *Nat. Plants* **4**, 90–97 (2018).

71. P. Dong, X. Tu, P.-Y. Chu, P. Lü, N. Zhu, D. Grierson, B. Du, P.-h. Li, S. Zhong, 3D chromatin architecture of large plant genomes determined by local A/B compartments. *Mol. Plant* **10**, 1497–1509 (2017).
72. Z. Duan, M. Andronescu, K. Schutz, S. McIlwain, Y. J. Kim, C. Lee, J. Shendure, S. Fields, C. A. Blau, W. S. Noble, A three-dimensional model of the yeast genome. *Nature* **465**, 363–367 (2010).
73. T.-H. S. Hsieh, A. Weiner, B. Lajoie, J. Dekker, N. Friedman, O. J. Rando, Mapping nucleosome resolution chromosome folding in yeast by micro-C. *Cell* **162**, 108–119 (2015).
74. F. Benedetti, D. Racko, J. Dorier, Y. Burnier, A. Stasiak, Transcription-induced supercoiling explains formation of self-interacting chromatin domains in *S. pombe*. *Nucleic Acids Res.* **45**, 9850–9859 (2017).
75. T. B. K. Le, M. V. Imakaev, L. A. Mirny, M. T. Laub, High-resolution mapping of the spatial organization of a bacterial chromosome. *Science* **342**, 731–734 (2013).
76. M. Marbouty, A. Le Gall, D. I. Cattoni, A. Cournac, A. Koh, J.-B. Fiche, J. Mozziconacci, H. Murray, R. Koszul, M. Nollmann, Condensin- and replication-mediated bacterial chromosome folding and origin condensation revealed by Hi-C and super-resolution imaging. *Mol. Cell* **59**, 588–602 (2015).
77. X. Wang, T. B. K. le, B. R. Lajoie, J. Dekker, M. T. Laub, D. Z. Rudner, Condensin promotes the juxtaposition of DNA flanking its loading site in *Bacillus subtilis*. *Genes Dev.* **29**, 1661–1675 (2015).
78. O. Espeli, R. Mercier, F. Boccard, DNA dynamics vary according to macrodomain topography in the *E. coli* chromosome. *Mol. Microbiol.* **68**, 1418–1427 (2008).
79. M. Trussart, E. Yus, S. Martinez, D. Baù, Y. O. Tahara, T. Pengo, M. Widjaja, S. Kretschmer, J. Swoger, S. Djordjevic, L. Turnbull, C. Whitchurch, M. Miyata, M. A. Marti-Renom, M. Lluch-Senar, L. Serrano, Defined chromosome structure in the genome-reduced bacterium *Mycoplasma pneumoniae*. *Nat. Commun.* **8**, 14665 (2017).
80. N. T. Tran, M. T. Laub, T. B. K. Le, SMC progressively aligns chromosomal arms in *Caulobacter crescentus* but is antagonized by convergent transcription. *Cell Rep.* **20**, 2057–2071 (2017).
81. X. Wang, H. B. Brandão, T. B. K. Le, M. T. Laub, D. Z. Rudner, *Bacillus subtilis* SMC complexes juxtapose chromosome arms as they travel from origin to terminus. *Science* **355**, 524–527 (2017).
82. X. Wang, A. C. Hughes, H. B. Brandão, B. Walker, C. Lierz, J. C. Cochran, M. G. Oakley, A. C. Kruse, D. Z. Rudner, In vivo evidence for ATPase-dependent DNA translocation by the *Bacillus subtilis* SMC condensin complex. *Mol. Cell* **71**, 841–847.e5 (2018).
83. L. J. T. Kaaij, R. H. van der Weide, R. F. Ketting, E. de Wit, Systemic loss and gain of chromatin architecture throughout zebrafish development. *Cell Rep.* **24**, 1–10.e4 (2018).
84. F. Ay, E. M. Bunnik, N. Varoquaux, S. M. Bol, J. Prudhomme, J.-P. Vert, W. S. Noble, K. G. Le Roch, Three-dimensional modeling of the *P. falciparum* genome during the erythrocytic cycle reveals a strong connection between genome architecture and gene expression. *Genome Res.* **24**, 974–988 (2014).
85. C.-T. Ong, V. G. Corces, Insulators as mediators of intra- and inter-chromosomal interactions: A common evolutionary theme. *J. Biol.* **8**, 73 (2009).
86. G. A. Busslinger, R. R. Stocsits, P. van der Lelij, E. Axelsson, A. Tedeschi, N. Galjart, J.-M. Peters, Cohesin is positioned in mammalian genomes by transcription, CTCF and Wapl. *Nature* **544**, 503–507 (2017).
87. Z. Misulovin, Y. B. Schwartz, X.-Y. Li, T. G. Kahn, M. Gause, S. MacArthur, J. C. Fay, M. B. Eisen, V. Pirrotta, M. D. Biggin, D. Dorsett, Association of cohesin and Nipped-B with transcriptionally active regions of the *Drosophila melanogaster* genome. *Chromosoma* **117**, 89–102 (2008).
88. C. A. Schaaf, Z. Misulovin, M. Gause, A. Koenig, D. W. Gohara, A. Watson, D. Dorsett, Cohesin and polycomb proteins functionally interact to control transcription at silenced and active genes. *PLOS Genet.* **9**, e1003560 (2013).
89. A. N. Boettiger, B. Bintu, J. R. Moffitt, S. Wang, B. J. Beliveau, G. Fudenberg, M. Imakaev, L. A. Mirny, C.-t. Wu, X. Zhuang, Super-resolution imaging reveals distinct chromatin folding for different epigenetic states. *Nature* **529**, 418–422 (2016).
90. Q. Szabo, D. Jost, J.-M. Chang, D. I. Cattoni, G. L. Papadopoulos, B. Bonev, T. Sexton, J. Gurgo, C. Jacquier, M. Nollmann, F. Bantignies, G. Cavalli, TADs are 3D structural units of higher-order chromosome organization in *Drosophila*. *Sci. Adv.* **4**, eaar8082 (2018).
91. D. I. Cattoni, A. M. Cardozo Gizzi, M. Georgieva, M. Di Stefano, A. Valeri, D. Chamousset, C. Houbron, S. Déjardin, J.-B. Fiche, I. González, J.-M. Chang, T. Sexton, M. A. Marti-Renom, F. Bantignies, G. Cavalli, M. Nollmann, Single-cell absolute contact probability detection reveals chromosomes are organized by multiple low-frequency yet specific interactions. *Nat. Commun.* **8**, 1753 (2017).
92. K. P. Eagen, T. A. Hartl, R. D. Kornberg, Stable chromosome condensation revealed by chromosome conformation capture. *Cell* **163**, 934–946 (2015).
93. M. R. Stadler, J. E. Haines, M. B. Eisen, Convergence of topological domain boundaries, insulators, and polytene interbands revealed by high-resolution mapping of chromatin contacts in the early *Drosophila melanogaster* embryo. *eLife* **6**, e29550 (2017).
94. V. Narendra, P. P. Rocha, D. An, R. Raviram, J. A. Skok, E. O. Mazzoni, D. Reinberg, CTCF establishes discrete functional chromatin domains at the *Hox* clusters during differentiation. *Science* **347**, 1017–1021 (2015).
95. G. Nir, I. Farabella, C. P. Estrada, C. G. Ebeling, B. J. Beliveau, H. M. Sasaki, S. D. Lee, S. C. Nguyen, R. B. McCole, S. Chattoraj, J. Erceg, J. A. Abed, N. M. C. Martins, H. Q. Nguyen, M. A. Hannan, S. Russell, N. C. Durand, S. S. P. Rao, J. Y. Kishi, P. Soler-Vila, M. Di Pierro, J. N. Onuchic, S. P. Callahan, J. M. Schreiner, J. A. Stuckey, P. Yin, E. L. Aiden, M. A. Marti-Renom, C.-t. Wu, Walking along chromosomes with super-resolution imaging, contact maps, and integrative modeling. *PLOS Genet.* **14**, e1007872 (2018).
96. I. M. Flyamer, J. Gassler, M. Imakaev, H. B. Brandão, S. V. Ulianov, N. Abdennur, S. V. Razin, L. A. Mirny, K. Tachibana-Konwalski, Single-nucleus Hi-C reveals unique chromatin reorganization at oocyte-to-zygote transition. *Nature* **544**, 110–114 (2017).
97. J. W. K. Ho, Y. L. Jung, T. Liu, B. H. Alver, S. Lee, K. Ikegami, K.-A. Sohn, A. Minoda, M. Y. Tolstorukov, A. Appert, S. C. J. Parker, T. Gu, A. Kundaje, N. C. Riddle, E. Bishop, T. A. Egelhofer, S. S. Hu, A. A. Alekseyenko, A. Rechtsteiner, D. Asker, J. A. Belsky, S. K. Bowman, Q. B. Chen, R. A.-J. Chen, D. S. Day, Y. Dong, A. C. Dose, X. Duan, C. B. Epstein, S. Ercan, E. A. Feingold, F. Ferrari, J. M. Garrigues, N. Gehlenborg, P. J. Good, P. Haseley, D. He, M. Herrmann, M. M. Hoffman, T. E. Jeffers, P. V. Kharchenko, P. Kolasinska-Zwierz, C. V. Kotwaliwale, N. Kumar, S. A. Langley, E. N. Larschan, I. Latorre, M. W. Libbrecht, X. Lin, R. Park, M. J. Pazin, H. N. Pham, A. Plachetka, B. Qin, Y. B. Schwartz, N. Shoresh, P. Stempor, A. Vielle, C. Wang, C. M. Whittle, H. Xue, R. E. Kingston, J. H. Kim, B. E. Bernstein, A. F. Dernburg, V. Pirrotta, M. I. Kuroda, W. S. Noble, T. D. Tullius, M. Kellis, D. M. MacAlpine, S. Strome, S. C. R. Elgin, X. S. Liu, J. D. Lieb, J. Ahringer, G. H. Karpen, P. J. Park, Comparative analysis of metazoan chromatin organization. *Nature* **512**, 449–452 (2014).
98. A. G. Larson, D. Elnatan, M. M. Keenen, M. J. Trnka, J. B. Johnston, A. L. Burlingame, D. A. Agard, S. Redding, G. J. Narlikar, Liquid droplet formation by HP1α suggests a role for phase separation in heterochromatin. *Nature* **547**, 236–240 (2017).
99. A. R. Strom, A. V. Emelyanov, M. Mir, D. V. Fyodorov, X. Darzacq, G. H. Karpen, Phase separation drives heterochromatin domain formation. *Nature* **547**, 241–245 (2017).
100. B. R. Sabari, A. Dall'Agnese, A. Boija, I. A. Klein, E. L. Coffey, K. Shrinivas, B. J. Abraham, N. M. Hannett, A. V. Zamudio, J. C. Manteiga, C. H. Li, Y. E. Guo, D. S. Day, J. Schuijers, E. Vasile, S. Malik, D. Hnisz, T. I. Lee, I. I. Cisse, R. G. Roeder, P. A. Sharp, A. K. Chakraborty, R. A. Young, Coactivator condensation at super-enhancers links phase separation and gene control. *Science* **361**, eaar3958 (2018).
101. W.-K. Cho, J.-H. Spille, M. Hecht, C. Lee, C. Li, V. Grube, I. I. Cisse, Mediator and RNA polymerase II clusters associate in transcription-dependent condensates. *Science* **361**, 412–415 (2018).
102. H. Lu, D. Yu, A. S. Hansen, S. Ganguly, R. Liu, A. Heckert, X. Darzacq, Q. Zhou, Phase-separation mechanism for C-terminal hyperphosphorylation of RNA polymerase II. *Nature* **558**, 318–323 (2018).
103. F. Erdel, K. Rippe, Formation of chromatin subcompartments by phase separation. *Biophys. J.* **114**, 2262–2270 (2018).
104. D. Hnisz, K. Shrinivas, R. A. Young, A. K. Chakraborty, P. A. Sharp, A phase separation model for transcriptional control. *Cell* **169**, 13–23 (2017).
105. T. Nagano, Y. Lubling, T. J. Stevens, S. Schoenfelder, E. Yaffe, W. Dean, E. D. Laue, A. Tanay, P. Fraser, Single-cell Hi-C reveals cell-to-cell variability in chromosome structure. *Nature* **502**, 59–64 (2013).
106. T. J. Stevens, D. Lando, S. Basu, L. P. Atkinson, Y. Cao, S. F. Lee, M. Leeb, K. J. Wohlfahrt, W. Boucher, A. O'Shaughnessy-Kirwan, J. Cramard, A. J. Faure, M. Ralser, E. Blanco, L. Morey, M. Sansó, M. G. S. Palayret, B. Lehner, L. Di Croce, A. Wutz, B. Hendrich, D. Klenerman, E. D. Laue, 3D structures of individual mammalian genomes studied by single-cell Hi-C. *Nature* **544**, 59–64 (2017).
107. L. Tan, D. Xing, C.-H. Chang, H. Li, X. S. Xie, Three-dimensional genome structures of single diploid human cells. *Science* **361**, 924–928 (2018).
108. L. Giorgetti, R. Galupa, E. P. Nora, T. Piolot, F. Lam, J. Dekker, G. Tiana, E. Heard, Predictive polymer modeling reveals coupled fluctuations in chromosome conformation and transcription. *Cell* **157**, 950–963 (2014).
109. R. Stadhouders, E. Vidal, F. Serra, B. di Stefano, F. Le Dily, J. Quilez, A. Gomez, S. Collombet, C. Berenguer, Y. Cuartero, J. Hecht, G. J. Filion, M. Beato, M. A. Marti-Renom, T. Graf, Transcription factors orchestrate dynamic interplay between genome topology and gene regulation during cell reprogramming. *Nat. Genet.* **50**, 238–249 (2018).
110. T. Nagano, Y. Lubling, C. Várnai, C. Dudley, W. Leung, Y. Baran, N. Mendelson Cohen, S. Wingett, P. Fraser, A. Tanay, Cell-cycle dynamics of chromosomal organization at single-cell resolution. *Nature* **547**, 61–67 (2017).
111. M. Lakadamyali, M. P. Cosma, Advanced microscopy methods for visualizing chromatin structure. *FEBS Lett.* **589**, 3023–3030 (2015).
112. A. S. Hansen, I. Pustova, C. Cattoglio, R. Tjian, X. Darzacq, CTCF and cohesin regulate chromatin loop stability with distinct dynamics. *eLife* **6**, e25776 (2017).
113. K. Fang, X. Chen, X. Li, Y. Shen, J. Sun, D. M. Czajkowsky, Z. Shao, Super-resolution imaging of individual human subchromosomal regions in situ reveals nanoscopic building blocks of higher-order structure. *ACS Nano* **12**, 4909–4918 (2018).

114. T. Nozaki, R. Imai, M. Tanbo, R. Nagashima, S. Tamura, T. Tani, Y. Joti, M. Tomita, K. Hibino, M. T. Kanemaki, K. S. Wendt, Y. Okada, T. Nagai, K. Maeshima, Dynamic organization of chromatin domains revealed by super-resolution live-cell imaging. *Mol. Cell* **67**, 282–293e7 (2017).
115. M. A. Ricci, C. Manzo, M. F. García-Parajo, M. Lakadamyali, M. P. Cosma, Chromatin fibers are formed by heterogeneous groups of nucleosomes in vivo. *Cell* **160**, 1145–1158 (2015).
116. S. Kundu, F. Ji, H. Sunwoo, G. Jain, J. T. Lee, R. I. Sadreyev, J. Dekker, R. E. Kingston, Polycomb repressive complex 1 generates discrete compacted domains that change during differentiation. *Mol. Cell* **65**, 432–446.e5 (2017).
117. D. Smeets, Y. Markaki, V. J. Schmid, F. Kraus, A. Tattermusch, A. Cerase, M. Sterr, S. Fiedler, J. Demmerle, J. Popken, H. Leonhardt, N. Brockdorff, T. Cremer, L. Schermelleh, M. Cremer, Three-dimensional super-resolution microscopy of the inactive X chromosome territory reveals a collapse of its active nuclear compartment harboring distinct Xist RNA foci. *Epigenetics Chromatin* **7**, 8 (2014).
118. J. Xu, H. Ma, J. Jin, S. Uttam, R. Fu, Y. Huang, Y. Liu, Super-resolution imaging of higher-order chromatin structures at different epigenomic states in single mammalian cells. *Cell Rep.* **24**, 873–882 (2018).
119. Y. Wang, S. Maharana, M. D. Wang, G. V. Shivashankar, Super-resolution microscopy reveals decondensed chromatin structure at transcription sites. *Sci. Rep.* **4**, 4477 (2014).
120. J. R. Dixon, I. Jung, S. Selvaraj, Y. Shen, J. E. Antosiewicz-Bourget, A. Y. Lee, Z. Ye, A. Kim, N. Rajagopal, W. Xie, Y. Diao, J. Liang, H. Zhao, V. V. Lobanenkov, J. R. Ecker, J. A. Thomson, B. Ren, Chromatin architecture reorganization during stem cell differentiation. *Nature* **518**, 331–336 (2015).
121. H. Chen, M. Levo, L. Barinov, M. Fujioka, J. B. Jaynes, T. Gregor, Dynamic interplay between enhancer-promoter topology and gene activity. *Nat. Genet.* **50**, 1296–1303 (2018).
122. T. Fukaya, B. Lim, M. Levine, Enhancer control of transcriptional bursting. *Cell* **166**, 358–368 (2016).
123. B. Gu, T. Swigut, A. Spencley, M. R. Bauer, M. Chung, T. Meyer, J. Wysocka, Transcription-coupled changes in nuclear mobility of mammalian cis-regulatory elements. *Science* **359**, 1050–1055 (2018).
124. F. Benedetti, J. Dorier, A. Stasiak, Effects of supercoiling on enhancer-promoter contacts. *Nucleic Acids Res.* **42**, 10425–10432 (2014).
125. R. D. Acemel, I. Maeso, J. L. Gómez-Skarmeta, Topologically associated domains: A successful scaffold for the evolution of gene regulation in animals. *Wiley Interdiscip. Rev. Dev. Biol.* **6**, e265 (2017).
126. N. Harmston, E. Ing-Simmons, G. Tan, M. Perry, M. Merkenschlager, B. Lenhard, Topologically associating domains are ancient features that coincide with Metazoan clusters of extreme noncoding conservation. *Nat. Commun.* **8**, 441 (2017).
127. N. H. Lazar, K. A. Nevonen, B. O'Connell, C. McCann, R. J. O'Neill, R. E. Green, T. J. Meyer, M. Okhovat, L. Carbone, Epigenetic maintenance of topological domains in the highly rearranged gibbon genome. *Genome Res.* **28**, 983–997 (2018).
128. J. Krefting, M. A. Andrade-Navarro, J. Ibn-Salem, Evolutionary stability of topologically associating domains is associated with conserved gene regulation. *BMC Biol.* **16**, 87 (2018).
129. C. Gómez-Marín, J. J. Tena, R. D. Acemel, M. López-Mayorga, S. Naranjo, E. de la Calle-Mustienes, I. Maeso, L. Beccari, I. Aneas, E. Vielmas, P. Bovolenta, M. A. Nobrega, J. Carvajal, J. L. Gómez-Skarmeta, Evolutionary comparison reveals that diverging CTCF sites are signatures of ancestral topological associating domains borders. *Proc. Natl. Acad. Sci. U.S.A.* **112**, 7542–7547 (2015).
130. G. Andrey, T. Montavon, B. Mascrez, F. Gonzalez, D. Noordermeer, M. Leleu, D. Trono, F. Spitz, D. Duboule, A switch between topological domains underlies *HoxD* genes collinearity in mouse limbs. *Science* **340**, 1234167 (2013).
131. J. M. Woltering, D. Noordermeer, M. Leleu, D. Duboule, Conservation and divergence of regulatory strategies at *Hox* loci and the origin of tetrapod digits. *PLOS Biol.* **12**, e1001773 (2014).
132. E. Rodríguez-Carballo, L. Lopez-Delisle, Y. Zhan, P. J. Fabre, L. Beccari, I. El-Idrissi, T. H. N. Huynh, H. Ozadam, J. Dekker, D. Duboule, The *HoxD* cluster is a dynamic and resilient TAD boundary controlling the segregation of antagonistic regulatory landscapes. *Genes Dev.* **31**, 2264–2281 (2017).
133. H. D. Ou, S. Phan, T. J. Deerinck, A. Thor, M. H. Ellisman, C. C. O'Shea, ChromEMT: Visualizing 3D chromatin structure and compaction in interphase and mitotic cells. *Science* **357**, eaag0025 (2017).
134. N. C. Durand, J. T. Robinson, M. S. Shamim, I. Machol, J. P. Mesirov, E. S. Lander, E. L. Aiden, Juicebox provides a visualization system for Hi-C contact maps with unlimited zoom. *Cell Syst.* **3**, 99–101 (2016).
135. C. Liu, C. Wang, G. Wang, C. Becker, M. Zaidem, D. Weigel, Genome-wide analysis of chromatin packing in *Arabidopsis thaliana* at single-gene resolution. *Genome Res.* **26**, 1057–1068 (2016).

Acknowledgments

Funding: Q.S. was supported by the French Ministry of Higher Education and Research and La Ligue Nationale Contre le Cancer. F.B. was supported by CNRS. Research in the G.C. laboratory was supported by grants from the CNRS, the European Research Council (ERC) under the European Union's Horizon 2020 research and innovation programme [grant agreements no. 676556 (MuG) and no. 788972 (3DEpi)], the Agence Nationale de la Recherche (ANR-15-CE12-0006 EpiDevoMath), the Fondation pour la Recherche Médicale (DEI20151234396), the INSERM, the French National Cancer Institute (INCa), and the Laboratory of Excellence EpiGenMed. **Author contributions:** Q.S., F.B., and G.C. wrote the manuscript. **Competing interests:** The authors declare that they have no competing interest. **Data and materials availability:** All data needed to evaluate the conclusions in the paper are present in the articles cited herein.

Submitted 23 November 2018
Accepted 20 February 2019
Published 10 April 2019
10.1126/sciadv.aaw1668

Citation: Q. Szabo, F. Bantignies, G. Cavalli, Principles of genome folding into topologically associating domains. *Sci. Adv.* **5**, eaaw1668 (2019).

1.5.3 The functional role of TADs

If TADs have been characterized across many species, their role in genome activity is not clear, especially considering that this appellation englobes different types of domains that have different properties and likely formed by different mechanisms. As mentioned above, in some species such as *Drosophila* or plants, they seem to reflect the underlying epigenome and they may exist as a consequence of chromatin activity. Consistently, the analysis of the effect of large chromosomal rearrangements in *Drosophila* leading to inversions, duplications or deletions revealed little impact of these topology modifications on gene expression (Ghavi-Helm et al., 2019). In mammals, TAD formation depends on cohesin and CTCF, and most of the investigations that exposed a tight link between TAD structure and gene regulation was done in this phylogenetic branch. In one of the two original papers discovering TADs in mammals (Nora et al., 2012; Dixon et al., 2012), the examination of changes in gene expression during early ESC differentiation showed correlated transcription profiles when genes belong to the same TAD (Nora et al., 2012). This suggested that TADs correspond to cis-regulatory landscapes that coordinate gene expression. Further analysis comparing ESCs to neural precursor cells showed that co-regulation of genes is maximized at the TAD scale, in which interactions between enhancers and promoters are privileged (Zhan et al., 2017). Consistently, insertion of a reporter gene driven by a weak promoter in hundreds of genomic locations revealed that its induction by enhancer activities spread over large regions that correlate with TADs (Symmons et al., 2014). Dissection of the locus containing *Tfap2c* and *Bmp7* genes indicated that they are regulated by distinct set of enhancers that lay in two different structurally defined domains (Tsujimura et al., 2015). Moreover, genome-wide analysis of contacts between enhancer and promoters indicated that they are mainly restricted within TADs (Bonev et al., 2017; Sun et al., 2019). Altogether, these studies suggested that TADs provide a physical basis for gene regulation by favoring functional contacts between gene promoters and cis-regulatory elements within spatially defined domains.

This model has been comforted by a series of studies linking topological rearrangement to ectopic enhancer-promoter contacts and ectopic gene expression (Spielmann et al., 2018). One of the first characterized example involved the *EPHA4* locus (Lupiáñez et al., 2015). Structural variations including deletions, inversions or duplications that modify the organization of the locus were linked to different types of limb malformations in human. These mutations were reproduced in mice and were shown to disrupt a CTCF-associated TAD border and generate new contacts between genes and an enhancer cluster which normally regulates *EPHA4*. Similarly, inversions of CTCF-binding sites in the β-globin locus were shown to reconfigure TAD topology and led to gene misregulation (Guo et al., 2015). CTCF-defined boundaries thus appeared crucial in the definition of such regulatory landscapes. It was shown that IDH mutant gliomas are associated with a hypermethylation of CTCF binding sites that compromise the binding of this protein, associated with a reduced insulation between the neighboring TADs and ectopic enhancer-driven activation of the *PDGFRA* oncogene (Flavahan et al., 2016). Investigations of

T-cell acute lymphoblastic leukemia tumor cell line showed that they are often associated with deletions of borders of TADs that contain proto-oncogenes (Hnisz et al., 2016). Consistently, oncogene activation could be driven by CRISPR-Cas9 mediated boundary deletion, confirming the importance of TADs in defining expression patterns. Further analysis showed that redistribution of enhancer-promoter contacts by changing TAD topology is a common process in cancer (Weischenfeldt et al., 2017). Genomic duplications have also been directly linked to diseases, such as an intra-TAD duplication associated with sex-reversal phenotype, or a duplication crossing TAD borders leading to the exposition of the duplicated gene to new cis-regulatory elements, associated with limb malformation (Franke et al., 2016). All these studies demonstrated the importance of TAD structural organization in regulating gene expression in mammals (Figure 5). Nevertheless, a simplified view of a strict regulation of gene regulation by defining spatial landscapes needs to be integrated with various other parameters, such as cell-types, locations of enhancer relative to promoters, or the need of specific transcription factors to activate gene expression.

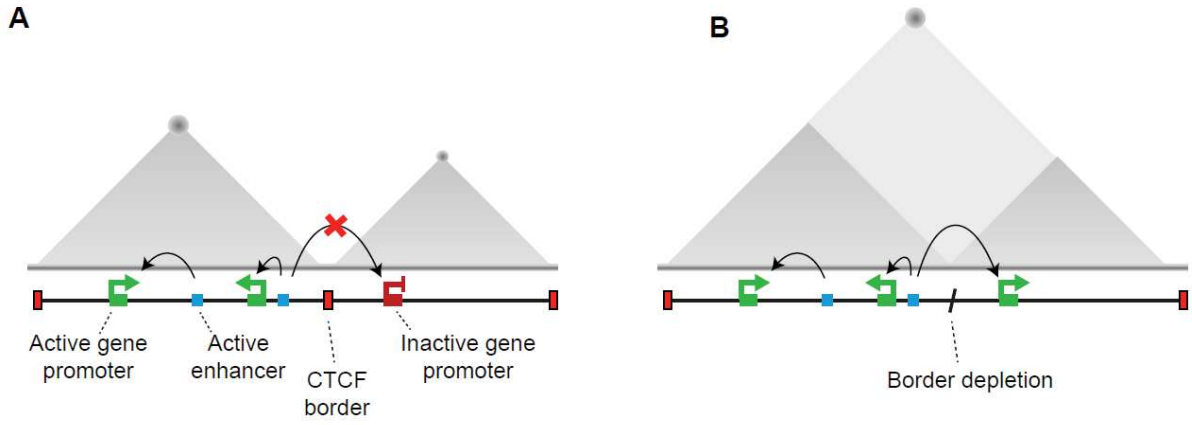

Figure 5. Model of genome regulation by TADs. (**A**) Two adjacent cis-regulatory landscapes defined by two TADs. The TAD on the left contains both active genes and enhancers and its borders are defined by the presence of inverted CTCF occupied sites. (**B**) Border depletion, for example by CTCF binding site deletion, eventually leads to the fusion of the two adjacent TADs and the activation of the previously inactive gene by ectopic contacts with active enhancers.

1.6 Polycomb-mediated higher-order chromatin architecture

One of the best-studied examples of the link between genome topology and activity involves the PcG proteins, well known for their role in transcriptional repression (Schuettengruber et al., 2017). First, these proteins were shown to remodel the ultra-structure of the chromatin fiber at the nucleosome scale [see section 1.2.1: Ultrastructure of the chromatin fiber (Francis et al., 2004; Dellino et al., 2004; King et al., 2018)]. Early works on *Hox* loci using 3C revealed the presence of discrete peaks of interactions between PcG bound regions, suggesting the establishment of functional hubs of repressive interactions (Lanzuolo et al., 2007; Ferraiuolo et al., 2010; Comet et al., 2011). Interestingly, this organization is dynamic, such as activation of genes results in their exclusion from the repressed topological structure (Lanzuolo et al., 2007; Noordermer et al., 2011; Cheutin and Cavalli, 2018; Mateo et al., 2019). The delimitation of active and repressed domains within *Hox* clusters were shown to rely on the presence of CTCF (Narendra et al., 2015). This dynamism is particularly well illustrated with a switch of the 3D conformation of a *Hox* cluster that allows the reading of different cis-regulatory element during development in mammals (Andrey et al., 2013). Recent studies using high-resolution Hi-C extended the 3C-based observations and showed that many Polycomb TADs display focal interactions between PREs in *Drosophila* (Eagen et al., 2017; Ogiyama et al., 2018). Their presence, which depend on the factor GAF, suggests that a particular architecture is required for the regulation of these loci. Indeed, abolition of one of these loops by inserting an insulator element can disrupt the transcriptional repression without removal of PcG proteins (Ogiyama et al., 2018). This is noticeable since it implies that a specific topology –and not the presence of specific factors bound to the gene- is required to ensure proper gene regulation.

At the TAD scale, super-resolution imaging of Polycomb domains in *Drosophila* indicated that they are more condensed than active or inactive 'void' domains, with a high degree of intermixing within themselves compared to the neighboring domains (Boettiger et al., 2016). This condensation was shown to rely on PRC1 both in *Drosophila* and mammals (Boettiger et al., 2016; Kundu et al., 2017). Interestingly, the loss of chromatin compaction upon the removal of PRC1 components can be observed independently of transcriptional activation, which indicates a primary role for these proteins in establishing 3D chromatin environment (Cheutin and Cavalli, 2018). In addition to their specific structures, Polycomb domains have been shown to undergo extensive long-range contact networks. Visualization of immuno-labeled PcG proteins revealed their organization as foci within the nucleus, the so-called Polycomb bodies (Buchenau 1998; Saurin et al., 1998; Wani et al., 2016). FISH labeling of the two *Hox* gene clusters in *Drosophila* that are separated by 10 Mb showed that they can contact each other within the nucleus, resulting in the formation of one large Polycomb body in which *Hox* are co-repressed (Bantignies et al., 2011). Perturbation of this interaction by mutating one of the two loci results in the weakening of the silencing of the other one. This points out a function for these long-range contacts in stabilizing transcriptional repression. These interactions are not restricted to *Hox* loci and

appeared as a general feature of Polycomb domains also conserved in mammals (Bantignies et al., 2011; Sexton et al., 2012; Schoenfelder et al., 2015). In mouse, ultra-long-range interactions among Polycomb loci are present in ESCs but are disrupted during neural differentiation (Bonev et al., 2017). This suggests that the establishment of such 3D hubs is a regulated mechanism, that rely at least in part on the polymerization activity of the sterile alpha motif domain of the Polyhomeotic PRC1 member (Schoenfelder et al., 2015; Wani et al., 2016; Isono et al., 2013; Szabo et al., 2018). Recent studies showed that the PRC1 subunit CBX2 is able to undergo liquid-liquid phase separation through its conserved intrinsically disordered domain and generate condensates in which chromatin is concentrated (Tatavosian et al., 2018; Plys et al., 2019). This may provide a mechanism for the segregation and the clustering of distal Polycomb domains within the nucleus.

Taken together, these results demonstrate that genome regulation associated with Polycomb is tightly linked to the formation of special higher-order chromatin architectures at multiple scales. At the finest scale, PRC1 compacts chromatin and remodels nucleosome organization which prevents transcription (Francis et al., 2004; Dellino et al., 2004; King et al., 2018). At the TAD scale, binding sites of PcG proteins undergo specific looping involving gene promoters and cis-regulatory elements that contribute to domain compaction and efficient gene silencing [Figure 6A (Eagen et al., 2017; Ogiyama et al., 2018)]. Finally, at the chromosomal scale, Polycomb domains form long-range hubs of interactions that shape a specific environment associated with transcriptional repression [Figure 6B (Bantignies et al., 2011; Schoenfelder et al., 2015)]. Importantly, PcG proteins regulate key biological processes, such as differentiation, proliferation or maintenance of pluripotency, and their deregulation is found in many cancers (Schuettengruber et al., 2017). Therefore, this multi-layer functional organization probably helps in the sharp and precise maintenance of crucial gene expression programs.

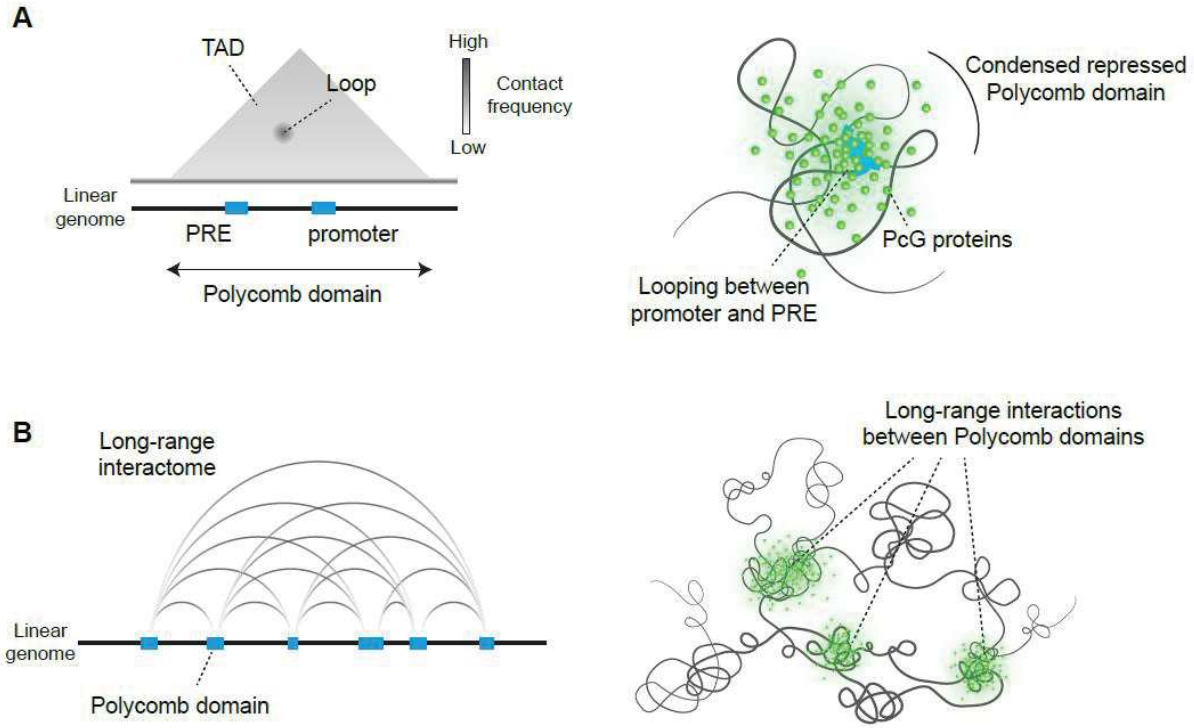

Figure 6. Multi-scale higher-order organization of Polycomb domain. (**A**) Schematic representation of a polycomb domain that harbors a loop between a PRE and a gene promoter. The domain, covered by the H3K27me3 mark, form a condensed chromosomal region with a high degree of chromatin mixing. (**B**) Polycomb domains undergo extensive mega-base, long-range interactions, resulting in the formation of repressive networks of interactions that can be visualized as polycomb foci in the nucleus.

1.7 Radial positioning and nuclear lamina

The non-random radial distribution of chromatin within the nucleus is another well studied feature of high-order nuclear organization. Heterochromatin is associated to the nuclear periphery, and euchromatin is preferentially located toward to the interior of the nucleus (Bickmore, 2013). It has been possible to identify and map the regions of the genome that are associated to the periphery with the DamID method (Pickersgill et al., 2006). This technique consists in using a Dam fused to a protein of interest, leading to the methylation of the adenines of the genomic loci in contact with. Typically, a Dam fused to the Lamin B, one of the component of the nuclear lamina, a filamentous network next to the inner nuclear membrane, allows the identification of the chromatin regions that are associated to the nuclear periphery. These regions have been named lamina-associated domains [LADs (Figure 7)]. In mammals, ~1000-1500 LADs are present on all chromosomes covering ~40% of the genome, with a size ranging from ~10 kb to ~10 Mb [median size of ~0.5 Mb (Guelen et al., 2008; Peric-Hupkes et al., 2010)]. In *Drosophila*, LADs are smaller, with a median size of ~90 kb (Pickersgill et al., 2006). LADs

are gene-poor, depleted of active histone marks, have a low transcriptional activity, and correspond to the B-type chromatin detected with Hi-C (Kind et al., 2015). Similarly to the ambiguous relationship between TADs and compartments in mammals, LADs and TADs do not always overlap, probably due to the fact that TADs can contain sub-TADs made of different chromatin types (Rao et al., 2014; van Steensel and Belmont, 2017). In individual cells, ~30% of the possible LADs are contacting the nuclear periphery and they are re-determined after mitosis, indicating that LADs-lamina contacts are variable (Kind et al., 2013). Moreover, some LADs appeared invariant in many cell-types, the so-called constitutive LADs, while others, facultative LADs (fLADs), are cell-type specific (Meuleman et al., 2013; Peric-Hupkes et al., 2010). Electron microscopy also showed that heterochromatin surrounds the nucleolus, and mapping of nucleolus-associated domains indicated that some of these regions can also be LADs [Figure 7 (van Koningsbruggen et al., 2010)]. Whether LADs are required to induce gene repression or whether relocation to the periphery is a consequence of gene inactivation has been a long-standing question. Artificial tethering of loci to the nuclear lamina can induce gene repression, yet not always (Finlan et al., 2008; Kumaran and Spector, 2008; Reddy et al., 2008). By inserting hundreds of LAD promoters into plasmids, it was shown that some of them stay repressed while others are activated when relocated outside from the LADs. On the other hand, inserting hundreds of promoters into LADs also result in different degree of repression (Leemans et al., 2019). These results indicate that intrinsic promoter properties as well as local chromatin features influence the degree of repression induced by the LADs.

Several studies investigated the role of the lamin proteins in the establishment of this organization. Lamins are sub-divided into two types, B-type lamins and A-type lamins, the latest being also found in the nuclear interior (van Steensel and Belmont, 2017). Depletion of the B-type lamin in a *Drosophila* cell line that lacks A-type lamins leads to the relocation of the chromatin towards the nucleus interior (Ulianov et al., 2019), and depletion of all lamins in mammalian cells also induces a detachment of some LADs from the nuclear lamina (Zheng et al., 2018). Furthermore, these depletions were associated with LAD decompaction and a modification of inter-TAD interactions, revealing a connection between radial positioning, chromatin condensation and long-range compartmentalization. Lamina is also associated with other proteins, such as lamin B receptor (LBR), LAP2-emerin-MAN1-domain proteins or barrier-to-autointegration factor (BAF). If LBR has been shown to be involved in the peripheral organization of the chromatin (Solovei et al., 2013), the role of these other factors remains to be elucidated. Last, a tight link between chromatin modifications and association to the lamina has been shown in *c. elegans*, in which anchoring to the nuclear periphery requires H3K9me1/2 marks and its recognition by the CEC-4 protein, while transcriptional repression is associated with H3K9me3 (Towbin et al., 2012; Gonzalez-Sandoval et al., 2015).

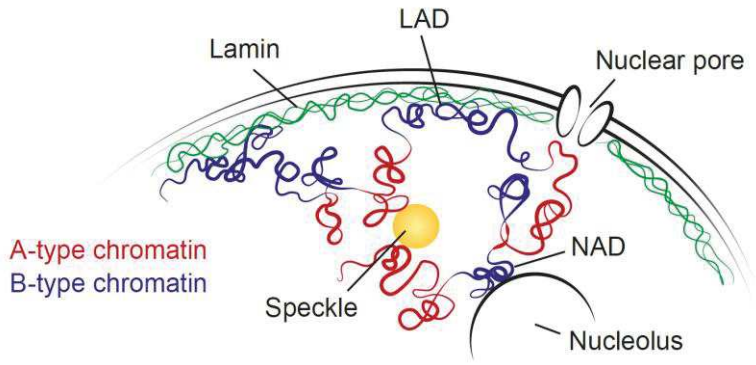

Figure 7. Radial organization of the chromatin. The nuclear lamina forms a filamentous network at the inner nuclear membrane. Repressed chromatin is preferentially located toward the nuclear periphery and can be anchored at the lamina as LADs. Some LADs can also be found attached to the nucleolus. Active chromatin is preferentially located toward the nuclear interior and can undergo long-range clustering, found for example at nuclear speckles. Active regions are also associated to nuclear pores (van Steensel and Belmont, 2017). These architectures associated with both transcriptional repression and activation may act as a "backbone" that constrains global chromosome organization.

1.8 Genome organization through development and differentiation

1.8.1 Early establishment of higher-order chromatin organization

The cells of a multicellular organism derive from the zygote, formed by the fusion of haploid gametes. How a functional nuclear organization is established –or inherited- through development, what are the processes involved, and what changes underlie cell-specific functions are questions of crucial interest, notably for the study of the epigenetic mechanisms that regulate cell-fate. In mammals, the male and female gametes display different chromosomal organization. In spermatozoa that are transcriptionally quiescent, compartments, TADs and loops are present despite the high degree of nucleus compaction compared to somatic cells (Jung et al., 2017; Ke et al., 2017). In female gametes, these features are also originally present in oocytes but disappear when they become mature and transcriptionally inactive (Flyamer et al., 2017; Ke et al., 2017). LADs are also absent in mature oocytes (Borsos et al., 2019). After fertilization, parental chromosomes are spatially segregated and differentially organized in the zygote, with a higher degree of A-B compartmentalization for the paternal genome. Higher-order chromatin organization is then progressively re-established with a strengthening of TADs and compartments (Ke et al., 2017; Du et al., 2017). Interestingly, the establishment of TADs appear to be independent of zygotic genome activation (ZGA) since transcription inhibition using α-Amanitin

doesn't abolish their formation. On the other hand, they don't form when DNA replication is prevented using Aphidicolin treatment (Ke et al., 2017). LADs seem to be immediately established after fertilization, even if inheritance from paternal genome cannot be exclude, and changes in nuclear positioning occur concomitantly with differential gene expression and *de novo* H3K4me3 deposition (Borsos et al., 2019).

In *Drosophila*, the genome is mostly unstructured before the ZGA. Boundaries appear then simultaneously with the binding of RNA pol II and the activation of transcription. The strength of the compartmentalization of the genome into TADs as well as the prominence of long-range contacts then progressively increases during embryogenesis (Hug et al., 2017; Ogiyama et al., 2018). As in mammals, blocking of transcription does not abolish TADs, yet their degree of insulation decreases, and long-range interactions between RNA pol II associated borders are diminished. Some TAD borders that are strongly bound by the pioneer Zelda TF disappear upon its depletion, suggesting a primary role of TFs in the formation of *Drosophila* TAD (Hug et al., 2017). Focal "looping" interactions are also gradually established during early embryogenesis. They are either enriched in active chromatin marks, with some of them also depend on the presence of Zelda, or correspond to interactions between PcG binding sites [(Ogiyama et al., 2018) see also section 1.6: Polycomb-mediated higher-order chromatin architecture].

1.8.2 Dynamic chromatin organization during cell fate

In vitro differentiation is a commonly used strategy to investigate the dynamics of nuclear organization during cell fate. Mouse ESCs are one of the best characterized cell types and can be further differentiated into different lineages. Hence, this provides a useful system to decipher the relationship between chromosome architecture and specific transcriptional programs. Importantly, TADs, compartments and LADs disappear during mitosis, indicating that they constantly need to be re-established (Naumova et al., 2013). Chromatin in ESCs is more open with less defined heterochromatic regions compared to differentiated cells (Mattout and Meshorer, 2010), and super-resolution analysis revealed that it assembles from dispersed and loosely packed nucleosome clutches (Ricci et al., 2015). Interestingly, in addition to a strong A-type chromatin compartmentalization (Bonev et al., 2017), ESCs display specific networks of long-range interactions. One of those involves pluripotency factors binding sites and is abrogated after differentiation (Apostolou et al., 2013; de Wit et al., 2013; Wei et al., 2013). The depletion of the Oct4, Nanog or Klf4 pluripotency-associated TFs disrupt theses interactions, indicating a role for TFs in mediating cell-type specific chromatin architecture. Strikingly, specific contacts between pluripotency factors-bound loci, rather than the binding of the TFs, were shown to be associated with efficient reprograming into induced pluripotent stem cells (Wei et al., 2013; Zhang et al., 2013). Another long-range interaction network in ESCs is mediated by the PcG proteins and is also progressively disrupted during cell differentiation (Schoenfelder et al., 2015; Bonev et al., 2017). Here

again, the role of the PcG proteins in the silencing of key lineage-specific developmental genes illustrates well how the pluripotent genome may be organized to ensure pluripotency.

During differentiation, most TAD boundaries remain stable while long-range A and B compartmentalization are extensively rewired (Dixon et al., 2015). Chromatin states and gene activity change concomitantly with changes in compartmentalization, with B to A transition being associated with an increase in gene expression and vice and versa. Compartment sizes tend to increase and are reinforced for the B-type chromatin, consistent with the strengthening of the heterochromatin (Bonev et al., 2017). If TADs appear relatively stable during differentiation, they become more defined, with stronger intra-TAD interactions and weaker inter-TAD contacts (Barrington et al., 2019). Moreover, *de novo* insulation correlated with transcriptional activation can be observed, but CRISPR/dCas9-induced transcription cannot reproduce these insulations, which may indicate a pivotal role of TFs in mediating local architecture. In agreement, extensive changes in enhancer-promoter contacts related to cell-type specific TFs are observed during differentiation and reprogramming (Bonev et al., 2017; Stadhouders et al., 2018). TF-mediated chromatin organization also occurs at extreme long-range distance and between different chromosomes. This has been illustrated with specific network of interactions between multiple enhancers and single olfactory receptor genes in the cells where they are active. These interactions rely on the presence of the LHX2 and LDB1 factors (Monahan et al., 2019). Gene locations within the nucleus are also subjected to changes during differentiation, with hundreds of genes being relocated toward the nuclear interior and others tethered to LADs. Detachment of the nuclear periphery is often associated with transcriptional activation while attachment to LADs with gene repression (Peric-Hupkes et al., 2010; Robson et al., 2016). A drastic change in radial positioning organization was observed in fully differentiated rod cells in which heterochromatin is relocated at the interior of the nucleus, which was proposed to allow efficient light passage toward the light-sensing rod outer segments (Solovei et al., 2009). This was shown to depend on both heterochromatin interactions and lack of contacts with lamina (Falk et al., 2019).

To conclude, the fundamental features of higher-order chromatin organization that are TADs, compartments, and associations to nuclear lamina, are mostly conserved during cell differentiation. However, in addition to the variations of the relative strength and the prominence of these different architectural layers, clear differences related to cell-type specific transcriptional programs are observed. Changes in compartment type and nuclear positioning seem to generally reflect - and may then just be a consequence of- the changes in expression profiles. Yet, specific and precise remodeling of contacts are established, often implicating gene promoters, enhancers and TFs that are tightly linked to the cell-type. Thus, on top of a rather conserved and constrained chromosome organization through its attachment to specific nuclear structures such as lamina, its long-range A- and B-type compartmentalization, and its folding into TADs, the establishment of specific and highly specialized networks of chromatin interactions may be critical to ensure cell identity.

Annexes

1.9 Breaking the diffraction limit with super-resolution microscopy

1.9.1 The diffraction limit in conventional fluorescence microscopy

Fluorescence microscopy has been a powerful tool to study nuclear organization, including the visualization of CTs, the nuclear distribution of proteins or the spatial positioning of genomic loci. However, morphological and structural features that are smaller than the spatial resolution offered by conventional diffraction-limited microscopy, approximately a few hundreds of nanometers, cannot be assessed.

The resolution of a microscope is defined as the shortest distance at which two points of a specimen can be distinguished. Due to diffraction, light emitted from a point source that passes through an optical system appears in the image as an Airy diffraction patterns, in which a central Airy disk is surrounded by a series of concentric diffraction rings. In the axial dimension, the Airy disk has an elliptical shape. The 3D intensity distribution of this Airy 'disk' is called the point spread function (PSF). Hence, the resolution can be defined as the minimum distance where two Airy disks or PSFs are still discernable as separate entities (Figure 8). The theoretical size of the Airy disk depends on the wavelength of the light (λ) and optical characteristics of the microscope, mainly the numerical aperture (NA) of the objective. Thus, both lateral and axial theoretical resolutions can be derived from the formula defined by the physicist Ernst Abbe at the end of the 19th century: Lateral Resolution ~ $\lambda/(2NA)$; Axial Resolution ~ $2\lambda/NA^2$. In addition, aberrations of the optical system, out-of-focus blur, light scattering or the signal-to-noise (SNR) ratio affect the resolution which is, after all, practically lower than the theoretical one. Generally, the resolution with a green fluorescent dye is limited to ~250 nm and ~700 nm in lateral and axial resolution, respectively.

Confocal laser scanning microscopy (CLSM) is one of the most used conventional microscopy methods (Cremer and Cremer, 1978) since its popularization in the 1990's. In CLSM, one single focal spot is illuminated and detected at a time. This is achieved using targeted beams of light from lasers that scan

the sample, and only the light emitted from the excited focus point is passing through a small aperture, the pinhole, prior detection. This leads to a significant improvement of the image quality due to, first, the removal of the out-of-focus light and, second, an improvement in resolution due to the superposition of the excitation and the emission PSFs.

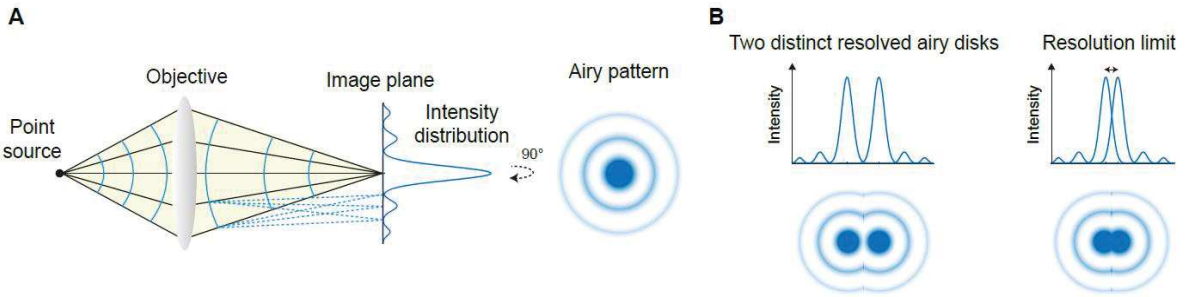

Figure 8. Resolution in conventional fluorescence microscopy. (**A**) Representation of microscope image formation from the light emitted from a point source (fluorophore). Diffraction and interferences generate a non-uniform distribution of the light to the image plane of the microscope that appears as a diffraction pattern known as Airy pattern (or PSF for its distribution in 3D). Note that the scheme is not at scale. (**B**) Two point-sources can be resolved when their two Airy disks are far enough from each other. The smallest distance that allows the separation of the two juxtaposed Airy disks before they merge corresponds to the limit of the resolution.

1.9.2 Structured Illumination Microscopy

SIM is a wide-field technique that can increase the diffraction-limited resolution by a factor two (Gustafsson, 2000). This method consists in using a non-uniform illumination pattern which interferes with the sample and allows for the recovery of higher spatial frequencies, corresponding to fine details, which cannot be otherwise detected in conventional microscopy (Vangindertaell et al., 2018). The Fourier space allows the description of spatial signals, such as the distribution of fluorophores in a microscopy image, as a sum of sinusoidal curves with different spatial frequencies and amplitudes. The frequency in the Fourier space contains a more convenient way to mathematically represent the resolution of a microscope and the amount of details it can provide. High spatial frequencies represent small distances between maxima (or fluorophore locations), i.e. the fine details of a sample, while low frequencies represent the components that form large objects, i.e. the coarse details of the sample (Figure 9A). In the Fourier transform of the image, the frequency is represented by the distance to the central point (Figure 9B).

As described before, an optical microscope is limited by a theoretical resolution (the minimum distance at which two objects can be distinguished). In other words, the sample information cannot be detected

beyond a maximum spatial frequency. The process of imaging represents the multiplication of the Fourier transform of the object by the Fourier transform of the PSF, named the optical transfer function (OTF), which describes the range of spatial frequencies that are transmitted through an optical system. The OTF displays a maximum frequency border that corresponds to the Abbe limit frequency (which is the inverse of the Abbe limit resolution). This OTF can then be illustrated in the Fourier space by a circle with a radius k_0 corresponding to the cut-off, limit frequency: $k_0 = 2NA/\lambda$. Hence, frequencies that are higher than this limit are not recorded in the image. Increasing the range of frequency that are detected will then provide higher resolution (Figure 9B).

SIM uses a structured illumination pattern that interferes with the sample, a process analogous to the Moiré effect, in which superimposed high spatial frequencies generate Moiré pattern (or Moiré fringes) with a lower spatial frequency (Figure 9C). In this way, original high spatial frequencies of the sample can be mathematically recovered from the lower frequency-shifted, collectable information generated by the interference with a well characterized excitation pattern. An illumination pattern with a spatial frequency k_1 close to the cutoff frequency k_0 (the illumination pattern being projected using the objective, it is also diffraction-limited) enables an extension of the highest detectable spatial frequency from k_0 to $k_0 + k_1$, which corresponds then to a 2-fold increase in resolution along its direction. Using 3 different angles, the extension of the resolution can be achieved in every direction (Figure 9D). Finally, these different illumination patterns are also generated using different phases to correctly position the detected high frequencies in the frequency space and to generate an excitation homogeneous over the whole field of view. SIM can be applied to double the resolution in both lateral and axial directions using an illumination pattern structured in 3D, here referred to as 3D-SIM (Gustafsson et al., 2008). This requires serial acquisitions in the axial direction using an illumination of 5 different phases and 3 different angles, i.e. 15 different images, per plane. Another extension of SIM called non-linear SIM, which generates nonlinear fluorescence responses that contain higher-frequency components by saturating the fluorophores, allows a gain of resolution beyond a factor two (Gustafsson, 2005).

To conclude, SIM allows the reconstruction of images at a sub-diffraction resolution (eight-fold improved volumetric resolution with 3D-SIM compared to conventional microscopy) with a high imaging speed when compared to other super-resolution techniques. This renders SIM suitable for live imaging. Moreover, a main advantage of SIM is its compatibility with conventional fluorophores and multi-color imaging, as well as with standard protocols of FISH or immuno-labeling. SIM is then particularly adapted for the super-resolution imaging of a large number of cellular components.

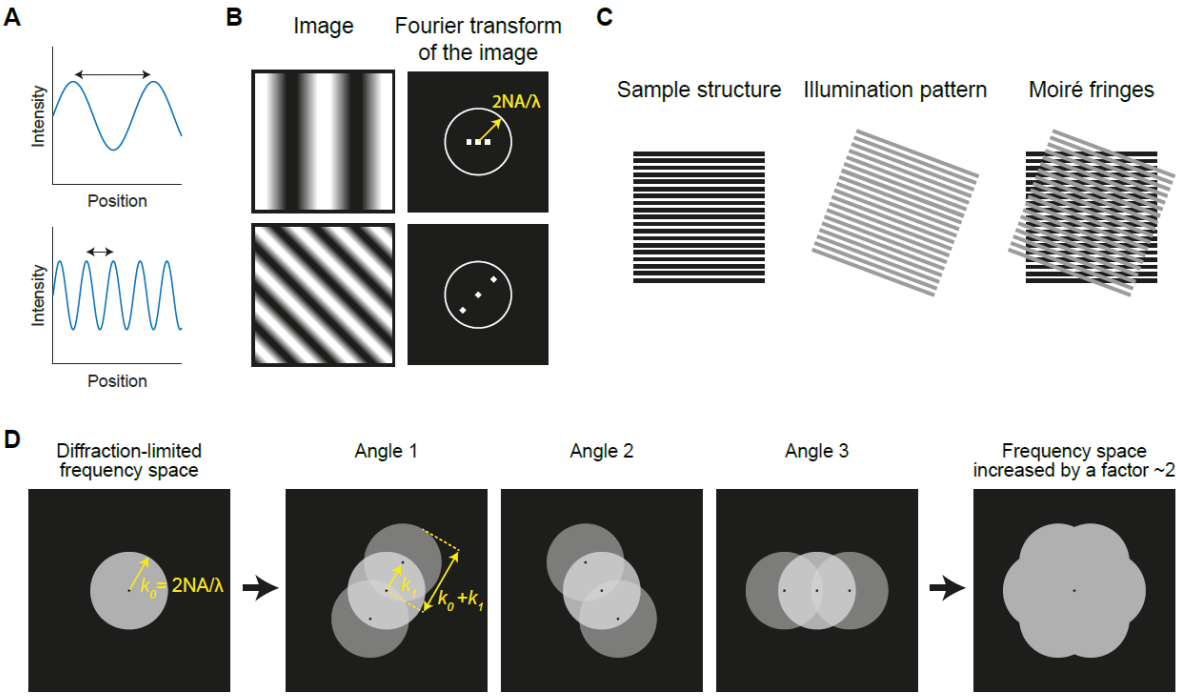

The Figure 9. Principle of SIM. (**A**) Large distances between fluorophores are associated with low spatial frequencies (top), while short distances are associated with high spatial frequencies (bottom). (**B**) Left: images of 2D sine waves with different frequencies and orientations. Right: representation in the Fourier space of the images, the frequency is represented by the distance to the central point (the representation is symmetrical). The shortest is the distance between maxima, the higher is the frequency, and the further the point representing the frequency component will be to the center of the image. The image on the bottom has a higher frequency (a finer pattern) than the one on the top, the distance to the central point in the Fourier space is then larger. The orientation of the points corresponds to the x-axis of the sine functions. White circles represent cutoff maximum frequency (Abbe resolution limit) that can be retrieved using diffraction-limited microscopy. (**C**) Representation of the generation of Moiré fringes by superposing two stripe patterns. The Moiré fringes depend on the orientation of the illumination pattern and have a lower spatial frequency. (**D**) Representation of the increase of the resolution using SIM. The first image represents a diffraction-limited image plane in the Fourier space, with a radius k_0 corresponding to the Abbe resolution limit. The three images in the middle represent the sequential increase of the frequency space using different illumination patterns: for each angle, the resolution increases from k_0 to $k_0 + k_1$ in the corresponding orientation. On the right, the frequency space using the combination of the different illumination patterns.

1.9.3 Single molecule localization microscopy and stimulated emission depletion

Other super-resolution methods are commonly used in biology, such as the family of single molecule localization microscopy (SMLM), based on the detection and localization of individual molecules, or the stimulated emission depletion (STED) microscopy. This paragraph will present the key concepts of these two methods.

SMLM represents a category of super-resolution microscopy including stochastic optical reconstruction microscopy [STORM (Rust et al., 2006)], photo-activated localization microscopy [PALM (Betzig et al., 2006)] or fluorescence photo-activated localization microscopy [FPALM (Hess et al., 2006)] which is based on the detection and the localization of individual fluorophores before their assembly in a full, super-resolved reconstructed image. Multiple fluorophores that are close in space cannot be distinguished since they give rise to overlapping PSFs. However, if individual PSFs from single fluorophores can be imaged at a time, localization of point sources can be extracted by determining the center position of their diffraction-limited signals. This implies that two overlapping fluorophores signals should not be simultaneously acquired. Practically, this is achieved using photoactivatable or photoswitchable dyes that can be turned in bright or dark states (Huang et al., 2010), and a low excitation intensity that allows a stochastic activation of the fluorophores. Sequential imaging using cycles of activation and deactivation of the different fluorophores that label the biological sample is used to generate super-resolution images from all the individual molecule localizations, in which the intensity value depends on the density of fluorophores. The resolution of SMLM is therefore not anymore limited by the diffraction but by the precision of the localization of individual emitters, which depends on the number of detected photons (Figure 10A). A large number of fluorophores in a densely labeled biomolecule will thus increase the resolution. Using SMLM, a lateral resolution of ~20 nm could be achieved (Rust et al., 2006). Several methods have been implemented to allow 3D imaging (Huang et al., 2010), such as the introduction of an astigmatism that renders the shape of the molecule image elliptical, which can be used to determine its axial position (Huang Zhuang 2008).

STED is a super-resolution method based on a configuration similar to CLSM with an additional light source, the depletion beam, used to reversibly switch off fluorophores around a focal spot (Hell and Wichmann, 1994; Klar et al., 2000). Basically, the depletion beam has a doughnut shape with a zero intensity at the center of the PSF generated by the excitation laser, and forces the fluorophores to return back in the ground-state around this center. Therefore, the detection of the fluorescence coming only from the center gives a sub-diffraction PSF. Super-resolution images are acquired by scanning the sample with the two lasers (Figure 10B). STED generally achieves a lateral resolution between 30 and 50 nm in biological samples. Increase in the axial resolution can also be achieved by modifying the shape of the depletion illumination (Klar et al., 2000). Potential limitations of STED method is the use of suitable fluorophores, which need to match the depletion wavelength, and the requirement of high laser powers that can lead to photobleaching of the fluorophores and phototoxicity. An extension of STED called reversible saturable optical fluorescence transitions (RESOLFT) uses photoswitchable fluorophores that are sent to dark states in the depletion zone and requires a lower beam intensity (Hoffman et al., 2005).

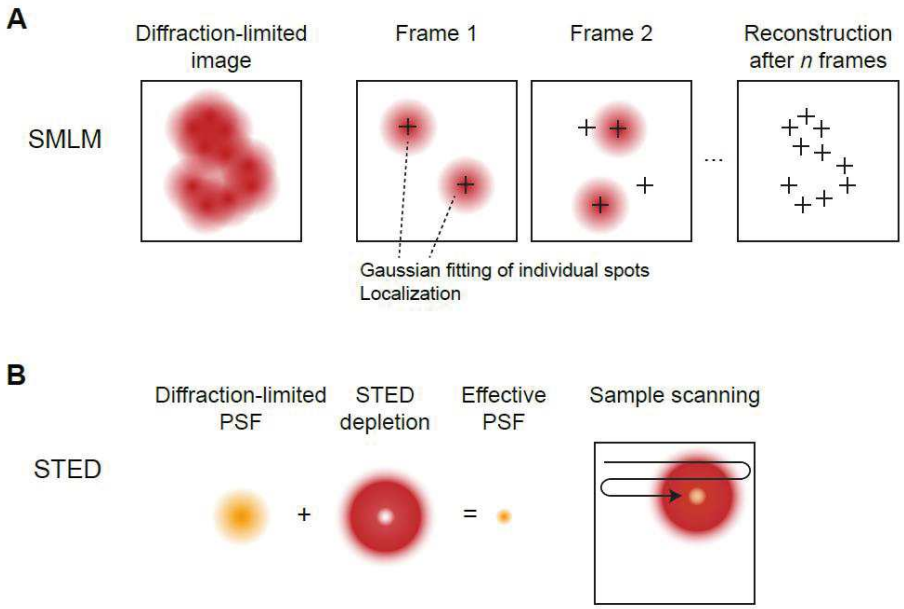

Figure 10. SMLM and STED strategies. (**A**) SMLM relies on the detection and localization of individual fluorophores to precisely reconstruct the structure of the imaged cellular component. Instead of exciting all the fluorophore at a time, just a subset is activated in a stochastic manner, which allows their separation and the recording of their locations before their deactivation. Super-resolution images are generated after repeated cycles of activation and deactivation. (**B**) STED uses a depletion beam which turns off the fluorophores excited by another laser around a precise focal point. This results in a modified effective PSF at a sub-diffraction resolution. The sample is scanned using the two lasers similarly to a confocal setup.

1.10 Review manuscript: Higher-order chromosomal structures mediate genome function

For this review, we chose to separate the writing of the different sections between the co-authors. I wrote the first part concerning the organization of the chromatin at the TAD scale and made the figure. Ivana Jerkovic wrote the second part concerning the organization of chromosomes at larger scale. These two sections were further improved by Frédéric Bantignies and Giacomo Cavalli. We then all reviewed and discussed the entire manuscript and finalize it before submission.

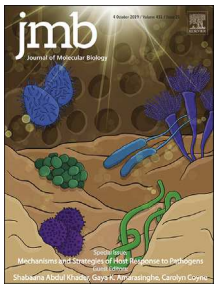

Higher-Order Chromosomal Structures Mediate Genome Function

Ivana Jerković[†], **Quentin Szabo**[†], **Frédéric Bantignies and Giacomo Cavalli**

Institute of Human Genetics, *CNRS and University of Montpellier, France*

Correspondence to Frédéric Bantignies and Giacomo Cavalli: *frederic.bantignies@igh.cnrs.fr, giacomo.cavalli@igh.cnrs.fr*

https://doi.org/10.1016/j.jmb.2019.10.014

Edited by Romain Koszul

Abstract

How chromosomes are organized within the tridimensional space of the nucleus and how can this organization affect genome function have been long-standing questions on the path to understanding genome activity and its link to disease. In the last decade, high-throughput chromosome conformation capture techniques, such as Hi-C, have facilitated the discovery of new principles of genome folding. Chromosomes are folded in multiple high-order structures, with local contacts between enhancers and promoters, intermediate-level contacts forming Topologically Associating Domains (TADs) and higher-order chromatin structures sequestering chromatin into active and repressive compartments. However, despite the increasing evidence that genome organization can influence its function, we are still far from understanding the underlying mechanisms. Deciphering these mechanisms represents a major challenge for the future, which large, international initiatives, such as 4DN, HCA and LifeTime, aim to collaboratively tackle by using a conjunction of state-of-the-art population-based and single-cell approaches.

Chromatin is a complex, plastic, and multifaceted cluster of proteins, DNA, and RNA that regulate gene expression. It is built in a hierarchical manner starting with DNA forming a single base-pair up to whole genomes comprising of multibillion base pairs, stretching over ten orders of magnitude. Understanding this hierarchy requires the deployment of different but overlapping approaches, both theoretical and experimental, that are suited for the investigation at different scales. In the past decade, the application of high-throughput chromosome conformation capture techniques such as Hi-C has remarkably increased our knowledge of the chromatin fiber organization at an intermediate scale, between the multinucleosomal level and chromosomal territories. At this scale of tens to hundreds of kilobases, the genome is organized into distinct domains, called Topologically Associating Domains (TADs) [1–4], which exhibit higher preference for internal interactions compared to interactions with adjacent domains. The genome, therefore, appears as a succession of these higher-order structures, demarcated by boundaries. TADs are made of heterogeneous and extensive multipartite interactions [5–8] representing dynamic and preferential contacts [9,10] that can also be observed in individual cells as spatially defined domains [11,12]. This domain-based genome architecture is present in eukaryotes and similar domains have been reported in some prokaryote species as well [13–15], but are likely formed by different mechanisms, suggesting existence of different types of TADs. In mammals, most TADs are formed by the cohesin complex and its interaction with the insulator protein CCCTC-binding factor (CTCF) [16–19], probably driven by a dynamic "loop extrusion" process [20,21]. Notably, different chromatin states can be found within the same TAD, although these chromatin states often assemble sub-TADs of the same epigenetic content [22], which is possibly partially masked by cohesin loop extrusion activity [19,23]. In other species such as *Drosophila*, the TAD pattern is closely associated with partitioning of the chromatin fiber into distinct epigenetic domains [2,4,24,25]. In this case, TADs could arise from the differential folding of chromatin regions with their specific epigenetic states by a "self-assembly"

Please cite this article as: I. Jerković, Q. Szabo, F.éé Bantignies, et al., Higher-Order Chromosomal Structures Mediate Genome Function, Journal of Molecular Biology, https://doi.org/10.1016/j.jmb.2019.10.014

mechanism depending on the nature of chromatin marks associated with the domains [25]. Finally, other mechanisms such as transcription-induced supercoiling have been implicated and could also explain the formation of self-interacting domains [26].

Importantly, the genomic size of the TADs, from tens to hundreds of kilobases, represents a favored scale for gene regulation [27] where genes tend to be coregulated [3,28] and in which functional enhancer-promoter contacts are privileged [29–31] (Fig. 1A). Moreover, TADs also correspond to timing-dependent replication domains, suggesting that they probably spatially segregate functional domains [32]. This role of TADs as regulatory units—mainly described in mammalian species—has been emphasized by the fact that disruption of TAD structures, for example, by disrupting TAD boundaries, can lead to *neo* functional landscapes associated with gene misexpression, as described in developmental diseases and cancer [33–36]. Understanding how functional contacts are controlled and established within TADs to ensure specific gene expression during development and cell differentiation has thus appeared as a crucial point. A striking example of this tight link between genome folding and function has been illustrated during mouse limb development, where *Hoxd* gene cluster is exposed to a dynamic switch in contacts between the two surrounding TADs defining proper and timely *Hoxd* expression [37].

Furthermore, although TAD borders are generally stable, TADs undergo substantial rewiring during cell fate change and reprogramming [29,38]. For example, predominantly confined within a TAD, cell-type specific interactions have been observed between promoters and their *cis*-regulatory elements [29]. Such enhancer-promoter contacts were also found in cell-type specific multipartite interactions where they interact simultaneously within compartmentalized domains, suggesting that differentiation-related 3D chromatin rewiring is possibly functional [39,40]. In order to accurately assess TAD structure and function, several studies employed recently developed novel microscopy methods based on sequential imaging of chromosomal loci combined with RNA labeling, enabling both single-cell reconstruction of the chromatin fiber and the detection of transcriptional state [41,42]. These single-cell approaches revealed that the intrinsic TAD structure varies depending on its chromatin state and its transcriptional activity, highlighting the diversity of TAD folding in different cell types and their role in gene regulation. Moreover, super-resolution microscopy studies revealed dynamic and stochastic nature of TADs in single cells, with inconsistent TAD borders that preferentially locate at CTCF sites [10,11]. This dynamic TAD behavior is further corroborated by the loop-extrusion model, by the measurement of CTCF/cohesin-chromatin residence time and by CTCF/cohesin depletion studies in which TAD-scale chromatin contacts dissociate and later reappear

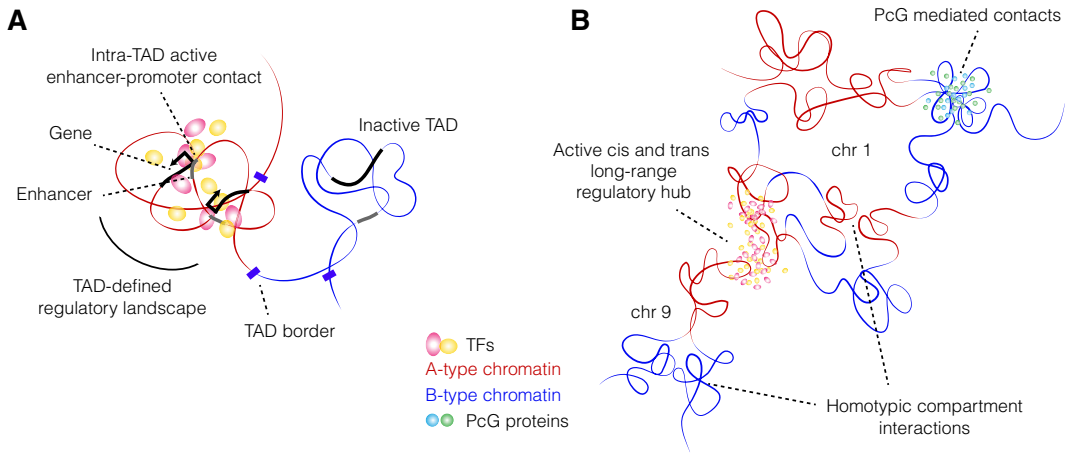

Fig. 1. A. Schematic representation of TAD-mediated gene regulation. TADs represent higher-order chromosomal units that privilege functional and dynamic contacts between promoters and *cis*-regulatory elements. Most contact and intra-TAD changes occur concomitantly with specific transcription factor (TF) binding in a cell-type specific manner, although, in most cases, the causative relationship remains elusive. **B. Schematic examples of extremely long-range interactions.** Global folding of chromosomes includes homotypic long-range contacts between large chromatin regions of the same underlying epigenetic content, building A-active and B-repressive compartments. In addition, preferential cell-type specific extremely distant contacts occur both, in *cis* and in *trans* and usually involve gene(s), super-enhancers, and sometimes cell-type specific TFs. Together, these elements can assemble into functional hubs associated with transcription thereby regulating the activity of target genes. Likewise, repressive interaction networks between Polycomb group (PcG) proteins mediate long-range interactions between distal genes favoring transcriptional repression.

Please cite this article as: I. Jerković, Q. Szabo, F.éé Bantignies, et al., Higher-Order Chromosomal Structures Mediate Genome Function, Journal of Molecular Biology, https://doi.org/10.1016/j.jmb.2019.10.014

upon reintroduction of the corresponding proteins [16–21,43,44]. However, it is still not clear with what kinetics do the TADs fold and dissipate in single cells and how does this affect gene regulation. Future studies integrating microscopy, biochemical, genetic, and computer modeling experiments are necessary in order to fully understand TAD dynamics in single cells and the role of TADs in the spatial regulation of functional contacts.

Above TAD organization, a higher-order chromatin folding also follows specific but distinct rules defining the overall chromosome conformation. In such fashion, chromosomes tend to segregate into regions of preferential long-range interactions (compartments) based on their underlying epigenetic content. This segregation occurs in a homotypic fashion, where active and inactive (repressive) chromatin intervals interact over tens to hundreds of megabases (Mb) building "A" and "B" compartments, respectively. Furthermore, both contiguous and noncontiguous local contacts and TADs assemble into compartments giving rise to higher-order structures [22,45]. When contiguous TADs interact, they can create a "meta-TAD," while noncontiguous TADs form extremely long-range multipartite *cis*- and *trans*-interactions (Fig. 1B). The formation of such extremely long-range interactions relies either on underlying heterochromatic marks (i.e., H3K9me3) assembling into "TAD-cliques" on active marks, such as H3K27ac, building multipartite enhancer hubs [46–50], or on H3K36me3, correlating with contacts between coding regions of very active, intron-rich genes [29,31]. Moreover, assembly of higher-order interchromosomal multipartite interactions has been shown to center at specific nuclear bodies; nuclear speckles for gene rich, active hubs, and nucleolus and lamina for gene poor, inactive or heterochromatic regions indicating that spatial positioning of these (in)active hubs in the nucleus is not random [49–51]. This large-scale chromatin folding appears highly heterogeneous, indicating that chromosomes adopt various conformations in single cells [5–7,9,10,12,52]. Nevertheless, this cell-to-cell variability likely reflects the dynamic nature of chromatin folding rather than the lack of functional importance of this organization. Moreover, the association of higher-order interactions with nuclear bodies and lamina may act as a backbone that molds the overall 3D genome organization in the nucleus as well as helping to modulate its function [50,51]. However, understanding the functional significance of higher-order interactions is a key issue that is difficult to address comprehensively. Historically, one of the best-studied examples of long-range chromatin contacts involves H3K27me3 Polycomb-regulated regions at *Hox* loci, in *cis* and in *trans*, both in *Drosophila* and in mammals [4,29,53–57]. Here, *Hox* loci engage in multipartite interactions with other H3K27me3 domains and segregate into Polycomb foci, which dissolve upon Polycomb component removal and *Hox* genes become misexpressed, leading to homeotic transformations under sensitized conditions [53,56]. Nevertheless, despite these and other functional studies, it is yet not clear if all higher-order structures depend on the underlying histone marks and/or their writers, or whether other factors could play a role as well. Notably, although not unambiguously uncoupled from the histone marks, the active, but not inactive transcriptional start sites (TSSs) were shown to cluster together in a manner that depends on their expression level, exon and splicing event number, indicating that additional mechanisms could be governing and/or stabilizing long-range interactions [29]. Furthermore, similarly to the cell-type specific TFs instigating contacts at the TAD level, Oct4, Nanog and Klf4 orchestrate higher-order chromatin folding in mESC, indicating that possible alternative folding mechanisms likely exist [29,54,58,59]. A recent striking example of cell-type specific TF driven higher-order interactions comes from olfactory sensory neurons where 63 enhancers scattered over 18 different chromosomes form a hub in the high local presence of LHX2 and LDB1 factors which stabilize the hub and facilitate the choice of the olfactory gene to be expressed in each neuron [60]. Therefore, although compartment-like homotypic domain interactions appear as a global feature of chromosome folding, specific long-range chromatin interactions, such as the ones in olfactory receptors, are cell-type specific, suggesting that they could represent a key feature driving cell identity.

Together, these examples indicate that higher-order chromatin folding relies on several distinct rules; however, the actual mechanism is still elusive. While CTCF and cohesin are instrumental at short- and intermediate-level chromatin folding, it is clear that this mechanism is not employed at the compartment-level organization, as proteasomal depletions of CTCF and cohesin almost entirely disrupt short- and intermediate-range chromatin folding but leave higher-order structures unaffected, or even exacerbated [16–19,44]. Yet, large-scale chromatin interactions also appear independent from one another, where the loss of Polycomb proteins specifically affects interaction among Polycomb target regions without altering the overall chromosome conformation [12,54]. Therefore, by their nature, higher-order chromatin interactions represent a heterogeneous but distinct form of architectural folding with an underlying functional component, proving that robust and precise gene regulation is rooted in several layers of chromatin folding as a prerequisite for life.

Please cite this article as: I. Jerković, Q. Szabo, F.éé Bantignies, et al., Higher-Order Chromosomal Structures Mediate Genome Function, Journal of Molecular Biology, https://doi.org/10.1016/j.jmb.2019.10.014

Conclusions and Perspectives

The last decade has been a game changer for research on nuclear organization, higher-order chromatin structure and gene expression. A panoply of technologies has surged, allowing us to describe and modulate nuclear architecture with unprecedented versatility. One can describe nuclear organization by microscopy with unprecedented resolution [61] and multiplicity of molecular signatures, both in terms of number of chromatin loci to be studied and of their expression [9,11,52,62,63]. One can pinpoint the DNA counterparts of chromatin contacts at subkilobase resolution in bulk and in single cells [6,45,46,51,64,65] as well as provide indications on molecular distances between specific loci and nuclear landmarks genome-wide [66]. Finally, it is now possible to modify genome and epigenome function genome-wide or at specific loci thanks to genome technologies like CRISPR/Cas [67–72]. These technologies can be applied to a variety of organisms and cell types, with a decreasing number of limitations due to cell number requirement, cell type specificity, and thickness of the tissue being partially or totally lifted as technologies progress. Furthermore, data analysis and machine learning algorithms are improving at a proportionate speed allowing us to extract relations between data and to identify candidates for causality with much higher efficiency and accuracy. Therefore, it is gradually becoming possible to move from the study of cells in culture to more complex systems such as tissue sections or organoids and, in a foreseeable future, it will be possible to move some of these technologies to the clinic. Large consortia are already funded (4D Nucleome https://www.4dnucleome.org/, Human Cell Atlas https://www.humancellatlas.org/) or are being organized (LifeTime https://lifetime-fetflagship.eu/) to tackle these issues on a large scale, in a way that will allow us to gain much deeper understanding on these exciting questions and to apply the ensuing knowledge to improve human health.

Acknowledgments

I.J. was supported by an EMBO fellowship nr. ALTF 559-2018 and the Laboratory of Excellence EpiGenMed. Q.S. was supported by the French Ministry of Higher Education and Research, and La Ligue Nationale Contre le Cancer. F.B. was supported by CNRS. Research in the G.C. laboratory was supported by grants from the CNRS, the European Research Council No 788972 (Advanced Grant 3DEpi), the European Union's Horizon 2020 research and innovation programme under grant agreement No 676556 (MuG), the Agence Nationale de la Recherche (ANR-15-CE12-0006 EpiDevo-Math), the Fondation pour la Recherche Médicale (DEI20151234396) and the French National Cancer Institute (INCa).

Received 29 May 2019;
Received in revised form 2 October 2019;
Accepted 18 October 2019
Available online xxxx

Keywords:
Chromatin structure;
Genome folding;
Transcriptional regulation;
Topologically Associating Domains;
Compartments

†Equal contribution.

References

[1] J.R. Dixon, S. Selvaraj, F. Yue, A. Kim, Y. Li, Y. Shen, et al., Topological domains in mammalian genomes identified by analysis of chromatin interactions, Nature 485 (2012) 376–380.
[2] C. Hou, L. Li, Z.S. Qin, V.G. Corces, Gene density, transcription, and insulators contribute to the partition of the Drosophila genome into physical domains, Mol. Cell 48 (2012) 471–484.
[3] E.P. Nora, B.R. Lajoie, E.G. Schulz, L. Giorgetti, I. Okamoto, N. Servant, et al., Spatial partitioning of the regulatory landscape of the X-inactivation centre, Nature 485 (2012) 381–385.
[4] T. Sexton, E. Yaffe, E. Kenigsberg, F. Bantignies, B. Leblanc, M. Hoichman, et al., Three-Dimensional folding and functional organization principles of the Drosophila genome, Cell 148 (2012) 458–472.
[5] I.M. Flyamer, J. Gassler, M. Imakaev, H.B. Brandao, S.V. Ulianov, N. Abdennur, et al., Single-nucleus Hi-C reveals unique chromatin reorganization at oocyte-to-zygote transition, Nature 544 (2017) 110–114.
[6] T. Nagano, Y. Lubling, T.J. Stevens, S. Schoenfelder, E. Yaffe, W. Dean, et al., Single-cell Hi-C reveals cell-to-cell variability in chromosome structure, Nature 502 (2013) 59–64.
[7] T.J. Stevens, D. Lando, S. Basu, L.P. Atkinson, Y. Cao, S.F. Lee, et al., 3D structures of individual mammalian genomes studied by single-cell Hi-C, Nature 544 (2017) 59–64.
[8] M. Zheng, S.Z. Tian, D. Capurso, M. Kim, R. Maurya, B. Lee, et al., Multiplex chromatin interactions with single-molecule precision, Nature 566 (2019) 558–562.
[9] D.I. Cattoni, A.M. Cardozo Gizzi, M. Georgieva, M. Di Stefano, A. Valeri, D. Chamousset, et al., Single-cell absolute contact probability detection reveals chromosomes are organized by multiple low-frequency yet specific interactions, Nat. Commun. 8 (2017) 1753.
[10] E.H. Finn, G. Pegoraro, H.B. Brandao, A.L. Valton, M.E. Oomen, J. Dekker, et al., Extensive heterogeneity and intrinsic variation in spatial genome organization, Cell 176 (2019) 1502–1515 e10.
[11] B. Bintu, L.J. Mateo, J.H. Su, N.A. Sinnott-Armstrong, M. Parker, S. Kinrot, et al., Super-resolution chromatin

tracing reveals domains and cooperative interactions in single cells, Science (2018) 362.

[12] Q. Szabo, D. Jost, J.M. Chang, D.I. Cattoni, G.L. Papadopoulos, B. Bonev, et al., TADs are 3D structural units of higher-order chromosome organization in Drosophila, Sci. Adv. 4 (2018), eaar8082.

[13] O. Espeli, R. Mercier, F. Boccard, DNA dynamics vary according to macrodomain topography in the E. coli chromosome, Mol. Microbiol. 68 (2008) 1418–1427.

[14] M. Marbouty, A. Le Gall, D.I. Cattoni, A. Cournac, A. Koh, J.B. Fiche, et al., Condensin- and replication-mediated bacterial chromosome folding and origin condensation revealed by Hi-C and super-resolution imaging, Mol. Cell 59 (2015) 588–602.

[15] X. Wang, T.B. Le, B.R. Lajoie, J. Dekker, M.T. Laub, D.Z. Rudner, Condensin promotes the juxtaposition of DNA flanking its loading site in Bacillus subtilis, Genes Dev. 29 (2015) 1661–1675.

[16] J.H.I. Haarhuis, R.H. van der Weide, V.A. Blomen, J.O. Yanez-Cuna, M. Amendola, M.S. van Ruiten, et al., The cohesin release factor WAPL restricts chromatin loop extension, Cell 169 (2017) 693–707 e14.

[17] E.P. Nora, A. Goloborodko, A.L. Valton, J.H. Gibcus, A. Uebersohn, N. Abdennur, et al., Targeted degradation of CTCF decouples local insulation of chromosome domains from genomic compartmentalization, Cell 169 (2017) 930–944 e22.

[18] S.S.P. Rao, S.C. Huang, B. Glenn St Hilaire, J.M. Engreitz, E.M. Perez, K.R. Kieffer-Kwon, et al., Cohesin loss eliminates all loop domains, Cell 171 (2017) 305–320 e24.

[19] W. Schwarzer, N. Abdennur, A. Goloborodko, A. Pekowska, G. Fudenberg, Y. Loe-Mie, et al., Two independent modes of chromatin organization revealed by cohesin removal, Nature 551 (2017) 51–56.

[20] G. Fudenberg, M. Imakaev, C. Lu, A. Goloborodko, N. Abdennur, L.A. Mirny, Formation of chromosomal domains by loop extrusion, Cell Rep. 15 (2016) 2038–2049.

[21] A.L. Sanborn, S.S. Rao, S.C. Huang, N.C. Durand, M.H. Huntley, A.I. Jewett, et al., Chromatin extrusion explains key features of loop and domain formation in wild-type and engineered genomes, Proc. Natl. Acad. Sci. U. S. A. 112 (2015) E6456–E6465.

[22] S.S. Rao, M.H. Huntley, N.C. Durand, E.K. Stamenova, I.D. Bochkov, J.T. Robinson, et al., A 3D map of the human genome at kilobase resolution reveals principles of chromatin looping, Cell 159 (2014) 1665–1680.

[23] J. Nuebler, G. Fudenberg, M. Imakaev, N. Abdennur, L.A. Mirny, Chromatin organization by an interplay of loop extrusion and compartmental segregation, Proc. Natl. Acad. Sci. U. S. A. 115 (2018) E6697–E6706.

[24] M.J. Rowley, M.H. Nichols, X. Lyu, M. Ando-Kuri, I.S.M. Rivera, K. Hermetz, et al., Evolutionarily conserved principles predict 3D chromatin organization, Mol. Cell 67 (2017) 837–852 e7.

[25] S.V. Ulianov, E.E. Khrameeva, A.A. Gavrilov, I.M. Flyamer, P. Kos, E.A. Mikhaleva, et al., Active chromatin and transcription play a key role in chromosome partitioning into topologically associating domains, Genome Res. 26 (2016) 70–84.

[26] F. Benedetti, D. Racko, J. Dorier, Y. Burnier, A. Stasiak, Transcription-induced supercoiling explains formation of self-interacting chromatin domains in S. pombe, Nucleic Acids Res. 45 (2017) 9850–9859.

[27] Y. Zhan, L. Mariani, I. Barozzi, E.G. Schulz, N. Bluthgen, M. Stadler, et al., Reciprocal insulation analysis of Hi-C data shows that TADs represent a functionally but not structurally privileged scale in the hierarchical folding of chromosomes, Genome Res. 27 (2017) 479–490.

[28] F. Ramirez, V. Bhardwaj, L. Arrigoni, K.C. Lam, B.A. Gruning, J. Villaveces, et al., High-resolution TADs reveal DNA sequences underlying genome organization in flies, Nat. Commun. 9 (2018) 189.

[29] B. Bonev, N. Mendelson Cohen, Q. Szabo, L. Fritsch, G.L. Papadopoulos, Y. Lubling, et al., Multiscale 3D genome rewiring during mouse neural development, Cell 171 (2017) 557–572 e24.

[30] F. Sun, C. Chronis, M. Kronenberg, X.F. Chen, T. Su, F.D. Lay, et al., Promoter-enhancer communication occurs primarily within insulated neighborhoods, Mol. Cell 73 (2019) 250–263 e5.

[31] O. Symmons, V.V. Uslu, T. Tsujimura, S. Ruf, S. Nassari, W. Schwarzer, et al., Functional and topological characteristics of mammalian regulatory domains, Genome Res. 24 (2014) 390–400.

[32] B.D. Pope, T. Ryba, V. Dileep, F. Yue, W. Wu, O. Denas, et al., Topologically associating domains are stable units of replication-timing regulation, Nature 515 (2014) 402–405.

[33] W.A. Flavahan, Y. Drier, B.B. Liau, S.M. Gillespie, A.S. Venteicher, A.O. Stemmer-Rachamimov, et al., Insulator dysfunction and oncogene activation in IDH mutant gliomas, Nature 529 (2016) 110–114.

[34] M. Franke, D.M. Ibrahim, G. Andrey, W. Schwarzer, V. Heinrich, R. Schopflin, et al., Formation of new chromatin domains determines pathogenicity of genomic duplications, Nature 538 (2016) 265–269.

[35] D. Hnisz, A.S. Weintraub, D.S. Day, A.L. Valton, R.O. Bak, C.H. Li, et al., Activation of proto-oncogenes by disruption of chromosome neighborhoods, Science 351 (2016) 1454–1458.

[36] D.G. Lupianez, K. Kraft, V. Heinrich, P. Krawitz, F. Brancati, E. Klopocki, et al., Disruptions of topological chromatin domains cause pathogenic rewiring of gene-enhancer interactions, Cell 161 (2015) 1012–1025.

[37] G. Andrey, T. Montavon, B. Mascrez, F. Gonzalez, D. Noordermeer, M. Leleu, et al., A switch between topological domains underlies Hoxd genes collinearity in mouse limbs, Science 340 (2013) 1234167.

[38] R. Stadhouders, E. Vidal, F. Serra, B. Di Stefano, F. Le Dily, J. Quilez, et al., Transcription factors orchestrate dynamic interplay between genome topology and gene regulation during cell reprogramming, Nat. Genet. 50 (2018) 238–249.

[39] A. Allahyar, C. Vermeulen, B.A.M. Bouwman, P.H.L. Krijger, M. Verstegen, G. Geeven, et al., Enhancer hubs and loop collisions identified from single-allele topologies, Nat. Genet. 50 (2018) 1151–1160.

[40] A.M. Oudelaar, J.O.J. Davies, L.L.P. Hanssen, J.M. Telenius, R. Schwessinger, Y. Liu, et al., Single-allele chromatin interactions identify regulatory hubs in dynamic compartmentalized domains, Nat. Genet. 50 (2018) 1744–1751.

[41] A.M. Cardozo Gizzi, D.I. Cattoni, J.B. Fiche, S.M. Espinola, J. Gurgo, O. Messina, et al., Microscopy-based chromosome conformation capture enables simultaneous visualization of genome organization and transcription in intact organisms, Mol. Cell 74 (2019) 212–222 e5.

[42] L.J. Mateo, S.E. Murphy, A. Hafner, I.S. Cinquini, C.A. Walker, A.N. Boettiger, Visualizing DNA folding and RNA in embryos at single-cell resolution, Nature 568 (2019) 49–54.

Please cite this article as: I. Jerković, Q. Szabo, F.éé Bantignies, et al., Higher-Order Chromosomal Structures Mediate Genome Function, Journal of Molecular Biology, https://doi.org/10.1016/j.jmb.2019.10.014

[43] A.S. Hansen, I. Pustova, C. Cattoglio, R. Tjian, X. Darzacq, CTCF and cohesin regulate chromatin loop stability with distinct dynamics, eLife 6 (2017).
[44] G. Wutz, C. Varnai, K. Nagasaka, D.A. Cisneros, R.R. Stocsits, W. Tang, et al., Topologically associating domains and chromatin loops depend on cohesin and are regulated by CTCF, WAPL, and PDS5 proteins, Embo J. 36 (2017) 3573–3599.
[45] E. Lieberman-Aiden, N.L. van Berkum, L. Williams, M. Imakaev, T. Ragoczy, A. Telling, et al., Comprehensive mapping of long-range interactions reveals folding principles of the human genome, Science 326 (2009) 289–293.
[46] R.A. Beagrie, A. Scialdone, M. Schueler, D.C. Kraemer, M. Chotalia, S.Q. Xie, et al., Complex multi-enhancer contacts captured by genome architecture mapping, Nature 543 (2017) 519–524.
[47] O. Delaneau, M. Zazhytska, C. Borel, G. Giannuzzi, G. Rey, C. Howald, et al., Chromatin three-dimensional interactions mediate genetic effects on gene expression, Science 364 (2019).
[48] J. Fraser, C. Ferrai, A.M. Chiariello, M. Schueler, T. Rito, G. Laudanno, et al., Hierarchical folding and reorganization of chromosomes are linked to transcriptional changes in cellular differentiation, Mol. Syst. Biol. 11 (2015) 852.
[49] H. Niskanen, I. Tuszynska, R. Zaborowski, M. Heinaniemi, S. Yla-Herttuala, B. Wilczynski, et al., Endothelial cell differentiation is encompassed by changes in long range interactions between inactive chromatin regions, Nucleic Acids Res. 46 (2018) 1724–1740.
[50] J. Paulsen, T.M. Liyakat Ali, M. Nekrasov, E. Delbarre, M.O. Baudement, S. Kurscheid, et al., Long-range interactions between topologically associating domains shape the four-dimensional genome during differentiation, Nat. Genet. 51 (2019) 835–843.
[51] S.A. Quinodoz, N. Ollikainen, B. Tabak, A. Palla, J.M. Schmidt, E. Detmar, et al., Higher-order inter-chromosomal hubs shape 3D genome organization in the nucleus, Cell 174 (2018) 744–757 e24.
[52] G. Nir, I. Farabella, C. Perez Estrada, C.G. Ebeling, B.J. Beliveau, H.M. Sasaki, et al., Walking along chromosomes with super-resolution imaging, contact maps, and integrative modeling, PLoS Genet. 14 (2018), e1007872.
[53] F. Bantignies, V. Roure, I. Comet, B. Leblanc, B. Schuettengruber, J. Bonnet, et al., Polycomb-dependent regulatory contacts between distant Hox loci in Drosophila, Cell 144 (2011) 214–226.
[54] M. Denholtz, G. Bonora, C. Chronis, E. Splinter, W. de Laat, J. Ernst, et al., Long-range chromatin contacts in embryonic stem cells reveal a role for pluripotency factors and polycomb proteins in genome organization, Cell Stem Cell 13 (2013) 602–616.
[55] O. Joshi, S.Y. Wang, T. Kuznetsova, Y. Atlasi, T. Peng, P.J. Fabre, et al., Dynamic reorganization of extremely long-range promoter-promoter interactions between two states of pluripotency, Cell Stem Cell 17 (2015) 748–757.
[56] S. Schoenfelder, R. Sugar, A. Dimond, B.M. Javierre, H. Armstrong, B. Mifsud, et al., Polycomb repressive complex PRC1 spatially constrains the mouse embryonic stem cell genome, Nat. Genet. 47 (2015) 1179–1186.
[57] M. Vieux-Rochas, P.J. Fabre, M. Leleu, D. Duboule, D. Noordermeer, Clustering of mammalian Hox genes with other H3K27me3 targets within an active nuclear domain, Proc. Natl. Acad. Sci. U. S. A. 112 (2015) 4672–4677.
[58] E. de Wit, B.A. Bouwman, Y. Zhu, P. Klous, E. Splinter, M.J. Verstegen, et al., The pluripotent genome in three dimensions is shaped around pluripotency factors, Nature 501 (2013) 227–231.
[59] Z. Wei, F. Gao, S. Kim, H. Yang, J. Lyu, W. An, et al., Klf4 organizes long-range chromosomal interactions with the oct4 locus in reprogramming and pluripotency, Cell Stem Cell 13 (2013) 36–47.
[60] K. Monahan, A. Horta, S. Lomvardas, LHX2- and LDB1-mediated trans interactions regulate olfactory receptor choice, Nature 565 (2019) 448–453.
[61] T.J. Lambert, J.C. Waters, Navigating challenges in the application of superresolution microscopy, J. Cell Biol. 216 (2017) 53–63.
[62] K.H. Chen, A.N. Boettiger, J.R. Moffitt, S. Wang, X. Zhuang, RNA imaging. Spatially resolved, highly multiplexed RNA profiling in single cells, Science 348 (2015) aaa6090.
[63] J.H. Lee, E.R. Daugharthy, J. Scheiman, R. Kalhor, J.L. Yang, T.C. Ferrante, et al., Highly multiplexed subcellular RNA sequencing in situ, Science 343 (2014) 1360–1363.
[64] M.J. Fullwood, M.H. Liu, Y.F. Pan, J. Liu, H. Xu, Y.B. Mohamed, et al., An oestrogen-receptor-alpha-bound human chromatin interactome, Nature 462 (2009) 58–64.
[65] B. van Steensel, S. Henikoff, Identification of in vivo DNA targets of chromatin proteins using tethered dam methyltransferase, Nat. Biotechnol. 18 (2000) 424–428.
[66] Y. Chen, Y. Zhang, Y. Wang, L. Zhang, E.K. Brinkman, S.A. Adam, et al., Mapping 3D genome organization relative to nuclear compartments using TSA-Seq as a cytological ruler, J. Cell Biol. 217 (2018) 4025–4048.
[67] M. Jinek, K. Chylinski, I. Fonfara, M. Hauer, J.A. Doudna, E. Charpentier, A programmable dual-RNA-guided DNA endonuclease in adaptive bacterial immunity, Science 337 (2012) 816–821.
[68] L. Cong, F.A. Ran, D. Cox, S. Lin, R. Barretto, N. Habib, et al., Multiplex genome engineering using CRISPR/Cas systems, Science 339 (2013) 819–823.
[69] L.S. Qi, M.H. Larson, L.A. Gilbert, J.A. Doudna, J.S. Weissman, A.P. Arkin, et al., Repurposing CRISPR as an RNA-guided platform for sequence-specific control of gene expression, Cell 152 (2013) 1173–1183.
[70] P.G. Maass, A.R. Barutcu, D.M. Shechner, C.L. Weiner, M. Mele, J.L. Rinn, Spatiotemporal allele organization by allele-specific CRISPR live-cell imaging (SNP-CLING), Nat. Struct. Mol. Biol. 25 (2018) 176–184.
[71] B. Chen, L.A. Gilbert, B.A. Cimini, J. Schnitzbauer, W. Zhang, G.W. Li, et al., Dynamic imaging of genomic loci in living human cells by an optimized CRISPR/Cas system, Cell 155 (2013) 1479–1491.
[72] H. Wang, X. Xu, C.M. Nguyen, Y. Liu, Y. Gao, X. Lin, et al., CRISPR-mediated programmable 3D genome positioning and nuclear organization, Cell 175 (2018) 1405–1417 e14.

Please cite this article as: I. Jerković, Q. Szabo, F.éé Bantignies, et al., Higher-Order Chromosomal Structures Mediate Genome Function, Journal of Molecular Biology, https://doi.org/10.1016/j.jmb.2019.10.014

Chapter 2: Results

When I started my thesis, TADs were recently discovered using Hi-C methods, leading to numerous studies dedicated to their deeper characterization and their role in genome regulation. Notably, a crucial issue was to determine whether TADs exist in individual cells. Although a study using single-cell Hi-C was performed at that time, the structure of TADs remained unclear and had never been directly observed. We reasoned that investigating the existence and the nature of TADs in single cells should be possible thanks to the application of relatively new and promising methods. First, the Oligopaint technology allowed the large-scale production of fluorescent probes to study by FISH the organization of chromosomes with a throughput and an efficiency difficult to reach before (Beliveau et al., 2012; Beliveau et al., 2015). Secondly, the development and democratization of super-resolution imaging methods made possible the characterization of chromatin folding at the nanoscale (Lakadamyali and Cosma, 2015). We thus decided to use a combination of these techniques to explore TAD 3D organization in *Drosophila*. This project is materialized by the publication of an article in the journal Science Advances which will be presented in the next part. At the same time, another study from the laboratory described the higher-order chromatin organization of mouse genome during neuronal differentiation using high-resolution Hi-C (Bonev et al., 2017). Given the different characteristics of *Drosophila* and mammalian TADs, the application of our imaging methods to this system appeared to be particularly appropriate to extend our characterization and improve our understanding of TAD folding in single cells. The results from this project will then be presented as a manuscript in preparation.

2.1 Research article: TADs are 3D structural units of higher-order chromosome organization in Drosophila

For this project, experiments were discussed and planned together with my thesis supervisors, Frédéric Bantignies and Giacomo Cavalli. Regarding the design and the production of FISH probes, I chose the location of probes based on Hi-C and ChiP-seq data, and Frédéric Bantignies generated the sequences of the DNA oligos by concatenating regions of genomic homology (Oligopaint website: https://oligopaints.hms.harvard.edu/) and primers. I then produced the probes from the libraries. I performed all FISH (and immunostaining) experiments, 3D-SIM and CLSM microscopy, and the related image processing and analysis, except dSTORM acquisition and analysis that were carried out by Diego Cattoni and Julian Gurgo under the supervision of Marcelo Nollmann. I performed the Hi-C in S2R+ cells with the help of Boyan Bonev, and Caroline Jacquier and Tom Sexton performed the Hi-C in Drosophila embryos. Sequencing data were analyzed by Jia-Ming Chang, Giorgio L. Papadopoulos and Boyan Bonev. Daniel Jost performed the modeling experiments. I handled cell culture, and Frédéric Bantignies handled flies. I made the figures and wrote the first draft the manuscript that was further improved by Frédéric Bantignies, Tom Sexton and Giacomo Cavalli.

GENETICS

TADs are 3D structural units of higher-order chromosome organization in *Drosophila*

Quentin Szabo,[1] Daniel Jost,[2] Jia-Ming Chang,[1]* Diego I. Cattoni,[3] Giorgio L. Papadopoulos,[1] Boyan Bonev,[1] Tom Sexton,[1†] Julian Gurgo,[3] Caroline Jacquier,[1] Marcelo Nollmann,[3] Frédéric Bantignies,[1‡] Giacomo Cavalli[1‡]

Deciphering the rules of genome folding in the cell nucleus is essential to understand its functions. Recent chromosome conformation capture (Hi-C) studies have revealed that the genome is partitioned into topologically associating domains (TADs), which demarcate functional epigenetic domains defined by combinations of specific chromatin marks. However, whether TADs are true physical units in each cell nucleus or whether they reflect statistical frequencies of measured interactions within cell populations is unclear. Using a combination of Hi-C, three-dimensional (3D) fluorescent in situ hybridization, super-resolution microscopy, and polymer modeling, we provide an integrative view of chromatin folding in *Drosophila*. We observed that repressed TADs form a succession of discrete nanocompartments, interspersed by less condensed active regions. Single-cell analysis revealed a consistent TAD-based physical compartmentalization of the chromatin fiber, with some degree of heterogeneity in intra-TAD conformations and in cis and trans inter-TAD contact events. These results indicate that TADs are fundamental 3D genome units that engage in dynamic higher-order inter-TAD connections. This domain-based architecture is likely to play a major role in regulatory transactions during DNA-dependent processes.

INTRODUCTION

The three-dimensional (3D) organization of the genome is closely related to the control of transcriptional programs (*1*). Recently, high-throughput variants of the chromosome conformation capture method (Hi-C) (*2*) have been extensively used to molecularly address the 3D spatial organization of genomes [see Bonev and Cavalli (*1*) for review]. A key architectural feature revealed by Hi-C was the existence of topologically associating domains (TADs) (*3*–*6*), corresponding to domains of highly interacting chromatin, with reduced interactions spanning borders between them. In *Drosophila*, TADs correlate well with functional epigenetic domains defined by chromatin marks (*4*, *6*–*8*). In mammals, an additional level of TAD organization involves dynamic cohesin-dependent loops between CTCF binding sites at convergent orientations (*9*–*13*). The correlation of TAD structures with epigenetic marks can be observed in mammals using high-resolution Hi-C maps (*7*, *11*). This compartmentalization, defined by the underlying chromatin state, appears to be reinforced upon removal of CTCF/cohesin loop components (*10*, *12*, *13*), suggesting a conserved mode of chromatin organization across species (*7*). TADs have been proposed to constrain gene regulation (*5*, *14*), for example, by spatially defining the limits of where an enhancer can act (*15*, *16*). However, this model requires TADs to be physical units when they could instead reflect a statistical feature that emerges when populations of nuclei are analyzed. Recent single-cell Hi-C studies (*17*–*19*) showed somewhat contrasting results in this respect. Although one study is compatible with the presence of TADs in individual nuclei (*18*), another suggests that TADs might reflect a statistical property that appears when individual cells are merged (*17*). Thus, to what extent the compartmentalization of chromatin into TADs is present in each cell nucleus is still unclear. Furthermore, the relation between TADs and higher-order chromosome folding remains to be explored. Recently, super-resolution microscopy has allowed finer-scale chromatin architecture to be analyzed at the single-cell level (*20*–*22*), suggesting that different types of chromatin are characterized by distinct degrees of compaction (*23*) and opening the possibility of studying the structural properties of chromosome domains.

RESULTS

Chromatin is organized in a series of discrete 3D nanocompartments

To investigate the nature of TADs in single cells, we used Oligopaint (*24*) and fluorescent in situ hybridization (FISH) to homogenously label an extended 3–million base pair (Mbp) region of *Drosophila* chromosome 2L (table S1) and imaged its nuclear organization using 3D-structured illumination microscopy (3D-SIM) (*25*, *26*). This region comprises three main types of *Drosophila* epigenetic domains: active chromatin (Red) enriched in trimethylation of histone 3 lysine 4 (H3K4me3), H3K36me3, and acetylated histones; Polycomb group (PcG) protein repressed domains (Blue), defined by the presence of PcG proteins and H3K27me3; and inactive domains (Black), which are not enriched in specific epigenetic components (Fig. 1A) (*6*). Although conventional wide-field (WF) microscopy imaging of this region did not reveal internal structures, 3D-SIM showed that this chromosomal region appears as a semicontinuous sequence of discrete globular structures, defined here as nanocompartments (Fig. 1, B to D, and fig. S1, A and B). These structures are interspersed by less intense gap regions despite uniform probe coverage across the 3 Mb (fig. S1C). In addition, the 3-Mb probe intensity variation displayed correlation with whole nucleus staining [4′,6-diamidino-2-phenylindole (DAPI); fig. S1, D to F]. We reasoned that these nanocompartments may reflect the presence of TADs, so we adapted the Oligopaint strategy to two-color chromatin labeling (see Materials and Methods and fig. S2, A and B), simultaneously visualizing the 3-Mb region and single TADs within it (Fig. 1E and table S1). We observed

[1]Institute of Human Genetics, CNRS, Univ Montpellier, Montpellier, France. [2]Univ Grenoble Alpes, CNRS, Grenoble INP, TIMC-IMAG, F-38000 Grenoble, France. [3]Centre de Biochimie Structurale, CNRS UMR5048, INSERM U1054, Univ Montpellier, 34090 Montpellier, France.
*Present address: Department of Computer Science, National Chengchi University, 11605 Taipei City, Taiwan.
†Present address: Institut de Génétique et de Biologie Moléculaire et Cellulaire, CNRS UMR 7104, INSERM U964, 67404 Illkirch, France.
‡Corresponding author. Email: frederic.bantignies@igh.cnrs.fr (F.B.); giacomo.cavalli@igh.cnrs.fr (G.C.)

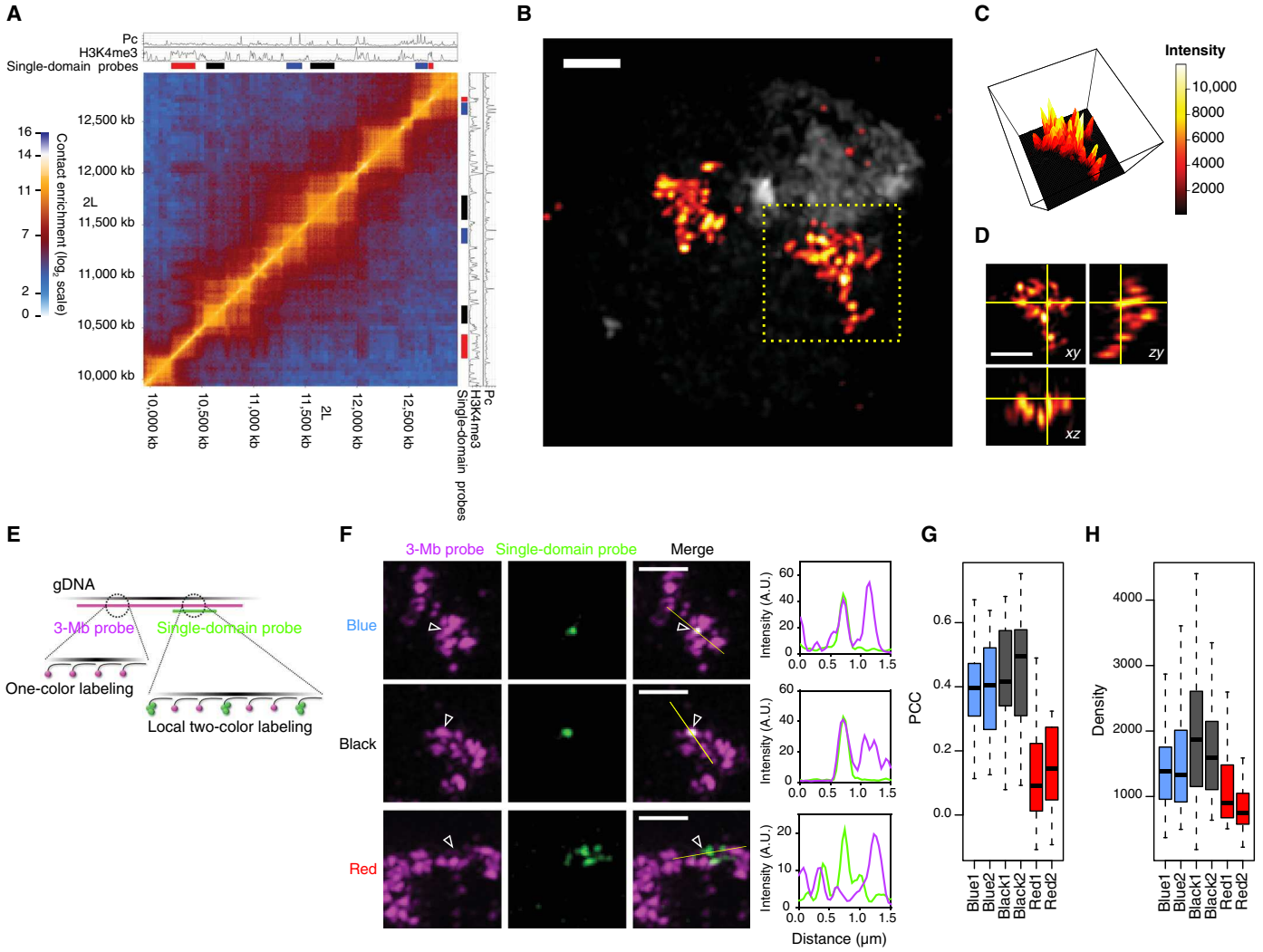

Fig. 1. Super-resolution microscopy reveals chromatin organization into discrete nanocompartments. (**A**) S2R+ Hi-C map of the labeled 3-Mb region with chromatin immunoprecipitation (ChIP) tracks of Pc and H3K4me3. Colored bars denote the positions of probes designed to label specific epigenetic domains (Blue, Black, and Red). (**B**) 3D-SIM image of an S2R+ nucleus labeled with the 3-Mb probe (DAPI in gray). (**C**) Intensity distribution (maximum projection) of the 3-Mb probe in (B). (**D**) Orthogonal views of the 3-Mb probe labeling in (B). (**E**) Schematic representation of the dual FISH Oligopaint labeling strategy. gDNA, genomic DNA. (**F**) Examples of dual FISH labeling (maximum projections) with the 3-Mb probe and a single epigenetic domain (Blue1, Black2, or Red1, indicated with arrowheads). Right: Intensity distributions of the two probes along the yellow line. A.U., arbitrary units. (**G**) Pearson's correlation coefficient (PCC) between the 3-Mb and the single-domain probe signals. Twenty nuclei were analyzed per conditions, and PCC distributions from all repressed domains were significantly different from those of active domains (at least $P < 0.01$) using Kruskal-Wallis and Dunn's multiple comparisons tests. (**H**) Oligopaint density (probe genomic size over 3D-segmented volume) of the single-domain probes. At least 57 nuclei were analyzed per condition, and density distributions from all repressed domains were significantly different from those of active domains (at least $P < 0.05$) using Kruskal-Wallis and Dunn's multiple comparisons tests. Scale bars, 1 µm.

that repressed TADs (Blue and Black) form globular structures that coincide with the nanocompartments in the 3-Mb region, suggesting that repressed TADs are true physical chromosomal domains. Conversely, Red active domains were situated in the fluorescence-poor zones of the 3-Mb region (Fig. 1F and fig. S2C), despite a similar probe coverage (fig. S2D). In support of this, the correlation of the fluorescence intensity distribution of the 3-Mb region with that of repressed TADs was much higher than with that of active regions (Fig. 1G). Moreover, active domains had a lower 3D density of Oligopaint signals (Fig. 1H), indicating that they are present in more open chromatin, consistent with the lower number of Hi-C contacts within active compared to repressed domains (fig. S2E) and with a previous report (*23*).

TAD-based 3D nanocompartments undergo dynamic cis and trans contact events

These data suggest that Hi-C patterns resulting from cell population average studies might reflect the partitioning of chromatin into physical entities in *Drosophila* chromosomes, organized in the cell nucleus as discrete compact chromatin nanocompartments (repressive TADs), interspersed by more open regions (active domains). To test this hypothesis, we asked whether the number of observed nanocompartments corresponds to the number of repressed TADs. Of importance for this study, most nuclei in Dipteran species like *Drosophila* have paired homologous chromosomes in interphase. Chromosome pairing has been shown to be important for appropriate gene regulation (*27*), but the ultrastructure of paired homologous loci is still unknown. Whereas

conventional WF microscopy often showed single unresolved foci for probes covering a single TAD, 3D-SIM resolved distinct nanocompartments (fig. S3, A and B). To address whether they correspond to the homologous TADs, we compared the numbers of foci observed in tetraploid S2R+ cells versus diploid embryonic (12 to 16 hours) cells, which have conserved TAD structures in Hi-C maps (fig. S4). In addition to single TADs and the 3-Mb probe that contains 12 repressed TADs, we designed additional Oligopaint probes: R2 (195 kb), R3 (805 kb), and R4 (495 kb), covering two, three, and four repressed TADs, respectively (fig. S4). We systematically observed an approximately twofold difference between the number of nanocompartments detected in tetraploid versus diploid cells, consistent with the predominant formation of juxtaposed yet spatially distinct TADs for each homolog in both cell types (Fig. 2, A and B). The distributions of the number of nanocompartments observed per cell indicated some degree of heterogeneity at the single-cell level. We could observe that homologous TADs

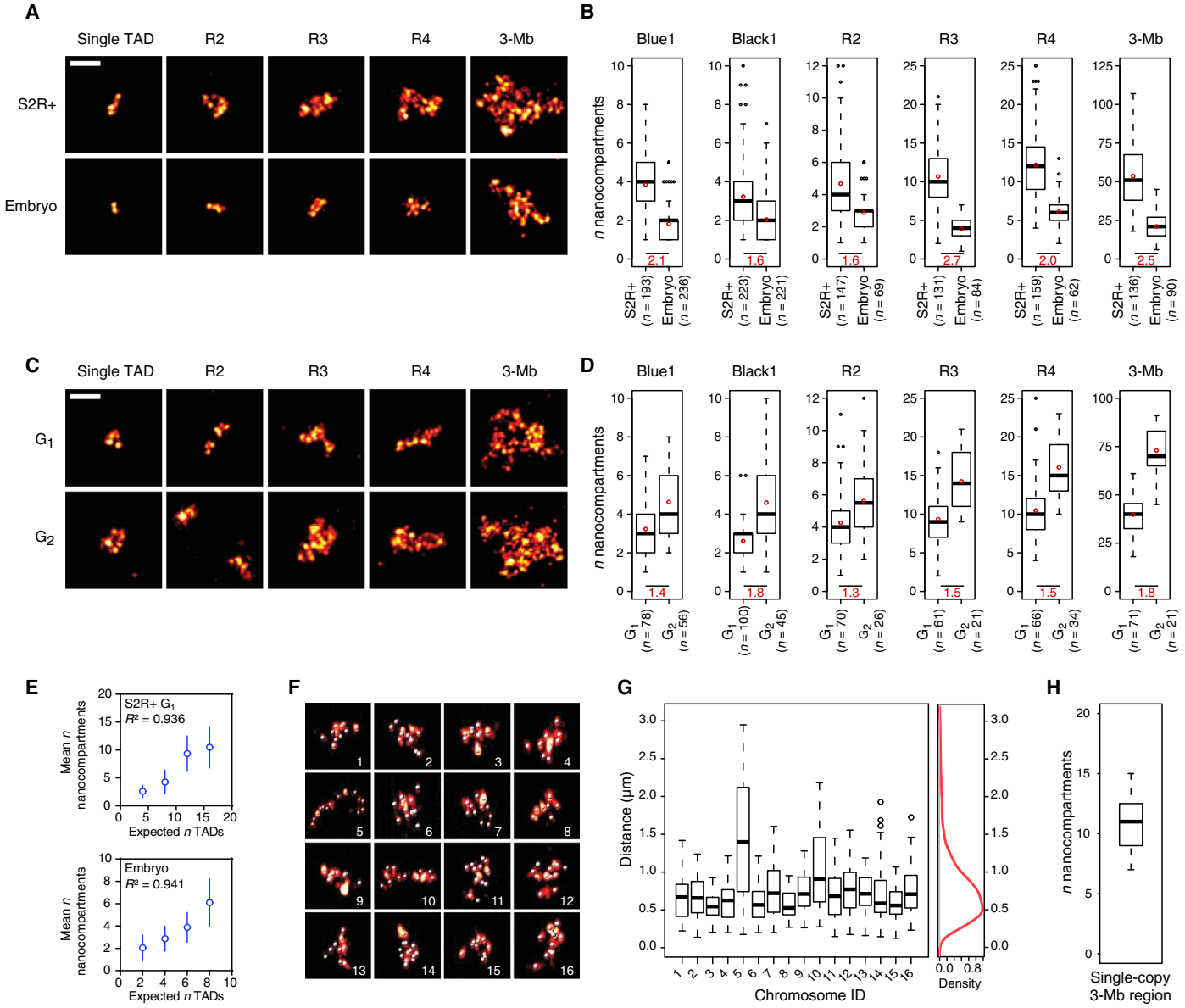

Fig. 2. Repressed TADs form 3D chromosomal units with dynamic contact events. (**A**) Examples of chromatin labeling (single Black1 TAD, R2, R3, R4, and 3-Mb probe, maximum projections) in (top) tetraploid S2R+ and (bottom) diploid embryonic cells. (**B**) Number of nanocompartments counted per nucleus in S2R+ and embryonic cells for the different labeling ($P < 0.0001$ in all conditions with two-tailed Mann-Whitney test). Bottom: Ratio of the means (indicated with red circles) between the two conditions. *n* indicates the number of nuclei analyzed. (**C**) Examples of chromatin labeling (single Blue1 TAD, R2, R3, R4, and 3-Mb probe, maximum projections) in tetraploid S2R+ cells in (top) G_1 and (bottom) G_2 phases of the cell cycle. (**D**) Number of nanocompartments counted per nucleus in S2R+ cells in G_1 and G_2 phases for the different labeling ($P < 0.0001$ in all conditions with two-tailed Mann-Whitney test, except for R2, $P < 0.01$). Bottom: Ratio of the means (indicated with red circles) between the two conditions. *n* indicates the number of nuclei analyzed. (**E**) Mean (±SD) number of nanocompartments counted per S2R+ cells in G_1 phase (top) or in embryonic cells (bottom) as a function of the number of TADs for Black1, R2, R3, and R4 labeling. R^2 values of linear regressions are indicated. (**F**) 3D view of single chromosome copies labeled with the 3-Mb probe. Nanocompartment positions are represented with 150-nm-diameter beads. (**G**) Pairwise distances between all nanocompartments identified in the individual chromosomes shown in (F) (one boxplot corresponds to one chromosome). Right: Averaged distance distribution from all the single chromosomes. (**H**) Number of nanocompartments counted for single chromosomes ($n = 19$). Scale bars, 1 μm.

can generate well-separated structures but also merge in a subset of the cells (fig. S3, C and D). Thus, chromatin fibers from paired homologous chromosomes do not appear to constantly intermingle, and instead, they form individual homologous TADs that engage in dynamic trans contact events. Some cells displayed more nanocompartments than would be expected based on the number of TADs multiplied by the ploidy (Fig. 2B). This observation was particularly evident for S2R+ cells, which have a sizeable proportion of G_2 cells, compared to embryonic cells, which are highly enriched in the G_0/G_1 phase of the cell cycle (*28*). To test whether these distributions could reflect differences in cell cycle stage and the fact that G_2 cells have replicated their DNA, we separated S2R+ cells into G_1 and G_2 populations based on DAPI signal (see Materials and Methods and fig. S5) (*29*). We could count more nanocompartments on average after replication, suggesting that, similar to chromosome homologs, sister chromatids behave largely as non-intermingled series of TADs (Fig. 2, C and D), consistent with the TADs observed by Hi-C in *Drosophila* polytene chromosomes (*30*). Moreover, there are very strong correlations between the mean number of nanocompartments observed and the number of TADs expected in both G_1 S2R+ cells and G_0/G_1 embryonic cells (Fig. 2E). To assess chromatin folding into TADs independently of pairing events, we also analyzed cells showing distinctly unpaired unique chromosomes, labeled with the 3-Mb probe (fig. S3E). We noticed heterogeneity in the higher-order arrangement of these TADs, ranging from a compact conformation to rarer unfolded chromosomes (Fig. 2, F and G). In this latter state, we were able to measure an average (±SD) nanocompartment diameter of 175 ± 27 nm (fig. S3, F and G). Again, the range of the number of nanocompartments detected in individual chromosomes fitted with the 12 repressed TADs predicted by Hi-C (Fig. 2H), although several cells showed a number of objects different from the expected number, suggesting that individual nanocompartments may contain multiple or split TADs. We thus conclude that the number of nanocompartments corresponds well with the number of repressed TADs, with a degree of cell-to-cell stochasticity due to the dynamics of intra- and inter-TAD contact events.

Repressed TADs form physical and structural chromosomal units

To rigorously quantify the single-cell variability of TAD behavior, we turned our analysis to TADs in a haploid context. We focused on a 400-kb region containing two distinct repressed TADs (Black) separated by an active region on the X chromosome of male embryos (Fig. 3A). We first used three-color FISH to measure intra-TAD (probes 2-1) versus inter-TAD (probes 2-3) 3D distances, with probes 1 and 3 being at the exact same genomic distance from probe 2. Our analysis revealed that intra-TAD distances are considerably shorter than inter-TAD distances (Fig. 3B). Moreover, inter-TAD distance distributions (1-3 and 2-3) were very similar, consistent with TAD structure strongly modulating the interdependence between physical and genomic distances. In support of this, analysis of FISH signal triplets showed that 75% of

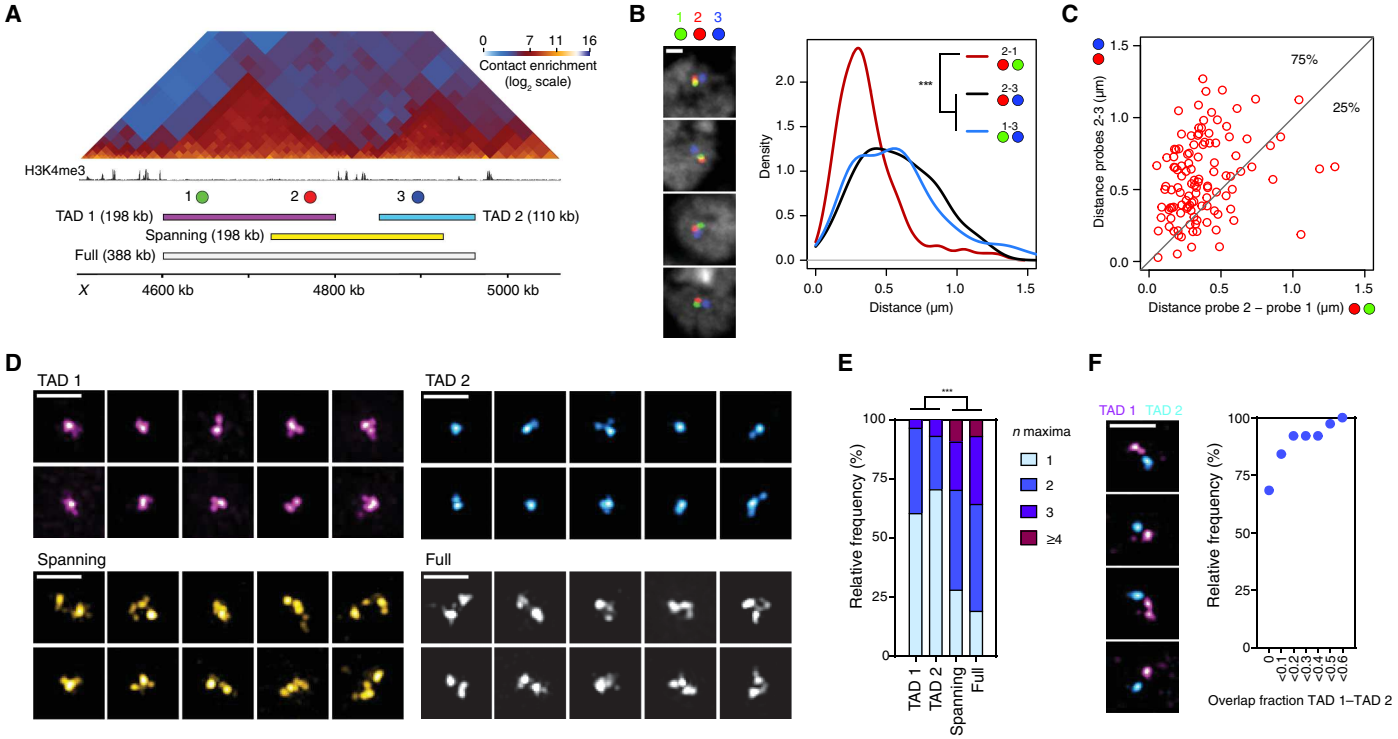

Fig. 3. Single-cell analysis of haploid chromosome reveals consistent TAD-based chromatin compartmentalization. (**A**) Sixteen- to 18-hour male embryo Hi-C map with H3K4me3 ChIP-seq profile (14- to 16-hour embryos) and FISH probe positions. (**B**) Representative examples of triple FISH-labeled nuclei (confocal microscopy, *z* slices) with probes 1 (green), 2 (red), and 3 (blue) and 3D distance distributions (from 115 nuclei) between the probes. (**C**) Scatter plot of paired distances between probes 2 and 1 (*x* axis) and probes 2 and 3 (*y* axis). The proportions of intra-TAD (2-1) distances shorter or larger than inter-TAD (2-3) distances are indicated (75 and 25%, respectively). (**D**) Representative examples of 3D-SIM images (maximum projections) of TAD 1, TAD 2, spanning, and full probes. (**E**) Number of FISH local maxima detected per nucleus with the different probes (at least 102 nuclei were analyzed per condition). (**F**) Representative examples of 3D-SIM images (maximum projections) of TAD 1 and TAD 2 double FISH experiments and quantification of the overlap fraction between TAD 1 and TAD 2 probes (38 nuclei were analyzed). Statistics were performed with Kruskal-Wallis and Dunn's multiple comparisons tests. ***$P < 0.0001$. Scale bars, 1 μm.

the 2-1 intra-TAD distances were shorter than the paired 2-3 inter-TAD distances (78% when considering the paired 1-3 inter-TAD distances; Fig. 3C). Previous studies compared 3D spatial distances between FISH probes corresponding to distinct regions and Hi-C interaction profiles (*17*, *20*, *31*), but the relationship between distance distribution and local chromatin conformation still remains unclear. We thus designed Oligopaint probes covering each single TADs independently (TAD 1 and TAD 2 probes), a probe of the same genomic size as TAD 1 but shifted to span the boundary (spanning probe), and a probe covering the entire region (full probe; Fig. 3A). We performed 3D-SIM imaging (Fig. 3D and fig. S6A) and observed that TAD 1 and TAD 2 displayed only one nanocompartment in the majority of cells, whereas most spanning and full probes were split into two or more nanocompartments, providing strong evidence for the physical compartmentalization of chromatin into TADs (Fig. 3E and fig. S6B). We then visualized TAD 1 and spanning probes using direct stochastic optical reconstruction microscopy (dSTORM) (*32*, *33*). Image analysis using this independent method confirmed that TAD 1 appeared as a single nanocompartment in the majority of cells, unlike most spanning probes (fig. S7), despite their same genomic size. Analysis of the sphericity of the 3D-segmented probes also revealed that single TADs have highly globular structures compared to the spanning and full regions (fig. S6C). Globular single TADs have a similar diameter range as the nanocompartments described above within larger chromosomal regions [mean ± SD, 192 ± 35 nm (TAD 1) and 182 ± 23 nm (TAD 2); fig. S6D], consistent with nanocompartments corresponding to TADs. We could occasionally resolve numerous substructures in TADs of haploid cells (Fig. 3, D and E, and fig. S6, A and B), arguing for a dynamic behavior of TAD conformations in a subset of the cells. Finally, to further explore whether TADs represent distinct physical units, we labeled the two repressed TADs in different colors. Inter-TAD contacts were not observed in 68% of the nuclei, and less than 10% of volume overlap was detected in 84% of cases (Fig. 3F). This result strongly suggests that inter-TAD contacts reflect restricted chromatin interactions, rather than TAD merging. We thus conclude that, despite variable intra- and inter-TAD contacts in each cell, the physical TAD-based compartmentalization of the chromatin fiber is a general feature of chromosomal domains.

Polymer modeling recapitulates the physical partitioning of chromosomes into TADs

We then tested whether TAD compartmentalization can be predicted by using a self-avoiding and self-interacting polymer model (*34*, *35*).

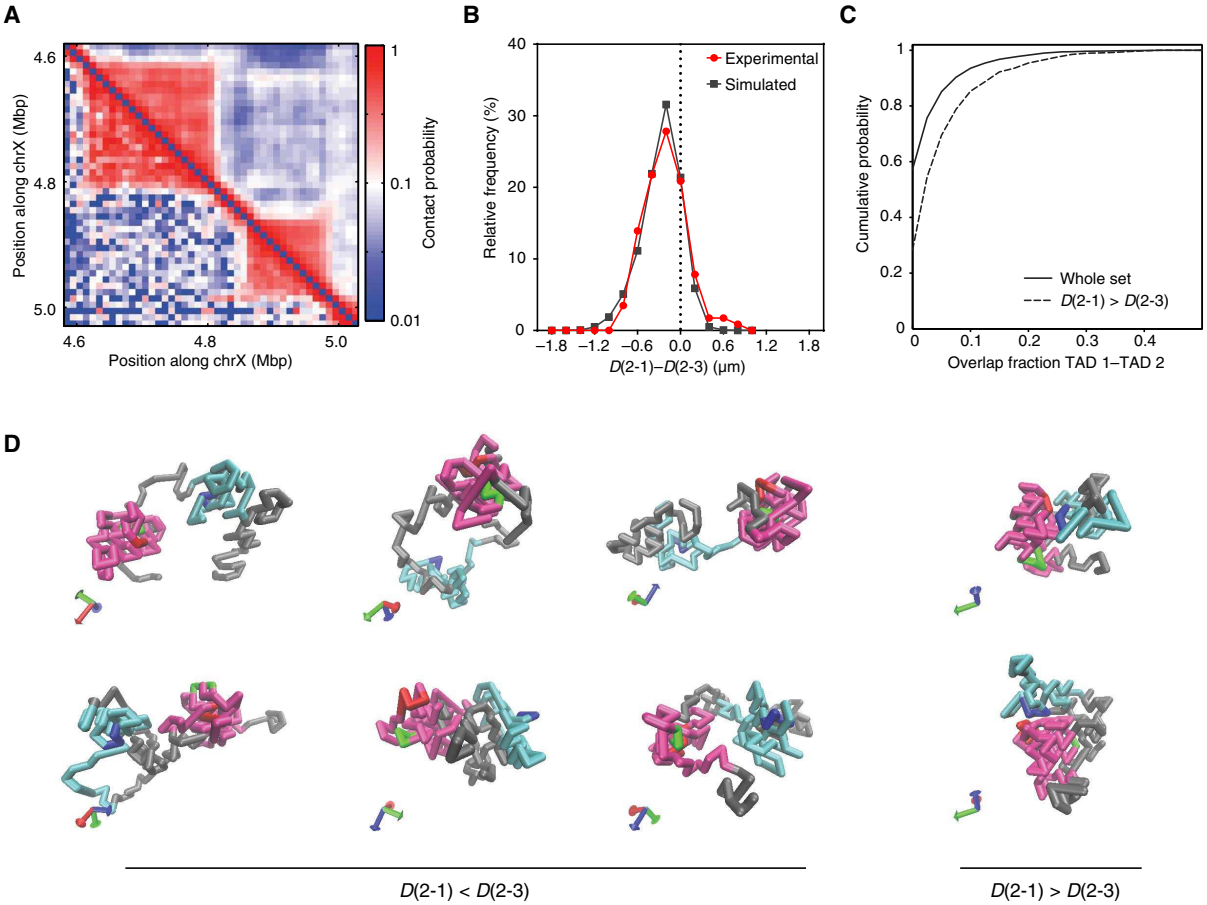

Fig. 4. Integrative view of chromosome conformation with polymer modeling. (**A**) Inferred (top) and experimental (bottom) contact probability maps. (**B**) Distributions of the differences between the paired distances (*D*) (2-1) and (2-3) from FISH experiments (red) and inferred model (gray). Values on the left of the dashed line indicate shorter intra-TAD than inter-TAD distances. (**C**) Cumulative distribution of the overlap fraction between TAD 1 and TAD 2 obtained from simulated conformations (full line) and from conformations when the inter-TAD distance (2-3) is smaller than the intra-TAD (2-1) distance (dashed line). (**D**) Representative examples of configurations of the inferred model, with the inter-TAD distance (2-3) larger (left) or smaller (right) than the intra-TAD (2-1) distance. Probe 1, 2, and 3 positions are represented with monomers in green, red, and blue, respectively; TAD 1 and TAD 2 are represented with magenta and cyan monomers, respectively.

First, we built a model of the same region described above, with monomers of 2 kb in which model parameters were fitted to reproduce the Hi-C data available for the same region (see Materials and Methods, Fig. 4A, and fig. S8, A and B). From the inferred ensemble of configurations, we computed distances for monomers corresponding to probes 1, 2, and 3 used in FISH (see Materials and Methods and Fig. 3A), and the comparison between model and FISH data shows a very good fit of the distance distributions (fig. S8C). The frequency for inter-TAD probe (2-3) distances smaller or equal to intra-TAD probe (2-1) distances is 15 ± 2%, in good agreement with experimental data (Fig. 4B and fig. S8D). To assess how

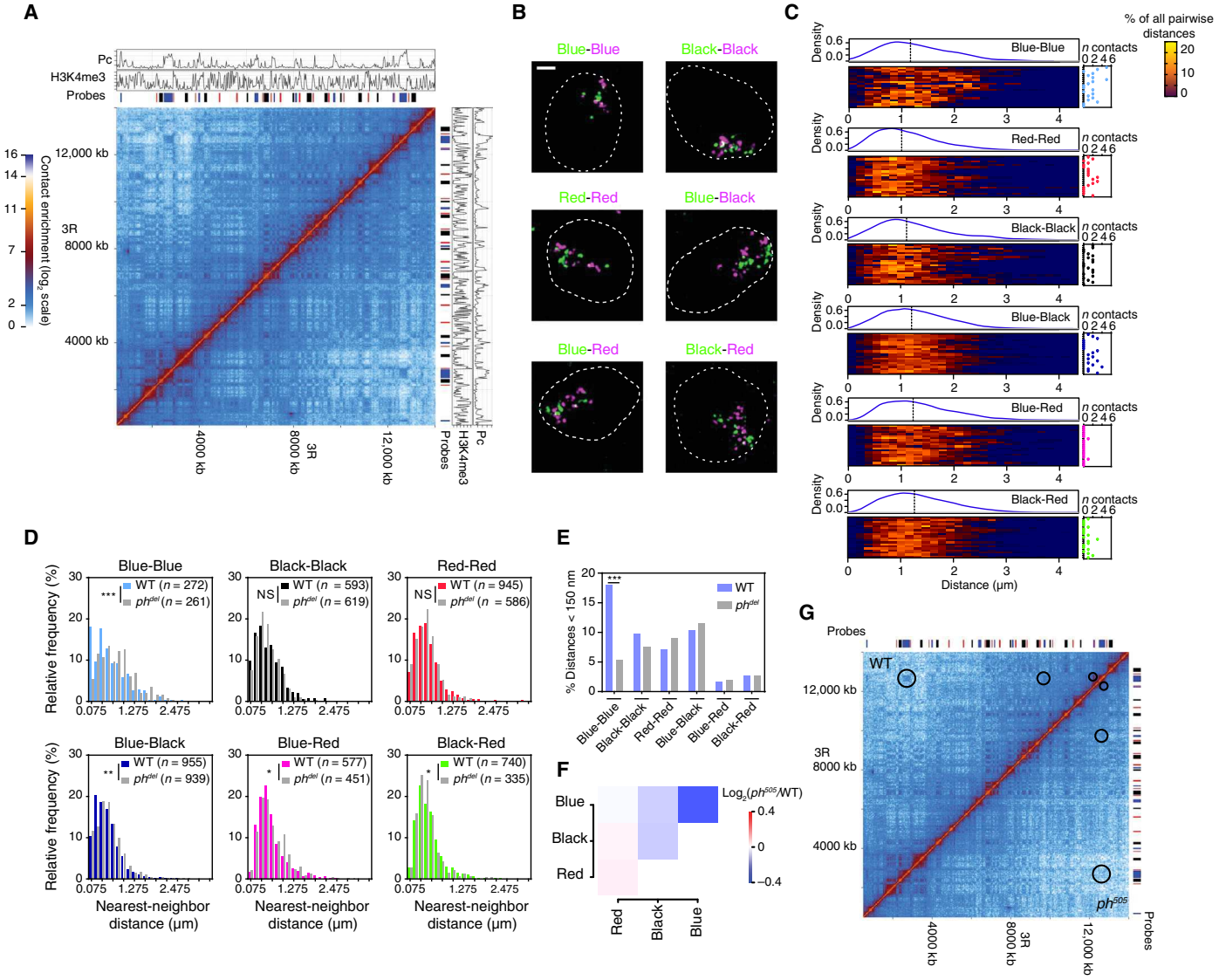

Fig. 5. Large-scale chromatin folding reflects heterogeneous, discrete, and specific interdomain contacts. (**A**) Sixteen- to 18-hour embryo Hi-C map of a 14-Mb region, along with ChIP-seq profiles of Pc and H3K4me3 (14- to 16-hour embryos). We designed a set of epigenetic state-specific probes (Blue, Black, and Red domains, indicated with colored bars) to perform two-color labeling of domains of the same type that were consecutive along the linear scale of the chromosome (that is, Blue-Blue, Black-Black, and Red-Red) or for different combinations of chromatin type (that is, Blue-Black, Blue-Red, and Black-Red). (**B**) 3D-SIM images from different two-color FISH labeling combinations in embryonic cells (maximum projections). Scale bar, 1 μm. (**C**) Distribution of all the pairwise distances between all differentially labeled domains in the different FISH combinations. Each line of the heat maps represents distance distribution within single-cell (color-coded in the percentage of all the distances within the cell). On top of each heat map, the distribution of the distances for the whole cell population is plotted, and dashed line indicates median. On the right of each heat map, the number of distances is <150 nm per cell (*n* contacts). Twenty nuclei (>1800 distances in total) were analyzed per condition. The broad distributions in all FISH combinations indicate a limited extensive clustering of the domains of the same epigenetic status. (**D**) Nearest-neighbor distance distributions for each labeling combination in wild-type (WT) and ph^{del} 12- to 16-hour embryos. The *x* axis is split into 150-nm bins. *n* indicates the number of distances (measured in at least 30 nuclei) for each condition. Statistics were performed using Kolmogorov-Smirnov tests; ***P < 0.001, **P < 0.01, *P < 0.05. The depletion of very short range distances in Blue-Red and Black-Red distributions suggests that active chromatin is spatially segregated from inactive chromatin at the nanoscale. NS, not significant. (**E**) Percentages of nearest-neighbor distances <150 nm in WT embryos versus ph^{505} embryos, showing the specific loss of contacts between Blue domains. Statistics were performed using two-tailed Fisher's exact tests, ***P < 0.0001. (**F**) Genome-wide differential Hi-C contact scores ($\log_2$ ph^{505}/WT normalized scores) between the chromatin domains in WT male versus ph^{505} male embryos show the specific loss of contacts between Blue domains. (**G**) Side-by-side Hi-C map of WT male (top) and ph^{505} male embryos (bottom) showing specific loss of contacts between Blue TADs in ph^{505} (indicated with circles). The contact enrichment color scale is the same as in (A).

changes in distances influence TAD structure (fig. S8E), we then used the inferred model to measure the overlap fraction (fig. S8F) for all simulated configurations or only for configurations where the inter-TAD probe (2-3) distance was smaller than the intra-TAD probe (2-1) distance. The configurations from the inferred model displayed weak overlap fraction between the TADs (≤10% overlap in 94% of the inferred configurations; Fig. 4C). Strikingly, the small overlap of TADs largely persists for configurations where the intra-TAD distance is higher than the inter-TAD distance (≤10% overlap in 85% of the inferred configurations; Fig. 4C). Therefore, polymer modeling using parameters that fit Hi-C maps supports the frequent folding of the two TADs into well-separated nanocompartments. The fraction of intra-TAD distances larger than the inter-TADs counterparts is thus explained by the dynamic relative positioning of the two TADs, rather than by TAD intermingling (Fig. 4D and fig. S8E). Overall, our microscopy and simulation results are consistent with TADs representing physical units of chromatin folding.

Large-scale chromatin folding reflects highly heterogeneous yet specific, long-range interdomain contacts

Finally, we asked whether large-scale active and repressed compartments (*2*, *11*) also represent physical entities or rather reflect statistical contact preference between highly heterogeneous chromosome configurations. We labeled chromatin domains of different epigenetic states and studied their relative 3D spatial organization (Fig. 5, A and B). This analysis revealed the presence of discrete interdomain contacts, with preference for contacts among TADs of the same epigenetic type (Fig. 5, C and D). These inter-TAD contacts are regulated, as the disruption of the *polyhomeotic* (*ph*) PcG gene specifically affects Pc inter-TAD contacts (*36*) without affecting contacts between other domains (Fig. 5, E to G). However, they are rare and the overall FISH configurations generated by the probe sets are highly heterogeneous (Fig. 5C). These results, consistent with previous reports (*17*, *18*), suggest that active and repressive compartments reflect stochastic inter-TAD contacts with statistical preference for TADs of the same kind. These findings thus identify a difference between the nature of compartments defined from Hi-C, which is statistical, and that of repressive TADs, which are physical entities.

DISCUSSION

This study demonstrates the partitioning of the chromatin fiber into discrete nanocompartments that correspond to repressed TADs intercalated with active chromatin domains. If individual TAD folding is dynamic and variable, then the meshwork of intra-TAD contacts is sufficient to hold them together to form nanocompartments. We thus propose that the high frequency and cooperativity, rather than the stability and the persistence, of intra-TAD interactions give rise to identifiable structures in single cells. Furthermore, the weak propensity of active chromatin, highly enriched in acetylated histones, to interact with inactive chromatin (*7*, *8*) may be sufficient to shape a chromatin pattern made of a succession of segregated TAD-based discrete domains. These conclusions thus reconcile previous observations using microscopy and Hi-C (*5*, *6*, *14*, *17*, *31*, *34*). Our data are consistent with TAD-based nanocompartments persisting through the interphase cell cycle, providing a role for TADs in the spatial segregation of autonomously regulated genomic regions. This chromosome organization is thus maintained in G_2 cells and may be the basis of chromosome pairing in interphase insect cells. Finally, the fact that TAD identity and architecture depend on cell fate regulation (*15*, *37*) calls for further analysis in different cell types and species to generalize these findings and understand the mechanistic basis of the relation between 3D chromosome organization and chromatin contact patterns.

MATERIALS AND METHODS

Experimental design

Probe design and synthesis

Oligopaint libraries were constructed following the procedures described by Beliveau *et al.* (*24*) [see the Oligopaints website (http://genetics.med.harvard.edu/oligopaints) for further details]. The 3-Mb (chr2L: 9935314-12973080) library, synthesized at the Wyss Institute (Harvard University, Boston, MA), was a gift from the laboratory of C.-T. Wu (Harvard Medical School, Boston, MA). All other libraries were ordered from CustomArray in the 12K Oligo pool format. Coordinates, size, number, and density of probes for the libraries are given in table S1.

All libraries consisted of 42-mer genomic sequences discovered by OligoArray 2.1 run in the laboratory of C.-T. Wu with the following settings: -n 30 -l 42 -L 42 -D 1000 -t 80 -T 99 -s 70 -x 70 -p 35 -P 80 -m 'GGGG;CCCC;TTTTT;AAAAA' -g 44. Each library contains a universal primer pair followed by a specific primer pair hooked to the 42-mer genomic sequences (126-mers in total). Single TAD probe libraries allowing dual labeling (named "1:3") contained one oligonucleotide of three potential genomic targets.

The 3-Mb Oligopaint probe was produced by emulsion polymerase chain reaction (PCR) amplification using universal primers followed by a "one-step PCR" and the lambda exonuclease procedure (*24*). In this case, each oligonucleotide contained a single fluorochrome. All other Oligopaint libraries were produced by emulsion PCR amplification from oligonucleotide pools followed by a "two-step PCR" procedure and the lambda exonuclease method (*24*). The two-step PCR leads to secondary oligonucleotide binding sites for signal amplification with a secondary oligonucleotide (Sec1 or Sec6) containing two additional fluorochromes. In this case, each oligonucleotide carried three fluorochromes in total. All oligonucleotides used for Oligopaint production were purchased from Integrated DNA Technologies. All oligonucleotide sequences (5′→3′) are listed below:

Emulsion PCR with universal primers

BB297-FWD: GACTGGTACTCGCGTGACTTG

BB299-REV: GTAGGGACACCTCTGGACTGG

3-Mb probe one-step PCR

BB291-FWD: /5Phos/CAGGTCGAGCCCTGTAGTACG

BB292-REV-ATTO565: /5ATTO565N/CTAGGAGACAGCCTCGGACAC

Two-step PCR

PCR1 with FWD 5′ phosphorylation and REV 53-mers:

A BB82-FWD: /5Phos/GTATCGTGCAAGGGTGAATGC

SecX-BB278-REV: /SecX/GAGCAGTCACAGTCCAGAAGG

B BB81-FWD: /5Phos/ATCCTAGCCCATACGGCAATG

SecX-BB281-REV: /SecX/GGACATGGGTCAGGTAGGTTG

C BB287-FWD: /5Phos/CGCTCGGTCTCCGTTCGTCTC

SecX-BB288-REV: /SecX/GGGCTAGGTACAGGGTTCAGC

D BB293-FWD: /5Phos/CCGAGTCTAGCGTCTCCTCTG

SecX-BB294-REV: /SecX/AACAGAGCCAGCCTCTACCTG

E BB298-FWD: /5Phos/CGTCAGTACAGGGTGTGATGC

SecX-BB187-REV: /SecX/TTGATCTTGACCCATCGAAGC

Binding sequence Sec1: CACCGACGTCGCATAGAACGGAAGAGCGTGTG

Binding sequence Sec6: CACACGCTCTCCGTCTTGGCCGTGGTCGATCA

PCR2 with labeled "back primer"
BB506-Alexa488: /5Alex488N/CACCGACGTCGCATAGAACGG
BB511-Cy3: /5Cy3/CACACGCTCTCCGTCTTGGC
BB511-ATTO565: /5ATTO565N/CACACGCTCTCCGTCTTGGC
Secondary oligos
Sec1-Alexa488-X2: /5Alex488N/CACACGCTCTTCCGTTC-TATGCGACGTCGGTGagatgttt/3AlexF488N/
Sec6-Cy3-X2: /5Cy3/TGATCGACCACGGCCAAGACGGA-GAGCGTGTGagatgttt/3Cy3Sp/
Sec6-ATTO565-X2: /5ATTO565N/TGATCGACCACGGC-CAAGACGGAGAGCGTGTGagatgttt/3ATTO565N/
Sec6-Alexa488-X2: /5Alex488N/TGATCGACCACGGCCAA-GACGGAGAGCGTGTGagatgttt/3AlexF488N/

In Fig. 5, for the labeling of domains of the same chromatin type (that is, Blue-Blue, Black-Black, and Red-Red), domains that were consecutive along the chromosome were alternatively labeled, that is, one in A488 followed by one in Cy3 or ATTO565, etc. For this purpose, the oligopools corresponding to nonconsecutive domains of the same chromatin type were on the same array, which allows their amplification as one library using the same primer set. For the labeling of domains of different chromatin type (that is, Blue-Black, Blue-Red, and Black-Red), all domains of the same chromatin type were labeled using one color.

Small probes 1, 2, and 3 used for triple FISH experiments (Fig. 3) were generated using four consecutive PCR fragments of 1.1 to 1.6 kb from *Drosophila* genomic DNA, each covering approximately 8 kb. The list below shows the amplicon size (bp) and the corresponding primers for each probe fragment.

Probe 1

Fragment 1	1299	1_FWD	AGGTGGAGTTGTGTATGCGA
		1_REV	GAGTGAAAAGGCGTTGGTGT
Fragment 2	1568	2_FWD	TCCACTTTCGCCTGATGTCT
		2_REV	GAGGTGTTTGTGCCAGGAAG
Fragment 3	1084	3_FWD	TTTCTTACCCCATCCACCCC
		3_REV	TATAAGCCCGGCCAAGTTGA
Fragment 4	1443	4_FWD	GAGCTGGGACGTAACCTCTT
		4_REV	ATGTTCACGCTTCTCCTCGA

Probe 2

Fragment 1	1446	1_FWD	CAGCGTGAGTGTCAAGTGAG
		1_REV	GCTGATGTTTTGGCTTCCGA
Fragment 2	1568	2_FWD	TGAAATACGACGAACCGCAG
		2_REV	TGTTTCGACTGTAAAGCCGC
Fragment 3	1310	3_FWD	CTGGGCGACAAGAACAACAA
		3_REV	AAGAAAATTGCCAGCCCCAG
Fragment 4	1305	4_FWD	TAACCAATTGCCGCGTTGAA
		4_REV	AAATCGGTGGGTGATGAGGT

Probe 3

Fragment 1	1421	1_FWD	CCACAAGAAAAGCACCCACA
		1_REV	TCTCGCTCTGTTCAAGGTGT
Fragment 2	1243	2_FWD	CCTCAGCAGCTTTTCGGATC
		2_REV	GCCCCGGATTGTTGATTCTC
Fragment 3	1481	3_FWD	ACCTCTACGCTCCAGATTCG
		3_REV	AGTGCTTATCAACGACCCCA
Fragment 4	1292	4_FWD	GCTCGCTCATTTGACCCAAT
		4_REV	CTTTCCGCTCATCTTGGGTG

Probes were labeled using the FISH Tag DNA Kit (Invitrogen Life Technologies) with Alexa Fluor 488, 555, and 647 dyes. All probe coordinates refer to Dm3/FlyBase R5 reference genome.

Three-dimensional FISH

3D-FISH was adapted from Bantignies and Cavalli (*38*). For optimal imaging, we used coverslips of 0.170 ± 0.005 mm (Zeiss). Coverslips were rinsed in 96% ethanol before incubation for 5 min in 1:10 poly-L-lysine (P8920, Sigma-Aldrich) diluted in water (final concentration at 0.01%, w/v). Briefly, cells in suspension (about 2×10^6 cells/ml) were deposited on a coverslip for 1-hour sedimentation in a humid chamber, or four to five dechorionated and selected embryos were squeezed directly on a coverslip with a Dumont #55 tweezer. Samples were fixed with phosphate-buffered saline (PBS)/4% paraformaldehyde (PFA), washed in PBS, permeabilized with PBS/0.5% Triton X-100 for 10 min, washed in PBS, and incubated for 30 min in PBS/20% glycerol. After PBS washes, cells were incubated with 0.1 M HCl for 10 min, washed in 2× SSCT (2× SSC/0.1% Tween 20), and incubated for 30 min in 50% formamide, 2× SSCT. Probe mixture contains 20 pmol of each probe with 20 pmol of their complementary secondary oligonucleotide (except for the 3-Mb region, used without secondary oligo), 0.8 μl of ribonuclease A (10 mg/ml), and FISH hybridization buffer [FHB; 50% formamide, 10% dextran sulfate, 2× SSC, and salmon sperm DNA (0.5 mg/ml)], in a total mixture volume of approximately 20 to 25 μl, keeping at least a 3:4 ratio of FHB/total volume. Probe mixture was added to the coverslip before sealing on a glass slide with rubber cement (Fixogum, Marabu). Cell DNA was denatured at 78°C for 3 min, and hybridization was performed at 37°C overnight in a humid dark chamber. Cells were then washed 3 × 5 min at 37°C in 2× SSC, 3 × 5 min at 45°C in 0.1× SSC, and 2 × 5 min in PBS before DNA counterstaining with DAPI (final concentration at 0.3 mg/ml in PBS). After final washing in PBS, coverslips were mounted on slides with Vectashield (CliniSciences) and sealed with nail polish.

Immunostaining

Cells in suspension (about 2×10^6 cells/ml) were deposited on coverslips for 1-hour sedimentation in a humid chamber. Cells were fixed in PBS/4% PFA, washed in PBS, treated with PBS/0.1% Triton X-100 for 15 min, and washed in PBS/0.02% Tween 20 (PBT) before blocking in PBT/2% bovine serum albumin (BSA) (A7906, Sigma-Aldrich) for 30 min. Cells were then incubated with cyclin B (CycB) antibody (Developmental Studies Hybridoma Bank, product F2F4), diluted in PBT/2% BSA (1:500 dilution) overnight at 4°C in a humid chamber. Cells were then washed with PBT, incubated with secondary antibody (1:200 dilution; A-31570, Life Technologies) for 1 hour at room temperature, washed

with PBT, and incubated in PBS and DAPI (final concentration at 0.5 mg/ml in PBS). Cells were then washed with PBS, and coverslips were mounted on slides with Vectashield (CliniSciences).

Image acquisition

3D-SIM super-resolution imaging was performed with a DeltaVision OMX V3/V4 microscope (GE Healthcare) equipped with a ×100/1.4 numerical aperture (NA) Plan Super Apochromat oil immersion objective (Olympus). Electron-multiplying charge-coupled device (EMCCD) (Evolve 512B, Photometrics) cameras for a pixel size of 79 nm at the sample were used. Diode lasers at 405, 488, and 561 nm and the standard corresponding emission filters were used. *Z*-stacks were acquired with five phases and three angles per image plane, with a *z*-step of 125 nm. Raw images were reconstructed using SoftWorx (version 6.5, GE Healthcare), using channel-specific optical transfer functions (pixel size of reconstructed images, 39.5 nm). TetraSpeck beads (200 nm) (T7280, Thermo Fisher Scientific) were used to calibrate alignment parameters between the different channels. Quality of reconstructed images was assessed using ImageJ and the SIMcheck plugin (*39*), and examples of quality controls are shown in fig. S9. Conventional WF images were generated from raw images using SoftWorx by averaging the different angles and phases for each plane. Automatic "Threshold and 16-bit Conversion" (SIMcheck plugin) was applied to the reconstructed images shown.

Confocal microscopy images were acquired with a Leica SP8 microscope (Leica Microsystems) equipped with a ×63/1.4 NA Plan-Apochromat oil immersion objective and photomultiplier tube and hybrid detectors for a pixel size of 59 nm (*z*-step, 300 nm).

dSTORM super-resolution imaging was carried out with a custom-made inverted microscope using an oil immersion objective (Plan-Apochromat, 100×, 1.4 NA oil DIC, Zeiss) mounted on a *z*-axis piezoelectric stage (P-721.CDQ, PICOF, PI). A 1.5× telescope was used to obtain a final imaging magnification of 150-fold corresponding to a pixel size of 105 nm. Two lasers were used for excitation/photoactivation: 642 nm (MPB Communications Inc.) and 405 nm (OBIS, LX 405-50, Coherent Inc.). Laser lines were expanded and coupled into a single beam using a dichroic mirror (427-nm LaserMUX, Semrock). An acousto-optic tunable filter (AOTFnc-400.650-TN, AA Opto-Electronics) was used to modulate laser intensity. Light was circularly polarized using an achromatic quarter wave plate. Two achromatic lenses were used to expand the excitation laser and an additional dichroic mirror (zt405/488/561/638rpc, Chroma Technology) to direct it toward the back focal plane of the objective. Fluorescence light was spectrally filtered with emission filters (ET700/75m, Chroma Technology) and imaged on an EMCCD camera (iXon X3 DU-897, Andor Technology). The microscope was equipped with a motorized stage (MS-2000, ASI) to translate the sample perpendicularly to the optical axis. To ensure the stability of the focus during the acquisition, a homemade autofocus system was built. A 785-nm laser beam (OBIS, LX 785-50, Coherent Inc.) was expanded twice and directed toward the objective lens by a dichroic mirror (z1064rdc-sp, Chroma Technology). The reflected infrared beam was redirected following the same path than the incident beam and guided to a CCD detector (Pixelfly, Cooke) by a polarized beam splitter cube. Camera, lasers, and filter wheel were controlled with software written in LabVIEW (*40*).

For image acquisition, an average of 15,000 frames was recorded at a rate of 10 ms per frame. To induce photoswitching, samples were imaged in a freshly prepared Smart Kit buffer (Abbelight). Continuous excitation and activation was used with output laser powers of 600 mW at 642 nm (for AF647 excitation) and 0 to 2.5 mW at 405 nm (for activation). The intensity of activation was progressively increased throughout the acquisition to ensure a constant amount of simultaneously emitting fluorophores within the labeled structures. These excitation powers were optimized to ensure single-molecule detection. Imaging data are available upon request.

Image analysis

3D image analysis was performed using Imaris software and its XT module. For all images analyzed in 3D, a background subtraction filter was applied. For fluorescence intensity correlation, the regions of interest were first segmented in 3D (the 3-Mb probe for fig. S1E or the single-domain probes for fig. S2B and Fig. 1G). PCCs were then calculated in single cell using the voxels within the regions of interest. To measure the probe density of the single domains (Fig. 1H), we divided the genomic size of the labeled regions by the volume occupied by the 3D-segmented probes (probes with full Oligopaint coverage) in each single nucleus analyzed. To count the number of nanocompartments in the different FISH experiments (and to identify the 3-Mb maxima in fig. S1F), we used the point-like structure function (spots) of Imaris. Examples of nanocompartment identification with this method are shown in Fig. 2F. Distances between nanocompartments were calculated between the centered voxels of the spots identified. The sizes of nanocompartments (figs. S3, F and G, and S6D) were determined using full width at half maximum of Gaussian curves fitted to the intensity profiles obtained along lines passing through single nanocompartments in *z*-stacked (maximum projections) images [processed with Threshold and 16-bit Conversion from SIMcheck (*39*)]. To investigate contact frequency and overlap between TAD 1 and TAD 2 (Fig. 3F), we segmented the probes in 3D and calculated the Jaccard index by dividing the volume of the colocalized voxels (intersection of the two probes) by the sum of the volumes of the segmented probes minus the colocalized volume (union of the volumes of the two probes). This Jaccard index was defined as the overlap fraction. The quantification of segmented objects (fig. S6B) was performed with ImageJ's Otsu automatic thresholding of FISH signals (minimum size of 6 pixels^2) in *z*-stacked (maximum projections) images (processed with Threshold and 16-bit Conversion from SIMcheck). Sphericity scores (fig. S6C) were calculated from probe 3D segmentation in individual nuclei. Specific epigenetic domains on the 3R chromosome (Fig. 5) were identified using the spot function of Imaris, and distances (all pairwise or nearest-neighbor distances) were measured in 3D from the centered voxels of the spots.

To measure the distances between small probes 1, 2, and 3 (Fig. 3, B and C), we applied a Gaussian filter ($\sigma = 1$ pixel) to the image before 3D segmentation of the spot signals and calculation of their center of mass. We then identified mutual nearest neighbors between the centers of mass of probes 2 and 1 and between the centers of mass of probes 2 and 3 and calculated combinatorial 3D distances for these triplets. To assess the experimental error, we used 200-nm TetraSpeck beads (T7280, Thermo Fisher Scientific) coupled with dyes of the same colors than the FISH probes, and we applied the same method for 3D distance measurements. We obtained from the beads a mean (±SD) of 164 ± 41 nm between red and green dyes (corresponding to probe 2 and 1 dyes, respectively), 107 ± 46 nm between red and far-red dyes (corresponding to probe 2 and 3 dyes, respectively), and 231 ± 67 nm between green and far-red dyes (corresponding to probe 1 and 3 dyes, respectively). This indicates that the shorter distance distribution between intra-TAD probes (2-1) compared to inter-TAD (2-3) is not due to technical bias.

For dSTORM image after processing and analysis, single-molecule localization was performed using the ImageJ ThunderSTORM plugin. Default values were used for the analysis (B-spline wavelet filter—order 3 and scale 2.0, approximate localization by eight-neighborhood local

maximum, subpixel localization by point spread function (PSF)–integrated Gaussian with the weighted least squares fitting method with a 3-pixel fitting radius and 1.6-pixel initial sigma). Particle coordinates and statistical properties were exported, and further analysis was conducted using MATLAB (MathWorks). Clustering of localizations was performed using an algorithm that was previously described by Cattoni *et al.* (*41*). A particle density and area threshold was set to define and quantify the number of objects per imaged probe. Automatic detection and quantification were further verified by visual inspection and comparison of conventional fluorescence and super-resolution rendered images using variable intensity thresholds.

Determination of cell cycle stage

We used the method published by Roukos *et al.* (*29*) to determine cell cycle stages of S2R+ cells. This method is based on DAPI fluorescence intensity after microscopy image acquisition (fig. S5). Briefly, DAPI channels of images were separated and projected along the *z* axis using average intensity, and nuclei were identified with CellProfiler software (http://cellprofiler.org/). The DAPI-integrated intensity was calculated for each nucleus, and the distribution for the whole population was plotted. The nuclei were then classified as G_1 or G_2 according to their DAPI-integrated intensity profile relative to the profile obtained for the population (fig. S5). To classify nuclei positive for CycB (fig. S5C), the CycB signal was segmented using CellProfiler software, and overlapped nuclei were counted.

Hi-C library preparation and sequencing

For S2R+ cells, Hi-C and library preparation was performed using the in situ method as published by Rao *et al.* (*11*) with minor modifications. Two biological replicates were done using 5×10^6 cells. Briefly, cells were digested overnight at 37°C using 500 U of Dpn II. After biotin filling, proximity ligation was carried out for 4 hours at 18°C with 2000 U of T4 DNA ligase, and after reverse cross-linking, DNA was purified with ethanol precipitation and sheared to 300- to 400-bp fragments using a Covaris S220 sonicator. Ligation fragments with biotin were pulled down using MyOne Streptavidin T1 beads (catalog no. 65602, Thermo Fisher Scientific), end-repaired, and adenylated as described. Fragments were then ligated with NEXTflex adaptors (catalog no. 514101, Bio-Scientific) and amplified by PCR using the KAPA HiFi Library Amplification Kit (catalog no. KK2620, Kapa Biosystems) for eight cycles. DNA size selection (300 to 800 bp) was performed using AMPure XP beads (catalog no. A63881, Agencourt). Libraries were validated qualitatively and quantitatively with Fragment Analyzer and by qPCR (Roche LightCycler 480). They were sequenced with 2 × 50–bp paired-end runs on an Illumina HiSeq 2500.

For embryo Hi-C, embryos were collected in a saline buffer (0.03% Triton X-100, 0.4% NaCl) 16 to 18 hours after egg laying and then dechorionated for 5 min in fresh bleach. About 3000 GFP^- (selection of ph^{505} null mutant males; see the "*Drosophila*" section for description) and GFP^+ (selection of WT males from the Y-GFP line) embryos each were sorted with a Union Biometrica COPAS large particle sorter (Union Biometrica Inc.) and then processed for Hi-C as in the study of Sexton *et al.* (*6*).

Hi-C analysis

Hi-C sequence mapping, read filtering, and normalization were performed as previously published (*6*). This provided statistics on the number of observed contacts for each pair of restriction fragments and the number of expected contacts from a low-level probabilistic model, which considers local GC content and the Dpn II restriction fragment length. Therefore, technically corrected matrices were generated by calculating ratios between the total observed reads and the expected reads based on the above model. We visualized contact maps as described by Sexton *et al.* (*6*). To maximize resolution, we used variable bin sizes from 5 to 160 kb, visualizing each point in the matrix using the ratio as computed for the minimal 2D bin with at least 30 observed contacts. S2R+ Hi-C map (Fig. 1A) was plotted based on merging two replicates for the 3-Mb region 2L:9935314..12973080 and aligned with the ChIP-sequencing (ChIP-seq) profile of Pc (S2 cells, GSM604723) and ChIP-chip of H3K4me3 (S2 cells, modENCODE305). Side-by-side Hi-C comparisons for R2 (2R:10534240..10729120), R3 (3R: 23547420..24352723), R4 (2R: 5203174..5698315), and the 3-Mb Oligopaint-labeled regions (fig. S4) show the contact map in S2R+ cells (merge of replicates) on the top left and embryos [16 to 18 hours, merge of two replicates published by Schuettengruber *et al.* (*42*)] on the bottom right, alongside with ChIP-seq of H3K4me3 (embryo 14 to 16 hours, modENCODE5096) and ChIP-chip of H3K4me3 (S2 cells, modENCODE305). The male embryo Hi-C map (Fig. 3A) is plotted based on merging two replicates for the region X:4502500..5061200 alongside with ChIP-seq of H3K4me3 (modENCODE5096). The embryo [16 to 18 hours, merge of two replicates published by Schuettengruber *et al.* (*42*)] Hi-C map (Fig. 5A) is plotted for the region 3R:500000..14000000 and aligned with ChIP-seq of Pc (modENCODE3957) and H3K4me3 (modENCODE5096). The side-by-side Hi-C comparison for the 3R:500000..14000000 region (Fig. 5G) shows the contact map in WT male embryos (merge of two replicates) on the top left and ph^{505} male embryos (merge of two replicates) on the bottom right. Data sets are available at GSE99107.

Cis-decay curve analysis

For each single domain (fig. S2E), the observed and expected interaction counts for different bins of genomic separation were computed (from 400 bp to the full TAD size and separated by at least two fragments). The expected scores were taken by computing over all possible pairwise fragment combinations. The observed scores were obtained by counting all interactions within Hi-C data, which correspond to a particular distance. The cis-decay curve was plotted as the observed/expected ratio (the probability of detecting a Hi-C interaction) over a particular genomic separation on a logarithmic scale.

Analysis of domain contacts between different chromatin colors

The boundaries of domains were demarcated using the topmost fifth percentile of 5 kb–smoothed inferred distance-scaling factors (*6*). Domains were merged when their length was smaller than 10 kb. Then, domains were colored as red, blue, and black according to *k*-means grouping results based on their average enrichments of H3K4me3, H3K27me3, HP1, and H1 marks (*6*). We generated a domain-level contact map by calculating ratios between observed contacts of associating fragments within each pair of domains and total expected contacts based on the distance-scaling model (factoring out the general tendency of adjacent domains to contact each other). Differential contacts between WT and *ph* null mutant male embryos are expressed as the $\log_2$ ratio of the ph^{505} normalized contacts and the WT normalized contacts (Fig. 5F).

Polymer modeling of haploid chromatin regions

We modeled the genomic region of chromosome X located between 4.58 and 5.03 Mbp by a flexible self-avoiding polymer containing $n = 225$ monomers, each monomer, of size a, representing 2 kbp. The chain dynamics was mapped on a face-centered cubic lattice following the kinetic Monte-Carlo scheme described by

Olarte-Plata *et al.* (*35*) driven by short-range contact interactions following the Hamiltonian

$$H = \sum_{i=1}^{n} \sum_{j=i+1}^{n} U_{i,j}\delta_{i,j}$$

where $U_{i,j}$ is the energy of interaction between monomers i and j, and $\delta_{i,j} = 1$ if the two monomers are nearest neighbor on the lattice, and $\delta_{i,j} = 0$ otherwise.

Parameters $\{U_{i,j}\}$ were inferred such that the predicted contact map at equilibrium is consistent with experiments. The corresponding target contact map (Fig. 4A, bottom) was derived from the experimental Hi-C map at 10-kbp resolution: Similar to previous work (*43*), we transformed the experimental normalized contact frequencies $C_{k,l}$ into contact probabilities $P_{k,l}$ (the observable that we can directly compare to simulations) using the following procedure: $P_{k,l} = \min\left(1, \frac{C_{k,l}}{\overline{C}_{\pm 1}}\right)$, where $\overline{C}_{\pm 1}$ is the median value of $\{C_{k,k+1}\}$. The underlying assumption is that in a polymer model, adjacent monomers are always in contact. Note that in our polymer model, a 10-kbp region (the experimental resolution we used to avoid too much sampling noise) is represented by five consecutive beads. Therefore, for a given simulated configuration, two 10-kbp regions will be predicted to be in contact if at least one 2-kbp monomer of the first region is closest than a cutoff distance R to a monomer of the second region. R corresponds to the maximal distance between two loci that is captured by Hi-C experiments as a contact. Using this definition, for a given set of parameters $\{U_{i,j}\}$ and a given value of R, we estimated the corresponding contact probability map at 10-kbp resolution from the sampling of 10,000 configurations at equilibrium (examples of configurations are given in Fig. 4D). For a fixed R, the values of $\{U_{i,j}\}$ were inferred by minimizing the χ^2 score

$$\chi^2 = \sum_{k,l} \frac{[P_{k,l}(\mathrm{sim}) - P_{k,l}(\mathrm{exp})]^2}{\sigma^2_{kl}(\mathrm{exp})}$$

where $\sigma^2_{kl}(\mathrm{exp})$ is the standard error of $P_{k,l}(\mathrm{exp})$ estimated using experimental replicates. We followed the scheme developed by Giorgetti *et al.* (*34*) that makes use of Boltzmann reweighting to numerically speed up the inference. Using this technique, convergence to a local minimum of χ^2 is fast (fig. S8B). We repeated this operation several times by varying also the values of R and took the realization with the lowest local minimum (Fig. 4A and fig. S8B for $R = 1.4a$). The length unit in the simulation ($a = 102 \pm 4$ nm) was then fixed by comparing the predicted distances between the three loci investigated by FISH to the corresponding experimental data accounting for a random experimental error of ~100 nm (fig. S8C; see the "Image analysis" section for the calculation of the experimental error).

For a given simulated configuration, the overlap fraction between TAD 1 and TAD 2 was computed by estimating the 3D convex envelope of each TAD using the MATLAB function convexhull and by computing the fraction of TAD 1 and TAD 2 monomers belonging to both envelopes (an illustration in 2D is given in fig. S8F). An overlap fraction of 0 (resp. 1) signifies that both TADs occupy separate (resp. common) volumes.

Cell culture

S2R+ cells (stock #150, Drosophila Genomics Resource Center) were grown at 25°C in Schneider's S2 medium (S0146, Sigma-Aldrich) complemented with 10% fetal bovine serum (FBS) (10500064, Gibco) and 1% penicillin-streptomycin (15140122, Gibco).

For S2R+ Hi-C, cells were incubated with enhanced green fluorescent protein (EGFP) double-stranded RNA (dsRNA). For each well (six-well plate), 1×10^6 cells in 1-ml serum-free medium were deposited with 17.5 μg of dsRNA and incubated for 30 min before addition of 2 ml of medium with 15% FBS. Cells were then grown for 5 days at 25°C before harvest. EGFP dsRNAs were obtained from plasmid PCR amplification (sequences given below), followed by in vitro transcription using the MEGAscript Kit (Ambion Inc.):

EGFP FWD-primer: 5′-T7-GACGTAAACGGCCACAAGTT-3′
EGFP REV-primer: 5′-T7-TGCTCAGGTAGTGGTTGTCG-3′
T7 sequence: 5′-TAATACGACTCACTATAGGG-3′

EGFP amplicon sequence: GACGTAAACGGCCACAAGTT-CAGCGTGTCCGGCGAGGGCGAGGGCGATGCCACCTACGG-CAAGCTGACCCTGAAGTTCATCTGCACCACCGG-CAAGCTGCCCGTGCCCTGGCCCACCCTCGTGACCACCCT-GACCTACGGCGTGCAGTGCTTCAGCCGCTACCCCGACCA-CATGAAGCAGCACGACTTCTTCAAGTCCGCCATGCCC-GAAGGCTACGTCCAGGAGCGCACCATCTTCTTCAAGGAC-GACGGCAACTACAAGACCCGCGCCGAGGTGAAGTTC-GAGGGCGACACCCTGGTGAACCGCATCGAGCTGAAGGG-CATCGACTTCAAGGAGGACGGCAACATCCTGGGGCA-CAAGCTGGAGTACAACTACAACAGCCACAACGTCTATAT-CATGGCCGACAAGCAGAAGAACGGCATCAAGGTGAACTT-CAAGATCCGCCACAACATCGAGGACGGCAGCGTG-CAGCTCGCCGACCACTACCAGCAGAACACCCCCATCGGC-GACGGCCCCGTGCTGCTGCCCGACAACCACTACCTGAGCA

Drosophila

For the FISH experiments, flies were raised in standard cornmeal yeast extract media at 21°C. Embryos were harvested on agar/vinegar plate at stages 15 to 16 after egg laying, equivalent to a development of 12 to 16 hours at 25°C. Embryos were manually dechorionated on a double-face adhesive tape and displayed on an agar/vinegar plate to avoid drying during manual selection under a GFP binocular. The Oregon-R w[1118] line was used as the WT control line. To analyze haploid regions on chromosome X in male embryos, a Y-GFP reporter line (Y-GFP line: y[1], w[67c23]; Dp(1;Y), y[+] P{ry+11} P{w[+mC]=ActGFP}JMR1) was used for the selection of WT GFP^+ male embryos. This line was a gift of S. Hayashi and is described by Hayashi (*44*). The ph^{del} stock was balanced over the *KrGFP-FM7c* balancer (obtained from BL#5193 of the Bloomington Drosophila Stock Center) for the selection of hemizygous ph^{del} GFP^- null mutant male embryos. The ph^{del} stock was a gift from the laboratory of J. Wang.

For embryo Hi-C, flies were raised in standard cornmeal yeast extract media at 25°C. The ph^{505} stock was balanced over the *KrGFP-FM7c* balancer for the selection of hemizygous ph^{505} GFP^- null mutant male embryos. The Y-GFP line described above was used for the selection of WT GFP^+ male embryos to be compared with the *ph* mutant male embryos.

Statistical analysis

Description of statistical analysis is included in the figure legends.

SUPPLEMENTARY MATERIALS

Supplementary material for this article is available at http://advances.sciencemag.org/cgi/content/full/4/2/eaar8082/DC1

fig. S1. Chromatin nanostructure visualization with 3D-SIM imaging.

fig. S2. Dual labeling Oligopaint FISH.

fig. S3. Resolution of homologous TADs with 3D-SIM.
fig. S4. Oligopaint probe–targeted regions in S2R+ cells and embryos.
fig. S5. Cell cycle staging of S2R+ cells.
fig. S6. Super-resolution imaging of haploid chromatin folding.
fig. S7. 2D dSTORM imaging of TAD 1 and spanning probes.
fig. S8. Modeling the X chromatin region.
fig. S9. Quality control of SI acquisitions.
table S1. Libraries for Oligopaint probes.

REFERENCES AND NOTES

1. B. Bonev, G. Cavalli, Organization and function of the 3D genome. *Nat. Rev. Genet.* **17**, 661–678 (2016).
2. E. Lieberman-Aiden, N. L. van Berkum, L. Williams, M. Imakaev, T. Ragoczy, A. Telling, I. Amit, B. R. Lajoie, P. J. Sabo, M. O. Dorschner, R. Sandstrom, B. Bernstein, M. A. Bender, M. Groudine, A. Gnirke, J. Stamatoyannopoulos, L. A. Mirny, E. S. Lander, J. Dekker, Comprehensive mapping of long-range interactions reveals folding principles of the human genome. *Science* **326**, 289–293 (2009).
3. J. R. Dixon, S. Selvaraj, F. Yue, A. Kim, Y. Li, Y. Shen, M. Hu, J. S. Liu, B. Ren, Topological domains in mammalian genomes identified by analysis of chromatin interactions. *Nature* **485**, 376–380 (2012).
4. C. Hou, L. Li, Z. S. Qin, V. G. Corces, Gene density, transcription, and insulators contribute to the partition of the *Drosophila* genome into physical domains. *Mol. Cell* **48**, 471–484 (2012).
5. E. P. Nora, B. R. Lajoie, E. G. Schulz, L. Giorgetti, I. Okamoto, N. Servant, T. Piolot, N. L. van Berkum, J. Meisig, J. Sedat, J. Gribnau, E. Barillot, N. Blüthgen, J. Dekker, E. Heard, Spatial partitioning of the regulatory landscape of the X-inactivation centre. *Nature* **485**, 381–385 (2012).
6. T. Sexton, E. Yaffe, E. Kenigsberg, F. Bantignies, B. Leblanc, M. Hoichman, H. Parrinello, A. Tanay, G. Cavalli, Three-dimensional folding and functional organization principles of the *Drosophila* genome. *Cell* **148**, 458–472 (2012).
7. M. J. Rowley, M. H. Nichols, X. Lyu, M. Ando-Kuri, I. S. M. Rivera, K. Hermetz, P. Wang, Y. Ruan, V. G. Corces, Evolutionarily conserved principles predict 3D chromatin organization. *Mol. Cell* **67**, 837–852.e7 (2017).
8. S. V. Ulianov, E. E. Khrameeva, A. A. Gavrilov, I. M. Flyamer, P. Kos, E. A. Mikhaleva, A. A. Penin, M. D. Logacheva, M. V. Imakaev, A. Chertovich, M. S. Gelfand, Y. Y. Shevelyov, S. V. Razin, Active chromatin and transcription play a key role in chromosome partitioning into topologically associating domains. *Genome Res.* **26**, 70–84 (2016).
9. J. H. I. Haarhuis, R. H. van der Weide, V. A. Blomen, J. O. Yáñez-Cuna, M. Amendola, M. S. van Ruiten, P. H. L. Krijger, H. Teunissen, R. H. Medema, B. van Steensel, T. R. Brummelkamp, E. de Wit, B. D. Rowland, The cohesin release factor WAPL restricts chromatin loop extension. *Cell* **169**, 693–707.e14 (2017).
10. E. P. Nora, A. Goloborodko, A. L. Valton, J. H. Gibcus, A. Uebersohn, N. Abdennur, J. Dekker, L. A. Mirny, B. G. Bruneau, Targeted degradation of CTCF decouples local insulation of chromosome domains from genomic compartmentalization. *Cell* **169**, 930–944.e22 (2017).
11. S. S. P. Rao, M. H. Huntley, N. C. Durand, E. K. Stamenova, I. D. Bochkov, J. T. Robinson, A. L. Sanborn, I. Machol, A. D. Omer, E. S. Lander, E. L. Aiden, A 3D map of the human genome at kilobase resolution reveals principles of chromatin looping. *Cell* **159**, 1665–1680 (2014).
12. S. S. P. Rao, S.-C. Huang, B. Glenn St Hilaire, J. M. Engreitz, E. M. Perez, K.-R. Kieffer-Kwon, A. L. Sanborn, S. E. Johnstone, G. D. Bascom, I. D. Bochkov, X. Huang, M. S. Shamim, J. Shin, D. Turner, Z. Ye, A. D. Omer, J. T. Robinson, T. Schlick, B. E. Bernstein, R. Casellas, E. S. Lander, E. L. Aiden, Cohesin loss eliminates all loop domains. *Cell* **171**, 305–320.e24 (2017).
13. W. Schwarzer, N. Abdennur, A. Goloborodko, A. Pekowska, G. Fudenberg, Y. Loe-Mie, N. A. Fonseca, W. Huber, C. H. Haering, L. Mirny, F. Spitz, Two independent modes of chromatin organization revealed by cohesin removal. *Nature* **551**, 51–56 (2017).
14. Y. Zhan, L. Mariani, I. Barozzi, E. G. Schulz, N. Blüthgen, M. Stadler, G. Tiana, L. Giorgetti, Reciprocal insulation analysis of Hi-C data shows that TADs represent a functionally but not structurally privileged scale in the hierarchical folding of chromosomes. *Genome Res.* **27**, 479–490 (2017).
15. B. Bonev, N. Mendelson Cohen, Q. Szabo, L. Fritsch, G. L. Papadopoulos, Y. Lubling, X. Xu, X. Lv, J.-P. Hugnot, A. Tanay, G. Cavalli, Multiscale 3D genome rewiring during mouse neural development. *Cell* **171**, 557–572.e24 (2017).
16. D. G. Lupiáñez, K. Kraft, V. Heinrich, P. Krawitz, F. Brancati, E. Klopocki, D. Horn, H. Kayserili, J. M. Opitz, R. Laxova, F. Santos-Simarro, B. Gilbert-Dussardier, L. Wittler, M. Borschiwer, S. A. Haas, M. Osterwalder, M. Franke, B. Timmermann, J. Hecht, M. Spielmann, A. Visel, S. Mundlos, Disruptions of topological chromatin domains cause pathogenic rewiring of gene-enhancer interactions. *Cell* **161**, 1012–1025 (2015).
17. I. M. Flyamer, J. Gassler, M. Imakaev, H. B. Brandão, S. V. Ulianov, N. Abdennur, S. V. Razin, L. A. Mirny, K. Tachibana-Konwalski, Single-nucleus Hi-C reveals unique chromatin reorganization at oocyte-to-zygote transition. *Nature* **544**, 110–114 (2017).
18. T. Nagano, Y. Lubling, T. J. Stevens, S. Schoenfelder, E. Yaffe, W. Dean, E. D. Laue, A. Tanay, P. Fraser, Single-cell Hi-C reveals cell-to-cell variability in chromosome structure. *Nature* **502**, 59–64 (2013).
19. T. Nagano, Y. Lubling, C. Várnai, C. Dudley, W. Leung, Y. Baran, N. Mendelson Cohen, S. Wingett, P. Fraser, A. Tanay, Cell-cycle dynamics of chromosomal organization at single-cell resolution. *Nature* **547**, 61–67 (2017).
20. D. I. Cattoni, A. M. Cardozo Gizzi, M. Georgieva, M. Di Stefano, A. Valeri, D. Chamousset, C. Houbron, S. Déjardin, J. B. Fiche, I. González, J. M. Chang, T. Sexton, M. A. Marti-Renom, F. Bantignies, G. Cavalli, M. Nollmann, Single-cell absolute contact probability detection reveals chromosomes are organized by multiple low-frequency yet specific interactions. *Nat. Commun.* **8**, 1753 (2017).
21. Y. Markaki, D. Smeets, S. Fiedler, V. J. Schmid, L. Schermelleh, T. Cremer, M. Cremer, The potential of 3D-FISH and super-resolution structured illumination microscopy for studies of 3D nuclear architecture: 3D structured illumination microscopy of defined chromosomal structures visualized by 3D (immuno)-FISH opens new perspectives for studies of nuclear architecture. *Bioessays* **34**, 412–426 (2012).
22. T. Nozaki, R. Imai, M. Tanbo, R. Nagashima, S. Tamura, T. Tani, Y. Joti, M. Tomita, K. Hibino, M. T. Kanemaki, K. S. Wendt, Y. Okada, T. Nagai, K. Maeshima, Dynamic organization of chromatin domains revealed by super-resolution live-cell imaging. *Mol. Cell* **67**, 282–293.e7 (2017).
23. A. N. Boettiger, B. Bintu, J. R. Moffitt, S. Wang, B. J. Beliveau, G. Fudenberg, M. Imakaev, L. A. Mirny, C.-t. Wu, X. Zhuang, Super-resolution imaging reveals distinct chromatin folding for different epigenetic states. *Nature* **529**, 418–422 (2016).
24. B. J. Beliveau, A. N. Boettiger, M. S. Avendaño, R. Jungmann, R. B. McCole, E. F. Joyce, C. Kim-Kiselak, F. Bantignies, C. Y. Fonseka, J. Erceg, M. A. Hannan, H. G. Hoang, D. Colognori, J. T. Lee, W. M. Shih, P. Yin, X. Zhuang, C.-t. Wu, Single-molecule super-resolution imaging of chromosomes and in situ haplotype visualization using Oligopaint FISH probes. *Nat. Commun.* **6**, 7147 (2015).
25. J. Demmerle, C. Innocent, A. J. North, G. Ball, M. Müller, E. Miron, A. Matsuda, I. M. Dobbie, Y. Markaki, L. Schermelleh, Strategic and practical guidelines for successful structured illumination microscopy. *Nat. Protoc.* **12**, 988–1010 (2017).
26. M. G. L. Gustafsson, L. Shao, P. M. Carlton, C. J. R. Wang, I. N. Golubovskaya, W. Z. Cande, D. A. Agard, J. W. Sedat, Three-dimensional resolution doubling in wide-field fluorescence microscopy by structured illumination. *Biophys. J.* **94**, 4957–4970 (2008).
27. J. A. Kassis, J. L. Brown, Polycomb group response elements in *Drosophila* and vertebrates. *Adv. Genet.* **81**, 83–118 (2013).
28. B. A. Edgar, P. H. O'Farrell, The three postblastoderm cell cycles of Drosophila embryogenesis are regulated in G2 by *string*. *Cell* **62**, 469–480 (1990).
29. V. Roukos, G. Pegoraro, T. C. Voss, T. Misteli, Cell cycle staging of individual cells by fluorescence microscopy. *Nat. Protoc.* **10**, 334–348 (2015).
30. K. P. Eagen, T. A. Hartl, R. D. Kornberg, Stable chromosome condensation revealed by chromosome conformation capture. *Cell* **163**, 934–946 (2015).
31. I. Williamson, S. Berlivet, R. Eskeland, S. Boyle, R. S. Illingworth, D. Paquette, J. Dostie, W. A. Bickmore, Spatial genome organization: Contrasting views from chromosome conformation capture and fluorescence in situ hybridization. *Genes Dev.* **28**, 2778–2791 (2014).
32. M. Heilemann, S. van de Linde, M. Schüttpelz, R. Kasper, B. Seefeldt, A. Mukherjee, P. Tinnefeld, M. Sauer, Subdiffraction-resolution fluorescence imaging with conventional fluorescent probes. *Angew. Chem. Int. Ed. Engl.* **47**, 6172–6176 (2008).
33. M. J. Rust, M. Bates, X. Zhuang, Sub-diffraction-limit imaging by stochastic optical reconstruction microscopy (STORM). *Nat. Methods* **3**, 793–796 (2006).
34. L. Giorgetti, R. Galupa, E. P. Nora, T. Piolot, F. Lam, J. Dekker, G. Tiana, E. Heard, Predictive polymer modeling reveals coupled fluctuations in chromosome conformation and transcription. *Cell* **157**, 950–963 (2014).
35. J. D. Olarte-Plata, N. Haddad, C. Vaillant, D. Jost, The folding landscape of the epigenome. *Phys. Biol.* **13**, 026001 (2016).
36. A. H. Wani, A. N. Boettiger, P. Schorderet, A. Ergun, C. Münger, R. I. Sadreyev, X. Zhuang, R. E. Kingston, N. J. Francis, Chromatin topology is coupled to Polycomb group protein subnuclear organization. *Nat. Commun.* **7**, 10291 (2016).
37. C. B. Hug, A. G. Grimaldi, K. Kruse, J. M. Vaquerizas, Chromatin architecture emerges during zygotic genome activation independent of transcription. *Cell* **169**, 216–228.e19 (2017).
38. F. Bantignies, G. Cavalli, Topological organization of Drosophila Hox genes using DNA fluorescent in situ hybridization. *Methods Mol. Biol.* **1196**, 103–120 (2014).
39. G. Ball, J. Demmerle, R. Kaufmann, I. Davis, I. M. Dobbie, L. Schermelleh, SIMcheck: A toolbox for successful super-resolution structured illumination microscopy. *Sci. Rep.* **5**, 15915 (2015).
40. J.-B. Fiche, D. I. Cattoni, N. Diekmann, J. M. Langerak, C. Clerte, C. A. Royer, E. Margeat, T. Doan, M. Nöllmann, Recruitment, assembly, and molecular architecture of the SpoIIIE DNA pump revealed by superresolution microscopy. *PLOS Biol.* **11**, e1001557 (2013).
41. D. I. Cattoni, J.-B. Fiche, A. Valeri, T. Mignot, M. Nöllmann, Super-resolution imaging of bacteria in a microfluidics device. *PLOS ONE* **8**, e76268 (2013).

42. B. Schuettengruber, N. Oded Elkayam, T. Sexton, M. Entrevan, S. Stern, A. Thomas, E. Yaffe, H. Parrinello, A. Tanay, G. Cavalli, Cooperativity, specificity, and evolutionary stability of Polycomb targeting in *Drosophila*. *Cell Rep.* **9**, 219–233 (2014).
43. B. Zhang, P. G. Wolynes, Topology, structures, and energy landscapes of human chromosomes. *Proc. Natl. Acad. Sci. U.S.A.* **112**, 6062–6067 (2015).
44. S. Hayashi, Male-specific GFP marker strain of *Drosophila melanogaster*. *Dros. Inf. Serv.* **93**, 224–225 (2010).

Acknowledgments: We thank H. Hoang, B. Beliveau, M. Hannan, and C.-T. Wu for help in the design of Oligopaints and for the 3-Mb Oligopaint probe. We thank the Montpellier Resources Imagerie facility (BioCampus Montpellier, CNRS, INSERM, Université de Montpellier) for microscopy support, especially J. Mateos-Langerak for help in SIM and J. Cau and A. Sarrazin for image analysis. We thank MGX sequencing and *Drosophila* facilities (BioCampus Montpellier, CNRS, INSERM, Université de Montpellier). We thank the Genotoul bioinformatics facility Toulouse Midi-Pyrenees (Bioinfo Genotoul) for providing computing and storage resources. We thank B. de Massy for critical reading of the manuscript. **Funding:** Q.S. was supported by the French Ministry of Higher Education and Research. J.-M.C. was supported by the Taiwan Ministry of Science and Technology (MOST 105-2218-E-004-003 and MOST 106-2221-E-004-011-MY2). B.B. was supported by Sir Henry Wellcome Postdoctoral Fellowship WT100136MA. Research in the laboratory of M.N. is funded by the European Research Council (ERC) under the European Union's Horizon 2020 research and innovation programme (grant agreement no. 724429) and by France-BioImaging (ANR-10-INBS-04-01). Research in the laboratory of D.J. was supported by the CIMENT infrastructure (supported by the Rhône-Alpes region, grant CPER07 13 CIRA) for computing resources, the Agence Nationale de la Recherche (ANR-15-CE12-0006 EpiDevoMath), the Fondation pour la Recherche Médicale (DEI20151234396), and the CNRS. F.B. was supported by CNRS and the Fulbright Visiting Program of the French-American Commission. Research in the laboratory of G.C. was supported by grants from the ERC (ERC-2008-AdG No 232947), the CNRS, the FP7 European Network of Excellence EpiGeneSys, the European Union's Horizon 2020 research and innovation programme under grant agreement no. 676556 (MuG), the Agence Nationale de la Recherche (ANR-15-CE12-0006 EpiDevoMath), the Fondation pour la Recherche Médicale (DEI20151234396), the INSERM, the French National Cancer Institute (INCa), and the Laboratory of Excellence EpiGenMed. **Author contributions:** Q.S., F.B., and G.C. initiated and led the project. Q.S. and F.B. designed Oligopaint probes. Q.S. produced FISH probes and performed FISH experiments, 3D-SIM and confocal microscopy acquisition, and image analysis. Q.S. performed Hi-C experiments in S2R+ cells. D.J. performed polymer modeling and analysis. J.-M.C. performed Hi-C bioinformatics analysis. D.I.C., J.G., and M.N. performed dSTORM imaging and analysis. B.B. and G.L.P. provided help analyzing Hi-C. T.S. and C.J. performed WT and *ph* null mutant embryo Hi-C experiments. F.B. performed fly handling. Q.S., F.B., and G.C. interpreted the data. Q.S., F.B., T.S., and G.C. wrote the paper. All the authors reviewed and discussed the data. **Competing interests:** The authors declare that they have no competing interests. **Data and materials availability:** All data needed to evaluate the conclusions in the paper are present in the paper and/or the Supplementary Materials. Additional data related to this paper may be requested from the authors.

Submitted 19 December 2017
Accepted 30 January 2018
Published 28 February 2018
10.1126/sciadv.aar8082

Citation: Q. Szabo, D. Jost, J.-M. Chang, D. I. Cattoni, G. L. Papadopoulos, B. Bonev, T. Sexton, J. Gurgo, C. Jacquier, M. Nollmann, F. Bantignies, G. Cavalli, TADs are 3D structural units of higher-order chromosome organization in *Drosophila*. *Sci. Adv.* **4**, eaar8082 (2018).

Science Advances

AAAS

advances.sciencemag.org/cgi/content/full/4/2/eaar8082/DC1

Supplementary Materials for

TADs are 3D structural units of higher-order chromosome organization in *Drosophila*

Quentin Szabo, Daniel Jost, Jia-Ming Chang, Diego I. Cattoni, Giorgio L. Papadopoulos, Boyan Bonev, Tom Sexton, Julian Gurgo, Caroline Jacquier, Marcelo Nollmann, Frédéric Bantignies, Giacomo Cavalli

Published 28 February 2018, *Sci. Adv.* **4**, eaar8082 (2018)
DOI: 10.1126/sciadv.aar8082

This PDF file includes:

Supplementary Materials

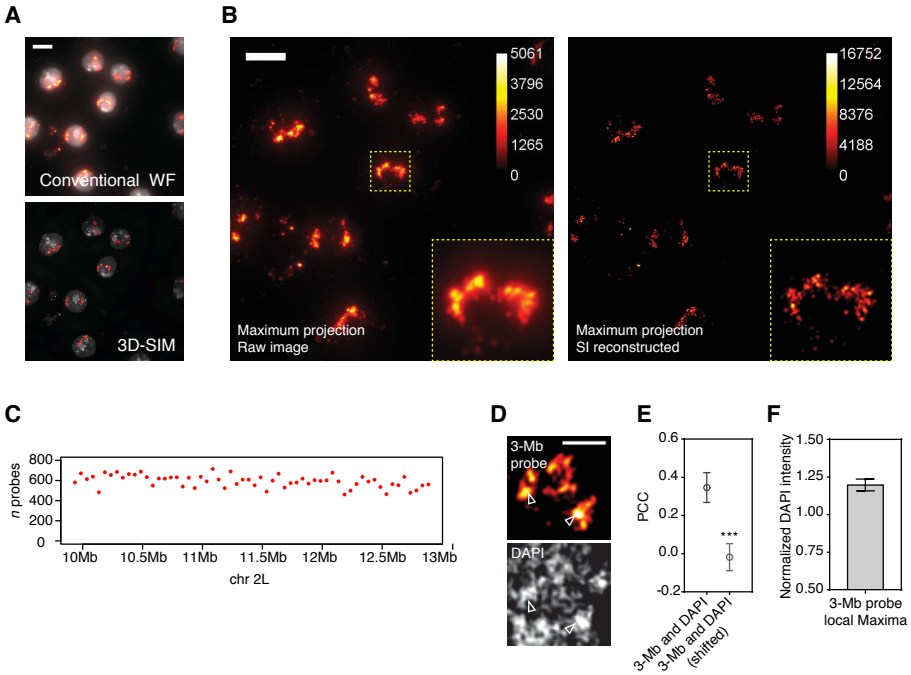

fig. S1. Chromatin nanostructure visualization with 3D-SIM imaging. (**A**) Example of conventional WF and 3D-SIM reconstructed image of DAPI (gray) and 3 Mb probe labeling in S2R+ nuclei. Scale bar: 5 µm. (**B**) Raw image and structured illumination (SI) reconstructed image of the 3 Mb probe shown in (**A**). Scale bars: 5 µm. (**C**) The 3 Mb region is homogenously covered by a mean of 11.85 oligonucleotide probes per kb. Graph shows probe numbers in 50 kb bins along the 3 Mb region. (**D**) 3 Mb probe (top) and DAPI (bottom) 3D-SIM imaging in an S2R+ nucleus (single *z*-slices). Arrowheads indicate dense compartments for both labels. Scale bar: 1 µm. (**E**) Pearson's correlation coefficient (PCC, mean ± SD) between 3 Mb probe signal and DAPI, before or after DAPI channel shift (3 voxels in *x*/*y*/*z*). *** corresponds to *p*-value <0.0001 using Wilcoxon matched-pairs signed rank test, 20 nuclei were analyzed. (**F**) DAPI intensity (mean ± SD) of the 3 Mb probe local maxima, normalized to the mean DAPI intensity of the 3D segmented 3 Mb probe. Ratios were calculated per image (7 images/55 nuclei in total).

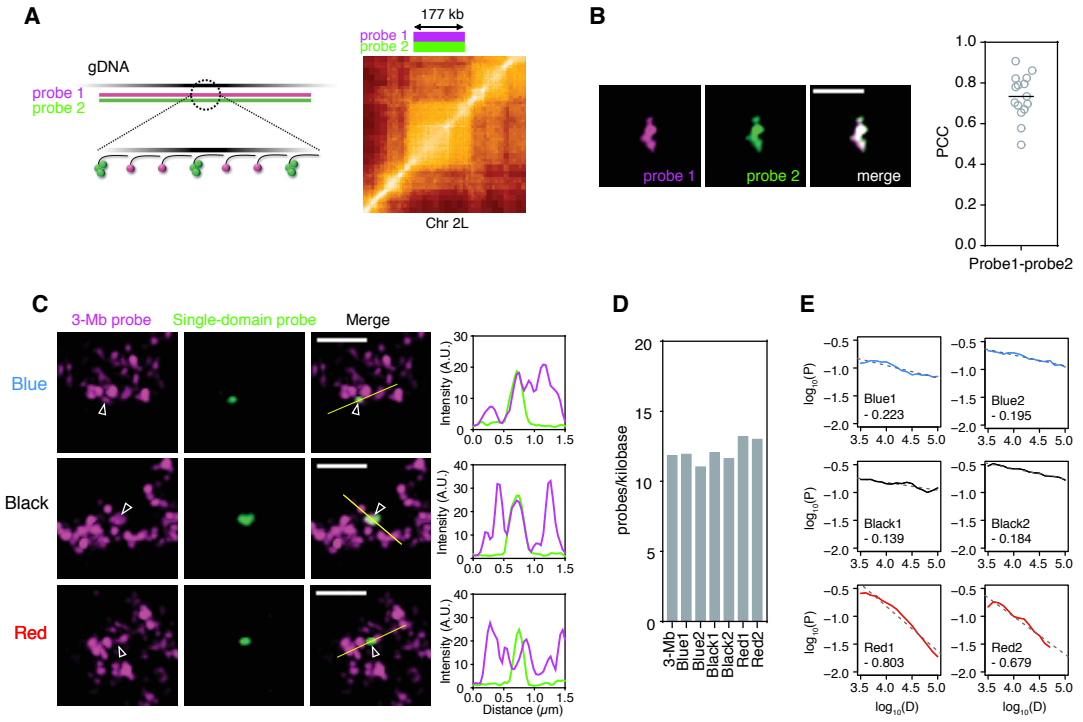

fig. S2. Dual labeling Oligopaint FISH. (**A**) Schematic representation of the dual FISH labeling. Probe 2 (green) has an oligonucleotide coverage of 1/3 of probe 1 (magenta), and is added in molar excess compared to probe 1 (at least 3:1 ratio), allowing efficient co-labeling of the same region. The probe 2 signal is increased using complementary secondary oligonucleotides carrying 2 additional fluorophores. On the right, Hi-C map around a single TAD (Black1), labeled with the two sets of probes. (**B**) Double labeled Black1 TAD (maximum projection). On the right, PCC between probe 1 and probe 2 intensities. 15 nuclei were analyzed, the black line indicates the mean. (**C**) Examples of dual FISH labeling (maximum projections) with the 3 Mb probe and single epigenetic domains (Blue2, Black1 or Red2, indicated with arrowheads). Right panel: intensity distributions of the two probes along the yellow line. (**D**) Average Oligopaint coverage of the 3 Mb probe in the whole region and in specific epigenetic domains targeted with single domain probes. (**E**) Cis-decay curves (contact probability as a function of genomic distance) within the single domains calculated in S2R+ Hi-C. On bottom left of the plots, the slope of fitted linear regression (dashed gray lines) are indicated. Scale bars: 1 µm.

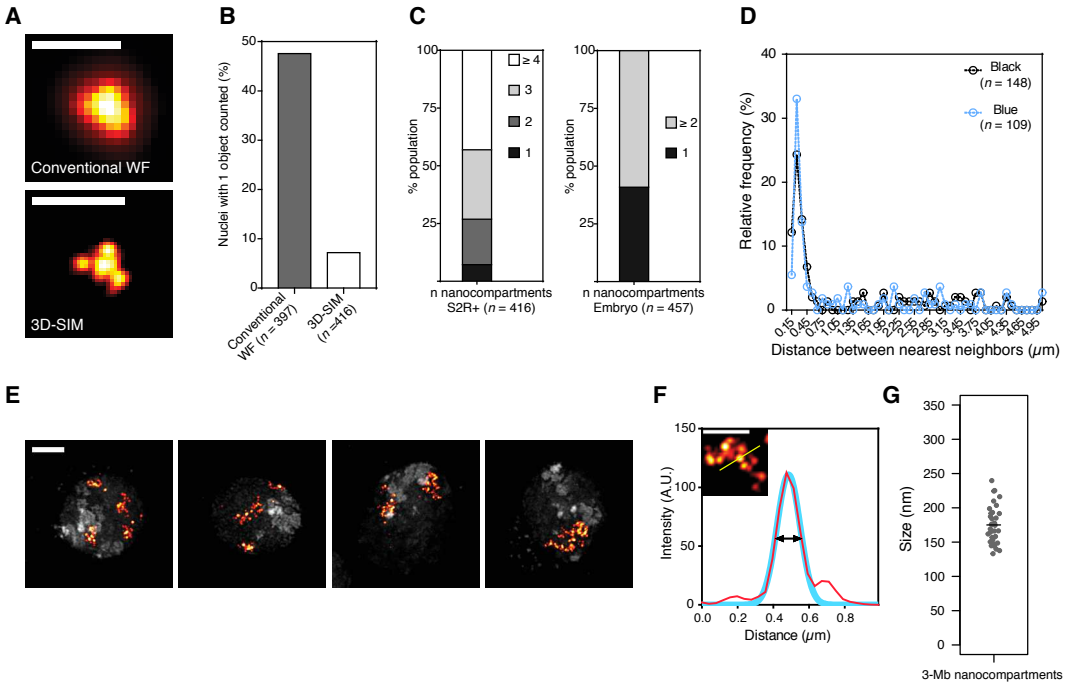

fig. S3. Resolution of homologous TADs with 3D-SIM. (**A**) Images of a single TAD (Blue1) in conventional microscopy (top) and after 3D-SIM reconstruction (bottom) in an S2R+ cell. Maximum projections, scale bars: 1 µm. (**B**) Percentages of nuclei with only one foci resolved in conventional WF microscopy or 3D-SIM (merge of Blue1 and Black1 FISH experiments). *n* represents the number of nuclei analyzed in each condition. (**C**) Distributions of resolved nano-compartment counts per nucleus in S2R+ and embryonic cells (merge of Blue1 and Black1 FISH experiments) with 3D-SIM. *n* represents the number of nuclei analyzed in each condition. (**D**) Histogram of distance distribution between nearest neighbor nano-compartments observed in Black1 and Blue1 single-TAD FISH experiments. The *X*-axis is split into 50 nm bins (last bin represents distances > 5 µm); *n* represents the number of distances measured from G1-staged S2R+ cell populations (37 and 58 nuclei for Blue1 and Black1, respectively; see fig. S5 for cell-cycle staging), to avoid measuring distances between sister chromatids. (**E**) Examples of S2R+ nuclei (DAPI in gray) labelled with the 3 Mb probe displaying different pairing states. From left to right: the four chromosomes unpaired, two chromosomes paired and two unpaired, two chromosomes paired twice, all chromosomes paired. Maximum projections, scale bar: 2 µm. (**F**) Intensity distribution (in red) along the line drawn in the image (single copy of the 3 Mb probe, maximum projection), with a Gaussian fitted curve (in blue). Arrow represents the full width at half maximum (FWHM). Scale bar: 1 µm. (**G**) FWHM-calculated diameters (black line indicates mean) of the nano-compartments observed in the 3 Mb probe (*n*=35).

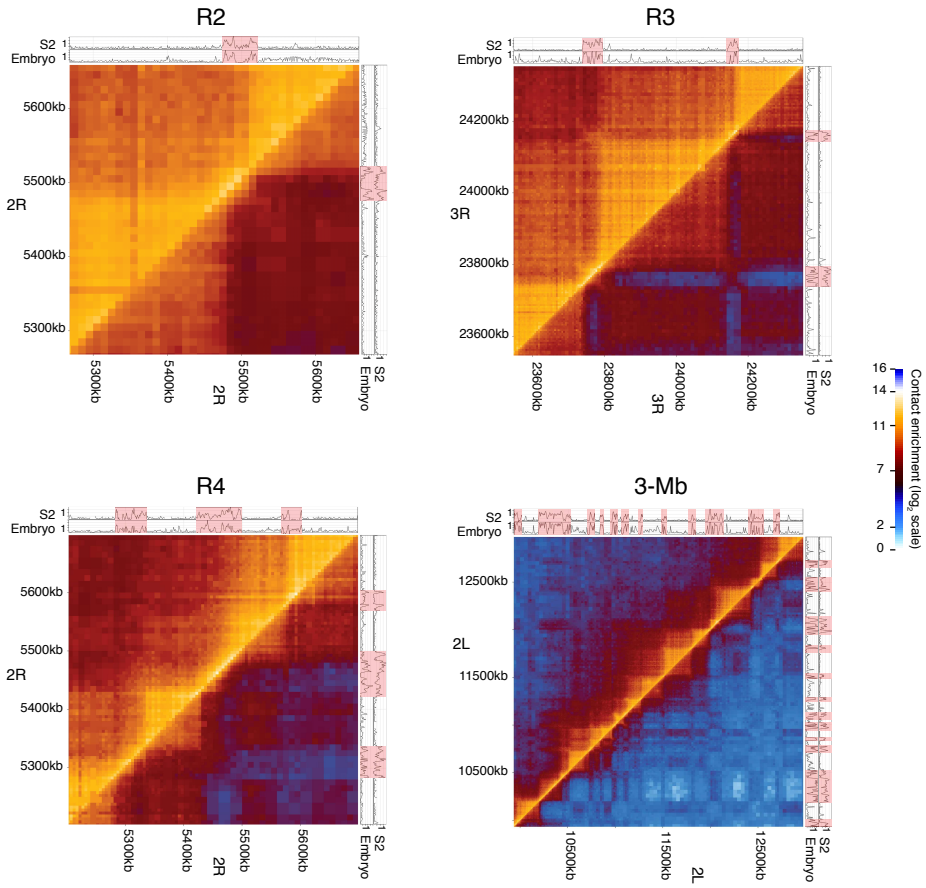

fig. S4. Oligopaint probe–targeted regions in S2R+ cells and embryos. Hi-C maps of Oligopaint labeled regions in S2R+ cells (top of the diagonal) and 16-18 hr embryos (bottom), showing conservation of the TADs. H3K4me3 ChIP profiles in both S2 cells and 14-16 hr embryos are also shown, allowing identification of repressed TADs. We counted 2, 3, 4 and 12 repressed TADs for R2, R3, R4 and the 3 Mb region, respectively.

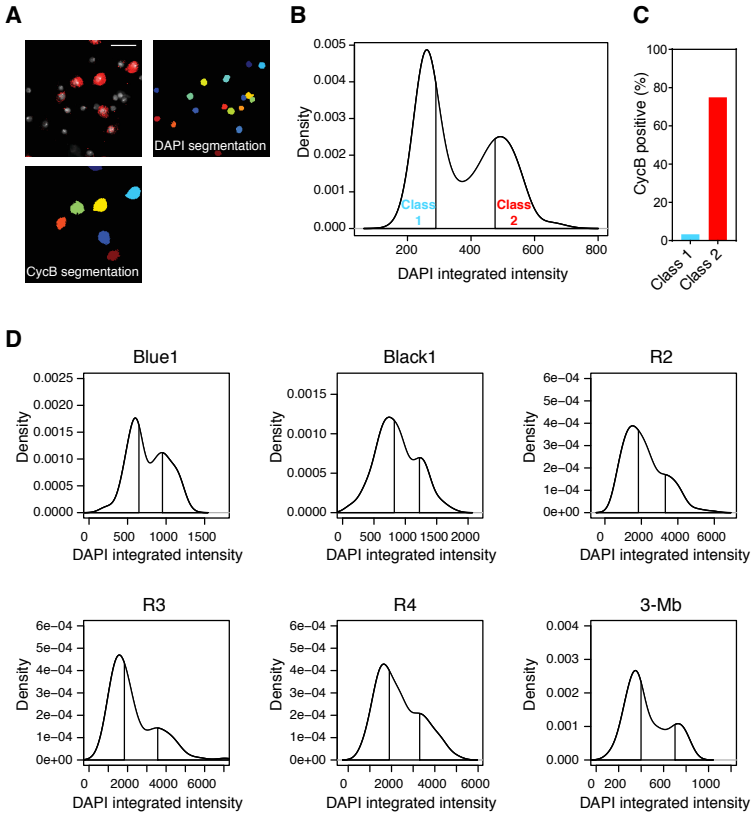

fig. S5. Cell cycle staging of S2R+ cells. (**A**) Confocal image S2R+ cells labeled with DAPI (in gray) and Cyclin-B (CycB, in red), and their 2D segmentation (individual segmented objects are represented with colored surfaces). Average projection, scale bar: 20 µm. (**B**) DAPI integrated intensity distribution of the S2R+ nuclei population labeled with CycB ($n = 414$). The DAPI integrated intensity reflecting the amount of DNA per nucleus (*29*), we obtained a profile of the cell cycle with G1 (class 1 of the distribution) and G2 (class 2 of the distribution) cells. (**C**) Percentage of nuclei positive for CycB segmentation in class 1 and class 2 of the distribution in (**B**), showing the efficiency of the cell cycle staging method. (**D**) DAPI integrated intensity distributions obtained in FISH experiments for Black1, Blue1, R2, R3, R4 and the 3 Mb probes (254, 213, 180, 136, 166 and 156 nuclei, respectively). Based on the DAPI integrated intensity distribution, we considered as G1 nuclei in left parts of the plots and as G2 nuclei in right part of the plots (delimitated by vertical lines).

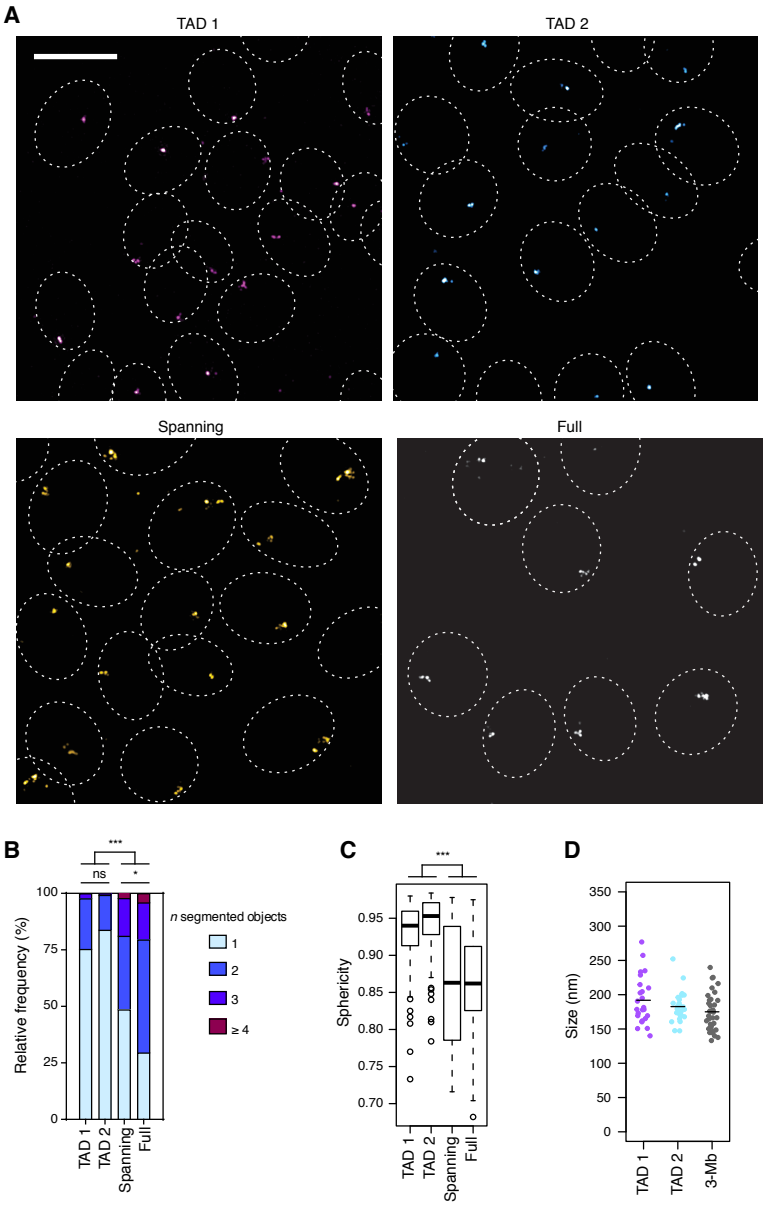

fig. S6. Super-resolution imaging of haploid chromatin folding. (A) 3D-SIM images of the TAD 1, TAD 2, Spanning and Full probes. Dashed lines indicate DAPI contours. Maximum projections, scale bar: 5µm. (**B**) Quantification of the number of segmented objects per nucleus (at least 122 nuclei per condition, analysis in maximum *z*-projected images). (**C**) Sphericity scores of the 3D-segmented probes (at least 68 nuclei per condition). (**D**) FWHM-calculated diameters (black lines indicate means) of TAD 1 (*n*=25), TAD 2 (*n*=25), and of nano-compartments observed in the 3 Mb probe (*n*=35). Statistics were performed with Kruskal-Wallis and Dunn's multiple comparisons tests, *** indicates *p*-value < 0.0001, * indicates *p*-value < 0.05).

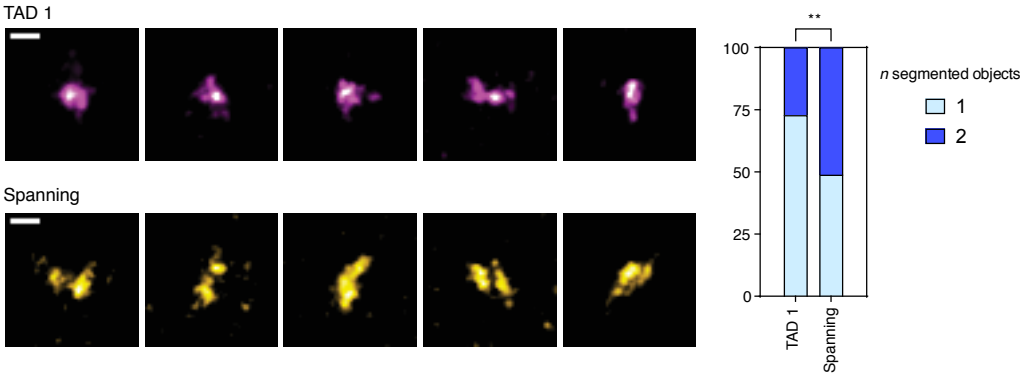

fig. S7. 2D dSTORM imaging of TAD 1 and spanning probes. On the left, representative examples of dSTORM imaging of TAD 1 and Spanning probes, both having the same genomic size. Scale bars: 250 nm. On the right, quantification of the number of segmented objects per nucleus (at least 55 nuclei per condition). ** indicates *p*-value < 0.01 using two-tailed Fisher's exact test.

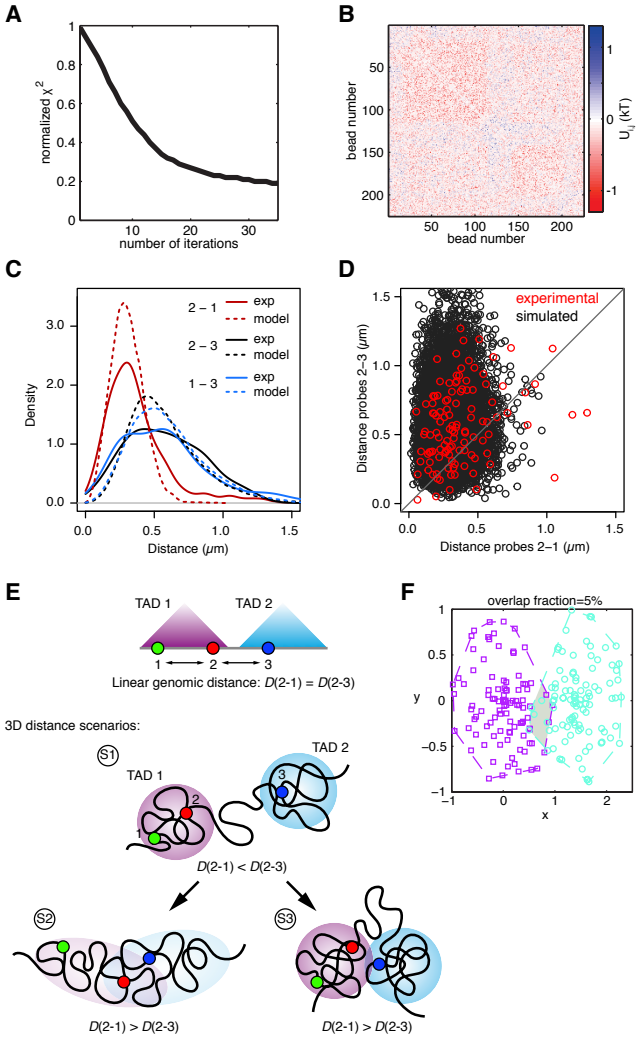

fig. S8. Modeling the X chromatin region. (**A**) Evolution of the normalized score χ^2 as a function of the number of iterations of the inference scheme, for an interaction radius *R=143* nm. (**B**) Corresponding inferred monomer-monomer interactions $\{U_{i,j}\}$. (**C**) 3D distances distributions between the probes 1, 2 and 3 from FISH experiment (full lines) and inferred model (dashed lines). (**D**) Scatter plot of paired distances between probe 2 and probe 1 (*X*-axis) versus probe 2 and probe 3 (*Y*-axis) from FISH experiments (red) and inferred model (gray). (**E**) Schematic representations of 3D chromatin structure scenarios that might explain FISH experiments with equidistant probes used here. Scenario 1 (S1) represents conformations where the intra-TAD (2-1) physical distance is shorter than the inter-TAD (2-3), consistent with the formation of an individual nano-compartment for each TAD. When the intra-TAD distance is larger than the inter-TAD one, we envisaged two different scenarios: in scenario 2 (S2) the shorter inter-TAD distance is due to intermingling between TADs and loss of individual TAD nano-compartments, while in scenario 3 (S3), this is due to a change of relative spatial positioning of the TADs with maintenance of two separated nano-compartments corresponding to each of the TADs. (**F**) Illustration of the computation of the overlap fraction in 2D between two ensembles of points (symbols). Dashed lines represents the convex envelopes of each ensemble (purple and blue for TAD 1 and TAD 2, respectively). The overlap fraction quantifies the proportion of points that belongs to the intersection between the two envelopes (gray area).

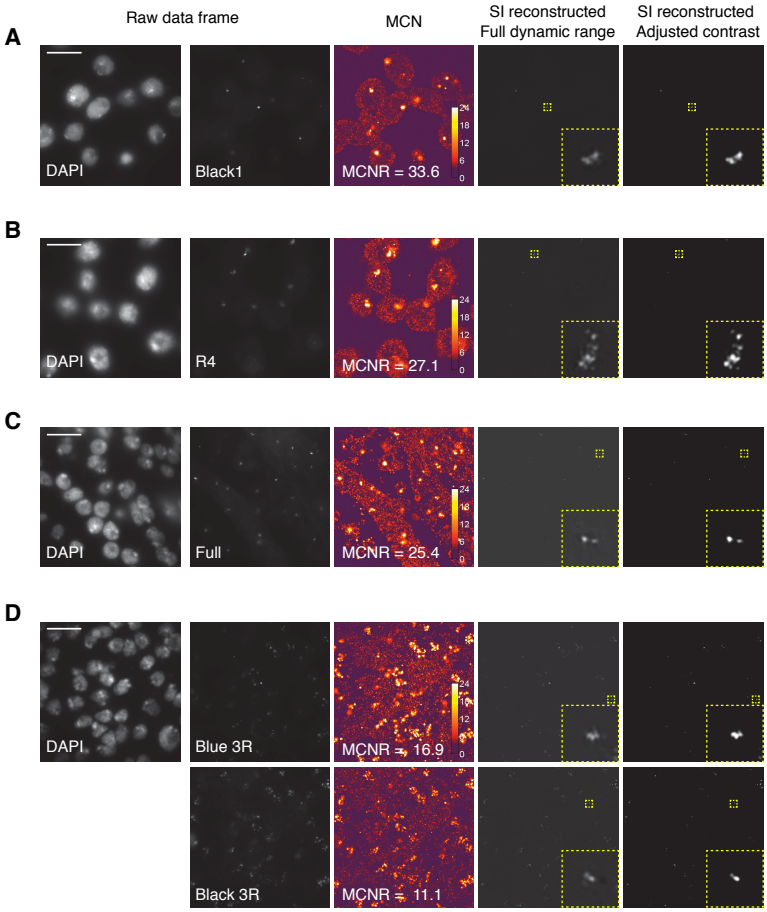

fig. S9. Quality control of SI acquisitions. (A-D) Examples of images and SI reconstruction outputs of FISH signals: Black1 FISH (Cy3 dye) in S2R+ cells; R4 (Atto-565 dye) FISH in S2R+ cells; Full (Atto-565 dye) FISH in embryonic cells, Blue 3R (Cy3 dye) and Black 3R (Alexa-488 dye) FISH in embryonic cells. From left to right: single frame of raw image; modulation contrast to noise (MCN) output from SIMcheck (*39*) plugin of ImageJ with average modulation contrast to noise ratio (MCNR) value (4-8 low to moderate, 8-12 good, > 12 good-excellent); reconstructed images with full dynamic range (from 32-bit data); reconstructed images with adjusted contrast after *Threshold and 16-bit Conversion* (SIMcheck) processing. Single *z*-slices, scale bars: 10 µm.

table S1. Libraries for Oligopaint probes. Coordinates, genomic sizes, number of probes and coverage of the Oligopaint probes. Library code refers to the primers used to amplify libraries (see Material and Methods). Probe names in italic refer to the epigenetic state specific probes used in Fig. 5: B for Blue; Bk for Black; R for Red.

Name	Chr	5' coordinates	3' coordinates	Genomic size (bp)	Number of probes	Density probes/kb	Library Code
3-Mb	2L	9935314	12973080	3037766	36001	11,85	-
Blue1	2L	11317986	11468388	150402	1797	11,95	B
Blue2	2L	12564906	12685026	120120	1326	11,04	C
Black1	2L	10540472	10717954	177482	2140	12,06	B
Black2	2L	11547196	11783436	236240	2748	11,63	C
Red1	2L	10203092	10436611	233519	3085	13,21	B
Red2	2L	12690712	12739196	48484	631	13,01	D
Blue1 1:3	2L	11317986	11468388	150402	599	3,98	B
Blue2 1:3	2L	12564906	12685026	120120	442	3,68	C
Black1 1:3	2L	10540472	10717954	177482	713	4,02	C
Black2 1:3	2L	11547196	11783436	236240	916	3,88	D
Red1 1:3	2L	10203092	10436611	233519	1028	4,40	D
Red2 1:3	2L	12690712	12739196	48484	210	4,34	E
R2	2R	10534240	10729120	194880	2353	12,07	A
R3	3R	23547420	24352723	805303	9681	12,02	A
R4	2R	5203174	5698315	495141	6124	12,37	B
Full	X	4602500	4961200	358700	3905	10,89	A
TAD1	X	4602500	4800500	198000	2211	11,17	B
TAD2	X	4851500	4961200	109700	1174	10,70	C
Spanning	X	4727000	4925000	198000	2164	10,93	D
B1	3R	652785	713391	60606	780	12,87	A
B2	3R	2496062	2870013	373951	4226	11,30	A
B3	3R	3960876	4035090	74214	851	11,47	A
B4	3R	6342956	6500513	157557	1815	11,52	A
B5	3R	7155430	7204894	49464	599	12,11	A
B6	3R	8066650	8143013	76363	1006	13,17	A
B7	3R	9675674	9769418	93744	1163	12,41	A
B8	3R	12199694	12252379	52685	605	11,48	A
B9	3R	12488250	12800730	312480	3526	11,28	A
Bk1	3R	2295136	2461552	166416	2002	12,03	A
Bk2	3R	3388064	3520312	132248	1620	12,25	A
Bk3	3R	4204574	4332372	127798	1512	11,83	A
Bk4	3R	6006587	6076245	69658	770	11,05	A
Bk5	3R	6734612	6947878	213266	2425	11,37	A
Bk6	3R	7950439	8030369	79930	1012	12,66	A
Bk7	3R	8556860	8764131	207271	2337	11,28	A
Bk8	3R	9304896	9449352	144456	1646	11,39	A
Bk9	3R	9966695	10042715	76020	798	10,50	A
Bk10	3R	10740256	10895936	155680	1848	11,87	A
Bk11	3R	11523771	11601926	78155	865	11,07	A
Bk12	3R	12989300	13190808	201508	2434	12,08	A
R1	3R	2176766	2217786	41020	547	13,33	A
R2	3R	2890321	2929421	39100	487	12,46	B
R3	3R	3825350	3863180	37830	545	14,41	A
R4	3R	4832892	4891933	59041	794	13,45	B
R5	3R	5567252	5631767	64515	955	14,80	A
R6	3R	6675854	6719646	43792	589	13,45	B
R7	3R	7027809	7070005	42196	588	13,93	A
R8	3R	7407477	7481767	74290	1005	13,53	B
R9	3R	8222335	8291151	68816	928	13,49	A
R10	3R	8809823	8857134	47311	643	13,59	B
R11	3R	9464906	9524338	59432	758	12,75	A
R12	3R	10112285	10152845	40560	525	12,94	B
R13	3R	11144574	11199314	54740	830	15,16	A
R14	3R	12257868	12296968	39100	547	13,99	B
R15	3R	12862169	12906743	44574	544	12,20	A

2.2 Super-resolution microscopy reveals principles of chromatin folding underlying TAD formation in mammals

Quentin Szabo, Axelle Donjon, Ivana Jerković, Giorgio L Papadopoulos, Boyan Bonev, Frédéric Bantignies, Giacomo Cavalli

2.2.1 Abstract

Chromosome conformation capture studies revealed the partitioning of genomes into topologically associating domains (TADs) that are proposed to spatially define functional regulatory landscapes. Deciphering the physical nature of TADs is therefore crucial to understand their relationship with gene regulation. Here we characterized the structural organization of the chromatin fiber underlying TADs in single cells using super-resolution microscopy. We observed that TAD structures, ranging from condensed and globular objects to dispersed and extended conformations, emerge from the heterogeneous assembly of smaller nanodomains. Yet, the physical intermingling of the chromatin is highly favored within TADs compared to adjacent TADs in a large majority of cells. This TAD-dependent spatial chromatin organization is enhanced during cell differentiation and abolished upon removal of CCCTC-binding factor. These results demonstrate that dynamic TAD organizations are associated with the establishment of chromosomal environments in which contacts are privileged, and thus reconcile the probabilistic nature of chromatin folding with the proposed role of TADs in the spatial regulation of DNA-dependent processes.

2.2.2 Introduction

A better understanding of the three-dimensional (3D) organization of the genome is important to apprehend the mechanisms underlying its regulation. Chromosome conformation capture methods such as Hi-C (Lieberman et al., 2009) provided crucial information on the principles governing higher-order genome organization, including chromatin loops (Rao et al., 2014), large-scale folding into mutually excluded compartments of interactions (Lieberman et al., 2009), and domains enriched in internal contacts, the so-called topologically associating domains [TADs (Nora et al., 2012; Dixon et al., 2012; Sexton et al., 2012; Hou et al., 2012)]. TADs have been identified in many species, indicating that they represent a fundamental layer of higher-order chromosome organization, yet their various features and structural properties suggest different types of TADs (Szabo et al., 2019). In mammals, TADs were proposed to delimit regulatory landscapes in which functional interactions between genes and cis-regulatory elements such as enhancers are confined. Consistently, genes within the same TADs tend to be co-regulated during cell-differentiation (Nora et al., 2012; Zhan et al., 2017). Many

chromosomal rearrangements or TAD border deletions that lead to structural remodeling and fusion of adjacent domains were shown to induce *de novo* contacts between genes and enhancers used to be insulated from each other, which can result in gene misregulation that are associated with developmental diseases and cancer (Lupiáñez et al., 2015; Franke et al., 2016; Hsieh et al., 2016; Spielmann et al., 2018). These studies shed light on the role of TADs in gene regulation. In mammals, most TADs are defined by the binding of the CCCTC-binding factor (CTCF) in a convergent manner at their borders and by the action of the cohesin complex (Rowley and Corces, 2018). The loop-extrusion model, supported by several studies, proposes that the chromatin fiber is continuously extruded by the cohesin complex until it dissociates or reaches TAD borders occupied by CTCF, implying a dynamic mechanism of TAD formation (Sanborn et al., 2015; Fudenberg et al., 2016; Nora et al., 2017; Schwarzer et al., 2017; Rao et al., 2017; Haarhuis et al., 2017; Gassler et al., 2017). Consistently, single-cell Hi-C studies revealed highly heterogenous chromatin contacts, suggesting that TADs reflect probabilistic preferential interactions rather than stable higher-order chromosomal domains (Nagano et al., 2013; Stevens et al., 2017; Flyamer et al., 2017). However, the correspondence of scattered pair-wise interactions captured by single-cell Hi-C to integrated 3D organization of full chromosomal domains remains challenging, and our comprehension of TAD folding in individual cells has been mostly inferred from modeling (Stevens et al., 2017; Giorgetti et al., 2014). A direct characterization of their full structure is however still missing. Complementary to Hi-C data, microscopy approaches appeared powerful to apprehend chromatin organization (Boettiger et al., 2016; Wang et al., 2016; Cattoni et al., 2017; Nir et al., 2018; Szabo et al., 2018; Finn et al., 2019; Mateo et al., 2019). Notably, TAD-like structures that preferentially segregate at CTCF borders were recently observed (Bintu et al., 2018). Here, we used a combination of Hi-C, Oligopaint technology and super-resolution microscopy to address the specific organization of the chromatin fiber into TADs.

2.2.3 Results

Super-resolution microscopy reveals the structure of TADs in single cells

To investigate the structure of TADs in individual cells, we combined fluorescent in-situ hybridization (FISH) with Oligopaint and super-resolution 3D-structured illumination microscopy [3D-SIM (Gustafsson et al., 2008; Markaki et al., 2012; Demmerle et al., 2017)] to image at a sub-diffraction resolution a large number of chromosomal loci in mouse embryonic stem cells [ESCs (Figure S1)]. We designed Oligopaint probes to cover 10 entire TADs located in 5 different chromosomes, and used super-resolution imaging to characterize their structural features such as volumes and shapes that cannot be assessed with conventional microscopy (Figure S2A-S2E). Visual inspection of individual TAD structures revealed a high degree of cell-to-cell variability (Figure 1A, 1B, S2A and S2B). By calculating the volume, the sphericity score and the principal axis length of each imaged TAD, we observed that

their structural organization range from condensed and globular objects to stretched and decondensed conformations (Figure 1C and S2F). We next investigated the relationship between the folding of the chromatin fiber and its underlying epigenetic state. In addition to the 10 probes covering entire TADs, our Oligopaint design included 16 additional probes that labeled TAD subregions (Figure S1). We applied unsupervised hierarchical clustering to separate these 26 genomic regions into transcriptionally active or inactive using previously published chromatin immuno-precipitation sequencing (ChIP-seq) of histone post-translational modifications (PTMs), RNA-sequencing (RNA-seq) and ATAC-sequencing (ATAC-seq) data (Figure 1D). We observed that repressed chromatin regions were more condensed than active ones (Figure 1E). Interestingly, we calculated a moderate yet significant correlation between the degree of chromatin condensation and the normalized Hi-C contacts within regions labeled by the probes [Pearson's correlation coefficients $\rho = 0.52$; $P < 0.01$ (Figure S2G)]. Moreover, TADs rarely form homogeneous objects but rather often display internal substructures (Figure 1B and S2B). To separate contiguous regions within segmented probes, we applied watershed segmentation and observed that TADs emerge from miscellaneous assembly of smaller subdomains of a few hundreds of nanometers (Figure 1F-1H). This is consistent with previous super-resolution imaging which described the organization of the chromatin fiber into compact nanodomains estimated to be smaller than TADs (Nozaki et al., 2017). This also indicates that the folding of such large regions of hundreds of kilobases into one, large and homogeneous chromosomal structure is relatively rare and instead, TADs tend to fold into smaller chromatin nanodomains. Relative to their genomic size, active regions fold into more subdomains compared to the repressed ones (Figure 1I and S2H). These subdomains may emerge from simultaneous processes of loop extrusion by the action of cohesin. They may also reflect a general property of the chromatin fiber which would fold into higher order nanodomains up to a critical genomic size. Hence, our super-resolution imaging data has allowed the characterization of the dynamic nature of TADs in individual cells, revealing their various shapes and volumes that notably depend on their chromatin states.

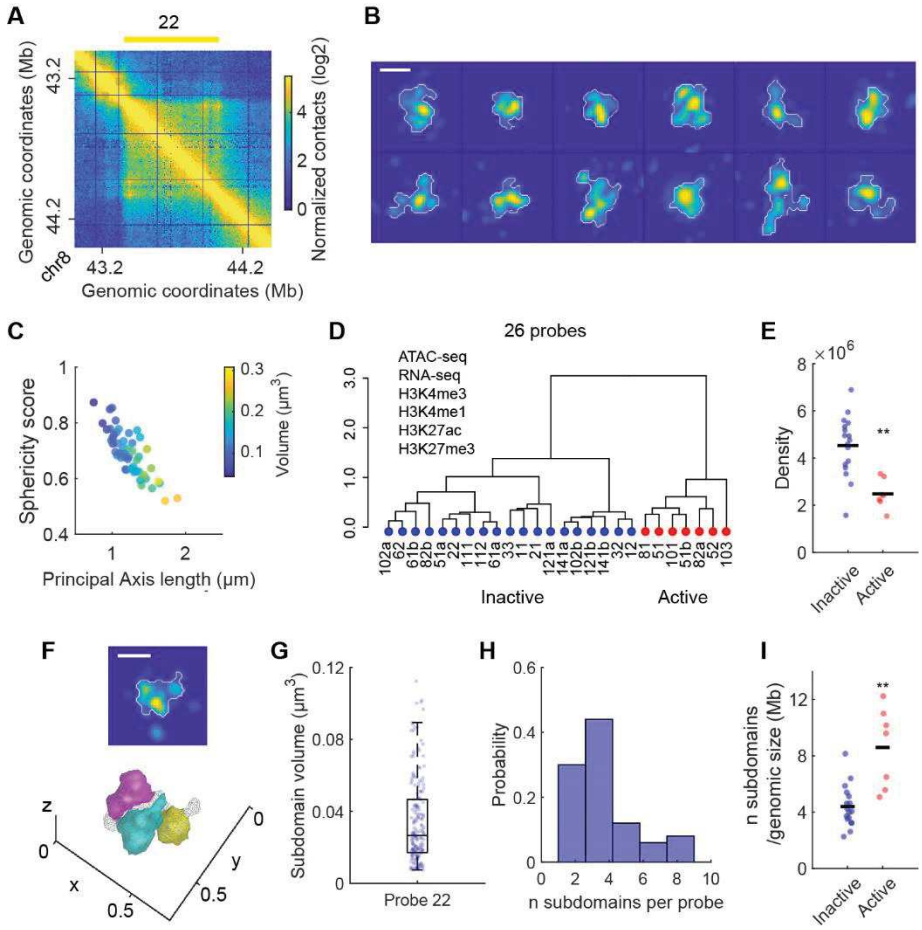

Figure 1. Super-resolution microscopy reveals the structure of TADs in single cells. (**A**) Hi-C map from ESCs along with the location of a FISH probe used to label a TAD. (**B**) 3D-SIM images of individual TADs (maximum projections) labeled with the probe show in (A). White lines represent the boundaries of their maximum-projected segmentations. (**C**) Sphericity score as a function of the principal axis length for each individual TAD labeled with the probe shown in (A). Color-code indicates the volume of TADs. $n = 50$. (**D**) Hierarchical clustering of the 26 loci labeled by our probes (Figure S1) using ATAC-seq, RNA-seq and ChIP-seq of the indicated histone PTMs. (**E**) Density (genomic size divided by mean volume) of the loci labeled by the probes. Black line indicates mean. A mean of 47 alleles was analyzed per probe. (**F**) Top: 3D-SIM image of an individual TAD as in (B). Bottom: 3D view of the segmented TAD (gray mesh) and watershed segmented subdomains (colored objects). Axes indicate coordinates in µm. (**G**) Volumes of the subdomains measured within the segmented TADs labeled by the probe shown in (A). $n = 181$. (**H**) Distribution of the number of subdomains identified per individual TAD labeled by the probe shown in (A). $n = 50$. (**I**) Mean number of subdomains per probe divided by the genomic size of the locus (in Mb). Black line indicates mean. A mean of 48 alleles was analyzed per probe. Scale bars: 500 nm. Statistics were done using Wilcoxon rank sum test, ** $P < 0.01$.

Chromatin intermingling is highly favored within TADs in most individual cells

Next, we wanted to address whether the observed heterogeneity in TAD folding is compatible with the partitioning of the chromatin fiber into physically insulated domains. We used pairs of differently labeled probes located within individual TAD or in two adjacent TADs and compared the degree of intermingling and the physical distances between probes (Figure 2A). The imaging of one probe simultaneously labeled in 2 colors indicated the precision of our approach [median 3D distance between the centroids of the two segmented colors = 34 nm (Figure S3A and S3B)]. The visualization of a pair of probes, either located within a TAD or separated by a border, confirmed the dynamic organization of the chromatin fiber (Figure 2A and 2B). Nevertheless, the quantification of the 3D overlap fractions (OF, defined by the Jaccard Index, i.e. the intersection volume of the probes divided by their union volume) revealed a striking difference between the intermingling of probes located within a TAD (median OF = 0.21; 17% of the cell population displaying an OF < 0.1) compared to the ones situated in adjacent TADs [median OF = 0.06; 64% of the cell population displaying an OF < 0.1 (Figure 2C)]. These results revealed that in a large majority of single cells the intermingling of the chromatin is much higher within TAD compared to adjacent TADs. While interactions between probes separated by a border are regularly detected, the OFs between these probes rarely equal those calculated within the TAD, suggesting that border violation often corresponds to limited inter-TAD contacts rather than their merge. The calculation of 3D distances between probe centroids provided a complementary analysis to the OF measurements. Despite very similar genomic distance between probe centers (245 kb versus 275 kb), much shorter 3D distance distribution was observed for probes within TAD compared to probes between TADs (median distance of 185 nm versus 349 nm), thus reflecting the constrained arrangement of the chromatin fiber within TADs (Figure 2D). Generation of averaged pictures from all individual super-resolution structures reflected well the differential spatial organizations of probes, with those within TAD appearing to belong to the same unit while those between TADs being clearly physically separated (Figure 2A). We then investigated whether the results obtained with this locus reflect the general physical organization of TADs in single cells. We used a total of 15 pairs of probes that were similarly designed to locate either within individual TADs or between two adjacent TADs (Figure 2E and S1). For all tested pairs and despite variable genomic size among regions, we systematically measured higher OFs and shorter 3D distances within TADs (Figure 2F, 2G and S3C-E), suggesting that chromatin intermingling depends on TAD structure rather than on genomic distance. While the relative broad distributions of both OF and 3D distances reflects the probabilistic nature of chromatin folding, the substantial differences of the intermingling for probes within or between TADs indicate that in most individual nuclei, the chromatin fold in a TAD-dependent manner. Moreover, chromatin mixing and distance distributions also vary for probes within or between TADs, indicating that TAD structures and degree of insulations don't represent a constant level of organization but rather vary along the genome, consistent with previous Hi-C observations (Zhan et al., 2017). To further examine the

relationship between Hi-C and super-resolution imaging, we calculated an Hi-C enrichment score for each locus labeled by a pair of probes, defined as the Hi-C contacts measured between the labeled regions normalized by the contacts measured in the entire locus (Figure S3F), reasoning that this score may reflect the degree of chromatin intermingling. The Hi-C enrichment score was very well correlated with the OF [$\rho = 0.88$; $P < 0.001$ (Figure 2H)], and inversely correlated with the mean physical distances between probe centroids [$\rho = -0.85$; $P < 0.001$ (Figure 2H)]. These high correlations indicate a strong relationship between Hi-C contacts and the 3D distance and the level of mixing of chromatin loci. Thus, super-resolution imaging quantitatively captures the spectrum of the different strengths of contacts and insulations measured by Hi-C. Altogether, these data indicate that a dynamic TAD organization is compatible with the generation of domains in which chromatin contacts are highly favored at the single-cell level.

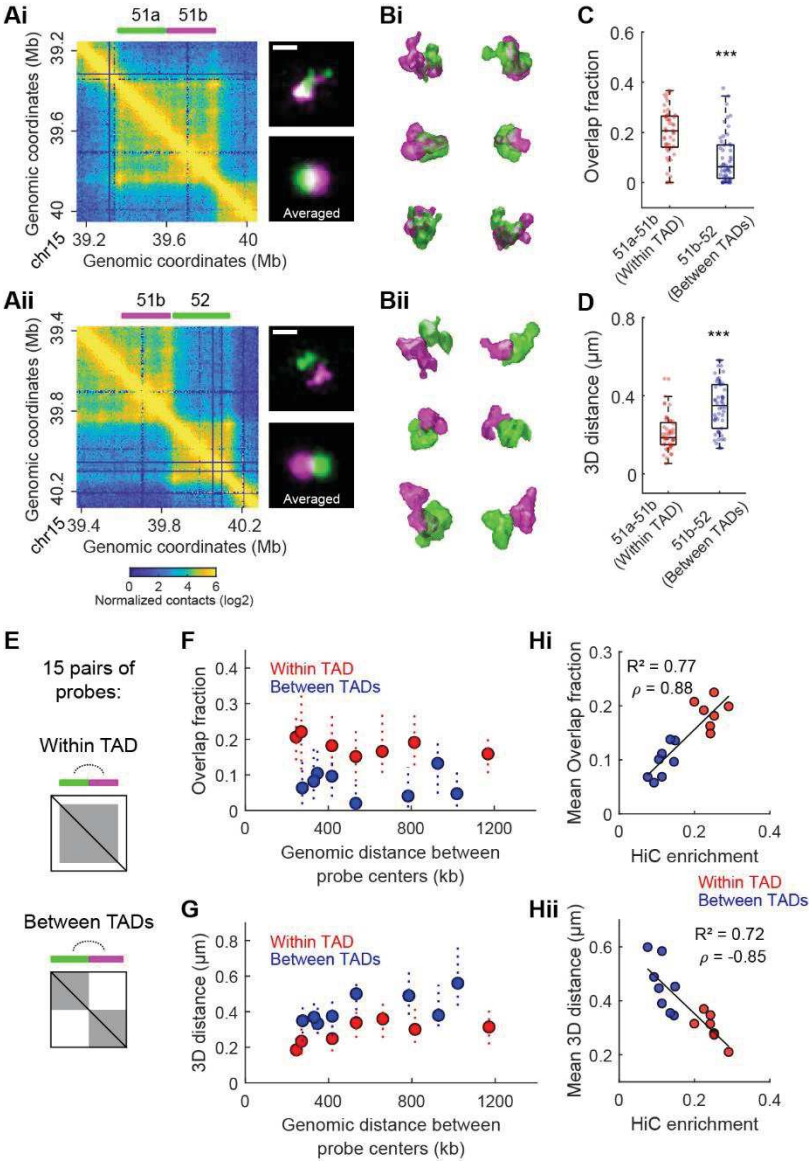

Figure 2. Chromatin intermingling is highly favored within TADs in most individual cells. (**A**) Left: Hi-C maps from ESCs along with the location of probes located either within a TAD (Ai) or between two adjacent TADs (Aii). Right: representative 3D-SIM images of the probes and averaged 3D-SIM images generated from all segmented pairs of probes ($n = 48$ and 50 for the pair 51a-51b and 51b-52, respectively). Scale bars: 500 nm. (**B**) 3D-view of the segmented pairs of probes shown in (A), located within the TAD (Bi) or between the adjacent TADs (Bii). (**C**) OFs between the probes shown in (A). $n = 48$ and 50 for the pair 51a-51b and 51b-52, respectively. (**D**) 3D distances between the centroids of the probes shown in (A). $n = 48$ and 50 for the pair 51a-51b and 51b-52, respectively. (**E**) Representation

of the experimental design used to label individual TADs or adjacent TADs. (**F**) OFs measured for each pair of probes as a function of the genomic distance separating their centers. Graph represents medians and interquartile ranges. A mean of 44 alleles was analyzed per pair of probes. (**G**) 3D distances between centroids measured for each pair of probes as a function of the genomic distance separating their centers. Graph represents medians and interquartile ranges. A mean of 44 alleles was analyzed per pair of probes. (**H**) Hi-C enrichment as a function of the mean OF (Hi) or the mean 3D distance between centroids (Hii) measured for each pair of probes (color-coded whether they were located within one TAD or between adjacent TADs) along with the goodness of fit of a linear regression and the Pearson's correlation coefficient ρ. Statistics were done using Wilcoxon rank sum test, *** $P <$ 0.001.

Neuronal differentiation is associated with chromatin condensation and restrictive TAD organization

ES cells have an open and flexible chromatin organization that may associate with more dynamic TAD structures compared to differentiated cells (Bonev et al., 2017; Barrington et al., 2019). To address this question, we used an in vitro differentiation system to generate neural progenitor cells (NPCs) from cultured ESCs [Figure 3A (Gaspard et al., 2009)]. We were able to study chromatin folding in a pure population of NPCs by combining FISH with an immunostaining of the Pax6 neuronal transcription factor (Figure S4A). Using our set of 26 probes, we first observed a global chromatin condensation in NPCs compared to ESCs (Figure 3B). We again clustered the regions labeled by these probes into transcriptionally inactive or active using ChIP-seq of histones PTMs, RNA-seq and ATAC-seq data from NPCs (Figure S4B). Consistently with our observations in ESCs, active regions were more decondensed and folded into more subdomains relatively to their genomic size compared to the inactive regions (Figure S4C-S4E). Here again, we observed a correlation between the condensation of loci and their amount of normalized Hi-C contacts [$\rho = 0.67$; $P < 0.001$ (Figure S4F)]. We next applied our 2-color imaging approach to characterize the organization of TADs in NPCs (Figure S1). OFs were systematically higher and physical distances shorter between probes located within individual TADs versus between TADs (Figure 3C, 3D and S4G-S4I). Moreover, Hi-C enrichment scores measured in NPCs were also remarkably well correlated with the OF [$\rho = 0.96$; $P < 0.001$ (Figure 3E)], and very well inversely correlated with the mean physical distances between probe centroids [$\rho = -0.94$; $P < 0.001$ (Figure 3E)]. Moreover, differences in chromatin intermingling within or between TADs appeared to be exacerbated in NPCs compared to ESCs. To better characterize this difference between these two cell types, we calculated the ratio of the mean OF for all probes falling within TAD over the mean OF for probes between TADs (hereafter defined as within/between TADs OF ratio) and obtained values of 1.94 and 2.60 in ESCs and NPCs, respectively, indicating a stronger spatial segregation of TADs in NPCs (Figure 3F). We then used this cell differentiation system to study regions that are structurally rewired, such as distinct TADs in ESCs merging into one in NPCs [pairs of probes 21-22, 32-33, 101-103 (Figure

S1)]. These probes, considered as between TADs in ESCs, appeared then as within TADs in NPCs (Figure 3C and 3D). One such example is represented by the *zfp42* locus, where the border between two TADs in ESCs associated with high expression of the *zfp42* gene becomes abolished in NPCs with the repression of the gene (Figure 3G). The abolition of the border corresponds to a fusion of the two genomic regions into a larger domain with higher degree of intermingling [ESCs versus NPCs, median OFs = 0.04 and 0.19, respectively; median 3D distances between centroids = 490 and 295 nm, respectively (Figure 3H-3J)]. Importantly, a similar structural organization of this locus was observed *in vivo* in NPCs from mouse neocortex (ncxNPCs) cryosections [median OF = 0.15; median 3D distance between centroids = 356 nm (Figure 3H-3J)]. We also investigated the reverse situation where an internal border was formed at the transcription start site of the activated *zfp608* gene in NPCs (Figure S4J). In this case, no significant changes were observed with both OF and physical distance parameters (Figure S4K and S4L). Consistently, Hi-C contact enrichment between the regions labeled by the probes were similar between the different cell types (Figure S4M). These results therefore suggest an internal rewiring of contacts within the TAD instead of a split into two different distinct physically insulated domains. Thus, *de novo* insulation associated with gene activation during cell differentiation can appear in pre-existing TAD structures. TADs may represent important structural bases established in ESCs that will help to spatially organize gene regulation through differentiation.

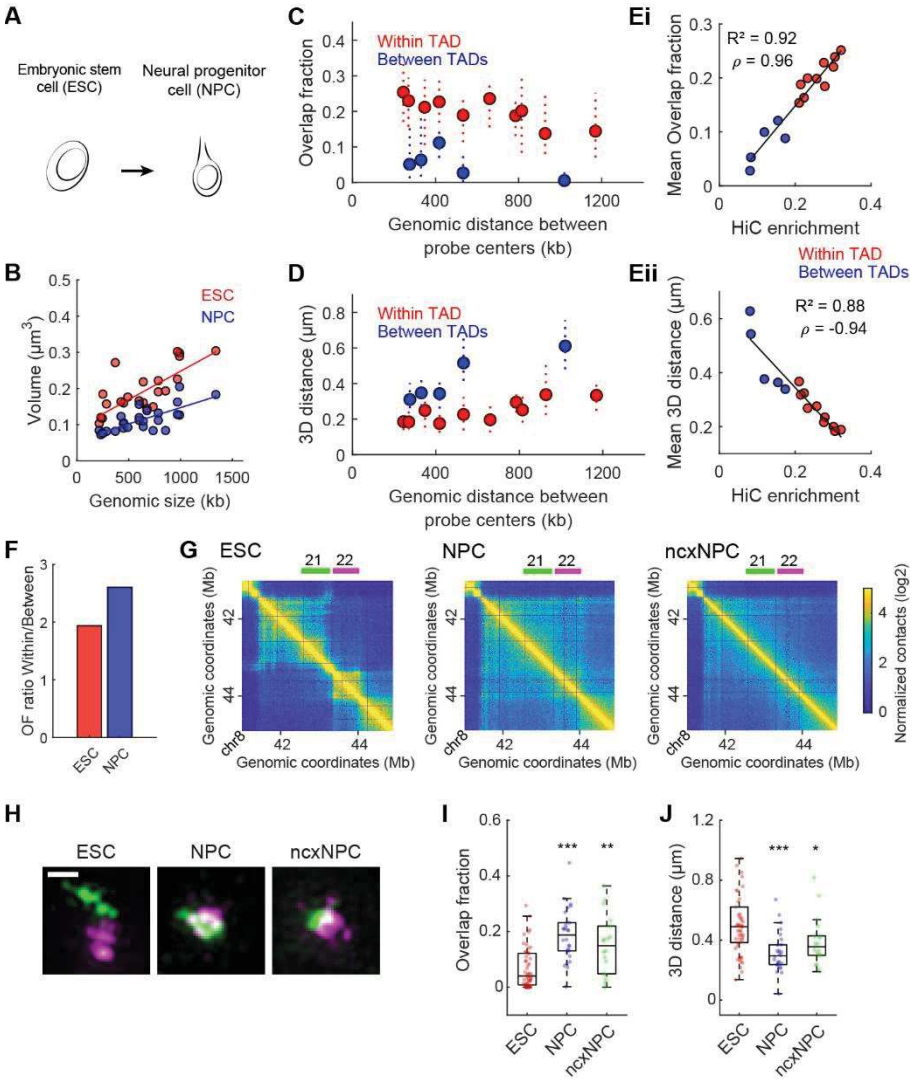

Figure 3. Neuronal differentiation is associated with chromatin condensation and restrictive TAD organization. (**A**) We used an in vitro differentiation system to generate NPCs from ESCs (Gaspard et al., 2009). (**B**) Mean volumes of the individual probes as a function of their genomic size in both ESCs and NPCs. A mean of 47 and 45 alleles was analyzed per probe in ESCs and NPCs, respectively. (**C**) OFs measured for each pair of probes as a function of the genomic distance separating their centers. Graph represents medians and interquartile ranges. A mean of 36 alleles was analyzed per pair of probes. (**D**) 3D distances between centroids measured for each pair of probes as a function of the genomic distance separating their centers. Graph represents medians and interquartile ranges. A mean of 36 alleles was analyzed per pair of probes. (**E**) Hi-C enrichment as a function of the mean OF (Ei) or the mean 3D distance between centroids (Eii) measured for each pair of probes (color-coded whether they were located within one TAD or between adjacent TADs) along with the goodness of fit of a linear regression and the Pearson's correlation coefficient ρ. (**F**) Mean OF measured from all pairs of probes within TADs divided by the mean OF from all pairs of probes between TADs. (**G**) Hi-C maps in ESCs, NPCs, and ncxNPCs along with the location of a pair of probes. (**H**) Representative 3D-SIM images of the probes shown in (G). Maximum projections, scale bar: 500 nm. (**I**) OFs between the probes shown in (G). n = 50, 26 and 18 for ESCs, NPCs, and ncxNPCs, respectively. (**J**) 3D distances between the centroids of the probes shown in (G). n =

50, 26 and 18 for ESCs, NPCs, and ncxNPCs, respectively. Statistics were done using Wilcoxon rank sum test, *** $P < 0.001$, ** $P < 0.01$, * $P < 0.05$.

Preferential chromatin intermingling within TADs is abolished upon CTCF depletion.

Our results indicate that TADs provide spatial environments in which chromatin intermingling is highly favored at the single-cell level. Previous Hi-C study revealed that the removal of CTCF abolishes the loops between CTCF binding sites at TAD borders and reduces insulation between TADs (Nora et al., 2017). We thus investigated the physical organization of TADs in individual cells that underlies the changes observed in Hi-C. In such way, we used the transgenic mouse embryonic stem cell line (referred to as CTCF-AID) developed in (Nora et al., 2017) in which the endogenous CTCF is tagged by an Auxin-Induced degradation (AID) motif that permits its proteasome-dependent degradation in the presence of auxin. We performed FISH and super-resolution imaging in untreated CTCF-AID cells and after 2 days in presence of auxin (Figure 4A). CTCF protein completely disappeared under auxin treatment (Figure S5A). CTCF removal did not induce obvious changes in nuclear morphology and did not significantly affect the degree of chromatin condensation or the folding into subdomains (Figure S5B-S5E). However, the TAD-dependent differences in chromatin intermingling were totally abolished (Figure 4B-4F). Indeed, the OFs and the 3D distances between probe centroids were very similar whether the probes were located within or between TADs defined in ESCs (Figure 4E and 4F). This effect was clearly illustrated by the within/between TADs OF ratio which equaled to 1.01, indicating that the folding dependent to TADs was completely disrupted (Figure 4G). We noticed that the differences in intermingling for probes within TADs or adjacent TADs in CTCF-AID untreated cells were not as strong as in ESCs [within/between TADs OF ratio = 1.58 and 1.94 in CTCF-AID and in ESCs, respectively (Figure 4G and 3F)]. This is presumably due to the previously reported 2- to 3- fold decrease of CTCF level in CTCF-AID untreated compared to wild-type cells (Nora et al., 2017). Finally, by comparing OFs and 3D distances in CTCF-AID untreated and treated cells, we observed a general tendency for an increase of intermingling for probes between TADs together with a decrease of intermingling for probes within TADs (Figure S5F and S5G). These results indicate that the abolition of TAD border not only induces ectopic intermingling between previously insulated regions but also leads to a reduction of interactions within TADs. Therefore, our imaging data provide additional insights into the architectural role of CTCF, which is crucial for the generation of spatially defined domains enriched in chromatin intermingling.

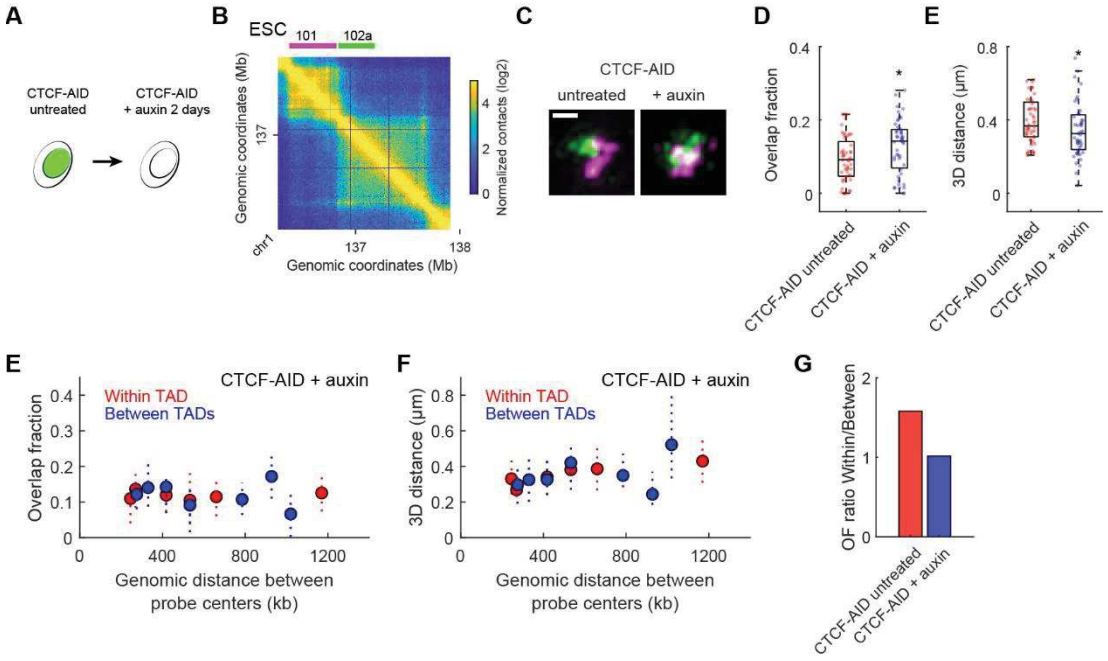

Figure 4. Preferential chromatin intermingling within TADs is abolished upon CTCF depletion. (**A**) We depleted endogenous CTCF using the CTCF-AID cell line (Nora et al., 2017). (**B**) Hi-C map from ESCs along with the location of FISH probes located in two adjacent TADs. (**C**) Representative 3D-SIM images of the probes shown in (B). Maximum projections, scale bar: 500 nm. (**D**) OFs between the probes shown in (B). (**E**) 3D distances between the centroids of the probes shown in (B). (**F**) OFs measured for each pair of probes as a function of the genomic distance separating their centers in CTCF-AID cells incubated with auxin for 2 days. Graph represents medians and interquartile ranges. (**G**) 3D distances between centroids measured for each pair of probes as a function of the genomic distance separating their centers in CTCF-AID cells incubated with auxin for 2 days. Graph represents medians and interquartile ranges. (**H**) Mean OF measured from all pairs of probes within TADs divided by the mean OF from all pairs of probes between TADs. Statistics were done using Wilcoxon rank sum test, * $P < 0.05$.

2.3.4 Discussion

By applying super-resolution microscopy to image many loci in in mouse cells, we were able to characterize the folding of the chromatin in single cells that underlies TAD formation. We observed a high degree of heterogeneity in their shapes and volumes, and such variability is then compatible with a dynamic mechanism of formation such as proposed by loop extrusion (Sanborn et al., 2015; Fudenberg et al., 2016). Our characterization of the folding of TADs into smaller subdomains is consistent with previous data revealing non-zero probabilities for physical insulations located at any genomic position outside CTCF borders in individual cells (Bintu et al., 2018). Likewise, the fact that such small domains are not clearly discernible in the Hi-C maps of the investigated regions suggests that they don't have preferential genomic borders. Subdomains are still present in the absence of CTCF which indicates that their formation is independent of this protein. These nanodomains may reflect the presence of multiple

processive loops encompassing few hundreds of kilobases formed by distinct cohesin complexes simultaneously loaded to the chromatin. They may also arise from intrinsic properties of the polymer nature of the chromatin fiber. Besides the structure of TADs, we also addressed how they spatially segregate from each other. These two characteristics may not necessarily be related and have proved difficult to integrate. For example, we previously reported the partitioning of the chromatin fiber into discrete structural units that correspond to TADs in *Drosophila* (Szabo et al., 2018). Multiplexed chromatin interaction profiles further revealed that they emerge from heterogeneous yet cooperative and high frequency contacts (Zheng et al., 2019), indicating that the formation of stable chromosomal patterns can arise from multiple and miscellaneous interactions. Importantly in this species, the correspondence of TADs to the alternation of chromatin states may indicate that *Drosophila* TAD organization emerges from the segregation of different chromatin states, a situation reminiscent to the formation of the A-B compartments in mammals (Lieberman et al., 2009; Sexton et al., 2012; Rowley et al., 2017). In mouse, the evidences for a loop extrusion mechanisms involved in TAD formation together with the fact that epigenetic states of the chromatin fiber don't accurately reflect their pattern (Rowley and Corces, 2018) interrogated whether the single-cell organization of the chromatin fiber into TADs is conserved in this species. Our imaging data revealed that mammalian TAD borders are not absolute and are commonly violated. Thus, physical borders are not constantly formed, in agreement with the dynamic binding of CTCF and cohesin on chromatin (Hansen et al., 2017). However, in most cells the chromatin intermingling within TADs is highly favored compared to adjacent TADs. This suggests that chromatin mixing between neighboring TADs, even if not infrequent, may correspond to local mixing at their edges when the border is not formed or to discrete interactions, for example due to the relative spatial positioning of the two TADs. The structural organization of TADs is then highly compatible with their proposed role in regulating functional contacts between genes and cis-regulatory elements. Importantly, the spatial organization of the chromatin fiber that depends on TADs is reinforced in NPCs compared to ESCs, reflecting concomitant constrained of chromatin organization and cell fate. In this context, TAD pattern can be subjected to changes upon transcriptional changes such as merges or internal rewiring. The disruption of the TAD-dependent spatial organization of the chromatin fiber upon CTCF removal further demonstrates that CTCF acts as a physical barrier and highlights its crucial role to confine chromatin intermingling inside domains. Our imaging data also directly link interactions detected by Hi-C with the structural organization of the chromatin fiber, revealing a quantitative relationship between contact frequency and 3D distances and degree of physical intermingling between loci. Altogether, our data demonstrate that TADs detected by averaged-interaction profiles arise from the establishment of dynamic higher-order units that spatially constrain chromatin fiber and favor contact exchanges through the action of CTCF. These results thus reconcile the cell-to-cell heterogeneity and the probabilistic nature of chromatin folding with the formation of 3D environments that are likely involved in the regulation genome activity.

Author contributions

For this project, we designed and planned experiments with my thesis supervisors, Frédéric Bantignies and Giacomo Cavalli. I chose the location of FISH probes based on Hi-C data, and Frédéric Bantignies designed the corresponding oligo sequences for library production. I then produced FISH probes with the help of Axelle Donjon. I performed all the FISH experiments, and the related image acquisitions and analysis. Giorgio L. Papadopoulos analyzed sequencing data. Regarding the cell culture, Ivana Jerkovic, Axelle Donjon and I handled ESCs. In vitro differentiation was performed by Axelle Donjon and Ivana Jerkovic. The handling of the CTCF-AID cell line was carried out by Axelle Donjon, who also tested the efficiency of CTCF degradation under auxin treatment by Western Blot. Finally, the dissection of mice brains to obtain in vivo NPCs was done by Boyan Bonev.

2.3.5 Material and methods

Cell culture and tissue preparation

ESC (E14Tg2a cell line) were cultured on 0.1% gelatin (Sigma-Aldrich, Cat.N: G1890-100G) coated dishes in GMEM (Gibco, Cat.N: 21710025), supplemented with 15% FBS qualified serum, USA origin (Thermofisher Scientific, Cat.N: 6140079), 1 mM Glutamax (Thermofisher Scientific, Cat.N: 35050038), 0.1 mM MEM Non-Essential Amino Acids (Thermofisher Scientific, Cat.N: 11140035), 50 U Penicillin-Streptomycin (Gibco Cat.N: 15140122), 0.1 mM Sodium Pyruvate (Gibco, Cat.N: 11360070), 0.1 mM 2-Mercaptoethanol (Gibco Cat.N: 31350010), and 1000 U/ml LIF (Sigma-Aldrich, Cat.N: ESG1107). Media was changed every day and cells were passaged every two days using StemPro Accutase (Gibco, Cat.N: A11105-01).

CTCF-AID cells were cultured as previously described and induced as in (Nora et al., 2017). Briefly, 500 µM of Indole-3-Acetic Acid, sodium salt (Auxin analog, Cayman, Cat.N: 16954) was added in the media for either 2 hours, 4 hours, 1 day or 2 days for the western blot, or 2 days for the FISH experiments.

ESCs were differentiated into NPCs as described in (Gaspard et al., 2009) with the following changes. Cells were plated at low density ($2.5x10^5$ cells per 10 cm dish) on 0.1% gelatin-coated dishes in ES media. After 1 day, cells were cultured in DDM media (DMEM/F-12, GlutaMAX Supplement (Gibco, Cat.N: 31331-028), supplemented with 500 µg/ml BSA (Gibco, Cat.N: 15260-037), 0.1 mM MEM Non-Essential Amino Acids (Thermofisher Scientific, Cat.N: 11140035), 50 U Penicillin-Streptomycin (Gibco, Cat.N: 15140122), 1X N-2 Supplement (Gibco, Cat.N: 17502-048), 1 mM Sodium Pyruvate (Gibco, Cat.N: 11360070) and 0.1 mM 2-Mercaptoethanol (Gibco, Cat.N: 31350010)). From day 2 to day 10, media was changed every 2 days and cyclopamine (Millipore, Cat.N: 239803-1MG) was added in the media. After 12 days of differentiation, cells were dissociated with StemPro Accutase (Gibco, Cat.N: A11105-01) plated on 6 well plates previously coated with Poly-L-lysine (Sigma, Cat.N:

P2636)/Laminin (Sigma, Cat.N: 11243217001), and cultured in a 1:1 ratio with DDM and Neurobasal (Gibco, Cat.N: 21103049), supplemented with 1X B27 (without vitamin A, Gibco, Cat.N: 12587-010), 2 mM GlutaMAX Supplement (Gibco, Cat.N: 31331-028) and 50 U Penicillin-Streptomycin (Gibco, Cat.N: 15140122) for additional 2 days (D12+2) to obtain NPCs.

Brains from E14.5 embryos were dissected and fixed in 4% PFA overnight at 4°C. They were then cryopreserved for 24h at 4°C in a PBS-20% sucrose solution. After embedding in OCT and fast freezing in isopentane, brains were sectioned at 10 µm width on slides with a cryostat (Leica).

Oligopaint probe design and synthesis

Oligopaint libraries were constructed following the procedures described in (Beliveau et al., 2015); see the Oligopaints website (https://oligopaints.hms.harvard.edu) for further details. Libraries were ordered from CustomArray (Bothell, WA) in the 92K Oligo pool format. Coordinates (mm10), size, number, density of probes and primers used for libraries for libraries are given in Table S1.

Oligopaint libraries were discovered using the archive mm9 bed files or the mm10 "balance" bed files (Beliveau et al., 2018), which consist of 32 mer or 35-41-mer genomic sequences throughout the regions of interest, respectively. Bed files can be retrieved from the Oligopaints website (https://oligopaints.hms.harvard.edu). Each library contains a universal primer pair followed by a specific primer pair hooked to the genomic sequences (114-116 or 117-125 mers in total, respectively). Oligopaint libraries were produced by emulsion PCR amplification from oligonucleotide pools followed by a "two-step PCR" procedure and the lambda exonuclease method described in (Beliveau et al., 2015). The "two-step PCR" leads to secondary oligonucleotide-binding sites for signal amplification with a secondary oligonucleotide (Sec1 or Sec6) containing two additional fluorophores, each oligonucleotide carrying three fluorophores in total. Alexa-488 and ATTO-565 fluorophores were used for 2-color imaging (or ATTO-647 and ATTO-565 for CTCF-AID line). All oligonucleotides used for Oligopaint production were purchased from Integrated DNA Technologies (IDT, Leuven, Belgium). Oligonucleotide sequences (5' -> 3') used in this study are listed below.

Emulsion PCR with universal primers

Univ1-FWD	BB297-FWD	GACTGGTACTCGCGTGACTTG
Univ1-REV	BB299-REV	GTAGGGACACCTCTGGACTGG
Univ2-FWD	BB295-FWD	GCGTTAGGGTGCTTACGTCTG
Univ2-REV	BB296-REV	CACCTCCGTCTCTCACCTCTC

Two-step PCR with specific primers

PCR1 with FWD 5' phosphorylation and REV 53mer primers:

A BB82-FWD: /5Phos/GTATCGTGCAAGGGTGAATGC

SecX-BB278-REV: /SecX/GAGCAGTCACAGTCCAGAAGG

B BB81-FWD: /5Phos/ATCCTAGCCCATACGGCAATG

SecX-BB281-REV: /SecX/GGACATGGGTCAGGTAGGTTG

C BB287-FWD: CGCTCGGTCTCCGTTCGTCTC

SecX-BB288-REV: GGGCTAGGTACAGGGTTCAGC

D BB293-FWD: /5Phos/CCGAGTCTAGCGTCTCCTCTG

SecX-BB294-REV: /SecX/AACAGAGCCAGCCTCTACCTG

E BB298-FWD: /5Phos/CGTCAGTACAGGGTGTGATGC

SecX-BB187-REV: /SecX/TTGATCTTGACCCATCGAAGC

F BB295-FWD: /5Phos/GCGTTAGGGTGCTTACGTCTG

SecX-BB296-REV: /SecX/CACCTCCGTCTCTCACCTCTC

G BB84-FWD: /5Phos/5Phos/GATACGTTGGGAGGCAATGAG

SecX-BB83-REV: /SecX/ATCCTAACAATCCCGCTGAGG

H BB302-FWD: /5Phos/5Phos/CGCACTGAACCAGACTACCTG

SecX-BB303-REV: /SecX/GAGAGGCGAGGACACCTACAG

I BB193-FWD: /5Phos/TTGATCTCGCTGGATCGTTCT

SecX-BB280-REV: /SecX/GGGAGTAGGGTCCTTTGTGTG

J BB291-FWD: /5Phos/CAGGTCGAGCCCTGTAGTACG

SecX-BB292-REV: /SecX/CTAGGAGACAGCCTCGGACAC

K BB300-FWD: /5Phos/CCAGTGCTCGTGTGAGAAGTC

SecX-BB301-REV: /SecX/CTGCAGAGAAGAGGCAGGTTC

L AB01-FWD: /5Phos/TGCGTTCGGTCTCCGTCAAC

SecX-AB02-REV: /SecX/ATCGCGACGTGTGATGGAAC

M AB05-FWD: /5Phos/ACATACGCCTCGGGTTGGAC

SecX-AB06-REV: /SecX/GTGTCGCGTCGGCCAGAAAC

N AB07-FWD: /5Phos/CCCGATACGTCGTGGGATTC

SecX- AB08-REV: /SecX/CTCGGCGTCTTCCGACGATG

O AB10-FWD: /5Phos/TGGTTCGGATTGCGAGACTC

SecX-B AB11-REV: /SecX/CACGGCGGAGGGATAAGTTG

P AB12-FWD: /5Phos/TCGGCCCTTATCGGTAGCAG

SecX- AB13-REV: /SecX/CAACGCGCTCGTGTACAACG

R AB19-FWD: /5Phos/CATTCGCGCACGCTAATGTC

SecX- AB20-REV: /SecX/AGCGGCGTTCGACACCTTTG

S AB21-FWD: /5Phos/GAGGGCGGTGCGGTACTAAG

SecX- AB22-REV: /SecX/CCGTCAGGTCGACGCTACAC

T AB23-FWD: /5Phos/AGGAGCGTCCGCACCGAATG

SecX- AB24-REV: /SecX/CATTGGGTGCGATGACGAAC

SecX: Secondary Binding Sequences (Sec1BS and Sec6BS):

Sec1BS: CACCGACGTCGCATAGAACGGAAGAGCGTGTG

Sec6BS: CACACGCTCTCCGTCTTGGCCGTGGTCGATCA

PCR2 with the labeled REV 'back primer':

BB506-Alexa488 /5Alex488N/CACCGACGTCGCATAGAACGG

BB511-Cy3 /5Cy3/CACACGCTCTCCGTCTTGGC

Secondary Oligos carrying two fluorochromes

Sec1-Alexa488-X2:

/5Alex488N/CACACGCTCTTCCGTTCTATGCGACGTCGGTGagatgttt/3AlexF488N/

Sec1-ATTO647-X2:

/5ATTO647NN/CACACGCTCTTCCGTTCTATGCGACGTCGGTGagatgttt/3ATTO647NN/

Sec6-ATTO565-X2:

/5ATTO565N/TGATCGACCACGGCCAAGACGGAGAGCGTGTGagatgttt/3ATTO565N/

FISH

FISH was adapted from (Bantignies and Cavalli, 2014). Cells were grown directly on coverslips [170 ± 5 µm (Zeiss)]. After PBS wash, cells were fixed for 10 min in PBS/4% paraformaldehyde, rinsed in PBS, permeabilized for 10 min in PBS/0.5% Triton X-100, rinsed in PBS, incubated for 10 min in 0.1M HCl and rinsed in 2× SSC/0.1% Tween 20 (2×SSCT). Cells were then incubated for 20 min in 50% formamide/2×SSCT at room temperature and for 20 min 50% formamide/2×SSCT at 60°C. Probe mixtures contained Oligopaint probe at ~1-3 µM (final concentration) with the same amount of their secondary oligo and 0.8µL of RNase A in FISH hybridization buffer [FHB; 50% formamide, 10% dextran sulfate, 2× SSC, and salmon sperm DNA (0.5 mg/ml)] for a total volume of 15-25 µL. Probe mixtures were added directly to coverslips that were then sealed on glass slides with rubber cement (Fixogum, Marabu). Cell DNA was denaturated for 3 min at 80°C on a heating block immersed in a water bath, and probes were hybridized overnight at 42°C in a dark and humid chamber. Cells were then washed for 15 min in 2×SSCT at 60°C, 10 min in 2×SSCT at room temperature, 10 min in 0.2×SSC, and twice 5 min in PBS. For FISH in NPCs, the FISH protocol was followed by an immunostaining after this washing step (See Immunostaining procedure). Cells were then incubated with DAPI (final concentration at 1 µg/mL) and washed again three times for 5 min each in PBS. Coverslips were mounted on slides with Vectashield (CliniSciences) and sealed with nail polish.

Immunostaining

After the washes of the FISH procedure following the hybridization of the probes, cells were washed in PBS/0.1% Tween 20 (PBT) and incubated for 1 hour in PBT/2%BSA. Incubation with Pax6 antibody solution (Covance, Cat.N: PRB-278P-0100; 1:1000 dilution in PBT/2%BSA) was done overnight at 4°C between coverslips and glass slides in a humid and dark chamber. Cells were then rinsed in PBT and incubated with Alexa-647 labeled secondary antibody (Invitrogen, Cat.N: A31573; 1:200 dilution in PBT/2%BSA) for 1 hour at room temperature between coverslips and glass slides in a humid and dark chamber. Cells were then washed in PBT, incubated with DAPI (final concentration at 1 µg/mL) and washed again three times for 5 min each in PBS. Coverslips were mounted on slides with Vectashield (CliniSciences) and sealed with nail polish.

Image acquisition

3D-SIM imaging was performed with an OMX-V4 microscope equipped with a 100x/1.4 numerical aperture (NA) Plan Super Apochromat oil immersion objective (Olympus) and electron-multiplying charge-coupled device (EMCCD) (Evolve 512B, Photometrics) cameras for a pixel size of 79 nm (pixel size of reconstructed images = 39.5 nm). LASERs at 405, 488, 561 and 647 nm were used with the standard corresponding emission filters. Z-stacks were acquired using 125nm stepping, five phases and three angles. Raw images were reconstructed using SoftWorx (version 6.5, GE Healthcare) using channel-specific optical transfer functions. Quality of reconstructed images was assessed using the SIMcheck plugin of ImageJ (Ball Schermelleh 2015). Conventional wide-field images were generated from raw images by averaging angles and phases for each plane.

Image analysis

For 2-color FISH, raw super-resolution reconstructed channels were first aligned using Chromagnon software (Matsuda et al., 2018) using as reference files images of individual probes simultaneously labeled with the two corresponding fluorophores. Super-resolution reconstructed images were processed using the "Threshold and 16-bit conversion" utility of the SIMcheck plugin of ImageJ (Ball et al., 2015) and regions of interests (2.2 × 2.2 µm) surrounding FISH loci were extracted for further processing. Image analysis was conducted using MATLAB and its "image processing toolbox". Images were smoothed using 3D Gaussian filters ($\sigma = 0.5$). FISH probes were segmented in 3D using Otsu's method, and segmented objects smaller than 0.04 μm^3 (0.008 μm^3 for the small 5d2 probe) or in contact to the image border were discarded for further analysis. Segmented images were systematically verified by visual inspection. All quantitative analysis of volumes, densities, sphericities, principal axis lengths and subdomain numbers and sizes were done using probes labeled with the ATTO-565 fluorophore to avoid eventual differences coming from resolution. Volumes were calculated by multiplying the number of segmented voxels by the voxel volume. Densities were calculated by dividing the genomic size (in bp) of the probes by their mean volume. Principal axis lengths were calculated with the lengths of the major axes of ellipsoids that have the same normalized second central moments as the segmented probes. Sphericity scores ψ were calculated using the following formula: $\psi = \frac{\pi^{\frac{1}{3}}(6V)^{\frac{2}{3}}}{A}$ in which V is a volume of the segmented object and A is its surface area (a sphericity of 1 corresponds to a perfect sphere). For probe subdomain quantification, the watershed function (image processing toolbox) was applied to the complement of the scaled intensity values (0 to 1) within probes segmented in 3D using Otsu's method. Subdomain objects smaller than 0.0072 μm^3 were discarded for further analysis. OFs were calculated using Jaccard Index of the segmented probes labeled in different colors and 3D distances were calculated between their centroids. To generate averaged images, individual segmented probes of each channel

were first maximum projected along the axial direction and the 2D distance between their centroid was calculated. For each color, all the binary segmented images were centered using probe centroids and summed. Composite images were generated by shifting the two different channels along one axis using the mean 2D distance calculated between the centroids.

Hi-C analysis

Publicly available ESC, NPC and ncxNPC Hi-C data were downloaded from GEO database (GSE96107). Raw Hi-C interaction counts were computed using in-house R scripts using the "misha" package (https://github.com/msauria/misha-package). Hi-C enrichment scores were computed using raw mapped interactions. Juicer KN normalized data (Durand et al., 2016) were used for map visualization (5 kb resolution) and for correlations with probe densities.

Collection and alignment of ESC and NPC ChIP-seq, ATAC-seq and RNA-seq datasets

Publicly available ESC and NPC ChIP-Seq data for H3K4me1, H3K4me3, H3K27Ac and H3K27me3 marks, ATAC-Seq and RNA-Seq data used in this study are listed below. Raw ChIP-Seq and ATAC-Seq sequencing data were collected and aligned to the mm10 version of the mouse genome using bowtie 2 with default parameters [v2.1.0, (Langmead and Salzberg, 2012)]. Reads with low mapping quality (mapq<30) were discarded using samtools (Li et al., 2009). RPKM-normalized bigwig binary files were generated using the bamCoverage function from Deeptools2 [v2.5.1 (Ramirez et al., 2016)] with the following parameters: -of=bigwig --samFlagExclude 128 --ignoreDuplicates -e 200 –normalizeUsingRPKM. Finally, replicates were merged using the bigWigMerge and bedGraphToBigWig tools from UCSC (Kent et al., 2010) with default parameters. Raw RNA-Seq data were aligned to the mm10 reference genome using STAR version 2.5.0b. PCR duplicates were removed, and RPM normalized coverage tracks were produced using STAR in "inputAlignmentsFromBAM" runMode. All the produced BigWig files were imported into R using the misha framework and probe signal quantification was computed as global percentile.

Method	Tissue	Condition	GSE/Ref	Original Publication
ATAC-seq	ESC		GSE84646	Xu et al; 2017
ChIP-Seq	ESC	H3K4me3	ENCSR000CGO	ENCODE
ChIP-Seq	ESC	H3K4me1	ENCSR032JUI	ENCODE
ChIP-Seq	ESC	H3K27Ac	ENCSR000CGQ	ENCODE
ChIP-Seq	ESC	H3K27me3	ENCSR059MBO	ENCODE
ATAC-seq	NPC		GSE84646	Xu et al; 2017
ChIP-Seq	NPC	H3K4me3	GSE96107	Bonev et al., 2017
ChIP-Seq	NPC	H3K4me1	GSE74330	Kloet et al., 2016
ChIP-Seq	NPC	H3K27Ac	GSE96107	Bonev et al., 2017
ChIP-Seq	NPC	H3K27me3	GSE96107	Bonev et al., 2017
Hi-C	ESC		GSE96107	Bonev et al., 2017
Hi-C	NPC		GSE96107	Bonev et al., 2017
Hi-C	ncxNPC		GSE96107	Bonev et al., 2017
RNA-Seq	ESC		GSE96107	Bonev et al., 2017
RNA-Seq	NPC		GSE96107	Bonev et al., 2017

2.3.6 Supplementary material

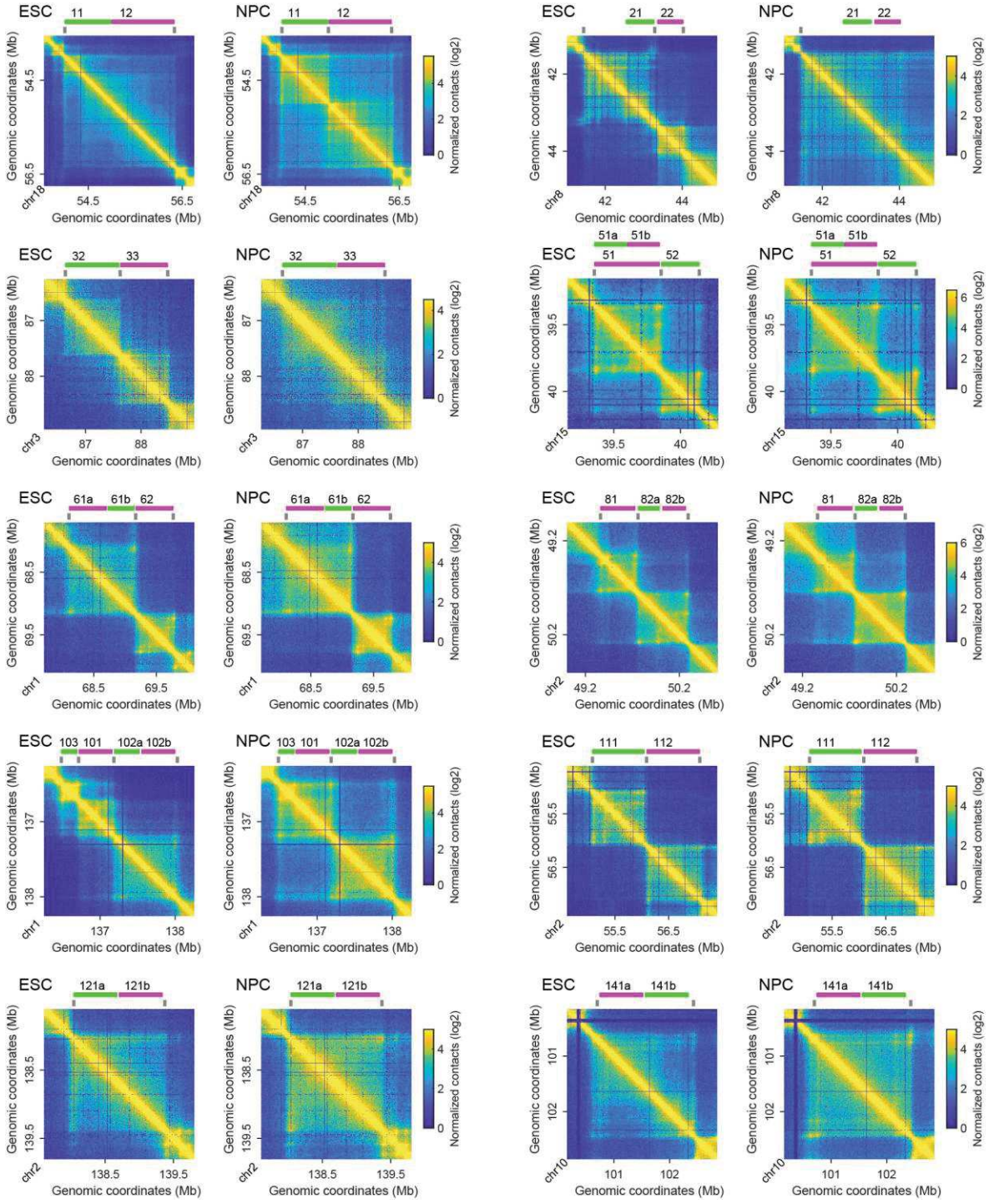

Figure S1. Oligopaint probe design. Hi-C maps from ESCs and NPCs along with the positions of the 26 FISH probes used. Gray ticks indicate borders defined from visual inspection.

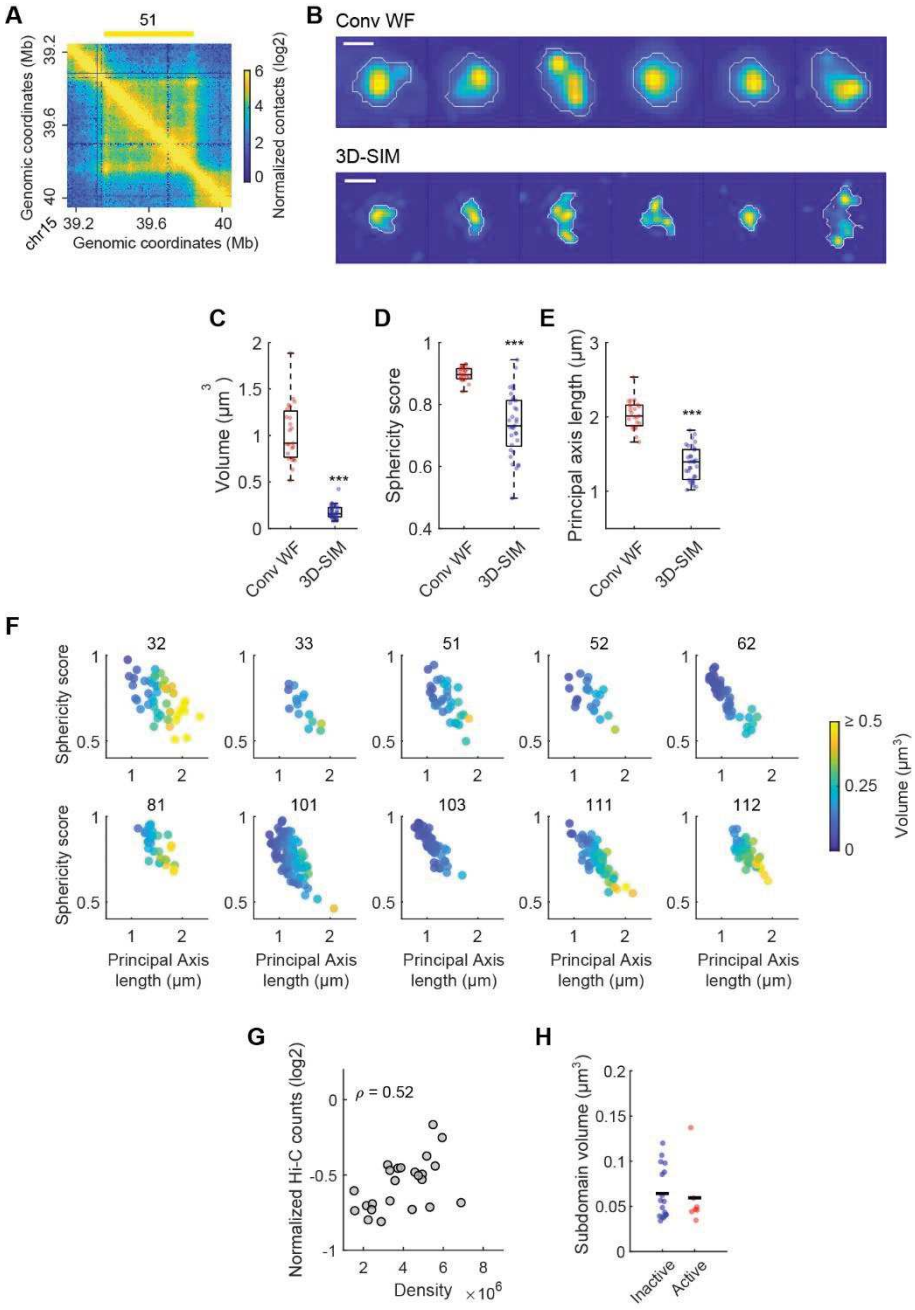

Figure S2. TAD structures revealed by 3D-SIM super-resolution imaging. A. Hi-C map from ESCs along with FISH probe position. **B.** Top: examples of individual TADs imaged with conventional widefield (WF) microscopy. Bottom: examples of individual TADs imaged with 3D-SIM. White lines represent the boundaries of their maximum-projected segmentations. **C.** Volumes of individual TADs imaged with conventional WF microscopy or 3D-SIM. n = 23 and 33 for conventional WF microscopy and 3D-SIM, respectively. **D.** Sphericity scores of individual TADs imaged with conventional WF microscopy or 3D-SIM. n = 23 and 33 for conventional WF and 3D-SIM, respectively. **E.** Principal axis length of individual TADs imaged with conventional WF microscopy or 3D-SIM. n = 23 and 33 for conventional WF and 3D-SIM, respectively. **F.** Sphericity score as a function of the principal axis length for each individual TAD labeled with different probes (see Figure S1 for the correspondence of the probes). Color-code indicates the volume of the TADs. A mean of 45 TADs was analyzed per probe. **G.** Mean volume of the subdomains identified for each locus. Black line indicates mean. A mean of 138 subdomains

was analyzed per probe. (**H**) Normalized Hi-C counts within the regions labeled by the probes as a function of their density along with the Pearson's correlation coefficient ρ. Statistics were done using Wilcoxon rank sum test, *** $P < 0.001$.

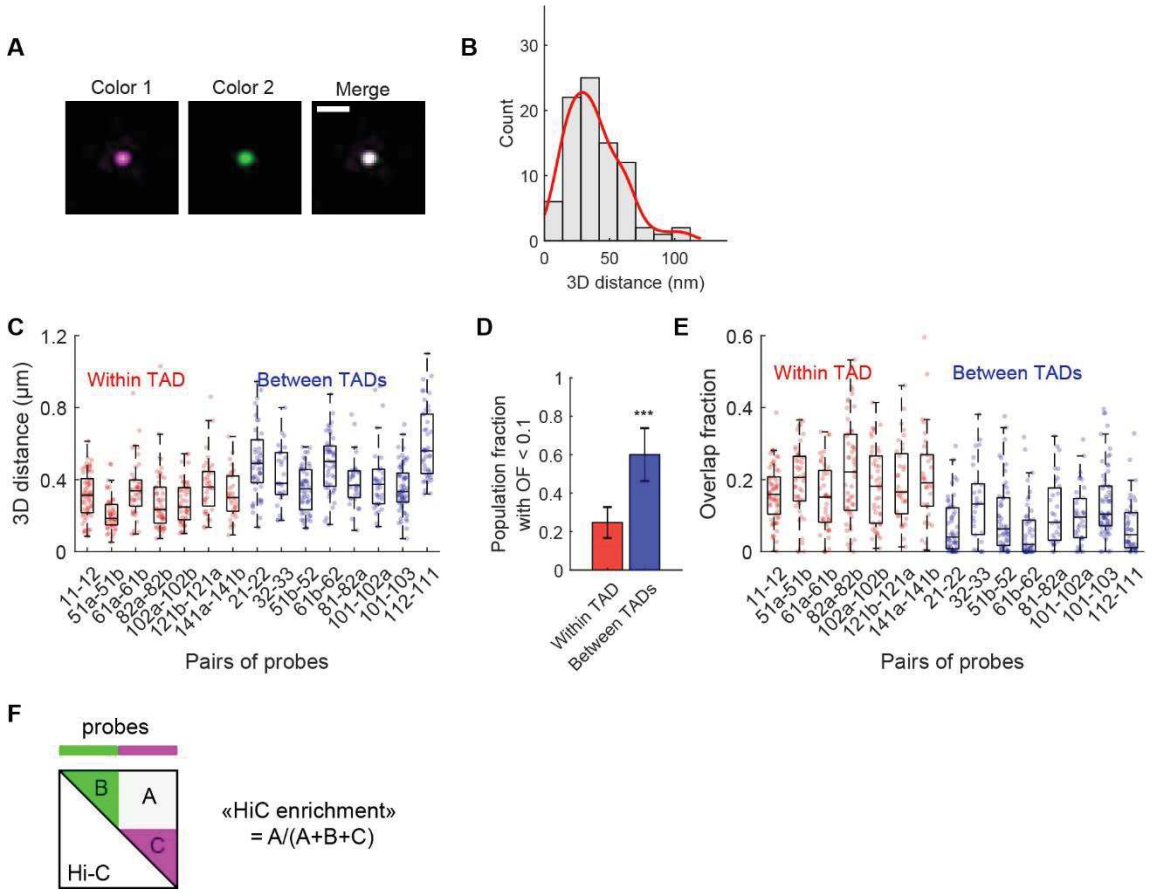

Figure S3. 2-color FISH to study TAD folding. (**A**) 3D-SIM image of a control probe (5d2) simultaneously labeled by Alexa-488 and ATTO-565 fluorophores. Maximum projections, scale bar = 500 nm. (**B**) Distribution of the distances measured between centroids of the two segmented colors. $n = 85$. (**C**) OF distributions measured for each pair of probes. A mean of 44 alleles was analyzed per pair of probes. (**D**) Fraction of the population of pairs of probes displaying an OF < 0.1. Bars represent mean ± SD from the different pairs of probes (7 within TADs, 8 between TADs). (**E**) Distributions of the 3D distances measured between the centroids of each pair of probes. A mean of 44 alleles was analyzed per pair of probes. (**F**) Representation of the Hi-C enrichment score, defined as the Hi-C contacts measured between the labeled regions (A) divided by the sum of contacts measured in (A) and measured within each labeled region (B and C). Statistics were done using Wilcoxon rank sum test, *** $P < 0.001$.

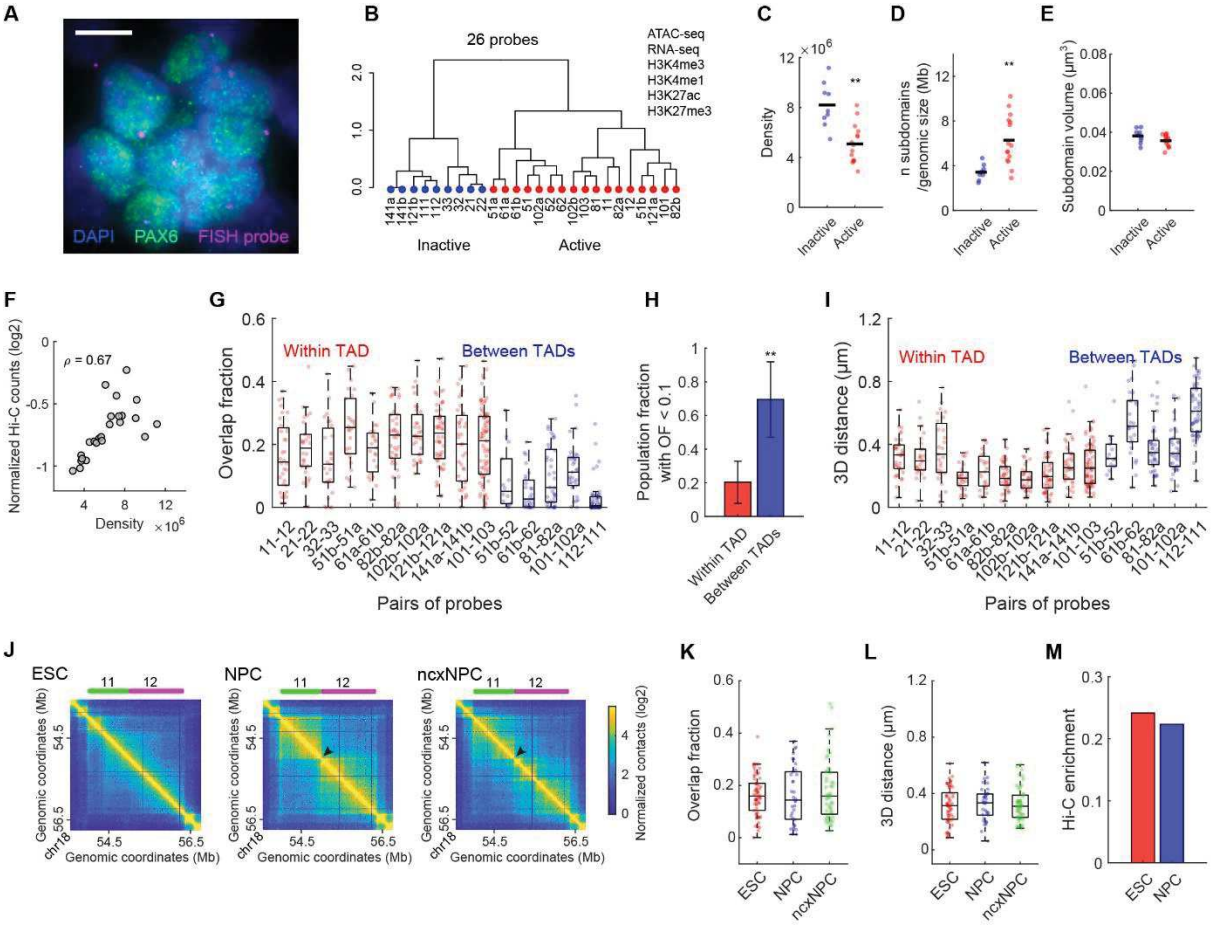

Figure S4. Structural organization of TAD in NPCs. (**A**) FISH combined with an immunostaining of the Pax6 neural transcription factor allows NPCs identification after in vitro differentiation. Conventional WF microscopy, scale bar: 10 µm. (**B**) Hierarchical clustering of the 26 regions labeled by probes using ATAC-seq, RNA-seq and the ChIP-seq of the indicated histone PTMs. (**C**). Density (genomic size divided by mean volume) of the loci labeled by the probes. Black line indicates mean. A mean of 45 alleles was analyzed per probe. (**D**). Mean number of subdomains per probe divided by the genomic size of the locus (in Mb). A mean of 48 alleles was analyzed per probe. (**E**) Mean volume of the subdomains identified for each locus. Black line indicates mean. A mean of 132 subdomains was analyzed per probe. (**F**) Normalized Hi-C counts within the regions labeled by the probes as a function of their density along with the Pearson's correlation coefficient ρ. (**G**) OF distributions measured for each pair of probes. A mean of 36 alleles was analyzed per pair of probes (**H**) Fraction of the population of pairs of probes displaying an OF < 0.1. Bars represent mean ± SD from the different pairs of probes (10 within TADs, 5 between TADs). (**I**) Distributions of the 3D distances measured between the centroids of each pair of probes. A mean of 36 alleles was analyzed per pair of probes. (**J**) Hi-C maps in ESCs, NPCs, and ncxNPCs along the location of pair of probes. Arrowheads indicate the border formed at the transcription start site of the *zfp608* gene. (**K**) OFs between the probes shown in (J). n = 62, 34 and 48 for ESCs, NPCs and ncxNPCs, respectively. (**L**) 3D distances between the centroids of the probes shown in (J). n = 62, 34 and 48 for ESCs, NPCs and ncxNPCs, respectively. (**M**) Hi-C enrichment measured in the region labeled by the probe shown in (J). Statistics were done using Wilcoxon rank sum test, ** $P < 0.01$.

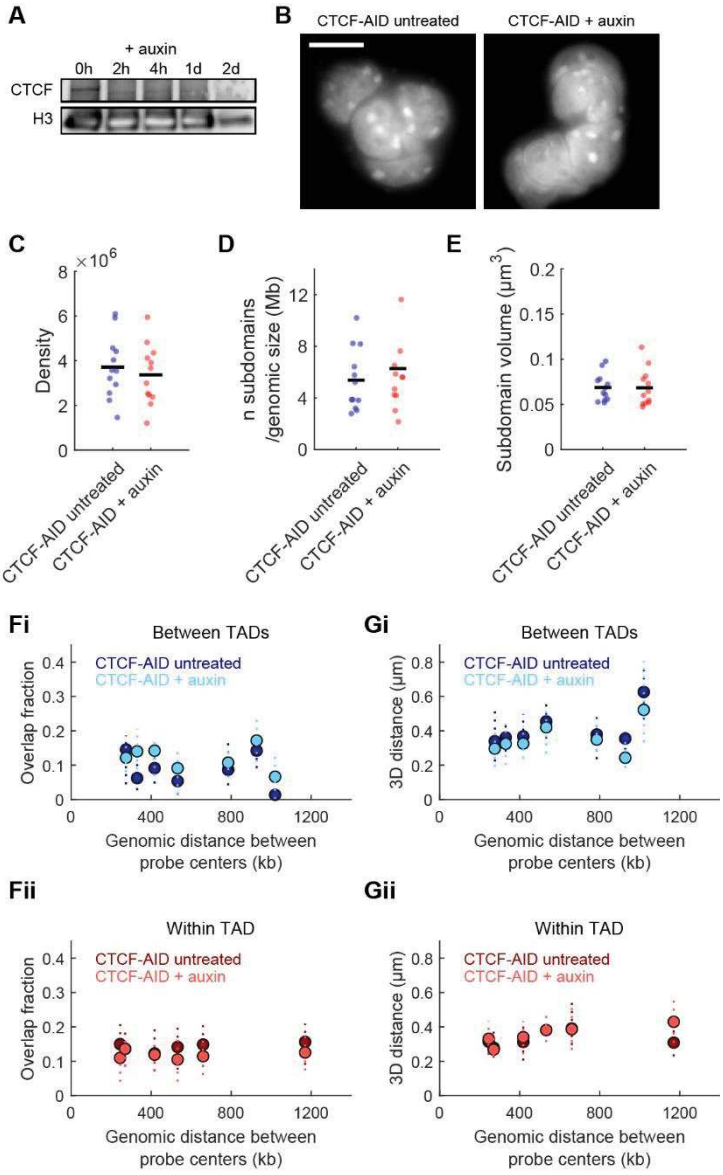

Figure S5. Structural organization of TADs upon CTCF depletion. (**A**) Western Blot of CTCF and H3 in CTCF-AID cells incubated with auxin. (**B**) DAPI staining in CTCF-AID untreated cells or treated with auxin for 2 days. Conventional WF microscopy, scale bar: 10 µm. (**C**) Density (genomic size divided by mean volume) of the loci labeled by the probes. Black line indicates mean. (**D**) Mean number of subdomains per probe divided by the genomic size of the locus (in Mb). Black line indicates mean. **(E**) Mean volume of the subdomains identified for each locus. Black line indicates mean. (**F**) OF measured for each pair of probes, either within TAD (Fi) or between TADs (Fii), as a function of the genomic distance separating their centers in CTCF-AID untreated cells or treated with auxin for 2 days. Graph represents medians and interquartile ranges. (**G**) 3D distances between centroids measured for each pair of probes, either within TAD (Gi) or between TADs (Gii), as a function of the genomic distance separating their centers in CTCF-AID untreated cells or treated with auxin for 2 days. Graph represents medians and interquartile ranges.

probe name	chr	start	end	size (bp)	n probes	density	primer
probe_11	chr18	54000000	54990180	990180	13453	13.587	A
probe_12	chr18	54995000	56335000	1340000	17829	13.306	B
probe_21	chr8	42540000	43275000	735000	7664	10.428	C
probe_22	chr8	43355000	44030000	675000	6124	9.074	D
probe_32	chr2	86490000	87460000	970000	6954	7.172	F
probe_33	chr2	87475000	88330000	855000	5837	6.827	G
probe_51	chr15	39355000	39845000	490000	5824	11.887	K
probe_51a	chr15	39355000	39600000	245000	2518	10.285	M
probe_51b	chr15	39600000	39845000	245000	3305	13.512	N
probe_52	chr15	39855000	40140000	285000	3481	12.22	L
probe_61a	chr1	68105000	68705000	600000	6074	10.125	I
probe_61b	chr1	68725000	69150000	425000	4907	11.547	J
probe_62	chr1	69170000	69770000	600000	7951	13.253	K
probe_101	chr1	136765000	137215000	450000	6254	13.913	F
probe_102a	chr1	137235000	137580000	345000	4232	12.324	G
probe_102b	chr1	137600000	138050000	450000	5658	12.599	H
probe_103	chr1	136535000	136750000	215000	1975	9.246	M
probe_111	chr2	55080000	56050000	970000	3063	3.168	A
probe_112	chr2	56090000	57080000	990000	4359	4.405	B
probe_121a	chr2	138040000	138680000	640000	4622	7.227	D
probe_121b	chr2	138700000	139340000	640000	3559	5.567	E
probe_81	chr2	49360000	49730000	370000	3403	9.201	G
probe_82a	chr2	49760000	49990000	230000	2781	12.103	H
probe_82b	chr2	50020000	50270000	250000	2477	9.92	I
probe_141a	chr10	100740000	101525000	785000	3028	3.858	N
probe_141b	chr10	101555000	102340000	785000	2774	3.54	O
probe_5d2	chr15	39825000	39875000	50000	750	15.028	P

Table S1. Coordinate, size, number of oligos, density of oligos (per kb) and primer code of Oligopaint probes.

Chapter 3: Discussions and perspectives

The discovery of domains of interactions as a general feature of genome folding at an intermediate scale between the ~11 nm chromatin fiber and full chromosome territories has led to extensive work dedicated in deciphering the principles of their formation and their functional relevance. However, understanding the nature of TADs has remains challenging. First, even the definition of TAD is not clear. Across and even within a given species, TADs are not equivalent in terms of genomic size, structural properties, epigenomic content and are likely formed by different mechanisms (Szabo et al., 2019). Furthermore, because of the nature of the Hi-C method, finer patterns of contacts at the TAD scale have progressively appeared concomitantly with the increase of the resolution offered by higher sequencing depths. Those include discrete loops, internal insulations such that TADs eventually split into different subdomains, or interactions stripes, which turned in redefining previously identified domains. These discrepancies have led to different appellation for various types of domains, such as compartmental domains for *Drosophila* TADs (Rowley et al., 2017), loop domains or insulated neighborhood for TADs with interaction peaks at their edges in mammals (Hnisz et al., 2016b; Rao et al., 2017), globules for *S.pombe* (Mizuguchi et al., 2014), self-associating domains in *S.cerevisiae* (Hsieh et al., 2015)… This may be useful to avoid any confusion between the different natures of TADs. However, it seems that no consensus really emerged for the use of these different appellations. It is nevertheless clear that there are different types of domains or TADs, and this aspect is therefore important for their description or to apprehend the mechanisms responsible for their formation.

During my thesis, my work has been mainly focusing on the 3D structural organization of TADs in individual cells in both *Drosophila* and mouse species. Because Hi-C assays represent averaged-interaction profiles that come from an ensemble of cells, the very existence of TADs as genuine

architectural units has been questioned. The first single-cell Hi-C did suggest a conserved domain organization in individual cells (Nagano et al., 2013), but subsequent studies highlighted the fact that contacts at the TAD-scale observed in single cells do not always match those observed in cell-population (Flyamer et al., 2017, Stevens et al., 2017), suggesting that TADs are not stable units. However, single-cell Hi-C rarely capture more than one million contacts, i.e. just a few percentages of all possible ligation junctions. Furthermore, pair-wise interactions detected in Hi-C are not informative on the relative spatial positioning of different pairs of loci. Nevertheless, various cell-to-cell TAD conformations were also observed using microscopy-based studies as indicated by the broad distance distributions between individual loci (Lanzuolo et al., 2007; Giorgetti et al., 2014; Cheutin and Cavalli, 2018). Yet, because of the few numbers of loci that can be labeled at a time in FISH studies, integrated TAD structures have proven difficult to characterize. We reasoned that a direct characterization in individual cells of the folding of large sets of TADs would be crucial to better understand the 3D organization principles underlying their formation. We also reasoned that the use of different model organisms would allow us to compare the conservation and/or the specificity of the structural organization of different types of TADs.

In *Drosophila*, TAD pattern mostly corresponds to repressed domains rarely larger than 200 kb interspersed by short active regions composed of dense clusters of transcribed genes that have been defined as active TADs or inter-TAD regions (Sexton et al., 2012; Ulianov et al., 2016; Rowley et al., 2017). At a scale of tens of kb, repressed or active epigenetic marks appear relatively homogeneous within repressed or active TADs, respectively. This organization reflects the mutual exclusion between these two types of chromatin, as identified for long-range A and B compartments (Lieberman et al., 2009; Rowley et al., 2017). Our super-resolution imaging data indicate that repressed TADs often fold into discrete globular objects. An even better resolution would certainly reveal further internal substructures, yet the meshwork of presumably heterogeneous contacts within individual TADs gives rise to discrete and spherical structures at a scale of ~150-200 nm. On the other hand, we observed that active TADs or inter-TAD regions appeared more decondensed, consistent with a previous study (Boettiger et al., 2016). Active and repressed chromatin regions thus have distinct structural properties and are mutually excluded from each other in averaged interactions maps. By labeling different regions spanning repressed and active TADs, we observed that the partitioning of the chromatin fiber into TADs exists in individual *Drosophila* cells. Certainly, this doesn't preclude that in every single-cell each TAD is distinctly isolated from another one, or that each physical insulation exactly corresponds to those identified in Hi-C averaged interaction profiles. We indeed observed that discrete globular objects identified using microscopy sometimes correspond to substructures of individual TADs, or on the contrary, to distal TADs contacting each other such that they cannot be resolved. The latest was notably illustrated by the high degree of variability in cis and trans interactions between TADs, consistent with the extensive heterogeneity of cell-to-cell long-range chromosome interactions (Cattoni et al., 2017;

Finn et al., 2019). Yet, the overall folding of individual chromatin fibers into physical and discrete domains that most often correspond to the TADs identified from Hi-C appeared as a general characteristic of interphase chromosome organization. Interestingly, a recent study using a derivative of Hi-C in single-cells (ChIA-Drop) corroborated our results, revealing that despite a high heterogeneity of contacts, the very large majority of multiplexed chromatin interactions fall within TADs (Zheng et al., 2019). Then, dynamic TAD structures are compatible with a more stable partitioning of the chromatin fiber into spatially segregated units. In *Drosophila*, given the genomic distribution of alternated repressed domains and dense clusters of transcribed genes, the affinity of a chromatin type to interact with itself, for example due to nucleosome-nucleosome contacts, nucleosome spacing, binding of specific factors (Rowley et al., 2019; Gibson et al., 2019), together with the exclusion -or the repulsion- of different chromatin types would generate a pattern of interaction resembling that of TADs. On top of this active-inactive segregation, it also appeared that the PcG TADs are peculiar. Their folding is different than that of inactive TADs, with a higher degree of condensation and internal chromatin intermingling (Boettiger et al., 2016). This specific organization is presumably due to the capacity of PcG proteins to remodel nucleosome organization and to condense chromatin, together with the ability of the Polyhomeotic component to oligomerize (Wani et al., 2016) and other PRC1 member to undergo phase separation (Tatavosian et al., 2018; Plys et al., 2019).

In mouse cells, we observed different TAD 3D organizations than in *Drosophila*. This is not surprising given their much larger genomic size (~1 Mb versus ~100 kb in average for mammals and *Drosophila*, respectively). Indeed, the resolution offered by 3D-SIM (lateral resolution of ~120 nm) can resolve various shapes and structures that could not be distinguished for smaller TADs in *Drosophila* (~175 nm). Our characterization of various mouse TAD conformations is in line with polymer modeling (Giorgetti et al., 2014), and we could provide further information for many different genomic loci on their structural properties such as volume and shape variability. Interestingly, we observed that mammalian TADs rarely form homogeneous structures but rather often display internal subdomains of several hundreds of nanometers. These results indicate that the folding of the chromatin into homogeneous structural units that correspond to full ~Mb-scaled TADs is uncommon, and that a finer scale of chromatin higher-order organization formation may actually exist in between nucleosome and TAD levels. Nanodomains were previously described using super-resolution imaging of histones although they were smaller [tens to few hundreds of nanometers (Ricci et al., 2016; Nozaki et al., 2017)] than those we identified (several hundreds of nanometers). This is nevertheless expected given these studies applied SMLM approaches, which provide a higher spatial resolution, to native chromatin while we used FISH. Moreover, size quantification strongly relies on the method used, and the 3D segmentation we applied is likely identifying objects of a larger size than what would be measured using 2D areas or 1D radii (the axial resolution being lower than the lateral one). The presence of subdomains within TADs is also consistent with the identification of sub-TADs using high-resolution Hi-C (Rao et

al., 2014). They were shown to correspond to domains of a median length of 185 kb enriched in specific chromatin marks that undergo fine long-range A- and B-type compartments, a situation reminiscent to *Drosophila* TADs. This would suggest that, as in *Drosophila*, such subdomains may be identified in individual cells from a segregation of different types of chromatin. Consistently, different organizations at the nanoscale were observed for active or repressed chromatin states related to histone marks (Xu et al., 2018; Smeets et al., 2014). A spatial organization of the chromatin fiber into small nanodomains that correspond to regions enriched in specific epigenetic marks may then represent a conserved principle of chromosome folding in metazoan. Nevertheless, the presence of interacting domains associated to chromatin states is not obvious at the sub-Mb scale in mammalian Hi-C maps. The loop-extrusion mechanism has been proposed to be an additional feature of genome folding in mammals that would partially blur the formation of such subdomains by mixing them within TADs (Nuebler et al., 2018). Further investigations in wild-type and cohesin depleted cells would certainly help in characterizing the existence and the structure of epigenetically defined domains in individual cells. Moreover, our data also suggest that nanodomains observed in microscopy do not only result from epigenetic landscapes within TADs. Indeed, our Oligopaint design included regions rather homogeneous in terms of chromatin marks, yet we kept observing their folding into distinct smaller globules. This suggests that if sub-TAD structures may arise from specific epigenetic domains, the chromatin fiber would anyway fold into globular structures encompassing several hundreds of kilobases. What could be the mechanism that underlies the formation of these nanodomains? An evident candidate was the CTCF insulator protein, as suggested by its role in generating physical barriers between adjacent TADs. However, our data showed that subdomains persist in the absence of CTCF. Another obvious candidate is the cohesin complex. Indeed, nanodomains may be formed by processive loops generated by multiple cohesin simultaneously loaded onto chromatin. TAD internal borders in cell-population averaged assays would not be observed because of the cell-to-cell heterogeneity of subdomain borders positioning. The depletion of cohesin -an experiment currently planned- will certainly provide critical answers regarding its eventual role in generating these structures. In this way, a previous study using super-resolution imaging of histones showed that the inhibition of the cohesin subunit RAD21 or the cohesin loader NIPBL caused a decondensation of chromatin nanodomains (Nozaki et al., 2017). However, and intriguingly, chromatin folding into TAD-like structures was still observed in the absence of cohesin (Bintu et al., 2016), although the correspondence between those and the subdomains we characterized remains to be investigated. Their persistence would suggest that they form independently of a loop extrusion process and that chromatin cannot fold into one discrete 3D unit after a critical genomic size. Thus, they may arise from intrinsic properties of the chromatin fiber, for example driven by nucleosome-nucleosome interactions. Importantly, we observed that the propensity of the chromatin to fold into nanodomains seems to be related with its transcriptional and epigenetic state, such as active regions tend to fold into more subdomains than inactive ones, which is then consistent with the differential organization of distinct histone PTMs (Xu et al., 2018; Smeets et al., 2014). The comparison of

chromatin nanodomains between different species would help in elucidating their nature. In *Drosophila*, repressed TADs of ~100-250 kb often appear as discrete globular objects resembling nanodomains identified in mouse. Nonetheless, we observed that individual TADs can split into substructures in a subset of cells. This occurred more frequently for a TAD of 200 kb compared than for a TAD of only 125 kb. It would therefore be important to address whether an even larger TAD would fold into various globules in this species, in which there is so far no evidences for a loop extrusion mechanism. In addition, the use of sequential-imaging methods to generate 3D TAD reconstructions in single-cells while keeping the information of the positioning of internal loci appears as a promising approach to characterize their organization (Wang et al., 2016; Bintu et al., 2018; Nir et al., 2018; Cardozo Gizzi et al., 2019; Mateo et al., 2019). Matrices of distances or overlaps between loci within TADs would allow the identification of globule locations, and thus their genomic size, their cell-to-cell variability, and their eventual relationship with epigenomic features. We are currently planning experiments in this direction to investigate internal TAD folding by using microscopy-based chromosome conformation capture [Hi-M (Cardozo Gizzi et al., 2019)]. We are hoping that this approach will allow us to better understand the rules of subdomain formation and chromatin folding into TADs.

Last, an exciting perspective would be to integrate our characterization of TAD structures to dynamic gene regulation during cell differentiation. The transcriptional regulation through contacts between genes and their cis-regulatory elements is at the center of the model according to which TADs regulate gene expression. Consistently, our imaging data demonstrate a much higher degree of chromatin intermingling within TADs compared to adjacent TADs in a large majority of individual cells. These results reconcile then the cell-to-cell heterogeneity of chromatin folding with the role proposed of TADs in the spatial regulation of functional landscapes, and provide then a physical basis for domains in which contacts between genes and enhancers are favored (Zhan et al., 2017; Bonev et al., 2017; Sun et al., 2019). However, the folding of individual chromatin fibers associated to such contacts remains obscure. How are functional interactions established within TAD structures? What is the relationship between these specific architectures and gene expression? The application of Hi-M in our cell differentiation system is an approach of choice to address these questions, and we have planned further experiments to study functional TAD organization. As a model region, we focused on a TAD containing the *zfp608* gene that is dynamically rewired during cell differentiation. In ESCs, *zfp608* is very lowly expressed and in a bivalent state, i.e. decorated with both H3K27me3 and H3K4me3. When the gene is activated in NPCs, the TAD undergoes architectural changes with the appearance of a network of contacts between the gene TSS and multiple sites, presumably enhancers, marked by H3K4me1 and H3K27ac (Figure 1). In ESCs, no clear internal substructures are observed in Hi-C, while we observed the formation of subdomains using super-resolution imaging. Hi-M would then allow us to characterize the genomic correspondence of the subdomains and their cell-to-cell variability, as mentioned above. In addition, we have also designed probes targeting the intronic sequence of the *zfp608* gene to visualize

at the same time the configuration of the TAD and its transcriptional state using tyramine signal amplification. A second probe design within the same region but centered on the gene and the neighboring enhancers would extend our characterization of the organization of this locus with a better genomic resolution.

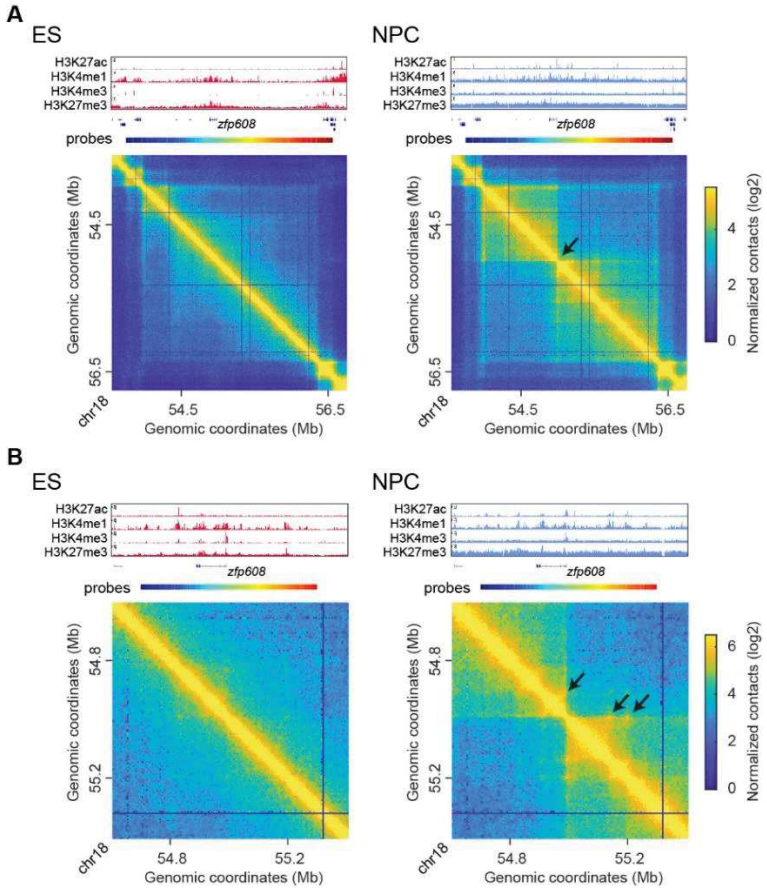

Figure 1. Model region to study functional TAD organization during cell differentiation. (**A**) Hi-C maps of a large TAD along with ChIP-seq tracks of histone PTMs and the position of barcoded probes (118 probes each covering ~25 kb represented by one color). In ESCs, the *zfp608* gene is very lowly expressed and no specific internal TAD architecture are discernable. In NPCs, *zfp608* is activated together with the appearance of an internal TAD border at its TSS (black arrowhead) and new patterns of interaction. (**B**) More resolutive Hi-M design centered on the *zfp608* gene and the adjacent putative enhancers that contact the TSS in NPCs (black arrowheads).

With these future experiments, we hope to better understand the nature of TADs by integrating the organization of functional contacts within global TAD topology. More generally, further work dedicated to an ever-deeper characterization of chromosome architecture and to the relationship between the structural and functional organization of TADs will certainly help to better understand the role of 3D chromosome folding in genome regulation.

Supplementary material

4.1 Barrier-to-autointegration factor regulates genome organization and function in *Drosophila*

Quentin Szabo, Giorgio L Papadopoulos, Filippo Ciabrelli, Niroshi Senaratne, Eric Joyce, Brian Beliveau, Boyan Bonev, Tiao Xie, Ting Wu, Frédéric Bantignies, and Giacomo Cavalli

In parallel to my thesis work focusing on the folding of TADs using super-resolution microscopy, I was also involved in the study of the role of *baf* in chromosome organization. The project was initiated by my thesis supervisors, Frédéric Bantignies and Giacomo Cavalli, in collaboration with the lab of Chao-Ting Wu (Harvard Medical School, Boston). It started with a screen using Hi-throughput FISH aiming to identify genes involved in chromatin architecture regulation, and *baf* appeared as one of the best hits. This gene codes for a small DNA-binding protein associated to the components of the nuclear lamina and to nucleosomes, yet its function on chromatin is poorly defined. We combined various approaches including microscopy, genomics and fly genetics to better understand the role of this protein in genome regulation. In this section, I will summarize the principal results obtained for this ongoing project.

4.1.1 Introduction

The molecular mechanisms that lead chromosome folding remain largely elusive, and the identification of novel factors involved is crucial to better understand the links between chromosome organization and genome function. Here, we isolated *barrier-to-autointegration factor* (*baf*) as a new player of chromosome organization using RNA interference (RNAi) screen and high-throughput fluorescent in-situ hybridization (Hi-FISH). The *baf* gene codes for the Barrier-to-autointegration factor (BAF), a small (10-kDa) protein that is highly conserved among metazoans, with human and *Drosophila* BAF sharing 69% identical (Segura-Totten and Wilson, 2004). BAF binds DNA on its phosphate backbone and interacts with lamins and LEM (LAP2-emerin-MAN1) domain proteins, as well as with mononucleosomes and post-translationally-modified histones (Margalit et al., 2007; Montes De Oca et al., 2011), suggesting that BAF is a bridging factors between the genome and the nuclear lamina. This feature is particularly interesting in the context of the Polycomb domains, which have a propensity to localize at the periphery in *Drosophila* cells and are sensitive to lamina dosage (Cesarini et al., 2015). BAF is also involved in nucleus reformation after mitosis (Samwer et al., 2017; Margalit et al., 2005; Margalit et al., 2007b). BANF1 (the human homologous of *baf*) mutation was identified as a cause of a hereditary progeroid syndrome that partially phenocopies Hutchinson-Gilford progeria syndrome,

emphasizing its crucial role in genome regulation (Puente et al., 2011). However, the role of BAF on chromatin remains unclear. Using a combination of microscopy, Hi-C, RNA-seq and drosophila genetics, we showed that BAF regulates interconnected mechanisms of chromosome organization that are essential to ensure proper gene regulation.

4.1.2 Results

In order to isolate new candidate genes involved in chromosome folding, we developed a Hi-FISH assay using as a readout the three-dimensional (3D) distance between two Polycomb TADs, *spineless* (*ss*) and the *Fab-7* locus from the homeotic bithorax complex [BX-C (Figure 1A)]. We produced highly sensitive Oligopaint probes (Beliveau et al., 2015) against these loci for large-scale usage, and we performed an RNAi screen in tetraploid *Drosophila* S2R+ cells against 177 candidate genes, including genes involved in the regulation of the 3D distribution of Polycomb foci (Gonzalez et al., 2014), plus other genes chosen from the literature. In parallel, we developed an automated image analysis pipeline allowing us to systematically score inter-distance measurements between the two Polycomb probes in a high-throughput manner (Figure 1B). Hi-FISH allowed the identification of several candidate genes, and best hits were chosen for further FISH validation using the same read-out and confocal laser scanning microscopy [CLSM (Figure 1B-1D)]. Among the identified genes, *baf* had the strongest effect on chromosome folding, seen as a great reduction of the distance between the loci, and retained our attention because of its links with chromatin and lamina (Margalit et al., 2007; Kind and van Steensel, 2014).

Our FISH assay also allowed the characterization of the prevalence of the pairing between homologous chromosomes, observed in most *Drosophila* interphasic nuclei, which is likely to impact chromosome topology (Bauer et al., 2012; Hartl et al., 2008; Joyce et al., 2012; Li et al., 2017). To address the connection between long-range chromosome folding (hereafter referred to as “folding”) and pairing, we compared the distances between the loci in cells in which *Fab-7* was paired (i.e. one FISH spot detected) to cells in which it was fully or partially unpaired (i.e. more than one FISH spot detected). In control cells [EGFP knockdown (KD)], we found a strong interplay between folding and pairing, with the two phenomena anti-correlated, i.e. more folding was associated to less pairing and more pairing to less folding (Figure 2A). Interestingly, the KD of *baf* [~94% of RNA reduction tested by reverse-transcription and real-time polymerase chain reaction (RT-qPCR)] led to both more folded and less paired chromosomes (Figure 2B-D). This highlighted our observation that chromosome folding and pairing are in equilibrium (Figure 2E). To discriminate if the KD of *baf* affects primarily the folding or the pairing, we analyzed distances in nuclei that have paired and unpaired FISH loci (Figure 2F). We observed a significant reduction of the distance distribution in both cases, which indicates that *baf* KD

can affect chromatin folding independently of pairing. Then, we addressed whether eventual changes in cell cycle could affect chromosome organization by combining FISH and cell-cycle profiling using DAPI staining. Under *baf* KD, the proportion of cells in G2 phase was reduced, indicating a perturbation of cell-cycle progression (Figure 2G), consistent with the role of BAF in the re-establishment of nucleus envelope after mitosis (Margalit et al., 2005; Margalit et al., 2007b; Samwer et al., 2017). However, we did not observe strong cell death after 5 days of KD (~25% reduction of the number of cells compared to control EGFP KD). Both folding and pairing were significantly affected in G1-staged cells, which indicates that the changes in chromatin organization observed in *baf* KD cannot simply be explained by a G1 shift in the cell population (Figure 2H and 2I). In addition, distances between loci were higher in

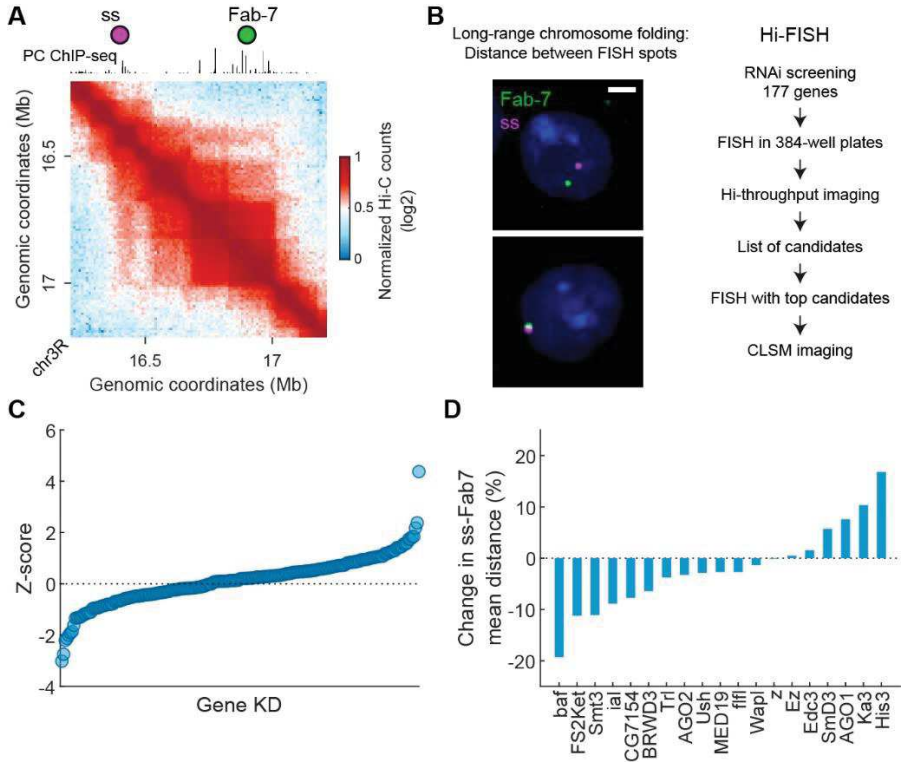

Figure 1. Hi-FISH revealed novel players of chromosome organization. (**A**) Hi-C map from S2R+ cells of the model region used to study chromosome folding. Two Polycomb TADs that undergo long-range contacts, *ss* and BX-C, were labeled using FISH probes (*ss* and *Fab-7*) separated by 500 kb. (**B**) Experimental design used to identify genes involved in chromosome folding regulation. The 3D distance between loci was used as a readout for chromosome folding. (**C**) Z-scores ($z = \frac{x-\mu}{\sigma}$; x = mean distance in gene KD, μ = mean distance in control KD, σ = standard deviation in gene KD) obtained for each of the 177 candidate genes. (**D**) Mean distance between probes in gene KDs (best hits chosen from their Z-score values in the primary screen) relative to the mean distance in control KD.

G2 compared to G1 cells, which suggests that paired sister chromatids play additional constraints to genome folding. Altogether, our results reveal an unprecedent link between folding and homologous chromosome pairing/sister chromatid adhesion. Although *baf* doesn't seem to have a role in modifying equilibrium after replication (Figure 2H-2I, both distances and pairing were not significantly affected in G2 *baf* KD cells when compared to control), it clearly has an effect in the equilibrium between chromatin folding and pairing in G1 phase.

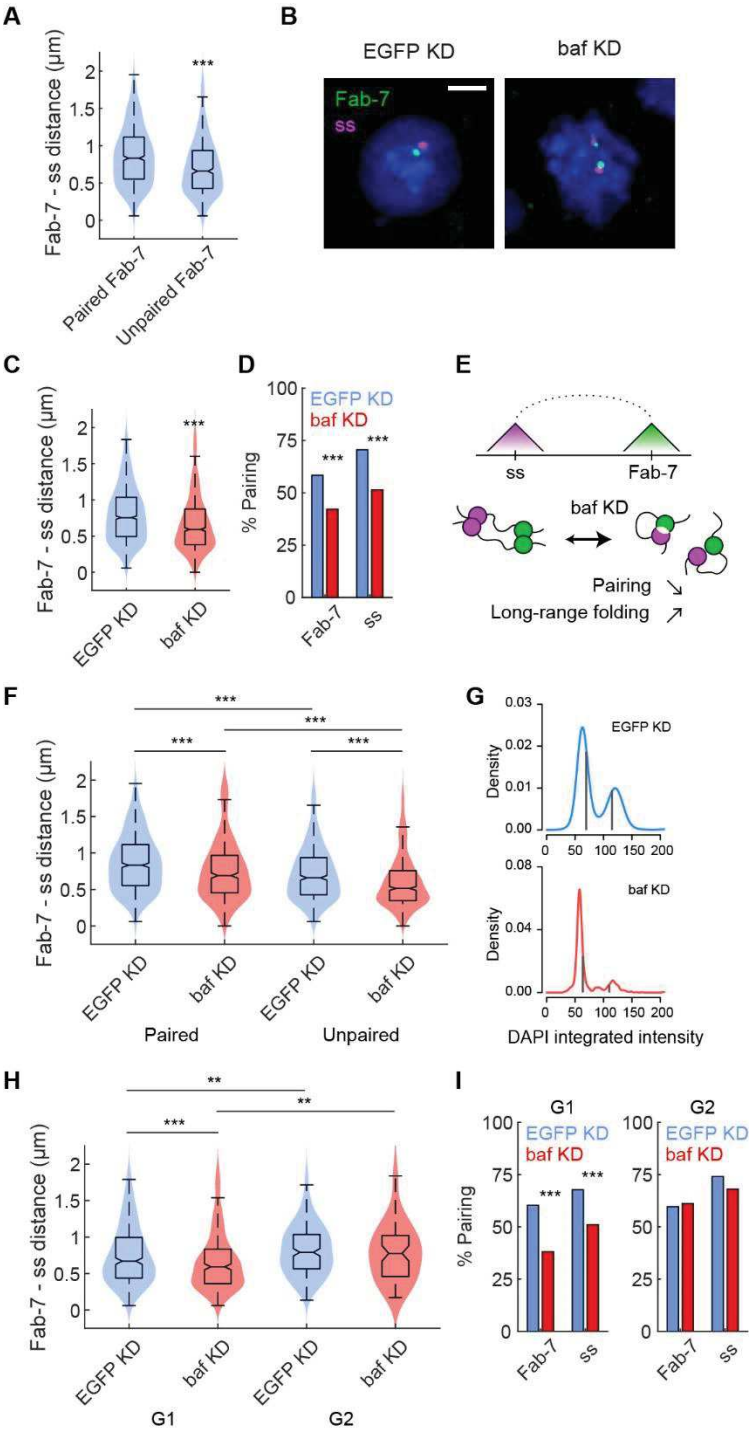

Figure 2. Chromatin folding and homologous pairing: a connected mechanism of chromosome organization regulated by BAF. (**A**) Distance distribution between Fab-7 and *ss* probes in nuclei with paired or unpaired *Fab-7*; *n* = 880 and 592, respectively. (**B**) Representative images of *Fab-7* and *ss* FISH in S2R+ cells. Maximum projections, scale bar: 1 µm. (**C**) Distance distribution between *Fab-7* and *ss* probes; *n* = 1472 and 1063 for EGFP and *baf* KD respectively. (**D**) Frequency of nuclei with paired *Fab-7* or *ss* loci; *n* = 1472 and 1063 for EGFP and *baf* KD respectively. (**E**) Schematic representation of antagonized long-range chromosome folding and homologous pairing. *baf* KD induces both an increase in long-range folding and a decrease of pairing. (**F**) Distance distribution between *Fab-7* and *ss* probes in nuclei with paired or unpaired *Fab-7*; *n* = 880 and 592 for paired and unpaired nuclei in EGFP KD, respectively; *n* = 457 and 606 for paired and unpaired nuclei in *baf* KD, respectively. (**G**) Cell-cycle staging using the distributions of the DAPI integrated intensity. Gray lines indicate the intensity cutoff used to define G1 (distribution up to the left line) or G2

(distribution after the right line) cells. (**H**) Distance distribution between *Fab-7* and *ss* probes in G1 or G2 nuclei; n = 406 and 208 for G1 and G2 nuclei, respectively, in EGFP KD; n = 333 and 72 for G1 and G2 nuclei, respectively, in *baf* KD. (**I**) Frequency of nuclei with paired *Fab-7* or *ss* loci; n = 406 and 208 for G1 and G2 nuclei in EGFP KD, respectively; n = 333 and 72 for G1 and G2 nuclei in *baf* KD, respectively. Statistics were done using Wilcoxon rank sum test (panels A, C, F and H) and two-tailed Fisher's exact test (panels D and I), *** $P <$ 0.001, ** $P < 0.01$.

We next addressed how the changes in chromatin organization observed at Polycomb loci may impact transcriptional regulation. We first combined FISH on the *Fab-7* locus with an immunostaining (FISH-immunostaining) of the Polycomb (PC) protein. The enrichment of PC on the locus was reduced in *baf* KD (Figure 3A and 3B), and moreover, was even lower when the locus was unpaired, suggesting that the decrease of pairing in *baf* KD is associated with a further reduction of PC binding (Figure 3C). Likewise, quantitative chromatin immunoprecipitation (qChIP) assay supported the diminution of PC on the locus (Figure 3D). As PC binding on *Fab-7* is associated to the transcriptional repression of the *Abdominal-B* (*Abd-B*) homeotic gene, we tested its expression using RT-qPCR. *Abd-B* was upregulated in *baf* KD, revealing that the disrupted organization of the locus and the diminished PC binding is linked to improper gene repression (Figure 3E). To assess the function of *baf* in whole organisms, we then developed classical genetic tests using *baf* null mutant alleles. The partial loss-of-function of *baf* (heterozygous conditions) induced the de-repression of *Abd-B* in *Fab-7*^{1} flies, which represent a sensitive background for the *Abd-B* gene regulation (Figure 3F). To better understand the mechanisms underlying the upregulation of Polycomb targets, we took advantage of the *Fab-X* transgenic fly line, in which the Polycomb repression is also dependent on pairing, one copy of the transgene being less repressed than two copies, a phenomenon called pairing-sensitive silencing [PSS (Bantignies et al., 2003; Figure 3G-3I)]. We introduced *Psc,* a member of the PRC1 Polycomb complex, or *baf* null mutations in the *Fab-X* line. While the removal of one *Psc* copy leads to the de-repression of both one or two transgenic copies (Figure 3H and 3I), the removal of one *baf* copy leads to the de-repression of *Fab-X* transgene only in the homozygous state, i.e. where the silencing is sensitive to pairing. These results indicate that the influence of *baf* loss of function on Polycomb silencing is in part due to the loss of pairing, which may lead to less recruitment of Polycomb complexes at their target loci.

We then asked whether *baf* has a more global role on chromosome organization. We designed Oligopaint probes that target different TADs according to their epigenetic features: Polycomb group (PcG) repressed TADs, inactive TADs (repressed independently of the PcG proteins) and active TADs [Figure 4A (Szabo et al., 2018)]. For each type of chromatin, TADs were alternatively labeled using 2 different fluorophores and imaged using super-resolution 3D-structured illumination microscopy (3D-SIM). We first measured 3D distances between nearest neighbors for all chromatin types. As nuclei in

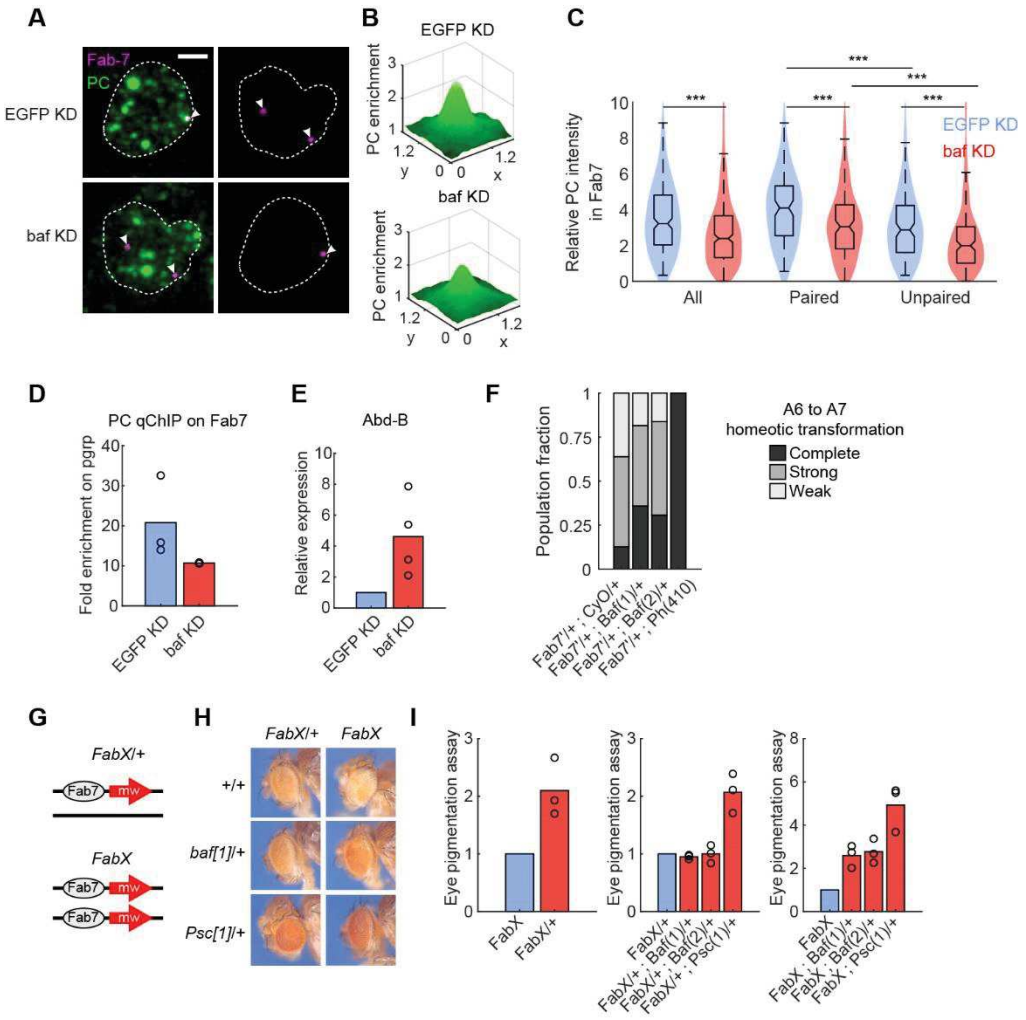

Figure 3. *baf* loss of function disrupts Polycomb-dependent gene repression. (**A**) Representative images of *Fab-7* FISH and PC immunostaining in S2R+ cells. Dashed line indicates DAPI contour. Maximum projections, scale bar = 1 µm. (**B**) PC normalized intensity distribution in 1.86 × 1.86 µm region centered on Fab-7 centroid obtained from the merge of 230 and 285 maximum projected images in EGFP and baf KD, respectively. x and y axes indicate coordinates in µm. (**C**) Normalized PC intensity in *Fab-7* centroids in all nuclei or whether Fab-7 was paired or unpaired. (**D**) qChIP of PC on Fab-7 locus (enrichment normalized using the negative control locus pgrp). (**E**) RT-qPCR of *Abd-B* (normalized on pgrp expression). (**F**) Fraction of drosophila displaying the homeotic transformation associated to *Abd-B* upregulation (transformation of the abdominal A6 segment into A7 segment). (**G**) The *Fab-X* transgene (top: heterozygous; bottom: homozygous) is composed of the *Fab-7* regulatory element and the mini-white gene rapporteur. (**H**) Expression of the mini-white rapporteur induces the red color of the eyes. When the transgene is present in two copies (homozygous), the repression of the mini-white gene is enhanced (eyes are whiter than whit just one copy), a phenomenon called PSS. (**I**) Eye pigmentation assay indicating the degree of mini-white expression. Statistics were done using Wilcoxon rank sum test, *** $P < 0.001$.

baf KD were smaller than in control cells (mean volume ± SD = 141 ± 32 and 96 ± 27 μm^3 in EGFP and *baf* KD, respectively), we normalized for each cell the FISH distances by the mean distance between the centroid of the nucleus and the contour of its segmentation. We consistently observed a significant reduction of nearest neighbor distances between FISH spots, revealing that *baf* KD induces global increase in long-range chromatin folding (Figure 4B). Similarly, we observed a decrease of the pairing for all chromatin states (Figure 4C). We also noticed that nuclei in *baf* KD display irregular contour and invaginations, suggesting an alteration of the chromatin organization at the nuclear lamina (Figure 2B, 3A and 4A). We thus took advantage of the large number of labeled loci to assess whether the radial organization of the chromatin was affected. In control cells, we observed that PcG and inactive TADs were more often located at the nuclear periphery than active TADs (Figure 4D). However, under *baf* KD both PcG and inactive TADs were no longer preferentially found at the periphery, which indicates a release of the subset of TADs located near the nuclear periphery (Figure 4D). These results are coherent with the proposed role of BAF in bridging repressed chromatin regions to the nuclear lamina (Margalit et al., 2007).

To better address the role of *baf* in 3D genome organization, we next performed high-resolution Hi-C in S2R+ cells (Figure 5A). Upon *baf* KD, we observed dramatic changes in contact distribution, with a reduction of contacts at relatively short genomic distances (up to ~150 kb, i.e. at the TAD scale) and an increase at long-range scale, consistent with our Oligopaint 3D-FISH observation (Figure 5A and 5B). These modification of contact distributions were observed for the different types of chromatin, reflecting again well the global effect of *baf* in chromosome organization (Figure 5C). The decrease of contacts at the TAD scale in *baf* KD may be due to the reduction of pairing but could also reflects local chromatin decondensation. However, since gain or loss of contacts observed in Hi-C must be compensated in the distribution, we cannot exclude that the decrease of contacts at short-range distances is due to the increase of long-range contacts, the latest being validated by FISH. We did not observe changes in TAD patterning such as border modifications, merge or split of TADs. Yet, the insulation between adjacent TADs was significantly reduced (Figure 5D). To characterize the relationship between these architectural modifications and gene regulation, we performed RNA-sequencing (RNA-seq). We observed a stark bias toward gene upregulation with 1581 significantly upregulated genes and 900 down regulated genes. Repressed or lowly expressed genes, such as those in PcG and inactive TADs, were particularly affected by *baf* KD, suggesting a prominent alteration of transcriptional repression (Figure 5F and 5G).

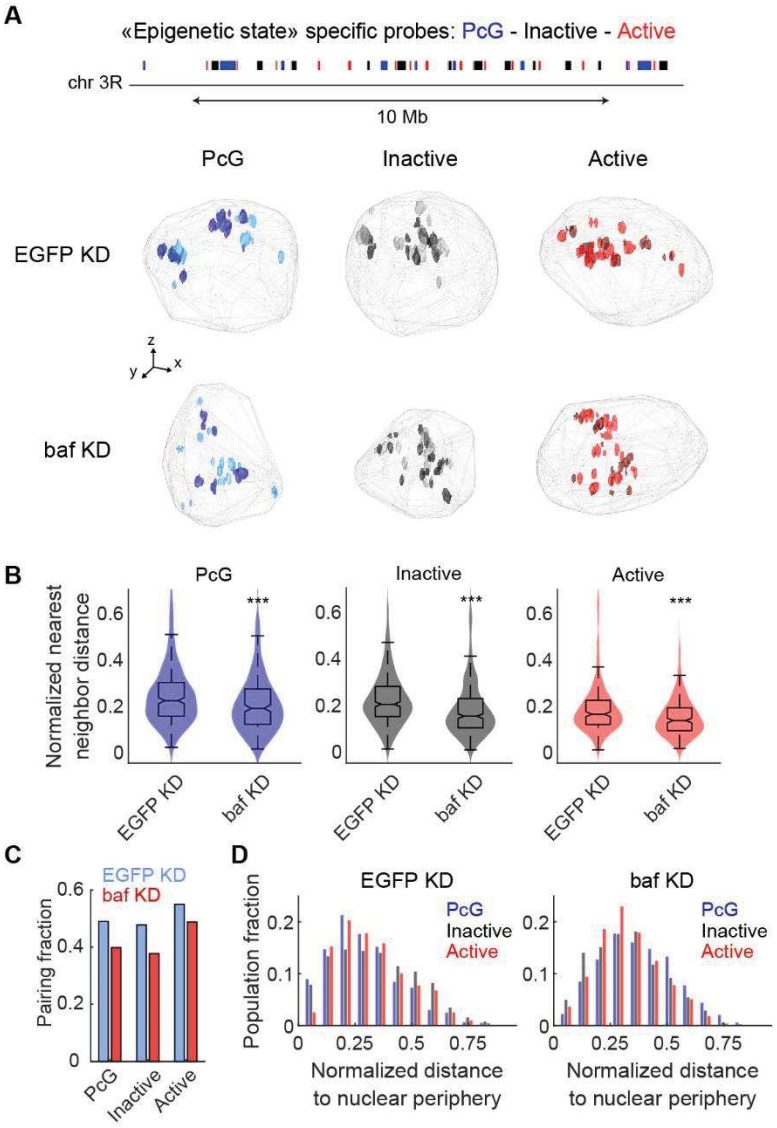

Figure 4. *baf* KD induces global chromosome reorganization. (**A**) Schematic representation of the position of "epigenetic state specific" probes on 3R chromosome and example of 3D segmented nuclei and probes. Gray meshes represent convex hulls of segmented nuclei; colored objects represent segmented probes that were alternatively labeled in 2 colors for each type of chromatin. (**B**) Distance distributions between differentially labeled nearest neighbor probe centroids for the different epigenetic states. Distances were normalized for each nucleus by the mean distance between its centroid and its contour. *n* = 296, 398, 240, 246, 408 and 249 for EGFP-PcG, EGFP-inactive, EGFP-active, baf-PcG, baf-inactive and baf-active, respectively. (**C**) Pairing fraction (mean probes counted per nucleus divided by the number of labeled domains) for the different epigenetic states. *n* nuclei = 33, 31, 19, 24, 26 and 18 for EGFP-PcG, EGFP-inactive, EGFP-active, baf-PcG, baf-inactive and baf-active, respectively. (**D**) Distance distributions between probe centroids and nucleus contour for the different epigenetic states. Distances were normalized for each nucleus by the mean distance between its centroid and its contour. *n* = 606, 779, 518, 542, 827 and 553 for EGFP-PcG, EGFP-inactive, EGFP-active, baf-PcG, baf-inactive and baf-active, respectively. Statistics were done using Wilcoxon rank sum test, *** $P < 0.001$.

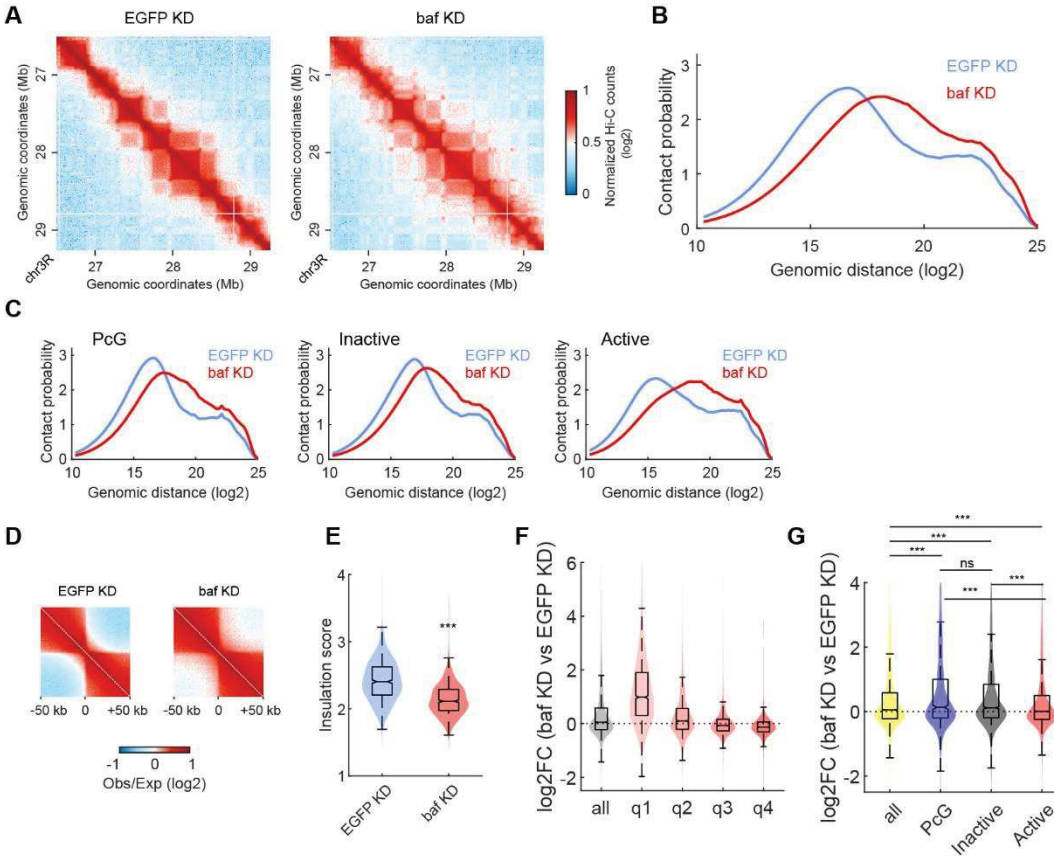

Figure 5. Chromatin reorganization in baf KD associates with gene misregulation. (**A**) Hi-C maps of a 2.75 Mb region in control EGFP KD and *baf* KD S2R+ cells. (**B**) Contact probability as a function of the genomic distance. (**C**) Contact probability as a function of the genomic distance for loci in PcG, inactive or active chromatin states. (**D**) Averaged Hi-C map from all borders identified in EGFP KD. (**E**) Insulation scores measured from all the borders identified in EGFP KD. (**F**) Fold change (log2) of gene expression in *baf* over EGFP KD for all genes (FPKM > 0) or based on expression levels (quantiles of expression from q1 to q4). (**G**) Fold change (log2) of gene expression in *baf* over EGFP KD for all genes or genes located in PcG, inactive or active TADs. Statistics were done using Wilcoxon rank sum test, *** $P < 0.001$.

These data demonstrate a crucial role of BAF in chromosome organization and gene regulation. Many layers of chromatin folding are affected by its depletion, revealing a close relationship between long-range interactions, homologous pairing, radial positioning, and TAD organization. The attachment to the nuclear lamina has been shown to be important for gene repression (Leemans et al., 2019), likewise, the pairing of homologous copies is also related to gene regulation, as illustrated by the PSS phenomenon associated to the repression of Polycomb-target loci. Moreover, our microscopy and Hi-C analysis revealed an augmentation of long-range chromatin interactions, accompanied with a general weakening of TAD insulation and maybe a decrease of their condensation. Hence, we propose that the multifaceted changes of chromatin organization observed in *baf* loss of function lead to less efficient transcriptional repression at inactive chromatin (Figure 6).

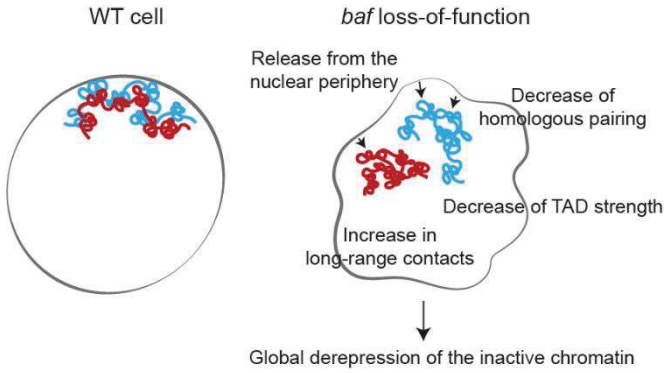

Figure 6. Working model of chromosome reorganization upon *baf* KD. *baf* KD induces various modifications of chromatin organization, including an increase in long-range folding, a decrease of TAD insulation, a reduction of homologous pairing and a disruption of the attachment to the periphery. The repressed chromatin becomes globally upregulated, which suggests that efficient gene repression is altered by the chromatin reorganization induces by BAF depletion.

4.1.3 Discussion

Our Hi-FISH strategy has allowed the identification of a novel role of *baf* in genome organization and function. BAF was shown to shape nuclei in mitotic exit by forming a dense DNA network at chromosomal surfaces (Samwer et al., 2017; Margarit et al., 2005; Margalit et al., 2007b). Its ability to dimerize and condense DNA by looping (Skoko et al., 2009; Bradley et al., 2005), together with its interactions to the lamin associated proteins, suggests that BAF acts as a bridging factor between chromatin and the nuclear lamina meshwork. Consistently, a previous study in mammalian cells showed that BAF binding regions superimposed with those associated with lamins, particularly lamin A/C (Kind and van Steensel 2014). We observed that many layers of chromatin organization are affected in *baf* KD, including radial positioning and inter- and intra-TAD contacts, consistent with previous observations in lamin depleted cells (Zheng et al., 2018; Ulianov et al., 2019). The relationship and/or the hierarchy between these different features of nuclear organization remains to be investigated in more details. For example, our data revealed that long-range chromosome folding and homologous pairing are in equilibrium, and that an increase in trans pairing frequency counteracts the folding in cis of the chromatin fiber. This is consistent with the strong reduction of long-range contacts in tetraploid S2R+ cells compared to diploid embryonic cells observed in both Hi-C and super-resolution experiments (Szabo et al., 2018 and Cattoni et al., 2017). Interestingly, integration of Hi-C, microscopy and modeling approaches also suggested a correlation between pairing frequency and radial positioning (Li et al., 2017). Elucidating whether the primary role of BAF consists in organizing the chromatin at the nuclear lamina, and if its release from the periphery is sufficient to induce all the observed changes would help in understanding general rules of genome organization. Although we cannot exclude that the disruption of chromatin organization may arise from non-properly reformed nuclei after mitosis (Samwer et al., 2017), several sources of evidences converged toward a direct role of BAF in maintaining the integrity of chromatin organization in interphasic nuclei. For instance the fact that BAF binding sites correspond to lamin associated domains, the fact that inactive chromatin, including Polycomb repressed chromatin

are located toward the periphery, as well as the fact that BAF interacts with Polycomb proteins (personal communication). In the future, it would be interesting to address whether BAF depletion in non-dividing cells displays similar effects. Last, the fact that changes in chromatin organization are broad and do not seem restricted to specific loci and that BAF binds DNA in a sequence-independent manner would suggests that transcriptional changes come from altered chromatin organization. Further studies focusing on the integration of the interplay between different layers of chromatin organization will help to better understand the epistasis of genome architecture and activity.

Author contributions

This projected was initiated before I joined the lab by my supervisors, Giacomo Cavalli and Frédéric Bantignies, and Chao-Ting Wu, a collaborator located at Harvard Medical School in Boston. Frédéric Bantignies spent a year in the lab of Chao-Ting Wu to realize the primary FISH screen. There, he designed and produced Oligopaint probes with Brian Beliveau, and performed FISH experiments with Eric Joyce and Niroshi Senaratne. The screen analysis was done using a pipeline developed by Tiao Xie. When I joined the lab after Frédéric Bantignies returned to France, we made FISH probes and performed FISH experiments to validate the best hits obtained from the primary screen. Further experiments were then planned and discussed with my supervisors. I performed the following FISH, immunostaining, qChIP, RT-qPCR, Hi-C and RNA-seq experiments. Sequencing data were analyzed by Boyan Bonev and Giorgio L. Papadopoulos. I handled cell culture, and Frédéric Bantignies and Filippo Ciabrelli handled fly genetics.

4.1.4 Material and methods

Cell culture

S2R+ cells (stock #150, Drosophila Genomics Resource Center) were grown at 25°C in Schneider's S2 medium (Sigma-Aldrich, Cat.N: S0146,) complemented with 10% fetal bovine serum [FBS (Gibco, Cat.N: 10500064)] and 1% penicillin-streptomycin (Gibco, Cat.N: 15140122). KDs were performed in 6-well plates by incubating in each well 1×10^6 cells with 17.5 µg double-stranded RNA (dsRNA) in 1 ml serum-free medium. After 30 min, 2ml of medium with 15% FBS were added to the wells. Cells were then grown for 5 days at 25°C. dsRNAs were obtained from plasmid (EGFP) or genomic DNA (*baf*) PCR amplification followed by in vitro transcription using the MEGAscript Kit (Ambion Inc., Cat.N: AMB13345):

EGFP FWD-primer: 5′-T7-GACGTAAACGGCCACAAGTT-3′

EGFP REV-primer: 5′-T7-TGCTCAGGTAGTGGTTGTCG-3′

baf FWD-primer : 5'-T7-GTGCGTCATTTTCAGAAACG-3'

baf REV-primer : 5'-T7-CAGCACCAGATACTGTCCCA-3'

T7 sequence: 5′-TAATACGACTCACTATAGGG-3′

Primers used to generate dsRNA from genomic PCR amplification for the candidates tested in the screen were chosen from (Gonzalez et al., 2014).

Fly genetics

Flies were raised in standard cornmeal yeast extract media at 21°C. The *Fab-7*^{1} deletion line, the *Fab-X* transgenic line, the *Ph*^{410} and *Psc*^{1} mutant alleles were described in (Bantignies et al., 2003). The *baf*^{1}/*Cyo* et *baf*^{2}/*Cyo* null allele were described in (Furukawa et al., 2003).

Probe design and production

For the Hi-FISH screen, we produced 50 kb Oligopaint probes (approximately 400 primary oligos) for the *ss* and the *Fab-7* (BX-C) loci (Beliveau et al., 2015). The *ss* Oligopaint was labeled in Alexa-488 and the *Fab-7* probe in Alexa-647. For standard FISH, *ss* and *Fab-7* probes were produced by nick translation from genomic PCR fragments (list of primers below) as described in (Bantignies and Cavalli, 2014)). The *ss* probe was labelled in Alexa-555 and the *Fab-7* probe in Alexa-488. Design and production of Oligopaints used in Figure 4 are described in Chapter 2, section 2.1 (Szabo et al., 2018).

Fab7ND1_sens CTGAGCTTTTCCTTGCTGCT

Fab7ND1_as GCCAGTGTGCGTGTGTATCT

Fab7ND2_sens GGAAATGCATCCACATACCC

Fab7ND2_as GCAAATAACTCGGGCAGAGA

Fab7ND3_sens CAGGGCTAAAACGAAACCAG

Fab7ND3_as CATCAAACCTAGCCGCTCTC

Fab7ND4_sens CACGCTCTCTTTCACATCCA

Fab7ND4_as GGGGCGTTAAATGCTCTACA

Fab7ND5_sens CACGACCCTGGAACAGATTT

Fab7ND5_as AAAGGTGAAAGCCAGGGAGT

Fab7ND6_sens CACAAGCGACAAAGATCGAA

Fab7ND6_as GAATCCCCCATTCCTCAAAC

ss1_sens AAAGTCCGACAAATCGATGG

ss1_as TGCAGCTGGTGTATCCTTTG

ss2_sens GTCGTAGCAAGAACGGAAGG

ss2_as GACCACCGATCGCTAATGTT

ss3_sens GGATCGGTATTGGTTTGTGG

ss3_as CGGCGGTCATTCACTTCTAT

ss4_sens AAGAACCCGATTGGACAGTG

ss4_as AGGCAAAACGAGGGGTAGAT

ss5_sens GTGCAATCTGGGCATACCTT

ss5_as GATAGGACCTGGCGATACGA

ss6_sens CTGAAGAGCCAGTTCGGTTC

ss6_as CTGCTCTCGACTCGTTTTCC

Image acquisition

The Hi-FISH screen was performed at the Drosophila RNAi Screening Center (DRSC) at Harvard Medical School Boston (HMS) using a high-throughput spinning-disk confocal microscope (Opera, Perkin Elmer) equipped with a 60×/1.2 numerical aperture (NA) water objective. The screen was performed in 384-well plate in duplicate containing for each duplicate 177 candidate genes, with 129 isolated from a previous screen (Gonzalez et al., 2014) and 48 chosen from the literature, plus 30 control wells (water or GFP-dsRNA).

Confocal imaging was performed with a Leica SP8 microscope (Leica Microsystems) equipped with a ×63/1.4 NA Plan Apochromat oil immersion objective and photomultiplier tube and hybrid detectors for a pixel size of 59 nm and a z-step of 300 nm.

3D-SIM imaging was performed with an OMX-V4 microscope equipped with a 100x/1.4 numerical aperture (NA) Plan Super Apochromat oil immersion objective (Olympus) and electron-multiplying charge-coupled device (EMCCD) (Evolve 512B, Photometrics) cameras for a pixel size of 79 nm (pixel

size of reconstructed images = 39.5 nm). LASERs at 405, 488, and 561 nm were used with the standard corresponding emission filters. Z-stacks were acquired using 125nm stepping, five phases and three angles. Raw images were reconstructed using SoftWorx (version 6.5, GE Healthcare) using channel-specific optical transfer functions. Quality of reconstructed images was assessed using the SIMcheck plugin of ImageJ (Ball et al., 2015).

Image analysis

Screen was analyzed using a MATLAB script developed by Tiao Xie at the IDAC facility (HMS). Output data retrieved mean distance between FISH spots (folding) and number of FISH spot per nucleus. Z-scores were calculated from mean distances obtained with water and GFP controls. Based on Z-scores, 19 candidate genes were identified and further validated using standard FISH protocol and a confocal microscope.

Cell-cycle analysis was performed as described as described in Chapter 2, section 2.1 (Szabo et al., 2018).

FISH combined with immunostaining analysis was conducted using MATLAB. Channels were first smoothed using a 3×3 (6×6 for DAPI) pixels average filter. DAPI and FISH were segmented using intensity-based thresholding. DAPI segmented objects smaller than 4.32 μm^3, larger than 540 μm^3 or in contact to image border were discarded for further analysis. FISH segmented object smaller than 0.0108 μm^3, larger than 0.54 μm^3 or outside DAPI segmented objects were discarded for further analysis. For metaplot of PC enrichment, the channel corresponding to PC signal was maximum projected and values were scaled from 0 to 1. For each FISH object, intensity values normalized by the minimum value within a 31×31-pixel matrix centered on FISH 2D centroid were extracted and summed. Values of the summed matrix were then normalized by the minimum value. For calculation of the relative PC intensity in *Fab-7* signals, the mean PC intensity at the centroid of FISH segmented object was divided by the mean PC intensity within the segmented DAPI. Paired and unpaired nuclei correspond to nuclei with 1 or > 1 FISH segmented object, respectively.

For 3D-SIM analysis, raw super-resolution images were first pre-processed using "Threshold and 16-bit conversion" of the SIMcheck plugin of ImageJ (Ball et al., 2015). Regions of interests (ROIs) surrounding unique nuclei were extracted. ROIs were then analyzed using MATLAB. Channels were smoothed using Gaussian filters (σ = 1 and 4 for FISH and DAPI channels, respectively). DAPI was segmented using Otsu's method and FISH were segmented using a threshold set at 15% of the maximum intensity value. FISH objects smaller than 0.002 μm^3, larger than 0.8 μm^3 or outside segmented DAPI were discarded for further analysis. Distances between FISH segmented objects were calculated between centroids of nearest neighbors labeled in different colors. Distances to the nuclear periphery were

calculated between centroids of FISH segmented objects and the nearest vertex of the convex hull of the DAPI segmented object. Distances were normalized by the mean distance between the centroid of the DAPI segmented object and the vertices of its convex hull. Pairing fraction was calculated by dividing the mean number of segmented FISH signal by the number of genomic domains labeled by the probes.

FISH

FISH was performed as described in Chapter 2, section 2.1 (Szabo et al., 2018).

Hi-C

Hi-C was performed as described in Chapter 2, section 2.1 (Szabo et al., 2018).

RNA extraction, RTq-PCR and RNA-seq library preparation

Medium was removed from wells and cells were incubated for 5 min in 1 mL of Trizol (Invitrogen, Cat.N: 15596026). After up and down pipetting, cells in solution were transferred to Eppendorf tubes and vortexed for 30 sec. 200 µL of chloroform were added and cells were centrifuged for 15 min at > 12,000 rpm at 4°C. Aqueous phase was then processed using RNeasy mini kit (QIAGEN, Cat.N: 74104) with DNase treatment. cDNA synthesis for RT-qPCR was performed using Maxima First Stand cDNA Kit for RT-qPCR (Thermo scientific, Cat.N: K1642) according to the manufacturer's instructions. cDNA quantification was then performed by qPCR (list of primers below) with a Roche Light Cycler and using Light Cycler FastStart DNA Master SYBR Green I Kit (Roche, Cat.N: 03003230001). Expression levels were normalized to pgrp expression. Libraries for RNA-seq were prepared using the TruSeq Stranded mRNA Sample Preparation kit of Illumina and were sequenced at 1x50bp single-end on Illumina HiSeq2500.

baf FWD-primer: 5'-TACACCGTTTTGGGACAGTATCT-3'

baf REV-primer: 5'-CGTGGCACACCTCCTTCATC-3'

Abd-B FWD-primer: 5'-CAAGGGTCACTGGTGCATCTTG-3'

Abd-B REV-primer: 5'-TTCGAGCAGCAACCACAACCAC-3'

pgrp FWD-primer: 5'-TGGGTTACAACAGGATCTCGCT-3'

pgrp REV-primer: 5'-ATATGTGACCATCCTCAACGCC-3'

RNA-seq analysis

Fastq files were aligned to the reference genome (Dm3) using TopHat2 (Kim et al., 2013) with standard parameters and reads were counted using HTSeq-count. Fragments per kilobase per million mapped fragments (FPKM) counts and differential expression were calculated using DESeq2 (Love et al., 2014). Only genes with FPKM > 0 were considered for subsequent analysis.

qChIP

qChIP protocol was adapted from (Schuettengruber et al., 2009) with minor modifications. Briefly, cells were resuspended in their medium and were cross-linked for 10 min in 1.8% paraformaldehyde. Chromatin extracts were sonicated using a Bioruptor (Diagenode) with 12 cycles; 30 sec on, 30 sec off, high power. Sheared chromatin had a size ranging from ~250 to ~750 bp. Immunoprecipitations (IPs) were carried in 500 µL using 5 µL of PC antibody (Schuettengruber et al., 2009) or 2 µL of normal rabbit IgG (Cell Signaling, Cat.N: 2729) for control IP. Immunoprecipitated DNA was analyzed by qPCR with a Roche Light Cycler using Light Cycler FastStart DNA Master SYBR Green I Kit (Roche Cat.N: 03003230001) and normalized to the enrichment on pgrp negative control.

Fab-7 FWD-primer: 5'-TGTGAAGTTCTTGCGACGTG-3'

Fab-7 REV-primer: 5'- AGTCCCTCGAAATTCCTCCG-3'

pgrp FWD-primer: 5'- CCTGGTGAATGATAGCTTACTCTG-3'

pgrp REV-primer: 5'- CTTACTCAAAACCGAAGAGATCG-3'

ChIP-seq Analysis

Publicly available S2 ChIP-seq data for H3K4me1, H3K4me3, H3K36me3, H3K27Ac, H3K27me1, H3K27me2, H3K27me3 and H2AK118ub data (Lee et al., 2015; Herz et al., 2012; Gan et al., 2010) used in this study are listed below. Raw ChIP-Seq sequencing data were collected and aligned to the dm6 version of the fly genome using bowtie 2 with default parameters [v2.1.0, (Langmead and Salzberg, 2012)]. Reads with low mapping quality (mapq<30) were discarded using samtools (Li et al., 2009). RPKM-normalized bigwig binary files were generated using the bamCoverage function from Deeptools2 (v2.5.1) (Ramirez et al., 2016) with the following parameters: -of=bigwig --samFlagExclude 128 --ignoreDuplicates -e 200 –normalizeUsingRPKM. Finally, replicates were merged using the bigWigMerge and bedGraphToBigWig tools from UCSC (Kent et al., 2010) with default parameters. All the linear density bigWig files were imported into R using the "misha" framework (https://github.com/msauria/misha-package).

ChIP	SRA ID	REP	PMID	CELLS
H2AK118ub	SRR1573141	R1	25986499	S2
H2AK118ub	SRR1573142	R2	25986499	S2
H3K27me3	SRR1573145	R1	25986499	S2
H3K27me3	SRR1573146	R2	25986499	S2
H3K27me2	SRR1573149	R1	25986499	S2
H3K27me2	SRR1573150	R2	25986499	S2
H3K27me1	SRR1573153	R1	25986499	S2
H3K27me1	SRR1573154	R2	25986499	S2
H3K4me1	SRR585054	R1	23166019	S2
H3K4me1	SRR585055	R2	23166019	S2
H3K4me3	SRR585056	R1	23166019	S2
H3K4me3	SRR585057	R2	23166019	S2
H3K36me3	SRR038286	R1	20398323	S2

Hi-C analysis

Raw Hi-C sequencing data were processed using the "scHiC2" pipeline (Nagano et al., 2017). Construction of expected models, Hi-C contact scoring and Hi-C aggregate plots was were performed using the "shaman" R package (https://bitbucket.org/tanaylab/shaman). Contact probability decay, insulation score and downstream analyses were conducted using in-house R scripts using the "misha" package (https://github.com/msauria/misha-package). Iced normalized Hi-C maps used for visualization were produced using the HiC-Pro pipeline [version 2.11.1 (Servant et al., 2015)] with default parameters and normalized at 5 and 10kb resolutions using the ice_norm flag. Finally, the hicpro2juicebox utility was used to convert the allValidPairs output of the pipeline into Juicebox .hic format at fragment resolution. TAD calling was performed using the TopDom software [v0.0.2 (Shin et al., 2016)] on the ICED normalized maps (10kb resolution) using win.size=5. TAD segmentation was performed using relative enrichment of each TAD for H3K4me1, H3K4me3, H3K36me3, H3K27Ac, H3K27me1, H3K27me2, H3K27me3 and H2AK118ub levels. Average ChIP-seq enrichments computed for all TADs were stratified using the "kmeans" function in R with centers=3 (R version 3.4.4, https://www.R-project.org).

4.2 Higher-order chromatin organization using 3D DNA Fluorescent in Situ Hybridization

For this manuscript, I wrote the first draft before further ameliorations based on discussions with Frédéric Bantignies. The FISH protocol is an update of the previous one published by my supervisors (Frédéric Bantignies and Cavalli, 2014), based on the benchmarking and improvements that I made to render it more efficient for Drosophila and mammalian cultured cells. I did the experiments and analysis for the figures associated with this protocol. I also sought advices from Thierry Cheutin, a researcher in the lab experienced with the FISH method, and Julio Mateos-Langerack, an engineer from the imaging platform of the institute. The final version was finally revised by Giacomo Cavalli before being submitted.

Higher-order chromatin organization using 3D DNA Fluorescent in Situ Hybridization

Quentin Szabo[1], Giacomo Cavalli[1] and Frédéric Bantignies[1]*

Affiliations:

[1] Institute of Human Genetics, CNRS and University of Montpellier, Montpellier, France.

*Corresponding author: frederic.bantignies@igh.cnrs.fr

Abstract

The comprehensive analysis of the tri-dimensional (3D) organization of the genome is crucial to understand gene regulation. 3D DNA fluorescent in situ Hybridization (3D-FISH) is a method of choice to study nuclear organization at the single-cell level. The labeling of DNA loci of interest provides information on their spatial arrangement, such as their location within the nucleus or their relative positioning. The single-cell information of spatial positioning of genomic loci can thus be integrated with functional genomic and epigenomic features, such as gene activity, epigenetic states, or cell-population averaged chromatin interaction profiles obtained using Chromosome Conformation Capture methods. Moreover, the development of a diversity of super-resolution (SR) microscopy techniques now allows the study of structural chromatin properties at subdiffraction-resolution, making a finer characterization of shapes and volumes possible, as well as allowing the analysis of quantitative intermingling of genomic regions of interest. Here, we present and describe a 3D-FISH protocol adapted for both conventional and SR microscopy such as 3D Structured Illumination Microscopy (3D-SIM), which can be used for the measurement of 3D distances between loci and the analysis of higher-order chromatin structures in cultured *Drosophila* and mammalian cells.

1. Introduction

Our understanding of the mechanisms underlying genome regulation has been recently expanded by a deeper characterization of the relationships between structural and functional properties of chromatin folding. DNA Fluorescent in situ Hybridization (FISH) has been a pioneer technique in

the study of nuclear organization, revealing for example the presence of chromosome territories or the differential location of active and inactive genes [1,2]. In the last decade, molecular biology experiments have allowed the genome-wide characterization of several chromosomal features, such as chromatin epigenetic status, chromatin interaction profiles, or attachment to the nuclear periphery. These methods have provided crucial information, but they cannot address the cell-to-cell variability within populations and therefore they do not provide information as to what extent these features reflect the single cell states. For example, the high-throughput version of the "Chromosome Conformation Capture" method, Hi-C [3], revealed the presence in many species of sub-megabase domains of preferential chromatin interactions, commonly named Topologically Associating Domains (TADs) [4-7]. TADs are often characterized by the enrichment of chromatin interactions within a given genomic region compared to its surrounding chromatin. However, Hi-C experiments represent averaged chromatin interaction profiles typically obtained using millions of cells, hampering the understanding of the structural organization of the chromatin in single-cell. Therefore, FISH appears highly complementary to "Chromosome Conformation Capture" methods in order to decipher how TADs, or any other layer of chromosome organization, fold in individual cells. Recently, different studies have been using FISH to explore the correspondence between single-cell chromatin organizations and genomic-based assays [8-14], showing for instance differential degree of condensation for different chromatin states [9], the large-scale organization of chromosomes into active or repressive compartments [15,13], the absolute contact frequencies between TAD borders [10], or the TAD-based physical organization of chromosomes in *Drosophila* and human cells [8,12]. In this chapter, we will describe a detailed 3D-FISH protocol that can be applied in both *Drosophila* and mammalian cells, which allows investigating the 3D organization of specific genomic regions. Two complementary approaches will be presented: 3-color FISH used to systematically measure 3D distances using confocal laser scanning microscopy (CLSM), and 2-color FISH to characterize chromatin structure using 3D-SIM SR microscopy. This FISH protocol can be combined with immunostaining. In addition, we will briefly describe probe design, and present some guidelines for quantitative image analysis.

2. Materials

2.1 Materials for nick-translation based probe production and labeling

1. Genomic DNA
2. Primers
3. GoTaq G2 Hot Start Green Master Mix (Promega, M7422).
4. PCR purification kit.

5. DNA Marker and ladder
6. LE Agarose
7. FISH Tag DNA kits (Invitrogen Life Technologies, F32951 for the multicolor kit).

2.2 Materials for FISH

2.2.1 General equipment

1. Coverslips 0.170 ± 0.005 mm (also labeled as #1.5H) (Zeiss) (*see* **Note 1**).
2. Inox Tweezers (such as Dumont N°5).
3. Kimwipes Kimtech.
4. 6-well plates for cell culture.
5. Dark humid chamber for slides.
6. Rubber cement.
7. Transparent nail polish.
8. Aluminum block for heating.
9. Water bath with cover (such as VWR digital water bath 5L).
10. Vacuum.

2.2.2 Solutions

1. 0.01% Poly-L-Lysine: 1/10 (vol/vol) of 0.1% Poly-L-Lysine in distilled and deionized water (ddH20).
2. PBS.
3. 4% Paraformaldehyde (make it fresh): 1/10 (vol/vol) of 10× PBS and 1/4 (vol/vol) of 16% formaldehyde in ddH_20.
4. 0.5% Triton X-100 (make it fresh): 1/200 (vol/vol) of Triton X-100 in PBS (*see* **Note 2**).
5. 0.1M HCl: 415 µL of 37% HCl in 50 mL ddH_20 (make it fresh).
6. 2× SSCT: 1/10 (vol/vol) of 20× SSC and 1/1000 (vol/vol) of Tween 20 in ddH_20.
7. 50% Formamide, 2× SSCT (make it fresh): 1/2 (vol/vol) of deionized Formamide (Sigma, F-9037) and 1/2 (vol/vol) of 4× SSCT (4× SSCT made from 1/5 (vol/vol) of 20× SSC and 1/500 (vol/vol) of Tween 20 in ddH_20).
8. 2× SSC: 1/10 (vol/vol) of 20× SSC in ddH_20 (*see* **Note 3**).
9. 0.1× SSC: 1/200 (vol/vol) of 20× SSC in ddH20 (*see* **Note 3**).
10. 0.2× SSC: 1/100 (vol/vol) of 20× SSC in ddH20 (*see* **Note 3**).
11. DAPI (4,6-diamidino-2-phenylindole): 1/100 to 1/1000 of DAPI stock solution (stock solution at 0.1 mg/mL in 180mM Tris-HCl, pH 7.5, stored at -20°C) diluted in PBS (*see* **Note 4**).

2.2.3 Denaturation, hybridization and mounting

1. FISH Hybridization Buffer (FHB): 1/2 (vol/vol) of deionized Formamide, 1/10 (vol/vol) of 20× SSC, 1/5 (vol/vol) of 50% Dextran sulfate solution (made from Dextran sulfate Mw 500,000), sheared Salmon Sperm DNA at final concentration 0.5 mg/mL, volume adjusted in ddH_20. Store FHB in aliquots at -20°C (*see* **Note 5**).
2. RNase A stock in 10 mg/mL solutions at -20°C.
3. Probes.
4. Vectashield.

2.3 Materials for Immunostaining (if combined with FISH, see Note 17)

1. PBT: 1/1000 (vol/vol) Tween 20 diluted in PBS.
2. Blocking solution: 2% BSA diluted in PBT.

2.4 Software

1. Primer design: Primer 3 (for the nick-translation based probes, see section 3.1.1)
2. Image analysis: A wide range of software can be used for FISH analysis (see section 3.4)

3. Methods.

3.1 Probe design and production

Choose the genomic region of interest. After selecting the region, different approaches can be used to obtain DNA fluorescent probes. Here, we will use two different methods. The first one consists in amplifying the genomic region of interest using PCR, followed by direct labeling of DNA fragments by nick-translation. The second one uses the Oligopaint technology, developed in the laboratory of C.-T. Wu (Harvard Medical School Boston) and described in [16]. An example of probe design based on Hi-C map and using these two methods is shown in **Fig. 1**.

3.1.1 Probes labeled by nick-translation

Extract the genomic sequence of interest covering 10-12 kb (for *Drosophila* probes) or 20-24 kb (for mammalian probes) and subdivide the sequence into contiguous 2 kb segments, i.e. representing a total of 5-6 fragments for *Drosophila* and 10-12 fragments for mammals (*see* **Note 6**). It is crucial to avoid including repeat sequences such as transposable elements. For each segment, design PCR primers using Primer3 software (http://primer3.ut.ee/) in order to obtain amplicons of 1.2-1.7 kb, again avoiding repeat sequences by using the appropriate reference genome. After purification, the products can be re-amplified using a second round of PCR in order to increase the concentration, and purified again. PCR fragments are then directly labeled using the FISH Tag DNA kit, starting one given probe with 1µg of total DNA from every PCR fragments pooled in equimolar amount. Follow the procedure describe in the FISH Tag DNA kit protocol (*see* **Note 7**).

3.1.2 Oligopaint probes

To produce Oligopaint probes, we recommend to follow the procedures described by Beliveau et al. [16,17]. Additional information can be found on the Oligopaint website: https://oligopaints.hms.harvard.edu/. Briefly, this technique consists in producing series of DNA oligos composed of a homology genomic sequence targeting the region of interest and a non-genomic "MainStreet" tail labeled with a fluorophore. The MainStreet tail can be targeted with secondary oligos carrying additional fluorophores to increase the fluorescence signal.

3.1.3 Control probes

The very nature of light or, sometimes, the design of the microscope, introduces biases and systematic errors during image acquisition. Depending on the type of the analysis, it can thus

be necessary to assess errors such as chromatic aberrations by producing a set of probes labeled simultaneously with different fluorophores and/or produce color-swapped probes (two sets of probes where fluorophores are swapped) (see section 3.4.5). This is more accurate than simply imaging fluorescent labeled beads in mounting medium because the optical path between the control and the actual experiment environments is the same. In the case of nick-translation based probes, the series of the 1.2-1.7 kb fragments of one probe can be alternatively labeled with the different fluorophores, i.e. in a 6-fragments scenario and a 3-color FISH experiments, one color for fragments 1 and 4, another color for fragments 2 and 5, and another color again for fragments 3 and 6. For Oligopaints, secondary oligos labeled with a different fluorophore than the primary one can be used.

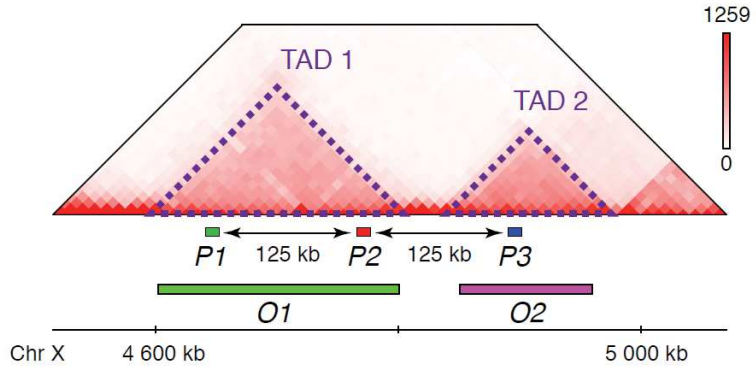

Fig. 1 Example of FISH experimental design to study TAD folding. Hi-C map (visualized with Juicebox [22]) from *Drosophila* S2R+ cells representing a specific chromosomal region along with the location of FISH probes. TADs are highlighted with dashed lines. *P1*, *P2*, and *P3* probes were produced using the nick-translation method starting from 6 PCR fragments each, and were labeled with Alexa-488, Alexa-555 and Alexa-647 fluorophores, respectively. P1-P2 and P2-P3 are at equivalent genomic distances, i.e. 125 kb. Control probes (2 PCR fragments each) were produced by alternatively labeling the PCR fragments of the *P2* region with Alexa-488, Alexa-555 and Alexa-647 fluorophores, respectively. *O1* and *O2* Oligopaint probes were labeled with Alexa-488 and ATTO-565, respectively. On one side, this design with the nick-translation based probes allows studying 3D distances between loci inside TADs versus between loci located in two adjacent TADs (see **Fig. 3**). On the other side, this design with the Oligopaint probes allows studying some physical properties of TADs in single cells, such as their size or the degree of overlap between two adjacent TADs (see **Fig. 4**).

3.2 FISH procedure

3.2.1 FISH

This protocol is designed for FISH on cells attached on coverslips (*see* **Note 8**). Individual coverslips are placed within a well of a 6-well plate. For each incubation step, 3 mL (or 4 mL for washes) of the appropriate solution are deposited within the well, and aspirated after the incubation time using vacuum before the next step. Unless specific indications, incubations are performed at room temperature.

1. Prepare coverslips: deposit each coverslip in a well of a 6-well plate, rinse with 100% ethanol, allow coverslips to dry 5-15 min, incubate for 5 min in 0.01% Poly-L-Lysine, and allow coverslips to dry again (*see* **Note 9**).
2. Deposit coverslips within a humid chamber, i.e. with water deposited in the bottom of the chamber without touching the coverslips (*see* **Note 10**).
3. Prepare a cell suspension of ~1.5-2.10^6 cells/ml in growth media and apply 100 µl of the cell suspension in the center of each coverslip. Allow cells to adhere to coverslips for approximately 1 h (*see* **Note 10**).
4. Take coverslips with tweezers, plunge them briefly in a recipient containing PBS, and deposit them (cells facing up) within wells of a 6-well plate (*see* **Note 10**).
5. Fix for 10 min in 4% Paraformaldehyde.
6. Wash three times for at least 2 min each in PBS.
7. Incubate for 10 min in 0.5% Triton X-100.
8. Wash three times for at least 2 min each in PBS.
9. Incubate for 10 min in 0.1 M HCl.
10. Wash twice for 2 min each in 2× SSCT.
11. Incubate for at least 30 min in 50% Formamide, 2× SSCT (*see* **Note 11**).
12. Prepare probe mixture: for nick-translation probes, mix 15-30 ng of each probe with 0.8 µL of RNase A in FHB for a total volume of 15-25 µL (*see* **Note 12 and 13**); for Oligopaint probes, mix probes (each at ~1-3 µM final concentration) with the same amount of their secondary oligo and 0.8µL of RNase A in FHB for a total volume of 15-25 µL. For both nick-translation and Oligopaint probes, keep the highest possible ratio of FHB/total volume (*see* **Note 14**).
13. Use tweezers to take out coverslips from wells, lay the coverslips with cells facing up and drain off the excess of liquid with Kimwipes without touching the cells.
14. Add probe mixtures directly on coverslips.
15. Invert coverslips onto slides, i.e. cells and probe mixture between the coverslip and the slide, and seal coverslips on slides with rubber cement. Allow rubber cement to air-dry about 10-15 min.

16. Denature DNA by putting slides, coverslips facing up, for 3 min at 78°C or 80°C on a heating block immersed in a water bath.
17. Remove slides from the heating block, and deposit them in a dark humid chamber for O/N hybridization (14 to 20 h), at 37-52°C (*see* **Note 15**).
18. Use tweezers to peel off rubber cement and deposit coverslips (cells facing up) into wells containing 2× SSC (*see* **Note 16**).
19. Wash three times for 5 min each at 37°C in 2× SSC by putting the 6-well plate floating within a water bath (*see* **Note 16**).
20. Wash three times for 5 min each at 45°C in 0.1× SSC by putting the 6-well plate floating within a water bath (*see* **Note 16**).
21. Wash twice in PBS (*see* **Note 17**).
22. Incubate for 10 min with DAPI (*see* **Note 4** for concentrations), with gentle agitation.
23. Wash three times with PBS (*see* **Note 18**).
24. Use tweezers to take out coverslips from wells, lay the coverslips with cells facing up and drain off the excess of liquid with Kimwipes without touching the cells.
25. Deposit one drop of Vectashield (~12 µL) on the cells.
26. Invert coverslips onto slides, i.e. cells and Vectashield between the coverslip and the slide, and seal coverslips on slides with nail polish. Allow nail polish to air-dry for ~1h (*see* **Note 19**).
27. Slides can be stored up to 2 weeks in the dark at 4°C before imaging.

3.2.2 FISH combined with Immunostaining

To combine FISH with immunostaining, proceed as following after step n° 21 of section 3.2.1 of the FISH procedure.

1. Wash three times for at least 1 min each with PBT.
2. Incubate in blocking solution for 30-60 min.
3. Use tweezers to take out coverslips from wells, lay the coverslips with cells facing up and drain off the excess of liquid with Kimwipes without touching the cells.
4. Add primary antibody diluted in blocking solution (total volume of ~20 µL) directly on coverslips.
5. Invert coverslips onto slides, i.e. cells and antibody solution between the coverslip and the slide, and incubate for 120 min at room temperature or overnight at 4°C in a dark humid chamber.

6. Wash for 1 min, 3 min and twice 5 min with PBT.
7. Use tweezers to take out coverslips from wells, lay the coverslips with cells facing up and drain off the excess of liquid with Kimwipes without touching the cells.
8. Add secondary antibody diluted in blocking solution (total volume of ~20 µL) directly on coverslips.
9. Invert coverslips onto a slide, i.e. cells and antibody solution between the coverslip and the slide, and incubate for 60 min at room temperature in a dark humid chamber.
10. Wash for 1 min, 3 min and twice 5 min with PBT.
11. Proceed as described in section 3.2.1 from step n° 21 (included).

3.3 Image acquisition

Conventional wide-field microscopy, CLSM, and SR methods such as 3D-SIM can be used to image 3D-FISH experiments. A good image quality with a good resolution and signal-to-noise ratio (SNR) is essential for analysis. Use objectives with the highest numerical aperture (NA), they will optimize both signal and resolution. To maximize the signal, use bright and photo-stable fluorophores. Increase the SNR by increasing exposure time and laser power rather than using detector gain. While doing so, keep under control the eventual photobleaching. The images should use as much as possible of the dynamic range of the camera, avoiding saturated pixels because the correspondence emitted photons and electrons (and therefore between the sample and the intensity) will be lost. To take advantage of the resolution offered by the microscope, the sampling distances in lateral (xy) and axial (z) directions should ideally be less than half the theoretical resolution accordingly to the Nyquist criterion. Most modern microscopes do provide tools to calculate those sampling densities.

1. **CLSM:** Here, CLSM images were acquired with a Leica SP8 microscope equipped with a ×63/1.4NA Plan Apochromat oil immersion objective and photomultiplier tube and hybrid detectors, for a pixel size of 59 nm and z-step size of 300 nm.

2. **3D-SIM:** To successfully perform 3D-SIM imaging, we strongly recommend to refer to the protocol published by Demmerle et al. [18], which provides comprehensive and detailed guidelines to obtain super-resolution images of quality. Here, 3D-SIM images were acquired with an OMX V4 microscope (GE Healthcare) equipped with a ×100/1.4NA PSF Plan Super Apochromat oil immersion objective (Olympus), electron-multiplying charge-coupled device (EMCCD) (Photometrics) cameras, for a pixel size of 80 nm and z-step size of 125 nm. Z-stacks were acquired with five phases and three angles per image plane. Raw images were reconstructed using SoftWoRx v6.5 or 7.0 (GE Healthcare), using channel-specific optical transfer functions (pixel size of reconstructed images: 40 nm). Quality of super-resolution reconstructed images were assessed using the SIMcheck plugin [19] on Fiji software [20]. Alignments of colors used for FISH probes was done with Chromagnon [21], using as

reference image Oligopaint FISH probe simultaneously labeled with Alexa-488 and ATTO-565 fluorophores (*see* **section 3.1.3**).

3.4 Image analysis

The following part is a basic guideline for FISH analysis. Quantitative image analysis can be addressed using a variety of software packages. For example, Image J is a widely used, free and open-source software enriched by many plug-ins. Other commercial software packages, such as Imaris or Volocity, allow image analysis with a polished and user-friendly graphic user interface. Programming using for example Matlab, Python or ImageJ's own scripting interfaces offer other advantages such as a high versatility and adaptability to specific aims. All the following steps of this part can be addressed using a wide range of software or programs and do not require particular knowledge in programing for image analysis.

3.4.1 Image pre-processing: Before starting the analysis, data can first be processed in order to reduce the noise of microscopic images (**Fig. 2a, b**). Image analysis software often proposes different types of filters, such as Gaussian, median or average filters. For example, a 3x3 average filter will replace each pixel value with the neighboring mean in a 3x3 pixel region. This will have a blurring effect on the image and thus reduce the noise, which can facilitate further segmentation processes. It will, however, come at the cost of losing resolution. Other more sophisticated techniques, such as image deconvolution, will increase SNR and resolution at the same time, but a certain experience is necessary to avoid the introduction of artifacts.

3.4.2 Segmentation: To separate and identify the labeled objects an intensity threshold value is defined in order to obtain a binary image in which pixels will be divided into two classes, one under the threshold corresponding to the background, and one above the threshold corresponding to the labeled objects. To define the threshold, it can be helpful to visualize the grayscale intensity value distribution of the image using histograms. Image analysis software often provides automatic thresholding algorithms (such as Otsu's method) that can be tested in order to obtain satisfying segmentation. However, it may be difficult to obtain acceptable thresholding using an automatic method, and a threshold value may be manually defined. It is important to have a visual feedback to verify the quality of the segmentation. Examples of segmentations using thresholding are shown in **Fig. 2c.** Volume range can be defined to discard too small or too large objects, and it can also be very useful to segment DAPI staining in order to define nuclei in which FISH signals will be analyzed (DAPI mask), i.e. FISH signals outside DAPI segmented objects will be automatically discarded for the analysis (**Fig. 2d**). This can be particularly helpful if some non-specific residual fluorescent signal remains outside nuclei. Moreover, it can be useful to identify individual nuclei for further single-cell analysis. However, if nuclei are too crowded, it may be difficult to automatically segment individual nuclei.

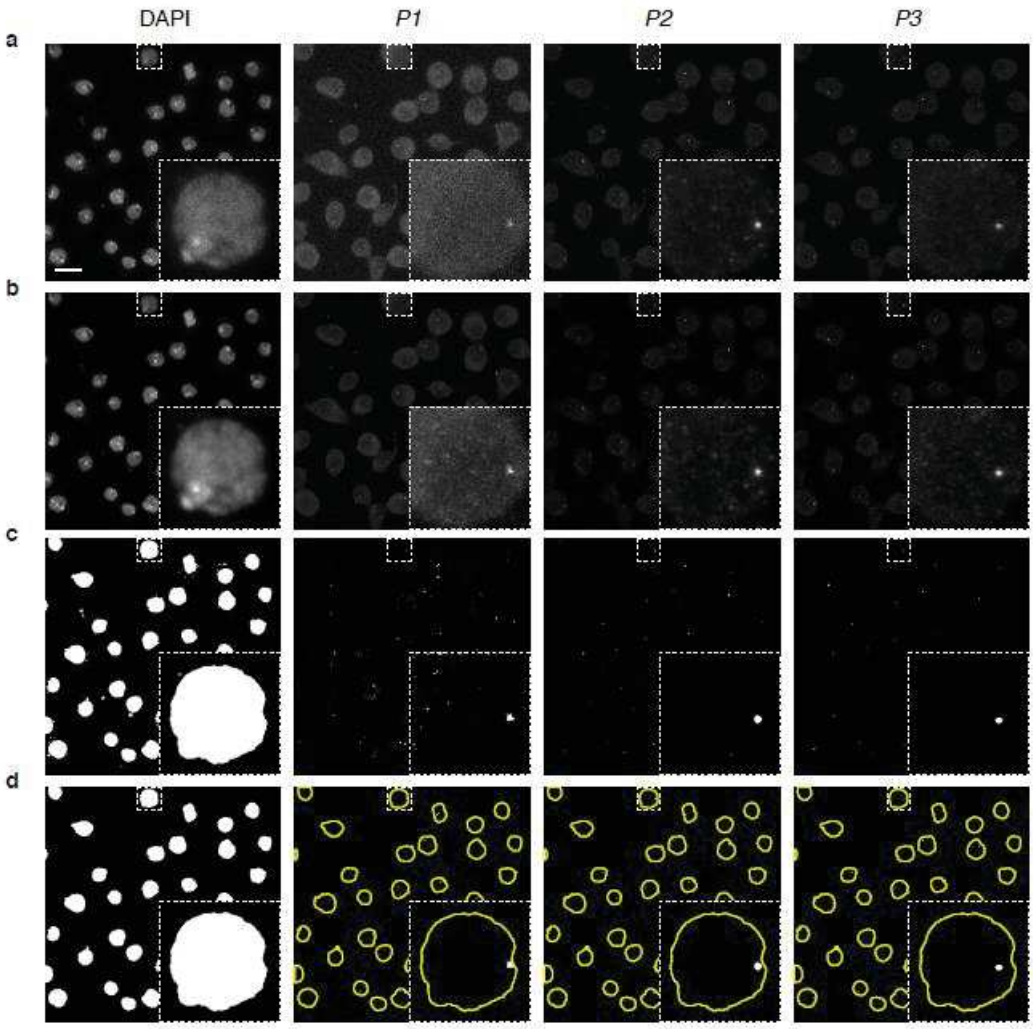

Fig. 2 Example of image processing and segmentation filtering. Each column represents a maximum projection of an individual channel from a 3-color FISH experiment (DAPI and *P1*, *P2*, *P3* probes shown in **Fig. 1**), along with a magnification of the region within the square. **(a)** Raw images. **(b)** Image pre-processing using a smoothing filter in order to reduce the noise. **(c)** Image segmentation. **(d)** Filtering of segmented objects using size criteria, i.e. too small and too large objects are discarded, and DAPI mask applied to FISH, i.e. segmented FISH outside of the DAPI segmented objects are discarded. Scale bar: 10 μm.

3.4.3 FISH object identification: FISH objects can be segmented using intensity-based routines as presented above. Keep in mind that structures of loci of tens to hundreds of kb cannot generally be resolved using conventional wide-field or CLSM microscopy (~200

nm lateral and ~500 nm axial resolution). In this case, segmented objects are larger than the real genomic loci. Loci can thus be defined by the subpixel weighted centroids of segmented FISH objects (**Fig. 3b**). Local intensity maxima approaches can also be used, which identify high intensity pixels that stand out from the surrounding pixels by more than a defined intensity value. However, if the labeled genomic regions are large enough to be resolved, FISH segmentation can also provide information such as the volume of the regions and their intermingling (number of segmented voxels multiplied by the voxel volume, **Fig. 4**), although, segmented volume may not accurately corresponds to the absolute volume of the real genomic loci (the error increasing with the volume decreasing). Indeed, the volume of the segmented object strongly depends on the defined threshold value, thus special care must be taken to interpret this type of analysis. Depending on the quality of the FISH probes, the SNR and the efficiency of the intensity-based FISH identification, some nuclei may display false positive signals and, on the other hand, not all nuclei may display FISH objects. If individual nuclei have been segmented, an efficient way to minimize errors is to define a minimum and maximum number of FISH objects per nucleus such that nuclei that do not respect these criteria will be discarded for the analysis. Further data processing can also be used to ensure proper analysis (see the following step).

3.4.4 3D distance measurements: After FISH objects identification, their *x*, *y* and *z* coordinates are extracted. If objects were identified as segmented objects instead of single voxels, these coordinates can be defined by their centroids. The Euclidean distance is then calculated between coordinates of the FISH signals of different colors, allowing for example identification of nearest neighbors using the shortest 3D distance for a given FISH object (**Fig. 3c**). Alternatively, computing the Euclidean distance transform of binary images can provide nearest distances between segmented objects. Keeping only the mutual nearest neighbors between the different channels can also remove outliers. For example, the nearest distance of a FISH object within a nucleus missing the FISH object from the other color may actually represent a distance between FISH objects from different nuclei or unpaired loci. The distance distribution can also inform on the presence of outliers, a distance cutoff can thus be used to remove them. Moreover, in 3-color FISH experiments, having triplets of mutually nearest neighbors allows paired analysis of distances, i.e. distance between one pair of colors compared to the other pairs from the same nucleus (**Fig. 3d**).

3.4.5 Control measurements: Errors such as chromatic aberrations or other biases induced by the different wavelengths of the probes, which can lead to systematic shifts between the different probes, have to be assessed. A way to do so is to perform the same experiment and analysis from control experiments with a set of probes labeled simultaneously with the different fluorophores. This control can be used to correct the positioning of target loci and/or to estimate the error of the measurement and calculate the distance distribution corresponding to a truly co-localized genomic region (**Fig. 3c**).

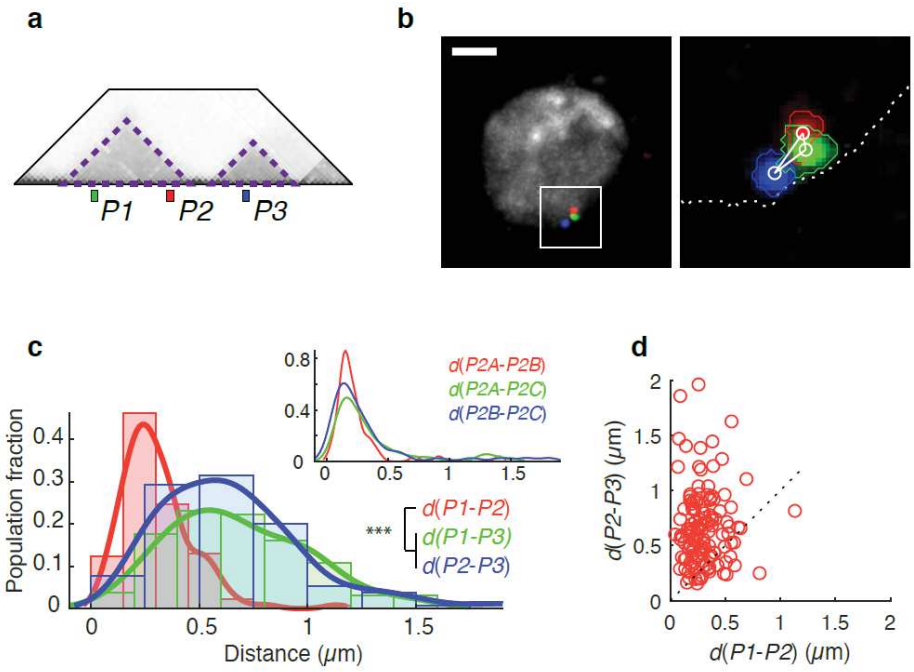

Fig. 3 Example of 3D-FISH analysis using CLSM. (**a**) *P1* (in green), *P2* (in red) and *P3* (in blue) probes were designed to measure 3D distances within a TAD (*d*(*P1-P2*)) and between two adjacent TADs (*d*(*P1-P3*) and *d*(*P2-P3*)). (**b**) Left, example of CLSM imaging of DAPI (in gray) and FISH probes in S2R+ cells; Right, zoom in the square showing processed image. Segmented object contours are shown (dashed line for DAPI, segmentation using Otsu's method automatic thresholding; colored lines for FISH, segmentation using a defined threshold value from intensity distribution and visual inspection), and circles indicate centroids of segmented FISH objects (mutual nearest neighbors linked to each other with white lines). Maximum intensity projections are shown. Scale bar: 2 µm. (**c**) Histograms and distribution fits of mutual nearest neighbor 3D distances (from 130 nuclei). On top right, mutual nearest neighbor 3D distance distributions between the different control probes (*P2a*, *P2b*, and *P2c* for Alexa-488, Alexa-555, and Alexa-647, respectively, from 49 nuclei). The differences in distance distribution observed in the actual experiments (*P1*, *P2* and *P3* probes) are not observed with the control probes, indicating that they are not due to technical bias. *** $P < 0.0001$ with Kruskal-Wallis and Dunn's multiple comparisons tests. (**d**) Single-cell paired distance analysis, with the *P1-P2* distance compared to the *P2-P3* distance from each triplets of mutual nearest FISH neighbors. The *P1-P2* distance is shorter than the *P2-P3* distance in 85% of the analyzed nuclei. This analysis indicates that the probes located in the same TADs are closer compare to probes located into adjacent TADs in a large majority of single-cells, although they are at the same genomic distance.

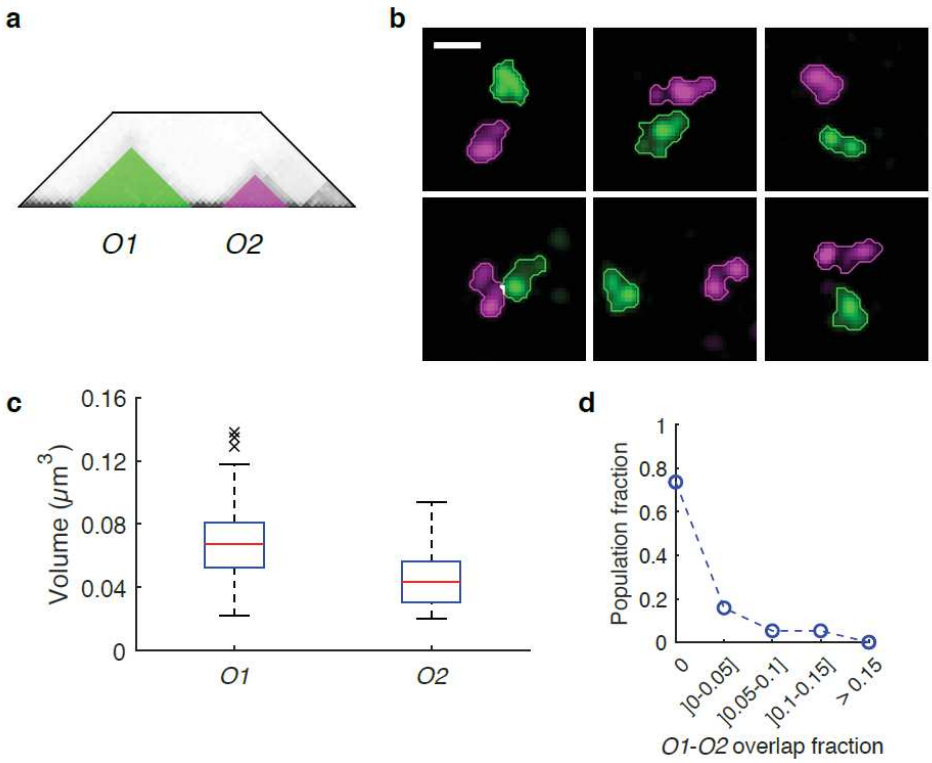

Fig. 4 Example of 3D-FISH analysis using 3D-SIM. (**a**) *O1* (in green) and *O2* (in magenta) probes were used to label two adjacent TADs. (**b**) Examples of 3D-SIM imaging of the probes with their segmentation (Otsu's method automatic thresholding) contour in S2R+ cells. Maximum intensity projections are shown, scale bar: 500 nm. (**c**) Super-resolution 3D-SIM allows the volume quantification of the segmented probes (from 38 nuclei). (**d**) Volume overlap fraction (using the Jaccard index) between *O1* and *O2* probes. This analysis illustrates the physical partitioning of the genome into TADs in *Drosophila* cells.

4. Notes

1. The thickness of the support of the cells is crucial for optimal imaging, especially with SR microscopy. We recommend to use coverslips of 170 ± 5 µm.
2. Triton X-100 is highly viscous. It can be convenient to do an initial 1/10 (vol/vol) solution in ddH_20 before further dilutions.
3. Prepare the SSC buffers according to the chosen washing steps of the FISH procedure (see section **3.2.1** and **Note 16**).
4. For conventional microscopy, we recommend a final DAPI concentration of 0.1µg/mL, for 3D-SIM, we recommend to increase up to 1 µg/mL. When using DAPI, we recommend a

relatively fresh batch. DAPI staining is very efficient and may last for many years, however, the quality of a DAPI staining for 3D-SIM is remarkably reduced using aged DAPI.

5. First prepare a 50% Dextran sulfate solution dissolving 5 g of Dextran sulfate with 7 mL of pre-warmed ddH_20 at 60°C (total volume of 10 mL) in a 50 mL falcon tube. Solution can be stored at 4°C.
6. The higher is the number of fragments, the better will be the fluorescent signal. 5-6 PCR fragments in *Drosophila* and 10-12 PCR fragments in mouse generally ensure good signals, although this number may eventually be reduced.
7. The labeling of probes is described in the FISH Tag DNA kit, however, we adapted the nick-translation reaction to optimize using a pool of 1.2-1.7 kb DNA fragments, representing 1 µg of total DNA. For this, we use 1.4-1.7 µL of DNase I working solution for a 50 µL nick-translation reaction during 90-120 min. We also recommend to first run a time-course test of nick-translation, for which the reaction is performed in the same manner, but 5 µL are taken out from the reaction mix every 30 min (from 0 to 120 min). As soon as 5 µL aliquots are taken out, vortex well to inhibit DNase I (you can also add EDTA), and freeze at -20°C before running every aliquots in gel electrophoresis. Gels should display smears decreasing gradually in size with time. Smears ranging from approximately 100 to 300 bp represent the optimal condition for the nick-translation reaction. You can also further increase or decrease the amount of DNase I in order to reach this optimal condition for a 90-120 min reaction. At the end of the labeling procedure, the efficiency of dye incorporation will depend on the fluorophore, and good probes should have approximately 5-10 pmol/µL of A488 dye, 1-3 pmol/µL of A555 dye, and 4-8 pmol/µL of A647 dye.
8. Because of the smaller thickness, we recommend to use coverslips rather than slides for optimal imaging (especially for SR microscopy). However, this protocol can also be used with cells attached to slides. In this case, incubation steps are performed with slides deposited in Coplin jars instead of coverslips deposited in 6-well plates.
9. Alternatively, grow cells on autoclaved and coated coverslips, each coverslip within a well of a 6-well plate.
10. If cells were directly grown in 6-well plates, aspirate the media with a vacuum and rinse with PBS instead of steps 2, 3 and 4.
11. Alternatively, incubate for at least 20 min in 50% Formamide, 2× SSCT, then incubate for 20 min in 50% Formamide, 2× SSCT at 60°C by putting the 6-well plate floating in a water bath. We obtain better results with mammalian cells using this step instead.

12. If you use nick-translation-based probes, denature probes for 10 min at 80°C and put them on ice until usage.
13. If you use mammalian cells and nick-translation-based probes, include within the probe mixture Cot-1 DNA. For example, for mouse cells, use mouse Cot-1 DNA (Invitrogen life technologies, 18440-016) at a final concentration of 0.1-0.2 µg/µL to suppress potential hybridization with repetitive sequences.
14. The higher the FHB/total volume ratio is, the better is the hybridization. A typical experiment uses approximately 2 µL of probes plus 0.8 µL of RNase, which gives a ~8-9/10 ratio for 20 µL of total volume. Do not go lower than a 3/4 ratio of FHB/total volume.
15. The hybridization temperature may vary depending on the probes, with stringency increasing with temperature. We obtain efficient hybridization at 37°C using both nick-translation based probes and Oligopaints with 42-mer genomic sequences in *Drosophila* cells; For Oligopaints, we recommend to refer to [17] to choose the optimal hybridization temperature.
16. This note is an alternative of the 18, 19 and 20 washing steps. Use tweezers to peel off rubber cement and deposit coverslips (cells facing up) into wells containing 2× SSCT. Wash for 15 min at 60°C in 2× SSCT, then wash for 10 min at room temperature in 2× SSCT, then wash for 10 min at room temperature in 0.2× SSC. We obtain better results with mammalian cells using this washing procedure instead.
17. FISH can be followed by immunostaining against proteins of interests (*see* Section 3.2.2). However, the FISH procedure can alter protein integrity and/or epitopes, and immunostaining may not be suitable with some proteins or antibodies.
18. If samples are going to be imaged using 3D-SIM, extensive washing of DAPI is crucial. Wash three times for at least 5 min each instead.
19. Manage the amount of Vectashield so that there is not too much. Clean the excess of mounting medium before sealing.

Acknowledgement

We thank Julio Mateos-Langerak and Thierry Cheutin for critical reading of the manuscript. We thank the Montpellier Resources Imagerie facility (BioCampus Montpellier, CNRS, INSERM, Université de Montpellier). Q.S. is supported by the French Ministry of Higher Education and

Research, and La Ligue Nationale Contre le Cancer. F.B. is supported by the CNRS. Research at the G.C. laboratory is supported by grants from the CNRS, the FP7 European Network of Excellence EpiGeneSys, the European Union's Horizon 2020 research and innovation programme under grant agreement No 676556 (MuG), the Agence Nationale de la Recherche (ANR-15-CE12-0006 EpiDevoMath), the Fondation pour la Recherche Médicale (DEI20151234396), the INSERM, the French National Cancer Institute (INCa) and the Laboratory of Excellence EpiGenMed.

References

1. Bickmore WA (2013) The spatial organization of the human genome. Annu Rev Genomics Hum Genet 14:67-84. doi:10.1146/annurev-genom-091212-153515

2. Cremer T, Cremer M (2010) Chromosome territories. Cold Spring Harb Perspect Biol 2 (3):a003889. doi:10.1101/cshperspect.a003889

3. Lieberman-Aiden E, van Berkum NL, Williams L, Imakaev M, Ragoczy T, Telling A, Amit I, Lajoie BR, Sabo PJ, Dorschner MO, Sandstrom R, Bernstein B, Bender MA, Groudine M, Gnirke A, Stamatoyannopoulos J, Mirny LA, Lander ES, Dekker J (2009) Comprehensive mapping of long-range interactions reveals folding principles of the human genome. Science 326 (5950):289-293. doi:326/5950/289 [pii] 10.1126/science.1181369

4. Dixon JR, Selvaraj S, Yue F, Kim A, Li Y, Shen Y, Hu M, Liu JS, Ren B (2012) Topological domains in mammalian genomes identified by analysis of chromatin interactions. Nature 485 (7398):376-380. doi:10.1038/nature11082

5. Hou C, Li L, Qin ZS, Corces VG (2012) Gene density, transcription, and insulators contribute to the partition of the Drosophila genome into physical domains. Mol Cell 48 (3):471-484. doi:10.1016/j.molcel.2012.08.031

6. Nora EP, Lajoie BR, Schulz EG, Giorgetti L, Okamoto I, Servant N, Piolot T, van Berkum NL, Meisig J, Sedat J, Gribnau J, Barillot E, Bluthgen N, Dekker J, Heard E (2012) Spatial partitioning of the regulatory landscape of the X-inactivation centre. Nature 485 (7398):381-385. doi:10.1038/nature11049

7. Sexton T, Yaffe E, Kenigsberg E, Bantignies F, Leblanc B, Hoichman M, Parrinello H, Tanay A, Cavalli G (2012) Three-Dimensional Folding and Functional Organization Principles of the Drosophila Genome. Cell 148:458-472. doi:10.1016/j.cell.2012.01.010

8. Bintu B, Mateo LJ, Su JH, Sinnott-Armstrong NA, Parker M, Kinrot S, Yamaya K, Boettiger AN, Zhuang X (2018) Super-resolution chromatin tracing reveals domains and cooperative interactions in single cells. Science 362 (6413). doi:10.1126/science.aau1783

9. Boettiger AN, Bintu B, Moffitt JR, Wang S, Beliveau BJ, Fudenberg G, Imakaev M, Mirny LA, Wu CT, Zhuang X (2016) Super-resolution imaging reveals distinct chromatin folding for different epigenetic states. Nature 529 (7586):418-422. doi:10.1038/nature16496

10. Cattoni DI, Cardozo Gizzi AM, Georgieva M, Di Stefano M, Valeri A, Chamousset D, Houbron C, Dejardin S, Fiche JB, Gonzalez I, Chang JM, Sexton T, Marti-Renom MA, Bantignies F, Cavalli G, Nollmann M (2017) Single-cell absolute contact probability detection reveals chromosomes are organized by multiple low-frequency yet specific interactions. Nature communications 8 (1):1753. doi:10.1038/s41467-017-01962-x

11. Fudenberg G, Imakaev M (2017) FISH-ing for captured contacts: towards reconciling FISH and 3C. Nat Methods 14 (7):673-678. doi:10.1038/nmeth.4329

12. Szabo Q, Jost D, Chang JM, Cattoni DI, Papadopoulos GL, Bonev B, Sexton T, Gurgo J, Jacquier C, Nollmann M, Bantignies F, Cavalli G (2018) TADs are 3D structural units of higher-order chromosome organization in Drosophila. Sci Adv 4 (2):eaar8082. doi:10.1126/sciadv.aar8082

13. Wang S, Su JH, Beliveau BJ, Bintu B, Moffitt JR, Wu CT, Zhuang X (2016) Spatial organization of chromatin domains and compartments in single chromosomes. Science 353 (6299):598-602. doi:10.1126/science.aaf8084

14. Williamson I, Berlivet S, Eskeland R, Boyle S, Illingworth RS, Paquette D, Dostie J, Bickmore WA (2014) Spatial genome organization: contrasting views from chromosome conformation capture and fluorescence in situ hybridization. Genes & development 28 (24):2778-2791. doi:10.1101/gad.251694.114

15. Nir G, Farabella I, Perez Estrada C, Ebeling CG, Beliveau BJ, Sasaki HM, Lee SD, Nguyen SC, McCole RB, Chattoraj S, Erceg J, AlHaj Abed J, Martins NMC, Nguyen HQ, Hannan MA, Russell S, Durand NC, Rao SSP, Kishi JY, Soler-Vila P, Di Pierro M, Onuchic JN, Callahan SP, Schreiner JM, Stuckey JA, Yin P, Aiden EL, Marti-Renom MA, Wu CT (2018) Walking along chromosomes with super-resolution imaging, contact maps, and integrative modeling. PLoS genetics 14 (12):e1007872. doi:10.1371/journal.pgen.1007872

16. Beliveau BJ, Boettiger AN, Avendano MS, Jungmann R, McCole RB, Joyce EF, Kim-Kiselak C, Bantignies F, Fonseka CY, Erceg J, Hannan MA, Hoang HG, Colognori D, Lee JT, Shih WM, Yin P, Zhuang X, Wu CT (2015) Single-molecule super-resolution imaging of chromosomes and in situ haplotype visualization using Oligopaint FISH probes. Nature communications 6:7147. doi:10.1038/ncomms8147

17. Beliveau BJ, Kishi JY, Nir G, Sasaki HM, Saka SK, Nguyen SC, Wu CT, Yin P (2018) OligoMiner provides a rapid, flexible environment for the design of genome-scale oligonucleotide in situ hybridization probes. Proc Natl Acad Sci U S A 115 (10):E2183-E2192. doi:10.1073/pnas.1714530115

18. Demmerle J, Innocent C, North AJ, Ball G, Muller M, Miron E, Matsuda A, Dobbie IM, Markaki Y, Schermelleh L (2017) Strategic and practical guidelines for successful structured illumination microscopy. Nature protocols 12 (5):988-1010. doi:10.1038/nprot.2017.019

19. Ball G, Demmerle J, Kaufmann R, Davis I, Dobbie IM, Schermelleh L (2015) SIMcheck: a Toolbox for Successful Super-resolution Structured Illumination Microscopy. Sci Rep 5:15915. doi:10.1038/srep15915

20. Schindelin J, Arganda-Carreras I, Frise E, Kaynig V, Longair M, Pietzsch T, Preibisch S, Rueden C, Saalfeld S, Schmid B, Tinevez JY, White DJ, Hartenstein V, Eliceiri K, Tomancak P, Cardona A (2012) Fiji: an open-source platform for biological-image analysis. Nat Methods 9 (7):676-682. doi:10.1038/nmeth.2019

21. Matsuda A, Schermelleh L, Hirano Y, Haraguchi T, Hiraoka Y (2018) Accurate and fiducial-marker-free correction for three-dimensional chromatic shift in biological fluorescence microscopy. Sci Rep 8 (1):7583. doi:10.1038/s41598-018-25922-7

22. Durand NC, Robinson JT, Shamim MS, Machol I, Mesirov JP, Lander ES, Aiden EL (2016) Juicebox Provides a Visualization System for Hi-C Contact Maps with Unlimited Zoom. Cell Syst 3 (1):99-101. doi:10.1016/j.cels.2015.07.012

References

Abney, J. R., Cutler, B., Fillbach, M. L., Axelrod, D., & Scalettar, B. A. (1997). Chromatin dynamics in interphase nuclei and its implications for nuclear structure. Journal of Cell Biology, 137(7), 1459–1468.

Albiez, H., Cremer, M., Tiberi, C., Vecchio, L., Schermelleh, L., Dittrich, S., … Cremer, T. (2006). Chromatin domains and the interchromatin compartment form structurally defined and functionally interacting nuclear networks. Chromosome Research, 14(7), 707–733.

Allahyar, A., Vermeulen, C., Bouwman, B. A. M., Krijger, P. H. L., Verstegen, M. J. A. M., Geeven, G., … de Laat, W. (2018). Enhancer hubs and loop collisions identified from single-allele topologies. Nature Genetics, 50(8), 1151–1160.

Andrey G., Montavon T., Mascrez B., Gonzalez F., Noordermeer D., Leleu M., … Duboule D. (2013). A switch between topological domains underlies HoxD genes collinearity in mouse limbs. Science. 2013 Jun 7;340(6137):1234167.

Apostolou, E., Ferrari, F., Walsh, R. M., Bar-Nur, O., Stadtfeld, M., Cheloufi, S., … Hochedlinger, K. (2013). Genome-wide chromatin interactions of the nanog locus in pluripotency, differentiation, and reprogramming. Cell Stem Cell, 12(6), 699–712.

Avery, O.T., MacLeod, C.M., McCarty, M. (1944). STUDIES ON THE CHEMICAL NATURE OF THE SUBSTANCE INDUCING TRANSFORMATION OF PNEUMOCOCCAL TYPES : INDUCTION OF TRANSFORMATION BY A DESOXYRIBONUCLEIC ACID FRACTION ISOLATED FROM PNEUMOCOCCUS TYPE III. J Exp Med. 79(2):137-58.

Ball, G., Demmerle, J., Kaufmann, R., Davis, I., Dobbie, I. M., & Schermelleh, L. (2015). SIMcheck: A toolbox for successful super-resolution structured illumination microscopy. Scientific Reports, 5, 1–11.

Bannister, A. J., & Kouzarides, T. (2011). Regulation of chromatin by histone modifications. Cell Research, 21(3), 381–395.

Bannister, A.J., Zegerman, P., Partridge, J.F., Miska, E.A., Thomas, J.O., Allshire, R.C., and Kouzarides, T. (2001). Selective recognition of methylated lysine 9 on histone H3 by the HP1 chromo domain. Nature 410, 120–124.

Bantignies F1, Cavalli G. (2014). Topological organization of Drosophila Hox genes using DNA fluorescent in situ hybridization. Methods Mol Biol. 1196:103-20.

Bantignies, F., Grimaud, C., Lavrov, S., Gabut, M., & Cavalli, G. (2003). Inheritance of polycomb-dependent chromosomal interactions in Drosophila. Genes and Development, 17(19), 2406–2420.

Bantignies, F., Roure, V., Comet, I., Leblanc, B., Schuettengruber, B., Bonnet, J., … Cavalli, G. (2011). Polycomb-dependent regulatory contacts between distant hox loci in drosophila. Cell, 144(2), 214–226.

Barbieri, M., Chotalia, M., Fraser, J., Lavitas, L.-M., Dostie, J., Pombo, A., & Nicodemi, M. (2012). Complexity of chromatin folding is captured by the strings and binders switch model. Proceedings of the National Academy of Sciences, 109(40), 16173–16178.

Barbieri, M., Xie, S. Q., Torlai Triglia, E., Chiariello, A. M., Bianco, S., De Santiago, I., … Pombo, A. (2017). Active and poised promoter states drive folding of the extended HoxB locus in mouse embryonic stem cells. Nature Structural and Molecular Biology, 24(6), 515–524.

Barrington, C., Georgopoulou, D., Pezic, D., Varsally, W., Herrero, J., & Hadjur, S. (2019). Enhancer accessibility and CTCF occupancy underlie asymmetric TAD architecture and cell type specific genome topology. Nature Communications, 10(1), 2908.

Baù, D., & Marti-Renom, M. A. (2011). Structure determination of genomic domains by satisfaction of spatial restraints. Chromosome Research, 19(1), 25–35.

Bauer, C. R., Hartl, T. A., & Bosco, G. (2012). Condensin II Promotes the Formation of Chromosome Territories by Inducing Axial Compaction of Polyploid Interphase Chromosomes. PLoS Genetics, 8(8), 1–12.

Beagrie, R. A., Scialdone, A., Schueler, M., Kraemer, D. C. A., Chotalia, M., Xie, S. Q., … Pombo, A. (2017). Complex multi-enhancer contacts captured by genome architecture mapping. Nature, 543(7646), 519–524.

Beliveau, B. J., Boettiger, A. N., Avendaño, M. S., Jungmann, R., McCole, R. B., Joyce, E. F., … Wu, C. T. (2015). Single-molecule super-resolution imaging of chromosomes and in situ haplotype visualization using Oligopaint FISH probes. Nature Communications, 6(May).

Beliveau, B. J., Joyce, E. F., Apostolopoulos, N., Yilmaz, F., Fonseka, C. Y., McCole, R. B., … Wu, C. -t. (2012). Versatile design and synthesis platform for visualizing genomes with Oligopaint FISH probes. Proceedings of the National Academy of Sciences, 109(52), 21301–21306.

Beliveau, B. J., Kishi, J. Y., Nir, G., Sasaki, H. M., Saka, S. K., Nguyen, S. C., … Yin, P. (2018). OligoMiner provides a rapid, flexible environment for the design of genome-scale oligonucleotide in situ hybridization probes. Proceedings of the National Academy of Sciences, 115(10), E2183–E2192.

Belmont, A. S., Braunfeld, M. B., Sedat, J. W., & Agard, D. A. (1989). Large-scale chromatin structural domains within mitotic and interphase chromosomes in vivo and in vitro. Chromosoma, 98(2), 129–143.

Benke, A., & Manley, S. (2012). Live-Cell dSTORM of Cellular DNA Based on Direct DNA Labeling. ChemBioChem, 13(2), 298–301.

Bernstein, B. E., Mikkelsen, T. S., Xie, X., Kamal, M., Huebert, D. J., Cuff, J., … Lander, E. S. (2006). A Bivalent Chromatin Structure Marks Key Developmental Genes in Embryonic Stem Cells. Cell, 125(2), 315–

Betzig E., Patterson G. H., Sougrat R., Lindwasser O.W., Olenych S., Bonifacino J.S., … Hess HF. (2006) Imaging intracellular fluorescent proteins at nanometer resolution. Science. 2006 Sep 15;313(5793):1642-5. Epub 2006 Aug 10.

Bianco, S., Annunziatella, C., Andrey, G., Chiariello, A. M., Esposito, A., Fiorillo, L., … Nicodemi, M. (2019). Modeling Single-Molecule Conformations of the HoxD Region in Mouse Embryonic Stem and Cortical Neuronal Cells. Cell Reports, 28(6), 1574-1583.e4.

Bickmore, W. A. (2013). The Spatial Organization of the Human Genome. Annual Review of Genomics and Human Genetics, 14(1), 67–84.

Bintu, B., Mateo, L. J., Su, J. H., Sinnott-Armstrong, N. A., Parker, M., Kinrot, S., … Zhuang, X. (2018). Super-resolution chromatin tracing reveals domains and cooperative interactions in single cells. Science, 362(6413).

Boettiger, A. N., Bintu, B., Moffitt, J. R., Wang, S., Beliveau, B. J., Fudenberg, G., … Zhuang, X. (2016). Super-resolution imaging reveals distinct chromatin folding for different epigenetic states. Nature, 529(7586),

Bohn, M., Diesinger, P., Kaufmann, R., Weiland, Y., Müller, P., Gunkel, M., … Cremer, C. (2010). Localization microscopy reveals expression-dependent parameters of chromatin nanostructure. Biophysical Journal, 99(5),

Bolzer, A., Kreth, G., Solovei, I., Koehler, D., Saracoglu, K., Fauth, C., … Cremer, T. (2005). Three-dimensional maps of all chromosomes in human male fibroblast nuclei and prometaphase rosettes. PLoS Biology, 3(5), 0826–0842.

Bonev, B., Mendelson Cohen, N., Szabo, Q., Fritsch, L., Papadopoulos, G. L., Lubling, Y., … Cavalli, G. (2017). Multiscale 3D Genome Rewiring during Mouse Neural Development. Cell, 171(3), 557-572.e24.

Borsos, M., Perricone, S. M., Schauer, T., Pontabry, J., de Luca, K. L., de Vries, S. S., … Kind, J. (2019). Genome–lamina interactions are established de novo in the early mouse embryo. Nature, 569(7758), 729–733.

Boutanaev, A. M., Mikhaylova, L. M., & Nurminsky, D. I. (2005). The Pattern of Chromosome Folding in Interphase Is Outlined by the Linear Gene Density Profile. Molecular and Cellular Biology, 25(18), 8379–8386.

Boyle S1, Gilchrist S, Bridger JM, Mahy NL, Ellis JA, Bickmore WA. The spatial organization of human chromosomes within the nuclei of normal and emerin-mutant cells. Hum Mol Genet. 2001 Feb 1;10(3):211-9.

Boyle, A. P., Davis, S., Shulha, H. P., Meltzer, P., Margulies, E. H., Weng, Z., … Crawford, G. E. (2008). High-Resolution Mapping and Characterization of Open Chromatin across the Genome. Cell, 132(2), 311–322.

Bradley, C. M., Ronning, D. R., Ghirlando, R., Craigie, R., & Dyda, F. (2005). Structural basis for DNA bridging by barrier-to-autointegration factor. Nature Structural and Molecular Biology, 12(10), 935–936.

Branco, M. R., & Pombo, A. (2006). Intermingling of chromosome territories in interphase suggests role in translocations and transcription-dependent associations. PLoS Biology, 4(5), 780–788.

Brown, J. M., Green, J., & Das Neves, R. P. (2008). Association between active genes occurs at nuclear speckles and is modulated by chromatin environment. Chemtracts, 21(10), 411–413.

Brown, J. M., Leach, J., Reittie, J. E., Atzberger, A., Lee-Prudhoe, J., Wood, W. G., … Buckle, V. J. (2006). Coregulated human globin genes are frequently in spatial proximity when active. Journal of Cell Biology,

Brown, S. W. (1966). Heterochromatin provides a visible guide to suppression. Science, 151(3709), 417–425.

Buchenau, P., Hodgson, J., Strutt, H., & Arndt-Jovin, D. J. (1998). The distribution of polycomb-group proteins during cell division and development in Drosophila embryos: Impact on models for silencing. Journal of Cell Biology, 141(2), 469–481.

Canzio, D., Liao, M., Naber, N., Pate, E., Larson, A., Wu, S., … Narlikar, G. J. (2013). A conformational switch in HP1 releases auto-inhibition to drive heterochromatin assembly. Nature, 496(7445), 377–381.

Cardozo Gizzi, A. M., Cattoni, D. I., Fiche, J. B., Espinola, S. M., Gurgo, J., Messina, O., … Nollmann, M. (2019). Microscopy-Based Chromosome Conformation Capture Enables Simultaneous Visualization of Genome Organization and Transcription in Intact Organisms. Molecular Cell, 74(1), 212-222.e5.

Cattoni, D. I., Gizzi, A. M. C., Georgieva, M., Di Stefano, M., Valeri, A., Chamousset, D., … Nollmann, M. (2017). Single-cell absolute contact probability detection reveals chromosomes are organized by multiple low-frequency yet specific interactions. Nature Communications, 8(1).

Cesarini, E., Mozzetta, C., Marullo, F., Gregoretti, F., Gargiulo, A., Columbaro, M., … Lanzuolo, C. (2015). Lamin A/C sustains PcG protein architecture, maintaining transcriptional repression at target genes. Journal of Cell Biology, 211(3), 533–551.

Cheutin, T., & Cavalli, G. (2018). Loss of PRC1 induces higher-order opening of Hox loci independently of transcription during Drosophila embryogenesis. Nature Communications, 9(1), 1–11.

Chuang, C. H., Carpenter, A. E., Fuchsova, B., Johnson, T., de Lanerolle, P., & Belmont, A. S. (2006). Long-Range Directional Movement of an Interphase Chromosome Site. Current Biology, 16(8), 825–831.

Chubb, J. R., Boyle, S., Perry, P., & Bickmore, W. A. (2002). Chromatin motion is constrained by association with nuclear compartments in human cells. Current Biology, 12(6), 439–445.

Cisse, I. I., Izeddin, I., Causse, S. Z., Boudarene, L., Senecal, A., Muresan, L., … Darzacq, X. (2013). Real-time dynamics of RNA polymerase II clustering in live human cells. Science, 341(6146), 664–667.

Cohen, I., Zhao, D., Bar, C., Valdes, V. J., Dauber-Decker, K. L., Nguyen, M. B., … Ezhkova, E. (2018). PRC1 Fine-tunes Gene Repression and Activation to Safeguard Skin Development and Stem Cell Specification. Cell Stem Cell, 22(5), 726-739.e7.

Cohen, I., Zhao, D., Menon, G., Nakayama, M., Koseki, H., Zheng, D., & Ezhkova, E. (2019). 287 Polycomb repressive complex 1 (PRC1) preserves epidermal tissue integrity independently of PRC2. Genes Dev. 2019 Jan 1;33(1-2):55-60.

Comet, I., Schuettengruber, B., Sexton, T., & Cavalli, G. (2011). A chromatin insulator driving three-dimensional Polycomb response element (PRE) contacts and Polycomb association with the chromatin fiber. Proceedings of the National Academy of Sciences, 108(6), 2294–2299.

Cremer, C., & Cremer, T. (1978). Considerations on a laser-scanning-microscope with high resolution and depth of field. Microscopica Acta, 81(1), 31–44.

Cremer, T., & Cremer, M. (2010). Chromosome territories. Cold Spring Harbor Perspectives in Biology, 2(3), 1–22.

Cremer, M., Küpper, K., Wagler, B., Wizelman, L., Hase, J. V., Weiland, Y., … Cremer, T. (2003). Inheritance of gene density-related higher order chromatin arrangements in normal and tumor cell nuclei. Journal of Cell Biology, 162(5), 809–820.

Croft J. A., Bridger J. M., Boyle S., Perry P., Teague P., Bickmore W. A. (1999). The Journal of Cell Biology Jun 1999, 145 (6) 1119-1131.

Cutter, A., & Hayes, J. (2015). A brief review of nucleosome structure. FEBS Letters. 2015. 589(20 Pt A). 589, 2914–2922.

de Laat, W. (2007). Long-range DNA contacts: romance in the nucleus? Current Opinion in Cell Biology, 19(3), 317–320.

De Wit, E., Bouwman, B. A. M., Zhu, Y., Klous, P., Splinter, E., Verstegen, M. J. A. M., … De Laat, W. (2013). The pluripotent genome in three dimensions is shaped around pluripotency factors. Nature, 501(7466), 227–231.

Dekker, J., Rippe, K., Dekker, M., & Kleckner, N. (2002). Capturing Chromosome Confirmaton. Science, 295(February), 1306–1311.

Dellino GI1, Schwartz YB, Farkas G, McCabe D, Elgin SC, Pirrotta V. Polycomb silencing blocks transcription initiation. Mol Cell. 2004 Mar 26;13(6):887-93.

Demmerle, J., Innocent, C., North, A. J., Ball, G., Müller, M., Miron, E., … Schermelleh, L. (2017). Strategic and practical guidelines for successful structured illumination microscopy. Nature Protocols, 12(5), 988–1010.

Dillon, N. (2004). Heterochromatin structure and function. Biology of the Cell, 96(8), 631–637.

Dixon, J. R., Jung, I., Selvaraj, S., Shen, Y., Antosiewicz-Bourget, J. E., Lee, A. Y., … Ren, B. (2015). Chromatin architecture reorganization during stem cell differentiation. Nature, 518(7539), 331–336.

Dixon, J. R., Selvaraj, S., Yue, F., Kim, A., Li, Y., Shen, Y., … Ren, B. (2012). Topological domains in mammalian genomes identified by analysis of chromatin interactions. Nature, 485(7398), 376–380.

Dostie J., Richmond T. A., Arnaout R. A., Selzer R. R., Lee W. L., Honan T.A., … Dekker J. Chromosome Conformation Capture Carbon Copy (5C): a massively parallel solution for mapping interactions between genomic elements. Genome Res. 2006 Oct;16(10):1299-309. Epub 2006 Sep 5.

Draizen, E. J., Shaytan, A. K., Mariño-Ramírez, L., Talbert, P. B., Landsman, D., & Panchenko, A. R. (2016). HistoneDB 2.0: A histone database with variants - An integrated resource to explore histones and their variants. Database, 2016, 1–10.

Du, Z., Zheng, H., Huang, B., Ma, R., Wu, J., Zhang, X., … Xie, W. (2017). Allelic reprogramming of 3D chromatin architecture during early mammalian development. Nature, 547(7662), 232–235.

Duan, Z., Andronescu, M., Schutz, K., McIlwain, S., Kim, Y.J., Lee, C., Shen- dure, J., Fields, S., Blau, C.A., and Noble, W.S. (2010). A three-dimensional model of the yeast genome. Nature 465, 363–367.

Eagen, K. P. (2018). Principles of Chromosome Architecture Revealed by Hi-C. Trends in Biochemical Sciences, 43(6), 469–478.

Eagen, K. P., Aiden, E. L., & Kornberg, R. D. (2017). Polycomb-mediated chromatin loops revealed by a subkilobase-resolution chromatin interaction map. Proceedings of the National Academy of Sciences, 114(33), 8764–8769.

Ernst, J. & Kellis, M. (2010) Discovery and characterization of chromatin states for systematic annotation of the human genome. Nat. Biotechnol. 28, 817–82.

Ernst, J., Kheradpour, P., Mikkelsen, T. S., Shoresh, N., Ward, L. D., Epstein, C. B., … Bernstein, B. E. (2011). Mapping and analysis of chromatin state dynamics in nine human cell types. Nature, 473(7345), 43–49.

Falk, M., Feodorova, Y., Naumova, N., Imakaev, M., Lajoie, B. R., Leonhardt, H., … Mirny, L. A. (2019). Heterochromatin drives compartmentalization of inverted and conventional nuclei. Nature, 570(7761), 395–399.

Fang, K., Chen, X., Li, X., Shen, Y., Sun, J., Czajkowsky, D. M., & Shao, Z. (2018). Super-resolution Imaging of Individual Human Subchromosomal Regions in Situ Reveals Nanoscopic Building Blocks of Higher-Order Structure. ACS Nano, 12(5), 4909–4918.

Ferraiuolo, M. A., Rousseau, M., Miyamoto, C., Shenker, S., Wang, X. Q. D., Nadler, M., … Dostie, J. (2010). The three-dimensional architecture of Hox cluster silencing. Nucleic Acids Research, 38(21), 7472–7484.

Ramírez F., Ryan D. P., Grüning B., Bhardwaj V., Kilpert F., Richter A. S… Manke1 T. (2016) deepTools2: a next generation web server for deep-sequencing data analysis Nucleic Acids Res. 2016 Jul 8;44(W1):W160-5.

Fields, B. D., Nguyen, S. C., Nir, G., & Kennedy, S. (2019). A multiplexed DNA FISH strategy for assessing genome architecture in Caenorhabditis elegans. ELife, 8, 2014–2016.

Filion, G. J., van Bemmel, J. G., Braunschweig, U., Talhout, W., Kind, J., Ward, L. D., … van Steensel, B. (2010). Systematic Protein Location Mapping Reveals Five Principal Chromatin Types in Drosophila Cells. Cell, 143(2), 212–224.

Finlan LE1, Sproul D, Thomson I, Boyle S, Kerr E, Perry P, Ylstra B, Chubb JR, Bickmore WA. Recruitment to the nuclear periphery can alter expression of genes in human cells. PLoS Genet. 2008 Mar 21;4(3):e1000039.

Finn, E. H., Pegoraro, G., Brandão, H. B., Valton, A. L., Oomen, M. E., Dekker, J., … Misteli, T. (2019). Extensive Heterogeneity and Intrinsic Variation in Spatial Genome Organization. Cell, 176(6), 1502-1515.e10.

Flavahan, W. A., Drier, Y., Liau, B. B., Gillespie, S. M., Venteicher, A. S., Stemmer-Rachamimov, A. O., … Bernstein, B. E. (2016). Insulator dysfunction and oncogene activation in IDH mutant gliomas. Nature, 529(7584), 110–114.

Flyamer, I. M., Gassler, J., Imakaev, M., Brandão, H. B., Ulianov, S. V., Abdennur, N., … Tachibana-Konwalski, K. (2017). Single-nucleus Hi-C reveals unique chromatin reorganization at oocyte-to-zygote transition. Nature, 544(7648), 110–114.

Francis, N. J., Kingston, R. E., & Woodcock, C. L. (2004). Chromatin compaction by a polycomb group protein complex. Science, 306(5701), 1574–1577.

Franke, M., Ibrahim, D. M., Andrey, G., Schwarzer, W., Heinrich, V., Schöpflin, R., … Mundlos, S. (2016). Formation of new chromatin domains determines pathogenicity of genomic duplications. Nature, 538(7624), 265–269.

Fraser, P., & Bickmore, W. (2007). Nuclear organization of the genome and the potential for gene regulation. Nature, 447(7143), 413–417.

Fudenberg, G., & Imakaev, M. (2017). FISH-ing for captured contacts: Towards reconciling FISH and 3C. Nature Methods, 14(7), 673–678.

Fudenberg, G., Imakaev, M., Lu, C., Goloborodko, A., Abdennur, N., & Mirny, L. A. (2016). Formation of Chromosomal Domains by Loop Extrusion. Cell Reports, 15(9), 2038–2049.

Fullwood, M. J., Liu, M. H., Pan, Y. F., Liu, J., Xu, H., Mohamed, Y. Bin, … Ruan, Y. (2009). An oestrogen-receptor-α-bound human chromatin interactome. Nature, 462(7269), 58–64.

Furukawa K., Sugiyama S., Osouda S., Goto H., Inagaki M., Horigome T., … Nishida Y. (2003). Barrier-to-autointegration factor plays crucial roles in cell cycle progression and nuclear organization in Drosophila. J Cell Sci. 2003 Sep 15;116(Pt 18):3811-23

Gan Q1, Schones DE, Ho Eun S, Wei G, Cui K, Zhao K, Chen X. Monovalent and unpoised status of most genes in undifferentiated cell-enriched Drosophila testis. Genome Biol. 2010;11(4):R42.

Gao, Z., Lee, P., Stafford, J. M., Schimmelmann, M. Von, Schaefer, A., & Reinberg, D. (2014). An AUTS2-Polycomb complex activates gene expression in the CNS. Nature, 516(7531), 349–354.

Gaspard, N., Bouschet, T., Herpoel, A., Naeije, G., van den Ameele, J., & Vanderhaeghen, P. (2009). Generation of cortical neurons from mouse embryonic stem cells. Nature Protocols, 4(10), 1456–1463.

Gassler, J., Brandão, H. B., Imakaev, M., Flyamer, I. M., Ladstätter, S., Bickmore, W. A., … Tachibana, K. (2017). A mechanism of cohesin-dependent loop extrusion organizes zygotic genome architecture. The EMBO Journal, 36(24), 3600–3618.

Ghavi-Helm, Y., Jankowski, A., Meiers, S., Viales, R. R., Korbel, J. O., & Furlong, E. E. M. (2019). Highly rearranged chromosomes reveal uncoupling between genome topology and gene expression. Nature Genetics.

Ghavi-Helm, Y., Klein, F. A., Pakozdi, T., Ciglar, L., Noordermeer, D., Huber, W., & Furlong, E. E. M. (2014). Enhancer loops appear stable during development and are associated with paused polymerase. Nature, 512(1),

Gibson, B. A., Doolittle, L. K., Schneider, M. W. G., Jensen, L. E., Gamarra, N., Henry, L., … Rosen, M. K. (2019). Organization of Chromatin by Intrinsic and Regulated Phase Separation. Cell, 1–15.

Giorgetti, L., & Heard, E. (2016). Closing the loop: 3C versus DNA FISH. Genome Biology, 17(1), 1–9.

Giorgetti, L., Galupa, R., Nora, E. P., Piolot, T., Lam, F., Dekker, J., … Heard, E. (2014). Predictive polymer modeling reveals coupled fluctuations in chromosome conformation and transcription. Cell, 157(4), 950–963.

Goetze, S., Mateos-Langerak, J., Gierman, H. J., de Leeuw, W., Giromus, O., Indemans, M. H. G., … van Driel, R. (2007). The Three-Dimensional Structure of Human Interphase Chromosomes Is Related to the Transcriptome Map. Molecular and Cellular Biology, 27(12), 4475–4487.

Gonzalez, I., Mateos-Langerak, J., Thomas, A., Cheutin, T., & Cavalli, G. (2014). Identification of regulators of the three-dimensional polycomb organization by a microscopy-based genome-wide RNAi screen. Molecular Cell, 54(3), 485–499.

Gonzalez-Sandoval, A., Towbin, B. D., Kalck, V., Cabianca, D. S., Gaidatzis, D., Hauer, M. H., … Gasser, S. M. (2015). Perinuclear Anchoring of H3K9-Methylated Chromatin Stabilizes Induced Cell Fate in C. elegans Embryos. Cell, 163(6), 1333–1347.

Grasser, F., Neusser, M., Fiegler, H., Thormeyer, T., Cremer, M., Carter, N. P., … Müller, S. (2008). Replication-timing-correlated spatial chromatin arrangements in cancer and in primate interphase nuclei. Journal of Cell Science, 121(11), 1876–1886.

Grewal, S. I. S., & Jia, S. (2007). Heterochromatin revisited. Nature Reviews Genetics, 8(1), 35–46.

Guelen, L., Pagie, L., Brasset, E., Meuleman, W., Faza, M. B., Talhout, W., … Van Steensel, B. (2008). Domain organization of human chromosomes revealed by mapping of nuclear lamina interactions. Nature, 453(7197), 948–951.

Guo, Y., Xu, Q., Canzio, D., Shou, J., Li, J., Gorkin, D. U., … Wu, Q. (2015). CRISPR Inversion of CTCF Sites Alters Genome Topology and Enhancer/Promoter Function. Cell, 162(4), 900–910.

Gustafsson, M. G. L. (2000). Surpassing the lateral resolution limit by a factor of two using structured illumination microscopy. Journal of Microscopy, 198(2), 82–87.

Gustafsson, M. G. L. (2005). PNAS-2005-Gustafsson-13081-6.pdf. 102(37), 13081–13086.

Gustafsson, M. G. L., Shao, L., Carlton, P. M., Wang, C. J. R., Golubovskaya, I. N., Cande, W. Z., … Sedat, J. W. (2008). Three-dimensional resolution doubling in wide-field fluorescence microscopy by structured illumination. Biophysical Journal, 94(12), 4957–4970.

Haarhuis, J. H. I., van der Weide, R. H., Blomen, V. A., Yáñez-Cuna, J. O., Amendola, M., van Ruiten, M. S., … Rowland, B. D. (2017). The Cohesin Release Factor WAPL Restricts Chromatin Loop Extension. Cell, 169(4), 693-707.e14.

Hansen, A. S., Pustova, I., Cattoglio, C., Tjian, R., & Darzacq, X. (2017). CTCF and cohesin regulate chromatin loop stability with distinct dynamics. ELife, 6, 1–33. https://doi.org/10.7554/eLife.25776

Hartl TA1, Smith HF, Bosco G. Chromosome alignment and transvection are antagonized by condensin II. Science. 2008 Nov 28;322(5906):1384-7.

Heintzman, N. D., Hon, G. C., Hawkins, R. D., Kheradpour, P., Stark, A., Harp, L. F., … Ren, B. (2009). Histone modifications at human enhancers reflect global cell-type-specific gene expression. Nature, 459(7243), 108–112.

Hell SW, Wichmann J. Breaking the diffraction resolution limit by stimulated emission: stimulated-emission-depletion fluorescence microscopy. Opt Lett. 1994 Jun 1;19(11):780-2.

Herz HM1, Mohan M, Garruss AS, Liang K, Takahashi YH, Mickey K, Voets O, Verrijzer CP, Shilatifard A. Enhancer-associated H3K4 monomethylation by Trithorax-related, the Drosophila homolog of mammalian Mll3/Mll4. Genes Dev. 2012 Dec 1;26(23):2604-20.

Hess, S. T., Girirajan, T. P. K., & Mason, M. D. (2006). Ultra-high resolution imaging by fluorescence photoactivation localization microscopy. Biophysical Journal, 91(11), 4258–4272.

Hnisz D., Weintraub A. S., Day D. S., Valton A.L., Bak R.O., Li C.H., … Young R.A. (2016). Activation of proto-oncogenes by disruption of chromosome neighborhoods. Science. 2016 Mar 25;351(6280):1454-1458.

Hnisz, D., Day, D. S., & Young, R. A. (2016b). Insulated Neighborhoods: Structural and Functional Units of Mammalian Gene Control. Cell, 167(5), 1188–1200.

Ho, J. W. K., Jung, Y. L., Liu, T., Alver, B. H., Lee, S., Ikegami, K., … Park, P. J. (2014). Comparative analysis of metazoan chromatin organization. Nature, 512(7515), 449–452.

Hofmann M., Eggeling C., Jakobs S., Hell S. W. (2005). Breaking the diffraction barrier in fluorescence microscopy at low light intensities by using reversibly photoswitchable proteins. Proc Natl Acad Sci U S A. 2005 Dec 6;102(49):17565-9. Epub 2005 Nov 28.

Horike, S. I., Cai, S., Miyano, M., Cheng, J. F., & Kohwi-Shigematsu, T. (2005). Loss of silent-chromatin looping and impaired imprinting of DLX5 in Rett syndrome. Nature Genetics, 37(1), 31–40.

Hou, C., Li, L., Qin, Z. S., & Corces, V. G. (2012). Gene Density, Transcription, and Insulators Contribute to the Partition of the Drosophila Genome into Physical Domains. Molecular Cell, 48(3), 471–484.

Hsieh, T. H. S., Weiner, A., Lajoie, B., Dekker, J., Friedman, N., & Rando, O. J. (2015). Mapping Nucleosome Resolution Chromosome Folding in Yeast by Micro-C. Cell, 162(1), 108–119.

Huang, B., Babcock, H., & Zhuang, X. (2010). Breaking the diffraction barrier: Super-resolution imaging of cells. Cell, 143(7), 1047–1058.

Hug, C. B., Grimaldi, A. G., Kruse, K., & Vaquerizas, J. M. (2017). Chromatin Architecture Emerges during Zygotic Genome Activation Independent of Transcription. Cell, 169(2), 216-228.e19.

Hughes, J. R., Roberts, N., Mcgowan, S., Hay, D., Giannoulatou, E., Lynch, M., … Higgs, D. R. (2014). Analysis of hundreds of cis-regulatory landscapes at high resolution in a single, high-throughput experiment. Nature Genetics, 46(2), 205–212.

Iborra, F. J., Pombo, A., Jackson, D. A., & Cook, P. R. (1996). Active RNA polymerases are localized within discrete transcription "factories'' in human nuclei." Journal of Cell Science, 109 Pt 6, 1427–1436.

Isono, K., Endo, T. A., Ku, M., Yamada, D., Suzuki, R., Sharif, J., … Koseki, H. (2013). SAM domain polymerization links subnuclear clustering of PRC1 to gene silencing. Developmental Cell, 26(6), 565–577.

Javierre B. M., Burren O. S., Wilder S. P., Kreuzhuber R., Hill S. M., Sewitz S., … Fraser P. (2016). Lineage-Specific Genome Architecture Links Enhancers and Non-coding Disease Variants to Target Gene Promoters. Cell. 2016 Nov 17;167(5):1369-1384.e19.

Joyce, E. F., Williams, B. R., Xie, T., & Wu, C. ting. (2012). Identification of genes that promote or antagonize somatic homolog pairing using a high-throughput FISH-based screen. PLoS Genetics, 8(5).

Jung, Y. H., Sauria, M. E. G., Lyu, X., Cheema, M. S., Ausio, J., Taylor, J., & Corces, V. G. (2017). Chromatin States in Mouse Sperm Correlate with Embryonic and Adult Regulatory Landscapes. Cell Reports, 18(6), 1366–

Kassis, J. A., & Brown, J. L. (2013). Polycomb Group Response Elements in Drosophila and Vertebrates. In Advances in Genetics (1st ed., Vol. 81).

Ke, Y., Xu, Y., Chen, X., Feng, S., Liu, Z., Sun, Y., … Liu, J. (2017). 3D Chromatin Structures of Mature Gametes and Structural Reprogramming during Mammalian Embryogenesis. Cell, 170(2), 367-381.e20.

Kent W. J., Zweig A. S., Barber G., Hinrichs A. S., Karolchik D. (2010). BigWig and BigBed: enabling browsing of large distributed datasets. Bioinformatics. 2010 Sep 1;26(17):2204-7

Kharchenko, P. V., Alekseyenko, A. A., Schwartz, Y. B., Minoda, A., Riddle, N. C., Ernst, J., … Park, P. J. (2011). Comprehensive analysis of the chromatin landscape in Drosophila melanogaster. Nature, 471(7339)

Kim, D., Pertea, G., Trapnell, C., Pimentel, H., Kelley, R., & Salzberg, S. L. (2013). TopHat2: Accurate alignment of transcriptomes in the presence of insertions, deletions and gene fusions. Genome Biology, 14(4), R36.

Kind, J., & Steensel, B. Van. (2014). Nucl-5-124. 5(2), 124–130.

Kind, J., Pagie, L., De Vries, S. S., Nahidiazar, L., Dey, S. S., Bienko, M., … Van Steensel, B. (2015). Genome-wide Maps of Nuclear Lamina Interactions in Single Human Cells. Cell, 163(1), 134–147.

Kind, J., Pagie, L., Ortabozkoyun, H., Boyle, S., De Vries, S. S., Janssen, H., … Van Steensel, B. (2013). Single-cell dynamics of genome-nuclear lamina interactions. Cell, 153(1), 178–192.

King, H. W., Fursova, N. A., Blackledge, N. P., & Klose, R. J. (2018). Polycomb repressive complex 1 shapes the nucleosome landscape but not accessibility at target genes. Genome Research, 28(10), 1494–1507.

Klar, T. A., Jakobs, S., Dyba, M., Egner, A., & Hell, S. W. (2000). Fluorescence microscopy with diffraction resolution barrier broken by stimulated emission Physical Principles and Setup. Proc Natl Acad Sci U S A, 97(15), 8206–8210.

Klemm, S. L., Shipony, Z., & Greenleaf, W. J. (2019). Chromatin accessibility and the regulatory epigenome. Nature Reviews Genetics, 20(4), 207–220.

Kouzarides, T. (2007). Chromatin Modifications and Their Function. Cell, 128(4), 693–705.

Kumaran, R. I., & Spector, D. L. (2008). A genetic locus targeted to the nuclear periphery in living cells maintains its transcriptional competence. Journal of Cell Biology, 180(1), 51–65.

Kundu, S., Ji, F., Sunwoo, H., Jain, G., Lee, J. T., Sadreyev, R. I., … Kingston, R. E. (2017). Polycomb Repressive Complex 1 Generates Discrete Compacted Domains that Change during Differentiation. Molecular Cell, 65(3), 432-446.e5.

Küpper, K., Kölbl, A., Biener, D., Dittrich, S., von Hase, J., Thormeyer, T., … Cremer, M. (2007). Radial chromatin positioning is shaped by local gene density, not by gene expression. Chromosoma, 116(3), 285–306.

Lachner, M., O'Carroll, D., Rea, S., Mechtler, K. & Jenuwein, T. Methylation of histone H3 lysine 9 creates a binding site for HP1 proteins. Nature 410, 116–120 (2001).

Lakadamyali, M., & Cosma, M. P. (2015). Advanced microscopy methods for visualizing chromatin structure. FEBS Letters, 589(20), 3023–3030.

Langmead B1, Salzberg SL. Fast gapped-read alignment with Bowtie 2. Nat Methods. 2012 Mar 4;9(4):357-9.

Lanzuolo, C., Roure, V., Dekker, J., Bantignies, F., & Orlando, V. (2007). Polycomb response elements mediate the formation of chromosome higher-order structures in the bithorax complex. Nature Cell Biology, 9(10), 1167–1174.

Lee H. G., Kahn T. G., Simcox A., Schwartz Y. B., Pirrotta V. (2015). Genome-wide activities of Polycomb complexes control pervasive transcription. Genome Res. 2015 Aug;25(8):1170-81.

Lee, C. K., Shibata, Y., Rao, B., Strahl, B. D., & Lieb, J. D. (2004). Evidence for nucleosome depletion at active regulatory regions genome-wide. Nature Genetics, 36(8), 900–905.

Leemans, C., van der Zwalm, M. C. H., Brueckner, L., Comoglio, F., van Schaik, T., Pagie, L., … van Steensel, B. (2019). Promoter-Intrinsic and Local Chromatin Features Determine Gene Repression in LADs. Cell, 177(4), 852-864.e14.

Li H1, Handsaker B, Wysoker A, Fennell T, Ruan J, Homer N, Marth G, Abecasis G, Durbin R; 1000 Genome Project Data Processing Subgroup. The Sequence Alignment/Map format and SAMtools. Bioinformatics. 2009 Aug 15;25(16):2078-9.

Li, Q., Tjong, H., Li, X., Gong, K., Zhou, X. J., Chiolo, I., & Alber, F. (2017). The three-dimensional genome organization of Drosophila melanogaster through data integration. Genome Biology, 18(1).

Lieberman-Aiden, E., Van Berkum, N. L., Williams, L., Imakaev, M., Ragoczy, T., Telling, A., … Dekker, J. (2009). Comprehensive mapping of long-range interactions reveals folding principles of the human genome. Science, 326(5950), 289–293.

Lomvardas, S., Barnea, G., Pisapia, D. J., Mendelsohn, M., Kirkland, J., & Axel, R. (2006). Interchromosomal Interactions and Olfactory Receptor Choice. Cell, 126(2), 403–413.

Loubiere, V., Delest, A., Thomas, A., Bonev, B., Schuettengruber, B., Sati, S., … Cavalli, G. (2016). Coordinate redeployment of PRC1 proteins suppresses tumor formation during Drosophila development. Nature Genetics, 48(11), 1436–1442.

Love, M. I., Huber, W., & Anders, S. (2014). Moderated estimation of fold change and dispersion for RNA-seq data with DESeq2. Genome Biology, 15(12), 1–21.

Luger, K., Dechassa, M. L., & Tremethick, D. J. (2012). New insights into nucleosome and chromatin structure: An ordered state or a disordered affair? Nature Reviews Molecular Cell Biology, 13(7), 436–447.

Luger, K., Mader, A. W., Richmond, R. K., Sargent, D. F. & Richmond, T. J. Crystal structure of the nucleosome core particle at 2.8 Å resolution. Nature 389, 251–260 (1997)

Lupiáñez, D. G., Kraft, K., Heinrich, V., Krawitz, P., Brancati, F., Klopocki, E., … Mundlos, S. (2015). Disruptions of topological chromatin domains cause pathogenic rewiring of gene-enhancer interactions. Cell, 161(5), 1012–1025.

Machida, S., Takizawa, Y., Ishimaru, M., Sugita, Y., Sekine, S., Nakayama, J. ichi, … Kurumizaka, H. (2018). Structural Basis of Heterochromatin Formation by Human HP1. Molecular Cell, 69(3), 385-397.e8.

Maison, C., & Almouzni, G. (2004). HP1 and the dynamics of heterochromatin maintenance. Nature Reviews Molecular Cell Biology, 5(4), 296–304. https://doi.org/10.1038/nrm1355

Margalit, A., Brachner, A., Gotzmann, J., Foisner, R., & Gruenbaum, Y. (2007). Barrier-to-autointegration factor - a BAFfling little protein. Trends in Cell Biology, 17(4), 202–208.

Margalit, A., Neufeld, E., Feinstein, N., Wilson, K. L., Podbilewicz, B., & Gruenbaum, Y. (2007b). Barrier to autointegration factor blocks premature cell fusion and maintains adult muscle integrity in C. elegans. Journal of Cell Biology, 178(4), 661–673.

Margalit, A., Segura-Totten, M., Gruenbaum, Y., & Wilson, K. L. (2005). Barrier-to-autointegration factor is required to segregate and enclose chromosomes within the nuclear envelope and assemble the nuclear lamina. Proceedings of the National Academy of Sciences, 102(9), 3290–3295.

Markaki, Y., Gunkel, M., Schermelleh, L., Beichmanis, S., Neumann, J., Heidemann, M., … Cremer, T. (2010). Functional nuclear organization of transcription and DNA replication: A topographical marriage between chromatin domains and the interchromatin compartment. Cold Spring Harbor Symposia on Quantitative Biology, 75, 475–492.

Markaki, Y., Smeets, D., Fiedler, S., Schmid, V. J., Schermelleh, L., Cremer, T., & Cremer, M. (2012). The potential of 3D-FISH and super-resolution structured illumination microscopy for studies of 3D nuclear architecture: 3D structured illumination microscopy of defined chromosomal structures visualized by 3D (immuno)-FISH opens new perspectives for stud. BioEssays, 34(5), 412–426.

Marshall, W. F., Straight, A., Marko, J. F., Swedlow, J., Dernburg, A., Belmont, A., … Sedat, J. W. (1997). Interphase chromosomes undergo constrained diffusional motion in living cells. Current Biology, 7(12), 930–939.

Mateo, L. J., Murphy, S. E., Hafner, A., Cinquini, I. S., Walker, C. A., & Boettiger, A. N. (2019). Visualizing DNA folding and RNA in embryos at single-cell resolution. Nature, 568(7750), 49–54.

Matsuda, A., Schermelleh, L., Hirano, Y., Haraguchi, T., & Hiraoka, Y. (2018). Accurate and fiducial-marker-free correction for three-dimensional chromatic shift in biological fluorescence microscopy. Scientific Reports, 8(1), 1–3.

Matsuda, A., Shao, L., Boulanger, J., Kervrann, C., Carlton, P. M., Kner, P., … Sedat, J. W. (2010). Condensed mitotic chromosome structure at nanometer resolution using PALM and EGFP- histones. PLoS ONE, 5(9), 1–12.

Mattout, A., & Meshorer, E. (2010). Chromatin plasticity and genome organization in pluripotent embryonic stem cells. Current Opinion in Cell Biology, 22(3), 334–341.

Mayer, R., Brero, A., von Hase, J., Schroeder, T., Cremer, T., & Dietzel, S. (2005). Common themes and cell type specific variations of higher order chromatin arrangements in the mouse. BMC Cell Biology, 6, 1–22.

Meuleman, W., Peric-Hupkes, D., Kind, J., Beaudry, J. B., Pagie, L., Kellis, M., … Van Steensel, B. (2013). Constitutive nuclear lamina-genome interactions are highly conserved and associated with A/T-rich sequence. Genome Research, 23(2), 270–280.

Mifsud, B., Tavares-Cadete, F., Young, A. N., Sugar, R., Schoenfelder, S., Ferreira, L., … Osborne, C. S. (2015). Mapping long-range promoter contacts in human cells with high-resolution capture Hi-C. Nature Genetics, 47(6), 598–606.

Mikkelsen, T. S., Ku, M., Jaffe, D. B., Issac, B., Lieberman, E., Giannoukos, G., … Bernstein, B. E. (2007). Genome-wide maps of chromatin state in pluripotent and lineage-committed cells. Nature, 448(7153), 553–560.

Mizuguchi, T., Fudenberg, G., Mehta, S., Belton, J. M., Taneja, N., Folco, H. D., … Grewal, S. I. S. (2014). Cohesin-dependent globules and heterochromatin shape 3D genome architecture in S. pombe. Nature, 516(7531), 432–435.

Monahan, K., Horta, A., & Lomvardas, S. (2019). LHX2- and LDB1-mediated trans interactions regulate olfactory receptor choice. Nature, 565(7740), 448–453.

Montes De Oca, R., Andreassen, P. R., & Wilson, K. L. (2011). Barrier-to-Autointegration Factor influences specific histone modifications Barrier-to-Autointegration Factor influences specific histone modifications retinoblastoma binding protein 4; 2X-SB, 2X-Sample Buffer. 1(December), 1–11.

Müller J., Hart C. M., Francis N. J., Vargas M. L., Sengupta A., Wild B., … Simon J. A. (2002). Histone methyltransferase activity of a Drosophila Polycomb group repressor complex. Cell. 2002 Oct 18;111(2):197-208.

Murmann, A. E., Gao, J., Encinosa, M., Gautier, M., Peter, M. E., Eils, R., … Rowley, J. D. (2005). Local gene density predicts the spatial position of genetic loci in the interphase nucleus. Experimental Cell Research, 311(1), 14–26.

Murrell, A., Heeson, S., & Reik, W. (2004). Interaction between differentially methylated regions partitions the imprinted genes Igf2 and H19 into parent-specific chromatin loops. Nature Genetics, 36(8), 889–893.

Nagano, T., Lubling, Y., Stevens, T. J., Schoenfelder, S., Yaffe, E., Dean, W., … Fraser, P. (2013). Single-cell Hi-C reveals cell-to-cell variability in chromosome structure. Nature, 502(7469), 59–64.

Nagano, T., Lubling, Y., Várnai, C., Dudley, C., Leung, W., Baran, Y., … Tanay, A. (2017). Cell-cycle dynamics of chromosomal organization at single-cell resolution. Nature, 547(7661), 61–67.

Narendra, V., Rocha, P. P., An, D., Raviram, R., Skok, J. A., Mazzoni, E. O., & Reinberg, D. (2015). CTCF establishes discrete functional chromatin domains at the. Science, 347(6225), 1–6.

Naumova, N., Zhan, Y., Lajoie, B. R., Dekker, J., Imakaev, M., Fudenberg, G., & Mirny, L. A. (2013). Organization of the mitotic chromosome. Science, 342(6161), 948–953.

Nègre, N., Hennetin, J., Sun, L. V., Lavrov, S., Bellis, M., White, K. P., & Cavalli, G. (2006). Chromosomal distribution of PcG proteins during Drosophila development. PLoS Biology, 4(6), 0917–0932.

Durand N. C., Shamim M. S., Machol I., Rao S. S. P., Huntley M. H., … Lieberman-Aiden E. (2016). Juicer provides a one-click system for analyzing loop-resolution Hi-C experiments Cell Syst. 2016 Jul; 3(1): 95–98.

Nir, G., Farabella, I., Pérez Estrada, C., Ebeling, C. G., Beliveau, B. J., Sasaki, H. M., … Wu, C. T. (2018). Walking along chromosomes with super-resolution imaging, contact maps, and integrative modeling. In PLoS Genetics (Vol. 14).

Noordermeer, D., Leleu, M., Splinter, E., Rougemont, J., De Laat, W., & Duboule, D. (2011). The dynamic architecture of Hox gene clusters. Science, 334(6053), 222–225.

Nora, E. P., Goloborodko, A., Valton, A. L., Gibcus, J. H., Uebersohn, A., Abdennur, N., … Bruneau, B. G. (2017). Targeted Degradation of CTCF Decouples Local Insulation of Chromosome Domains from Genomic Compartmentalization. Cell, 169(5), 930-944.e22.

Nora, E. P., Lajoie, B. R., Schulz, E. G., Giorgetti, L., Okamoto, I., Servant, N., … Heard, E. (2012). Spatial partitioning of the regulatory landscape of the X-inactivation centre. Nature, 485(7398), 381–385.

Nozaki, T., Imai, R., Tanbo, M., Nagashima, R., Tamura, S., Tani, T., … Maeshima, K. (2017). Dynamic Organization of Chromatin Domains Revealed by Super-Resolution Live-Cell Imaging. Molecular Cell, 67(2), 282-293.e7.

Nuebler, J., Fudenberg, G., Imakaev, M., Abdennur, N., & Mirny, L. A. (2018). Chromatin organization by an interplay of loop extrusion and compartmental segregation. Proceedings of the National Academy of Sciences, 115(29), E6697–E6706.

Ogiyama, Y., Schuettengruber, B., Papadopoulos, G. L., Chang, J. M., & Cavalli, G. (2018). Polycomb-Dependent Chromatin Looping Contributes to Gene Silencing during Drosophila Development. Molecular Cell, 71(1), 73-88.e5.

Olivares-Chauvet, P., Mukamel, Z., Lifshitz, A., Schwartzman, O., Elkayam, N. O., Lubling, Y., … Tanay, A. (2016). Capturing pairwise and multi-way chromosomal conformations using chromosomal walks. Nature, 540(7632), 296–300.

Osborne, C. S., Chakalova, L., Brown, K. E., Carter, D., Horton, A., Debrand, E., … Fraser, P. (2004). Active genes dynamically colocalize to shared sites of ongoing transcription. Nature Genetics, 36(10), 1065–1071.

Ou, H. D., Phan, S., Deerinck, T. J., Thor, A., Ellisman, M. H., & O'Shea, C. C. (2017). ChromEMT: Visualizing 3D chromatin structure and compaction in interphase and mitotic cells. Science, 357(6349)

Oudelaar, A. M., Davies, J. O. J., Hanssen, L. L. P., Telenius, J. M., Schwessinger, R., Liu, Y., … Hughes, J. R. (2018). Single-allele chromatin interactions identify regulatory hubs in dynamic compartmentalized domains. Nature Genetics, 50(12), 1744–1751.

Palstra, R. J., Tolhuis, B., Splinter, E., Nijmeijer, R., Grosveld, F., & De Laat, W. (2003). The β-globin nuclear compartment in development and erythroid differentiation. Nature Genetics, 35(2), 190–194.

Passarge, E. (1979). Emil Heitz and the concept of heterochromatin: longitudinal chromosome differentiation was recognized fifty years ago. American Journal of Human Genetics, 31(2), 106–115.

Peric-Hupkes, D., Meuleman, W., Pagie, L., Bruggeman, S. W. M., Solovei, I., Brugman, W., … van Steensel, B. (2010). Molecular Maps of the Reorganization of Genome-Nuclear Lamina Interactions during Differentiation. Molecular Cell, 38(4), 603–613.

Pickersgill, H., Kalverda, B., De Wit, E., Talhout, W., Fornerod, M., & Van Steensel, B. (2006). Characterization of the Drosophila melanogaster genome at the nuclear lamina. Nature Genetics, 38(9), 1005–1014.

Plys, A. J., Davis, C. P., Kim, J., Rizki, G., Keenen, M. M., Marr, S. K., & Kingston, R. E. (2019). Phase separation of Polycomb-repressive complex 1 is governed by a charged disordered region of CBX2. Genes & Development, 33(13–14), 799–813.

Puente, X. S., Quesada, V., Osorio, F. G., Cabanillas, R., Cadiñanos, J., Fraile, J. M., … López-Otín, C. (2011). Exome sequencing and functional analysis identifies BANF1 mutation as the cause of a hereditary progeroid syndrome. American Journal of Human Genetics, 88(5), 650–656.

Quinodoz, S. A., Ollikainen, N., Tabak, B., Palla, A., Schmidt, J. M., Detmar, E., … Guttman, M. (2018). Higher-Order Inter-chromosomal Hubs Shape 3D Genome Organization in the Nucleus. Cell, 174(3), 744-757.e24.

Rao, S. S. P., Huntley, M. H., Durand, N. C., Stamenova, E. K., Bochkov, I. D., Robinson, J. T., … Aiden, E. L. (2014). A 3D map of the human genome at kilobase resolution reveals principles of chromatin looping. Cell, 159(7), 1665–1680.

Rao, S., Huang, S.-C., Engreitz, J., Perez, E., Kieffer-Kwon, K.-R., Sanborn, A., … Lander, E. (2017). Cohesin Loss Eliminates All Loop Domains, Leading To Links Among Superenhancers And Downregulation Of Nearby Genes. 139782.

Reddy, K. L., Zullo, J. M., Bertolino, E., & Singh, H. (2008). Transcriptional repression mediated by repositioning of genes to the nuclear lamina. Nature, 452(7184), 243–247.

Redolfi, J., Zhan, Y., Valdes-Quezada, C., Kryzhanovska, M., Guerreiro, I., Iesmantavicius, V., … Giorgetti, L. (2019). DamC reveals principles of chromatin folding in vivo without crosslinking and ligation. Nature Structural and Molecular Biology, 26(6), 471–480.

Ricci, M. A., Manzo, C., García-Parajo, M. F., Lakadamyali, M., & Cosma, M. P. (2015). Chromatin fibers are formed by heterogeneous groups of nucleosomes in vivo. Cell, 160(6), 1145–1158.

Richmond and Davey. (2003). The structure of DNA in the nucleosome core. Nature, 423(6936), 145–150.

Risca, V. I., Denny, S. K., Straight, A. F., & Greenleaf, W. J. (2017). Variable chromatin structure revealed by in situ spatially correlated DNA cleavage mapping. Nature, 541(7636), 237–241.

Robson, M. I., de las Heras, J. I., Czapiewski, R., Lê Thành, P., Booth, D. G., Kelly, D. A., … Schirmer, E. C. (2016). Tissue-Specific Gene Repositioning by Muscle Nuclear Membrane Proteins Enhances Repression of Critical Developmental Genes during Myogenesis. Molecular Cell, 62(6), 834–847.

Rousseau, M., Crutchley, J. L., Miura, H., Suderman, M., Blanchette, M., & Dostie, J. (2014). Hox in motion: Tracking HoxA cluster conformation during differentiation. Nucleic Acids Research, 42(3), 1524–1540.

Rowley, M. J., & Corces, V. G. (2018). Organizational principles of 3D genome architecture. Nature Reviews Genetics, 19(12), 789–800. https://doi.org/10.1038/s41576-018-0060-8

Rowley, M. J., Lyu, X., Rana, V., Ando-Kuri, M., Karns, R., Bosco, G., & Corces, V. G. (2019). Condensin II Counteracts Cohesin and RNA Polymerase II in the Establishment of 3D Chromatin Organization. Cell Reports, 26(11), 2890-2903.e3.

Rowley, M. J., Nichols, M. H., Lyu, X., Ando-Kuri, M., Rivera, I. S. M., Hermetz, K., … Corces, V. G. (2017). Evolutionarily Conserved Principles Predict 3D Chromatin Organization. Molecular Cell, 67(5), 837-852.e7.

Rust, M. J., Bates, M., & Zhuang, X. (2006). Sub-diffraction-limit imaging by stochastic optical reconstruction microscopy (STORM). Nature Methods, 3(10), 793–795.

Saksouk, N., Simboeck, E., & Déjardin, J. (2015). Constitutive heterochromatin formation and transcription in mammals. Epigenetics and Chromatin, 8(1), 1–17.

Samwer, M., Schneider, M. W. G., Hoefler, R., Schmalhorst, P. S., Jude, J. G., Zuber, J., & Gerlich, D. W. (2017). DNA Cross-Bridging Shapes a Single Nucleus from a Set of Mitotic Chromosomes. Cell, 170(5), 956-972.e23.

Sanborn, A. L., Rao, S. S. P., Huang, S.-C., Durand, N. C., Huntley, M. H., Jewett, A. I., … Aiden, E. L. (2015). Chromatin extrusion explains key features of loop and domain formation in wild-type and engineered genomes. Proceedings of the National Academy of Sciences, 112(47), E6456–E6465.

Sati, S., & Cavalli, G. (2017). Chromosome conformation capture technologies and their impact in understanding genome function. Chromosoma, 126(1), 33–44.

Saurin, A. J., Freemont, P. S., Shiels, C., Williamson, J., Sheer, D., Satijn, D. P. E., & Otte, A. P. (1998). The human polycomb group complex associates with pericentromeric heterochromatin to form a novel nuclear domain. Journal of Cell Biology, 142(4), 887–898.

Schermelleh, L., Leonhardt, H., Carlton, P. M., Haase, S., Shao, L., Winoto, L., … Gustafsson, M. G. L. (2008). Subdiffraction multicolor imaging of the nuclear periphery with 3D structured illumination microscopy. Science, 320(5881), 1332–1336.

Schoenfelder S., Furlan-Magaril M., Mifsud B., Tavares-Cadete F., Sugar R., Javierre B. M., … Fraser P. (2015). The pluripotent regulatory circuitry connecting promoters to their long-range interacting elements. Genome Res. 2015 Apr;25(4):582-97.

Schoenfelder, S., Sexton, T., Chakalova, L., Cope, N. F., Horton, A., Andrews, S., … Fraser, P. (2010). Preferential associations between co-regulated genes reveal a transcriptional interactome in erythroid cells. Nature Genetics, 42(1), 53–61.

Schoenfelder, S., Sugar, R., Dimond, A., Javierre, B. M., Armstrong, H., Mifsud, B., … Elderkin, S. (2015). Polycomb repressive complex PRC1 spatially constrains the mouse embryonic stem cell genome. Nature Genetics, 47(10), 1179–1186.

Schuettengruber, B., Bourbon, H. M., Di Croce, L., & Cavalli, G. (2017). Genome Regulation by Polycomb and Trithorax: 70 Years and Counting. Cell, 171(1), 34–57.

Schuettengruber, B., Ganapathi, M., Leblanc, B., Portoso, M., Jaschek, R., Tolhuis, B., … Cavalli, G. (2009). Functional anatomy of polycomb and trithorax chromatin landscapes in Drosophila embryos. PLoS Biology, 7(1).

Schwarzer, W., Abdennur, N., Goloborodko, A., Pekowska, A., Fudenberg, G., Loe-Mie, Y., … Spitz, F. (2017). Two independent modes of chromatin organization revealed by cohesin removal. Nature, 551(7678), 51–56.

Segura-Totten, M., & Wilson, K. L. (2004). BAF: Roles in chromatin, nuclear structure and retrovirus integration. Trends in Cell Biology, 14(5), 261–266.

Servant, N., Varoquaux, N., Lajoie, B. R., Viara, E., Chen, C. J., Vert, J. P., … Barillot, E. (2015). HiC-Pro: An optimized and flexible pipeline for Hi-C data processing. Genome Biology, 16(1), 1–11.

Sexton, T., Yaffe, E., Kenigsberg, E., Bantignies, F., Leblanc, B., Hoichman, M., … Cavalli, G. (2012). Three-dimensional folding and functional organization principles of the Drosophila genome. Cell, 148(3), 458–472.

Shachar, S., Voss, T. C., Pegoraro, G., Sciascia, N., & Misteli, T. (2015). Identification of Gene Positioning Factors Using High-Throughput Imaging Mapping. Cell, 162(4), 911–923.

Shao, Z., Raible, F., Mollaaghababa, R., Guyon, J. R., Wu, C. T., Bender, W., & Kingston, R. E. (1999). Stabilization of chromatin structure by PRC1, a polycomb complex. Cell, 98(1), 37–46.

Shin, H., Shi, Y., Dai, C., Tjong, H., Gong, K., Alber, F., & Zhou, X. J. (2015). TopDom: An efficient and deterministic method for identifying topological domains in genomes. Nucleic Acids Research, 44(7), 1–13.

Shopland, L. S., Lynch, C. R., Peterson, K. A., Thornton, K., Kepper, N., Von Hase, J., … O'Brien, T. P. (2006). Folding and organization of a contiguous chromosome region according to the gene distribution pattern in primary genomic sequence. Journal of Cell Biology, 174(1), 27–38.

Simonis, M., Klous, P., Splinter, E., Moshkin, Y., Willemsen, R., De Wit, E., … De Laat, W. (2006). Nuclear organization of active and inactive chromatin domains uncovered by chromosome conformation capture-on-chip (4C). Nature Genetics, 38(11), 1348–1354.

Skoko, D., Li, M., Huang, Y., Mizuuchi, M., Cai, M., Bradley, C. M., … Mizuuchi, K. (2009). Barrier-to-autointegration factor (BAF) condenses DNA by looping. Proceedings of the National Academy of Sciences, 106(39), 16610–16615.

Smeets, D., Markaki, Y., Schmid, V. J., Kraus, F., Tattermusch, A., Cerase, A., … Cremer, M. (2014). Three-dimensional super-resolution microscopy of the inactive X chromosome territory reveals a collapse of its active nuclear compartment harboring distinct Xist RNA foci. Epigenetics and Chromatin, 7(1), 1–27.

Solovei, I., Cavallo, A., Schermelleh, L., Jaunin, F., Scasselati, C., Cmarko, D., … Cremer, T. (2002). Spatial preservation of nuclear chromatin architecture during three-dimensional fluorescence in situ hybridization (3D-FISH). Experimental Cell Research, 276(1), 10–23.

Solovei, I., Wang, A. S., Thanisch, K., Schmidt, C. S., Krebs, S., Zwerger, M., … Joffe, B. (2013). LBR and lamin A/C sequentially tether peripheral heterochromatin and inversely regulate differentiation. Cell, 152(3), 584–598.

Spielmann, M., Lupiáñez, D. G., & Mundlos, S. (2018). Structural variation in the 3D genome. Nature Reviews Genetics, 19(7), 453–467.

Spilianakis, C. G., Lalioti, M. D., Town, T., Lee, G. R., & Flavell, R. A. (2005). Interchromosomal associations between alternatively expressed loci. Nature, 435(7042), 637–645.

Stadhouders, R., Vidal, E., Serra, F., Di Stefano, B., Le Dily, F., Quilez, J., … Graf, T. (2018). Transcription factors orchestrate dynamic interplay between genome topology and gene regulation during cell reprogramming. Nature Genetics, 50(2), 238–249.

Stevens, T. J., Lando, D., Basu, S., Atkinson, L. P., Cao, Y., Lee, S. F., … Laue, E. D. (2017). 3D structures of individual mammalian genomes studied by single-cell Hi-C. Nature, 544(7648), 59–64.

Stewart, M. D., Li, J., & Wong, J. (2005). Relationship between Histone H3 Lysine 9 Methylation, Transcription Repression, and Heterochromatin Protein 1 Recruitment. Molecular and Cellular Biology, 25(7), 2525–2538.

Sun F., Chronis C., Kronenberg M., Chen X. F., Su T., Lay F. D., … Carey M. F. (2019). Promoter-Enhancer Communication Occurs Primarily within Insulated Neighborhoods. Mol Cell. 2019 Jan 17;73(2):250-263.e5.

Sutherland, H., & Bickmore, W. A. (2009). Transcription factories: Gene expression in unions? Nature Reviews Genetics, 10(7), 457–466.

Symmons, O., Uslu, V. V., Tsujimura, T., Ruf, S., Nassari, S., Schwarzer, W., … Spitz, F. (2014). Functional and topological characteristics of mammalian regulatory domains. Genome Research, 24(3), 390–400.

Szabo, Q., Bantignies, F., & Cavalli, G. (2019). Principles of genome folding into topologically associating domains. Science Advances, 5(4).

Szabo, Q., Jost, D., Chang, J. M., Cattoni, D. I., Papadopoulos, G. L., Bonev, B., … Cavalli, G. (2018). TADs are 3D structural units of higher-order chromosome organization in Drosophila. Science Advances, 4(2).

Szczurek, A., Klewes, L., Xing, J., Gourram, A., Birk, U., Knecht, H., … Cremer, C. (2017). Imaging chromatin nanostructure with binding-activated localization microscopy based on DNA structure fluctuations. Nucleic Acids Research, 45(8), 1–11.

Tan, L., Xing, D., Chang, C. H., Li, H., & Xie, X. S. (2018). Three-dimensional genome structures of single diploid human cells. Science, 361(6405), 924–928.

Tatavosian, R., Kent, S., Brown, K., Yao, T., Duc, H. N., Huynh, T. N., … Ren, X. (2019). Nuclear condensates of the Polycomb protein chromobox 2 (CBX2) assemble through phase separation. Journal of Biological Chemistry, 294(5), 1451–1463.

Thomson, I., Gilchrist, S., Bickmore, W. A., & Chubb, J. R. (2004). The Radial Positioning of Chromatin Is Not Inherited through Mitosis but Is Established de Novo in Early G1. Current Biology, 14(2), 166–172.

Thurman, R. E., Rynes, E., Humbert, R., Vierstra, J., Maurano, M. T., Haugen, E., … Stamatoyannopoulos, J. A. (2012). The accessible chromatin landscape of the human genome. Nature, 489(7414), 75–82.

Tiana, G., & Giorgetti, L. (2018). Integrating experiment, theory and simulation to determine the structure and dynamics of mammalian chromosomes. Current Opinion in Structural Biology, 49, 11–17.

Tolhuis, B., Blom, M., Kerkhoven, R. M., Pagie, L., Teunissen, H., Nieuwland, M., … van Steensel, B. (2011). Interactions among polycomb domains are guided by chromosome architecture. PLoS Genetics, 7(3).

Tolhuis, B., Muijrers, I., De Wit, E., Teunissen, H., Talhout, W., Van Steensel, B., & Van Lohuizen, M. (2006). Genome-wide profiling of PRC1 and PRC2 Polycomb chromatin binding in Drosophila melanogaster. Nature Genetics, 38(6), 694–699.

Tolhuis, B., Palstra, R. J., Splinter, E., Grosveld, F., & De Laat, W. (2002). Looping and interaction between hypersensitive sites in the active β-globin locus. Molecular Cell, 10(6), 1453–1465.

Towbin, B. D., González-Aguilera, C., Sack, R., Gaidatzis, D., Kalck, V., Meister, P., … Gasser, S. M. (2012). Step-wise methylation of histone H3K9 positions heterochromatin at the nuclear periphery. Cell, 150(5), 934–947.

Tsujimura, T., Klein, F. A., Langenfeld, K., Glaser, J., Huber, W., & Spitz, F. (2015). A Discrete Transition Zone Organizes the Topological and Regulatory Autonomy of the Adjacent Tfap2c and Bmp7 Genes. PLoS Genetics, 11(1).

Ulianov, S. V., Doronin, S. A., Khrameeva, E. E., Kos, P. I., Luzhin, A. V., Starikov, S. S., … Shevelyov, Y. Y. (2019). Nuclear lamina integrity is required for proper spatial organization of chromatin in Drosophila. Nature Communications, 10(1), 1–11.

Ulianov, S. V., Gavrilov, A. A., Flyamer, I. M., Razin, S. V., Khrameeva, E. E., Penin, A. A., … Imakaev, M. V. (2016). Active chromatin and transcription play a key role in chromosome partitioning into topologically associating domains. Genome Research, 26(1), 70–84.

Umbarger, M. A., Toro, E., Wright, M. A., Porreca, G. J., Baù, D., Hong, S. H., … Church, G. M. (2011). The three-dimensional architecture of a bacterial genome and its alteration by genetic perturbation. Molecular Cell, 44(2), 252–264.

van Koningsbruggen S., Gierlinski M., Schofield P., Martin D., Barton G. J., Ariyurek Y., … Lamond A. I. (2010). High-resolution whole-genome sequencing reveals that specific chromatin domains from most human chromosomes associate with nucleoli. Mol Biol Cell. 2010 Nov 1;21(21):3735-48.

van Steensel, B., & Belmont, A. S. (2017). Lamina-Associated Domains: Links with Chromosome Architecture, Heterochromatin, and Gene Repression. Cell, 169(5), 780–791.

van Steensel, B., & Furlong, E. E. M. (2019). The role of transcription in shaping the spatial organization of the genome. Nature Reviews Molecular Cell Biology, 20(6), 327–337.

Vangindertael, J., Camacho, R., Sempels, W., Mizuno, H., Dedecker, P., & Janssen, K. P. F. (2018). An introduction to optical super-resolution microscopy for the adventurous biologist. Methods and Applications in Fluorescence, 6(2).

Venkatesh, S., & Workman, J. L. (2015). Histone exchange, chromatin structure and the regulation of transcription. Nature Reviews Molecular Cell Biology, 16(3), 178–189.

Vernimmen, D., Gobbi, M. De, Sloane-Stanley, J. A., Wood, W. G., & Higgs, D. R. (2007). Long-range chromosomal interactions regulate the timing of the transition between poised and active gene expression. EMBO Journal, 26(8), 2041–2051.

Voigt, P., Tee, W. W., & Reinberg, D. (2013). A double take on bivalent promoters. Genes and Development, 27(12), 1318–1338.

Wang L., Brown J. L., Cao R., Zhang Y., Kassis J. A., Jones R. S. (2004). Mol Cell. 2004 Jun 4;14(5):637-46. Hierarchical recruitment of polycomb group silencing complexes.

Wang, J., Jia, S. T., & Jia, S. (2016). New Insights into the Regulation of Heterochromatin. Trends in Genetics, 32(5), 284–294.

Wang, R., Mozziconacci, J., Bancaud, A., & Gadal, O. (2015). Principles of chromatin organization in yeast: Relevance of polymer models to describe nuclear organization and dynamics. Current Opinion in Cell Biology, 34, 54–60.

Wang, S., Wang, S., Su, J. J.-H., Beliveau, B. J., Bintu, B., Moffitt, J. R., … Zhuang, X. (2016). Spatial organization of chromatin domains and compartments in single chromosomes. Science, 353(6299), 598–602.

Wani, A. H., Boettiger, A. N., Schorderet, P., Ergun, A., Munger, C., Sadreyev, R. I., … Francis, N. J. (2016). Chromatin topology is coupled to Polycomb group protein subnuclear organization. Nature Communications, 7.

Watson, J. D., & Crick, F. H. C. (2016). Molecular structure of nucleic acids: A Structure for deoxyribose nucleic acid. 50 Years of DNA, (4356), 83–84.

Wei Z., Gao F., Kim S., Yang H., Lyu J., An W., … Lu W. (2013). Klf4 organizes long-range chromosomal interactions with the oct4 locus in reprogramming and pluripotency. Cell Stem Cell. 2013 Jul 3;13(1):36-47.

Weischenfeldt, J., Dubash, T., Drainas, A. P., Mardin, B. R., Chen, Y., Stütz, A. M., … Korbel, J. O. (2017). Pan-cancer analysis of somatic copy-number alterations implicates IRS4 and IGF2 in enhancer hijacking. Nature Genetics, 49(1), 65–74.

Woodcock, C. L., & Ghosh, R. P. (2010). Chromatin higher-order structure and dynamics. Cold Spring Harbor Perspectives in Biology, 2(5).

Würtele, H., & Chartrand, P. (2006). Genome-wide scanning of HoxB1-associated loci in mouse ES cells using an open-ended Chromosome Conformation Capture methodology. Chromosome Research, 14(5), 477–495.

Xu J, Carter AC, Gendrel AV, Attia M et al. Landscape of monoallelic DNA accessibility in mouse embryonic stem cells and neural progenitor cells. Nat Genet 2017 Mar;49(3):377-386

Xu, J., Ma, H., Jin, J., Uttam, S., Fu, R., Huang, Y., & Liu, Y. (2018). Super-Resolution Imaging of Higher-Order Chromatin Structures at Different Epigenomic States in Single Mammalian Cells. Cell Reports, 24(4), 873–882.

Zessin, P. J. M., Finan, K., & Heilemann, M. (2012). Super-resolution fluorescence imaging of chromosomal DNA. Journal of Structural Biology, 177(2), 344–348.

Zhan, Y., Mariani, L., Barozzi, I., Schulz, E. G., Blüthgen, N., Stadler, M., … Giorgetti, L. (2017). Reciprocal insulation analysis of Hi-C data shows that TADs represent a functionally but not structurally privileged scale in the hierarchical folding of chromosomes Genome Res. Mar;27(3):479-490.

Zhang, H., Jiao, W., Sun, L., Fan, J., Chen, M., Wang, H., … Hu, J. F. (2013). Intrachromosomal looping is required for activation of endogenous pluripotency genes during reprogramming. Cell Stem Cell, 13(1), 30–35.

Zhao, Z., Tavoosidana, G., Sjölinder, M., Göndör, A., Mariano, P., Wang, S., … Ohlsson, R. (2006). Circular chromosome conformation capture (4C) uncovers extensive networks of epigenetically regulated intra- and interchromosomal interactions. Nature Genetics, 38(11), 1341–1347.

Zheng, M., Tian, S. Z., Capurso, D., Kim, M., Maurya, R., Lee, B., … Ruan, Y. (2019). Multiplex chromatin interactions with single-molecule precision. Nature, 566(7745), 558–562.

Zheng, X., Hu, J., Yue, S., Kristiani, L., Kim, M., Sauria, M., … Zheng, Y. (2018). Lamins Organize the Global Three-Dimensional Genome from the Nuclear Periphery. Molecular Cell, 71(5), 802-815.e7.